Universidad Autónoma de Madrid (UAM)
Facultad de Ciencias
Departamento de Física de la Materia Condensada

Formation of ordered III-V semiconductor nanostructures by different technological approaches

Memoria para optar al grado de Doctor en Ciencias Físicas presentada por:

Pablo Alonso González

Dirigida por la doctora:

Luisa González Sotos

Instituto de Microelectrónica de Madrid
Centro Nacional de Microelectrónica
Consejo Superior de Investigaciones Científicas

Tres Cantos, Madrid
Junio de 2009

La presente Tesis Doctoral ha sido llevada a cabo gracias a la financiación por parte del Consejo Superior de Investigaciones Científicas (CSIC) a través de una beca predoctoral I3P.

Esta Tesis Doctoral ha sido realizada en:

Instituto de Microeléctronica de Madrid (IMM-CNM-CSIC)

C/ Isaac Newton 8 (PTM), 28760 Tres Cantos (Madrid)

Summary

III-V semiconductor nanostructures show high potential as active elements in the fabrication of new generation devices in the quantum information technology field. The fabrication of nanostructures with simultaneous control of size (emission wavelength), density and surface location is an essential requisite in these technological approximations. As it is well known, self assembling processes during epitaxial growth provide random distributions of nanostructures with high optical quality. However, the simultaneous control of density, size and surface location of the formed nanostructures is not straightforward. In order to overcome these inherent constraints of spontaneous growth processes, the aim of the work in this thesis is to develop novel technological processes to fabricate patterned motives on the substrate that provide preferential sites for the posterior nucleation of high optical quality semiconductor nanostructures.
In this direction, this work presents results on the growth of position controlled III-V semiconductor nanostructures by using three different strategies to fabricate distributions of nanoholes on GaAs (001) and InP (001) substrates.

The first technique developed in this work is based on the formation of a monolithically integrated ordered porous alumina mask, by the electrochemical anodization of an aluminum layer epitaxially grown on the GaAs (001) substrate. By extending the electrochemical process a few nanometers in the substrate, a large area distribution of nanoholes was finally obtained.

In a second technological approximation, a mask fabricated by an external lithographic technique (laser interference lithography) on a resin layer deposited on the substrate was used to transfer its pattern to the substrate itself. The more relevant contribution of this work has been the development of a novel method based on the ozone selective oxidation of the underlying semiconductor substrate that permit to nucleate ordered quantum dots with high optical quality.

Finally, a novel *in situ* (into the MBE chamber) patterning technique based on the droplet epitaxy growth technique has been developed to form low density nanoholes ($2x10^8$ cm^{-2}) templates on GaAs (001) and InP (001) substrates. Once fabricated, these templates are further used for the formation of different low density III-V semiconductor nanostructures, as InAs quantum dots and InAs quantum dot molecules in lateral and vertical configuration, with a certain control of their size, aspect ratio and composition. Also, by varying the element V pressure used during the patterning process, type II Ga(As)Sb quantum rings have been obtained on GaAs(001) substrates.

An appropriate capping process of these low density III-V nanostructures, has resulted in a GaAs top surface with a characteristic mounding morphology that permits a direct localization of buried nanostructures even at cap layer thickness as large as 100nm.

Resumen

La formación de nanoestructuras semiconductoras III-V con control en forma, tamaño, densidad y localización espacial es fundamental para desarrollar con éxito dispositivos cuánticos avanzados, en los que es necesario ubicar una nanoestructura emisora de luz en el máximo del campo electromagnético de una microcavidad óptica. Debido a su carácter aleatorio, las técnicas de auto-ensamblado no permiten obtener un control preciso de estas propiedades en nanoestructuras semiconductoras. Mediante esta técnica de crecimiento se obtienen nanoestructuras que normalmente presentan una cierta relación densidad-tamaño prefijada a la vez que se forman con una distribución espacial aleatoria. Una estrategia bastante común para superar estos inconvenientes inherentes al proceso de formación espontánea de puntos cuánticos es el crecimiento de en substratos previamente grabados.

En este contexto, el trabajo que se presenta en esta memoria aborda tres procesos tecnológicos distintos que, mediante el uso de técnicas de pregrabado *ex situ* y técnicas específicas de crecimiento *in situ*, permiten diseñar nuevas nanoestructuras semiconductoras con cierto control en sus propiedades de emisión, densidad, composición y localización espacial.

La primera técnica desarrollada y presentada en este trabajo se basa en la formación de una máscara de alúmina porosa obtenida a partir de la anodización electroquímica de una capa epitaxial de aluminio crecida sobre un substrato de GaAs (001). Continuando el proceso electroquímico en el substrato semiconductor se ha conseguido fabricar un patrón de nanoagujeros en área extensa.

En una segunda aproximación tecnológica se han utilizado máscaras previamente fabricadas por litografía de interferencia láser con el objetivo de transferir su diseño ordenado al substrato semiconductor y así poder obtener distribuciones ordenadas de puntos cuánticos de InAs. En el contexto de esta aproximación se ha desarrollado un sistema experimental para la oxidación selectiva de substratos de GaAs (001) e InP (001) que ha permitido la formación de puntos cuánticos ordenados de alta calidad óptica.

Como última aproximación tecnológica se ha utilizado una novedosa técnica de grabado *in situ* (dentro de la campana de crecimiento) basada en la técnica de crecimiento por epitaxia de gotas (del inglés *droplet epitaxy*) que permite la formación de distribuciones de nanoagujeros de baja densidad ($2x10^8$ cm^{-2}) sobre substratos de GaAs (001) e InP (001). Una vez formados los nanoagujeros, estos son utilizados como centros de nucleación selectiva de InAs para la formación de puntos cuánticos de baja densidad con control en tamaño y el diseño de moléculas de puntos cuánticos en configuración lateral y vertical. También, mediante el uso de antimonio en el proceso de grabado de los nanoagujeros se ha conseguido la formación de anillos cuánticos de Ga(As)Sb sobre substratos de GaAs (001).

Finalmente, el proceso de crecimento a baja temperatura desarrollado para cubrir estas nanoestructuras de baja densidad ha permitido mantener su morfología en forma de montículo superficial permitiendo su localización final.

Index of contents

Chapter 1: Introduction

Chapter 2: Experimental techniques

Chapter 3: *Ex situ* patterning technologies

Chapter 4: *In situ* patterning technique by droplet epitaxy

Chapter 5: Conclusions

1

INTRODUCTION

1. INTRODUCTION

In this chapter the main properties and fabrication methods by self-assembling processes of the different III-V semiconductor nanostructures grown in this thesis are described. The main drawbacks that this standard growth process presents for the optimal integration of these nanostructures as active elements in novel devices are described in section 1.1.3. This section is in itself an introduction to the necessity of developing novel technological approximations for the patterning of semiconductor substrates in order to obtain the selective growth of nanostructures with control in shape, size, density and spatial location. Finally, section 1.2 concludes this chapter with the thesis outline.

1.1. III-V semiconductor nanostructures

In this section the properties of the different semiconductor nanostructures grown by molecular beam epitaxy (MBE) in this work are described in detail. In particular, section 1.1.2 presents an extensive overview of the properties and fabrication methods of quantum dots (QD), quantum dot molecules (QDM) and quantum rings (Qrings). Next, a brief description of the main drawbacks that self-assembling processes of these nanostructures present for their integration as active elements in novel devices is presented.

1.1.1. Semiconductor heterostructures

Semiconductor heterostructures are the basis of the majority of the current electronic and opto-electronic devices. These heterostructures consist in the deposition of superimposed thin layers of different semiconductors following a pre-established order. The great potential of semiconductor heterostructures was firstly demonstrated in 1969 by Esaki and Tsu [1]. The use of these heterostructures has many advantages as the possibility of controlling the spatial confinement of charge carriers, the design of waveguides and optical resonators or the fabrication of structures that permit to emit or absorb light at a desired wavelength.

Figure 1.1 shows a graph with the band-gap energy and lattice constant of various semiconductor materials that can be combined in a heterostructure. The lines that connect the binary compounds of groups III-V and II-VI (black dots) represent ternary semiconductor materials. Two kind of heterostructures can be distinguished depending on whether the lattice constant of the used materials is the same or not. The growth of materials with the same lattice constant was the most used initially due to the absence of strain between the layers that form the structure. However, the epitaxial growth has to be carried out on commercial substrates that present high structural and optical quality (Si, GaAs, InP, GaP, GaSb, ZnSe...), which restricts the accessible lattice constants in the growth of heterostructures without strain. Due to this

limitation and the demand of devices at certain wavelengths, it was initiated the growth of heterostructures of terials with different lattice constants.

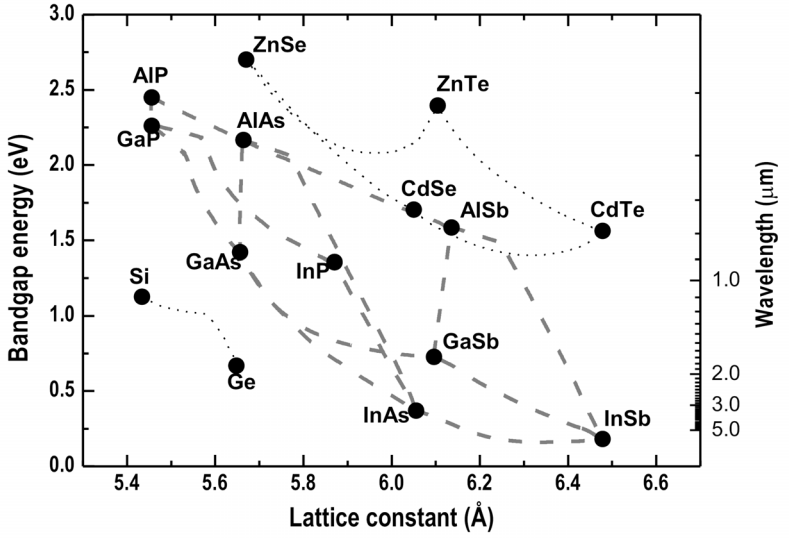

Figure 1.1. Bandgap energy and lattice constant of various semiconductor materials (black dots) and their alloys (lines).

There are three well-known modes of heteroepitaxial growth: Frank-van der Merwe (FvdM) [2], Volmer-Weber (VW) [3] and Stranski-Krastanow (SK) [4]. As shown in **Figure 1.2**, they represent layer-by-layer growth (FvdM, 2D), island growth (VW, 3D) and layer-by-layer plus islands (SK).

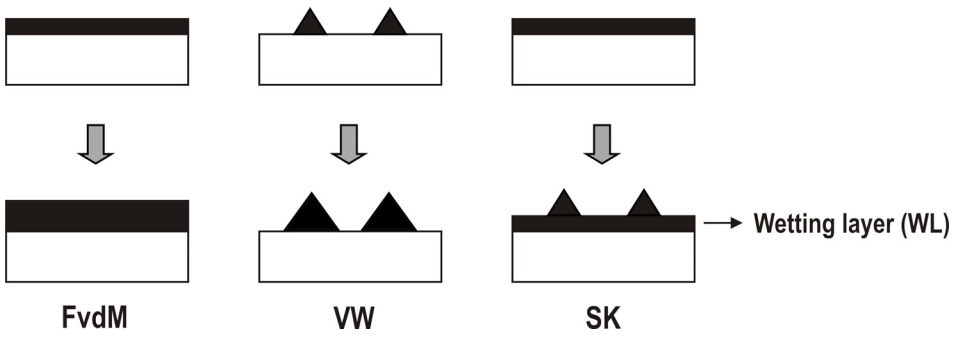

Figure 1.2. Schematic diagrams of the three possible growth modes: Frank-van der Merwe (FvdM), Volmer-Weber (VW) and Stranski-Krastanow (SK).

The particular growth mode for a given system depends on the surface energies of both materials, the interface energies and on the lattice mismatch. In lattice-matched systems, the growth mode is solely governed by the balance between the interface and surface energies. If the sum of the epilayer surface

energy γ_2 and of the interface energy γ_{12} is lower than the energy of the substrate surface, $\gamma_2 + \gamma_{12} < \gamma_1$, i.e., if the deposited material wets the substrate, the FvdM mode occurs. A change in $\gamma_2 + \gamma_{12}$ alone may drive a transition from the FvdM to the VW growth mode. SK growth mode is an intermediate situation where the initial growth occurs layer-by-layer (FvdM) but, as the thickness of the layer increases a strain energy is built-in; in that situation the system can lower its energy by forming 3D nuclei in which strain is relaxed. This last growth mode occurs when an epitaxial layer is grown with a different lattice constant to the substrate. At the beginning of the growth, the epitaxial layer grows coupled to the lattice constant of the substrate suffering a tetragonal deformation due to the biaxial strain (wetting layer in **Figure 1.2**). During this layer-by-layer growth the elastic energy increases linearly up to a critical thickness of material deposited. This critical thickness depends on the material properties and the growth conditions as substrate temperature and growth rate. From this critical thickness the energy accumulated on the layer is high enough to induce the apparition of relaxing mechanisms. This relaxing effect can be a plastic deformation by the formation of dislocations, or elastic, by the formation of 3D nuclei at the surface and coherent to the substrate (the lattice constant in the interface plane of these nuclei is the same of the substrate at their interface). These heterostructures formed by a flat layer and 3D nuclei on the surface have dimensions of several nanometers and are named as self-assembled nanostructures. The term "self-assembled" is related to the formation process that leads to nanostructures with characteristic size and spatial distribution driven by strain-mediated epitaxial growth. When these semiconductor nanostructures are embedded in a semiconductor with a wider band-gap, quantum confinement effects of carriers appear. These kind of structures, or quantum nanostructures, are then of high technological interest in the design of different opto-electronic devices.

Next section presents a brief description of the special properties of various quantum nanostructures.

1.1.2. Semiconductor nanostructures

Quantum effects start to be remarkable when the size of the structure is reduced on at least one of its dimensions on a length scale smaller than the *De Broglie* wavelength [5]. The *De Broglie* wavelength λ depends on the effective mass m^* of the carrier and on the temperature T as follows:

$$\lambda = \frac{h}{p} = \frac{h}{\sqrt{\left(3m^* k_B T\right)}} = \frac{1.22\,nm}{\sqrt{\left(E_{kin}/[eV]\right)}} \qquad \textbf{Equation (1.1)}$$

The mass of charged carriers entering **Equation (1.1)** is not the free electron mass but the effective mass of the electron (or hole) in the crystal. As this mass can be much smaller than the free electron mass, size quantization effects can be already observed at a thickness ten to a hundred times larger than the lattice

constant. For the case of the electron in InAs, which effective mass is 0.023 m_0, quantum effects could be observed for thicknesses smaller than 100 nm at 100 K or 50 nm at room temperature (RT).

The first studied heterostructures with quantum confinement were quantum wells (QW). A simple way to obtain quantum confinement is to fabricate a QW formed by a semiconductor layer with nanometric thickness embedded in a semiconductor with a wider band-gap. These semiconductor heterostructures provide a potential well for carriers. **Figure 1.3** shows schematically the energy bands structure for a type I QW where the electrons and holes are confined in the semiconductor with a narrower gap (semiconductor B in the figure).

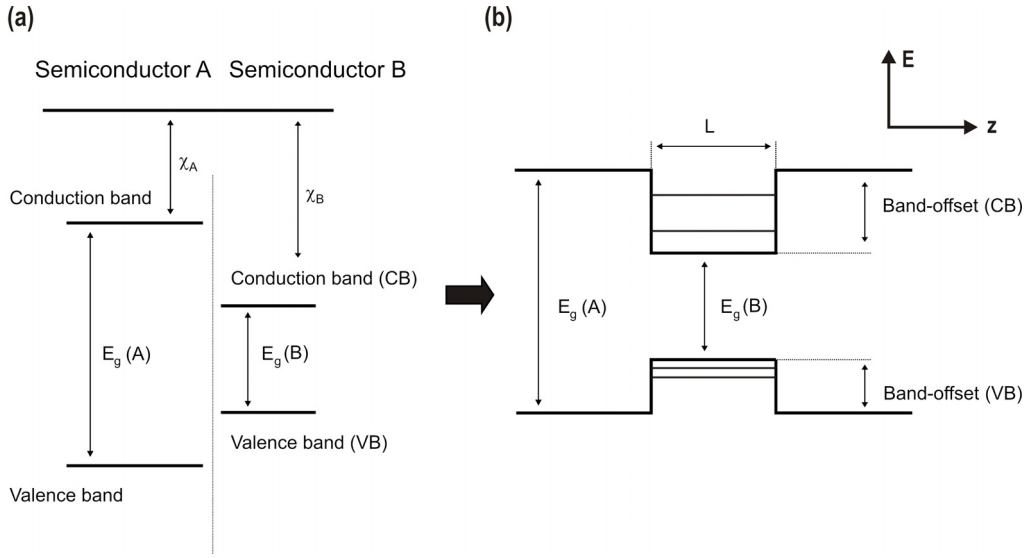

Figure 1.3. (a) Energy bands structure for two different semiconductors A and B. The band-gap of semiconductor A (E_g(A)) is wider than that of semiconductor B (E_g(B)). χ_A and χ_B are the electronic affinities for semiconductor A and B, respectively. **(b)** Band-offsets of the quantum well that results after growing the semiconductor B embedded in the semiconductor A. The energies of the subbands within the well are shown schematically.

The resulting band-offsets are intrinsic properties of the two materials involved. The narrower-gap material forms a one-dimensional potential well in the conduction and valence bands; thus, in the z (growth) direction, the electron and hole levels are bound states of the well, known as subbands. It is possible to solve the Schrödinger equation in one dimension for a quantum well and obtain the stationary states (eigenstates) for electrons and holes, which determine the corresponding QW optical transitions. In general, it is obtained that the thinner is the layer with lower bandgap (L in **Figure 1.3**); the larger is the energy for the confined states.

By the end of the 80s the main properties of quantum wells were rather well understood and the interest shifted toward structures with further reduced dimensionality, i.e., to quantum wires (QWr) and quantum dots. Complete reduction of the remaining “infinite” extension of a quantum well in two

dimensions to a nanometer level leads to carrier localization in all three dimensions. The main effect of the quantum confinement is to modify the energy spectrum and the density of states. The electrons in a bulk semiconductor material, or 3D structure, can have any energy above the band-gap energy E_g and the density of states is given by:

$$\frac{dN}{dE} \alpha \frac{d}{dE} E^{\frac{3}{2}} = E^{\frac{1}{2}} \quad , \qquad \textbf{Equation (1.2)}$$

this is a consequence of the free motion in all three dimensions (**Figure 1.4 (a)**). The effective dimensionality of the system decreases as the electrons are confined in each new direction, which alters the functional form of the density of states and increases the effective band-gap. For a QW (2D) it is obtained a step function (**Figure 1.4 (b)**):

$$\frac{dN}{dE} \alpha \frac{d}{dE} \sum_{\varepsilon_i < E} (E - \varepsilon_i) = \sum_{\varepsilon_i < E} 1 \quad , \qquad \textbf{Equation (1.3)}$$

for a QWr (1D) peaks (**Figure 1.4 (c)**) given by:

$$\frac{dN}{dE} \alpha \frac{d}{dE} \sum_{\varepsilon_i < E} (E - \varepsilon_i)^{1/2} = \sum_{\varepsilon_i < E} (E - \varepsilon_i)^{-1/2} \qquad \textbf{Equation (1.4)}$$

· Quantum dots

In QD (0D) the carrier motion is quantized in all three directions and there are no continuous bands at all. The density of states consists of a series of Dirac-δ functions at each quantized level:

$$\frac{dN}{dE} \alpha \frac{d}{dE} \sum_{\varepsilon_i < E} \Theta(E - \varepsilon_i) = \sum_{\varepsilon_i < E} \partial(E - \varepsilon_i) \qquad \textbf{Equation (1.5)}$$

The resulting energy level structure of QD is discrete (**Figure 1.4 (d)**), like in atomic physics, and the physical properties of QD resemble of those of an atom in a cage. Accordingly, QD are called “artificial atoms”. The band offsets of the conduction band (CB) and valence band (VB) for a QD of material A embedded in a matrix of material B ($E_g(A)<E_g(B)$) are shown in **Figure 1.5**. Due to the quantum confinement, the electron energy level (E_e) and the heavy hole energy level (E_{hh}) are quantized and lifted relative to the band edges of the bulk material. Quantization energies of both electron and heavy hole depend on the QD size, shape and composition, as well as intrinsic QD and matrix material properties. As it will be commented hereinafter, a control over these parameters is of high technological interest.

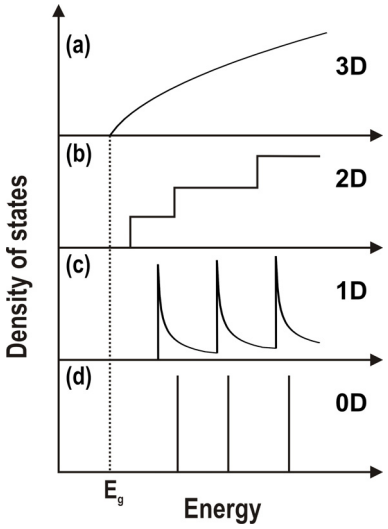

Figure 1.4. Generic shape of the density of states function for electrons in the conduction band of a semiconductor with band-gap E_g for: **(a)** the bulk material, **(b)** quantum well (QW), **(c)** quantum wire (QWr) and **(d)** quantum dot (QD).

When electron and hole are confined in a QD, the Coulomb attraction can bind them together if their binding energy is larger than the thermal energy k_BT. The electron-hole pair can then be described as a quasiparticle, i.e., an exciton. Annihilation of an exciton by electron-hole recombination provides a single photon emission. Due to the Pauli Exclusion Principle each level in the dot can accommodate just two carriers (of different spin), as shown in **Figure 1.5**. Electrons and holes can be produced in a dot either by electrical injection or by photo-exciting an electron from the valence band into the conduction band, leaving a hole in the valence band. Photo-excited carriers are usually created in the bulk material (above band excitation) and the generated electrons and holes relax after a short time into lower energy levels as those provided by QD.

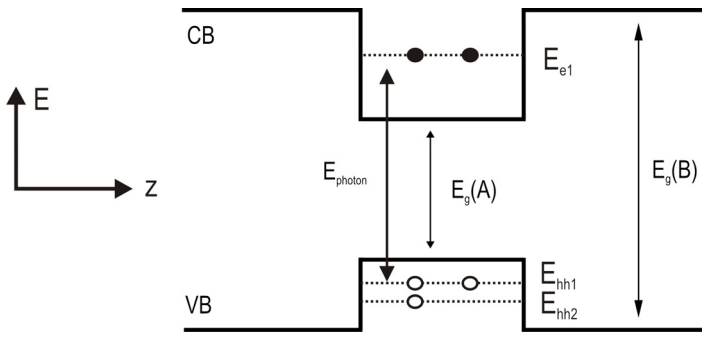

Figure 1.5. Simplified band diagram showing two electrons (black circles) and three heavy holes (open circles) confined in a quantum dot of material A, which is embedded in a material B. Conduction (CB) and valence (VB) bands are labelled.

Figure 1.6 shows schematically the different electron-hole species that usually are formed in a QD [6]. When a QD confines a single electron-hole pair with a total angular momentum m= ±1 (m= s_z+j_z, where

the heavy hole has a total angular momentum of j= ±3/2 and an electron has a spin of s= ±1/2) decay to the ground state through the emission of a single photon is possible and the state is known as a bright exciton (X_b). Conversely if the momentum of the pair is ±2 then simple single photon radiative decay is forbidden and the state is known as a dark exciton (X_d). **Figure 1.6 (a)** and **Figure 1.6 (b)** illustrates examples of these states. **Figure 1.6 (c)** shows the formation of a negatively charged exciton that is called trion (X^-). **Figure 1.6 (d)** consists of a pair of anti-aligned electrons and a pair of anti-aligned holes and is called biexciton (XX).

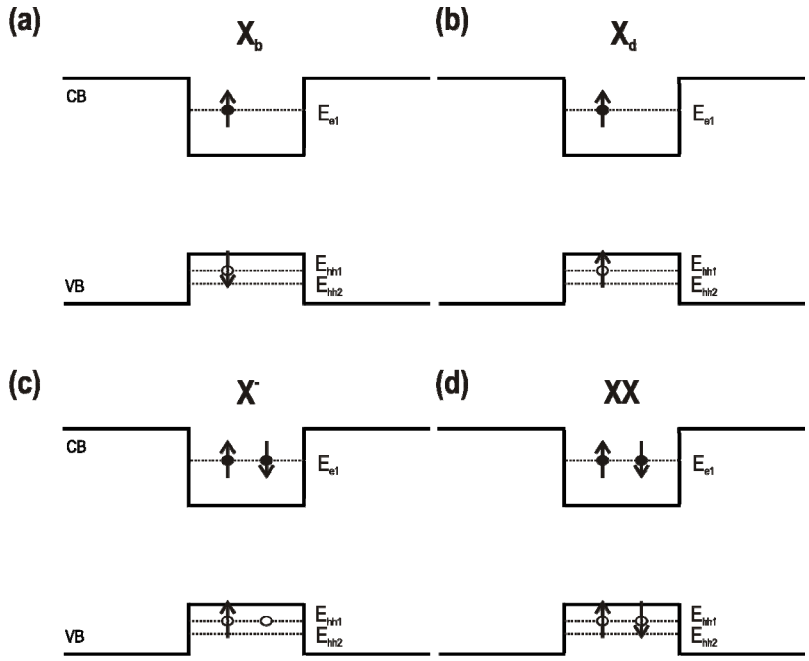

Figure 1.6. Illustrating examples of **(a)** a bright exciton (X_b), **(b)** a dark exciton (X_d), **(c)** a negatively charged exciton (X^-) and **(d)** a biexciton (XX).

QD have some subtle but important differences with respect to real atoms for potential applications. The emission properties of a QD can be adjusted by changing its structure. Once the QD are fabricated, their positions are permanently defined in the host matrix. In addition, the matrix containing QD can be further processed and functionalized using well-developed semiconductor technology. This allows QD to be incorporated in semiconductor devices such as light emitting diodes [7,8], lasers [7,9] and field effect transistors [10].

Recently, semiconductor QD have been widely used in devices with novel functionalities in the quantum optics field [11]. For instance, non-classical light sources using semiconductor QD as single photon emitters have been demonstrated [12-15]. Both electrical and optical injection can deterministically trigger the emission of a single photon. Single photon sources are interesting in the field of optical data communication, where data can be securely transmitted based on quantum cryptography schemes [16].

In solid-state cavity quantum electrodynamics experiments, excitonic states in semiconductor QD have been considered as two-level systems. Optical resonators have been fabricated around the QD in order to couple the optical modes to the excitonic states. In this direction, weak and strong coupling between excitonic and photonic states have been progressively investigated [17-21]. In the strong coupling regime, this coupled system can be used to coherently manipulate the excitonic states. This has been proposed as a promising building block for quantum information processing [22]. The qbit (quantum bit) defined by excitonic states can be initialized and modified by optical pulses. Entangled photons can also be generated [23]. The study of qbit operation and entangled states is indispensable for future use of QD in quantum communication and quantum computation [16].

Fabricating quantum dots

For the fabrication of QD on semiconductor materials, three main approximations have been tackled:

1. Fabrication processes based on lithographic techniques and chemical etching after epitaxial growth.
2. Fabrication processes based on self-assembling mechanisms.
3. Selective epitaxial growth on patterned substrates.

The first approximation uses different lithographic technologies once carried out the epitaxial growth of the bulk material [24-27]. This is generally known as a *top-down* approach. A two dimensional QW can be dimensionally reduced to a QD by etching around an area to leave a free standing pillar that contains a QW of reduced area in the structure. If the diameter of the pillar is less than the *De Broglie* wavelength then a QD will be formed.

This method of QD fabrication has been well studied because it utilises standard processing techniques; optical, X-ray, electron and focused ion beam lithography can all be used to pattern a QW sample, followed by a wet/dry etch stage leaves the QD. The main inconvenient of this fabrication method is that etching is usually a very destructive process incorporating different contaminants, also the rough air/semiconductor surface on the side of the pillar causes a large carrier-depleted region around the interface, Fermi level pinning by surface states often results in a significant residual electric field across a pillar and the etching can also leave a residual strain field. Finally, the density of nanostructures that can be obtained by these lithographic techniques are conditioned by their own limitation in spatial resolution.

The second approximation based on self-assembling mechanisms has already been commented. When a thin layer of a semiconductor is grown on top of another semiconductor which is lattice mismatched to the first, after a few monolayers (1.7 ML in our system for the InAs/GaAs system) the strain

built-in by the lattice mismatch causes the grown layer to form small islands and QD for elastic energy relaxation, the final result is that 3D nuclei appear on the 2D layer grown. This is the known Stranski-Krastanov growth technique and is illustrated in **Figure 1.2**. After growth of the QD layer the sample is usually capped by a thick layer of the first material. The QD are left embedded with no air-semiconductor interface and hence they do not generally suffer from the problems encountered with etched QD. The exact shape and size of the dots formed by the SK growth technique is a function of growth conditions and can greatly change their fundamental properties. A large number of QD are created in one sample by this technique, normally $1x10^{10}$ cm^{-2}, though this can be partially controlled by varying the growth conditions. One of the drawbacks of this growth mechanism is that normally size and density of QD are inter-dependent parameters [28]. The random nature of this process leads to a certain distribution in the size, shape and composition of the QD on a given sample, no two dots grown under the same conditions will be identical. Furthermore, the spatial distribution of QD on the surface is arbitrary, obeying to their stochastic formation mechanism.

The third approximation is the selective epitaxial growth on patterned substrates that in principle permits to obtain QD distributions with control in size into pre-defined locations on the surface of a sample [29-42]. This approximation is normally known as a *bottom-up* approach. In particular, it is based on a combination of self-assembling processes and selective growth of new material to form nanostructures into those pre-patterned locations on the surface by means of *ex situ* (not in the growth chamber) [29,40] (see chapter 3) or *in situ* (into the growth chamber) [41-44] technologies (see chapter 4). Regularity in size is crucial when studying the physical properties of nanostructures (as a function of their size, shape and interactions), because the majority of analysis techniques are based on averages over large numbers of these structures. Organized growth is characterised by the fact that the nano-objects arrange themselves into an array with periodicity dictated by the way the substrate has been pre-structured. This is known as the template effect. The substrate is pre-patterned either naturally, taking advantage of the surface physics or *in situ* etching mechanisms [43,44], or artificially, imposing a given periodicity by lithography and chemical etching [29-40,45].
The main drawback of this growth method is the incorporation of impurities or contaminants to the semiconductor interface during the patterning process. This circumstance is naturally avoided if the patterning process is carried out in an *in situ* context [41-44].

· Quantum dot molecules (QDM)

The simplest interacting QD system is a QD molecule (QDM) composed of two closely spaced QD [11,46]. QDM are receiving much attention both as playground for studying coupling and energy transfer processes between “artificial atoms” and as new systems, which substantially extend the range of possible applications of QD. The distance between these two QD has to be small enough to allow their

coupling, **Figure 1.7**. The main interactions between the QD are electron (or hole) tunnelling and Förster resonant energy transfer (FRET). FRET consists in a dipole-dipole interaction that allows the exciton energy to be transferred from a short-wavelength-emitting QD (donor) to a longer-wavelength-emitting QD (acceptor) through a virtual photon [46].

On the other hand, QDM with coupling mediated by coherent electron or hole tunnelling are appealing in the field of quantum information and processing, as they could be used to implement quantum gates [22,47-50].

In the ideal case, the two QD in a molecule are identical and their quantized energy levels are degenerate. Due to the coupling, the quantized energy levels of these two QD are split and the wavefunctions become delocalized. Symmetric (bonding) and anti-symmetric (anti-bonding) states are characteristic for such a QD molecule.

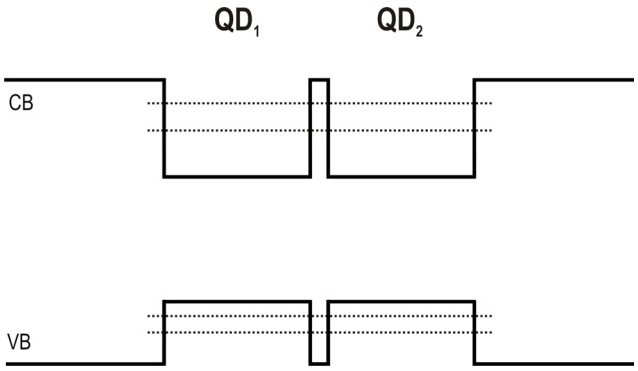

Figure 1.7. Schematic illustration of the energy bands in a QD molecule formed by two identical QD (QD_1 and QD_2) (QDM).

In the real case, the two QD forming the molecule are not fully identical in size. Thus, in order to bring the electronic states into resonance, an external electric field must be applied. In that case, the typical signature of electronic coupling consists in anticrossing patterns of the excitonic emission with applied field.

Practically, the QDM can be obtained by coupling two QD either vertically (in the growth direction) (VQDM) or laterally (in the growth plane) (LQDM).

Vertical quantum dot molecules (VQDM)

The first experimental attempt to realize VQDM based on self-assembled QD was reported in 2001 [51]. It was found that the energetic spacing between the emission of excitons in two nearby QD increased when the barrier width between the two QD decreased [52].

Deliberate design of the sample structures allows for the selection of the type of carrier mediating the coupling [53]. Great efforts have been dedicated to the formation of vertical coupled QD by self

assembling processes. The fabrication process leading to vertically aligned QD is normally based on the elastic-stress fields induced by QD from lower-lying layers on the top surface, promoting by further InAs deposition the growth of a second QD above it. By this growth procedure, it should be possible in principle, to actuate on the size of one of the QD at the same time that is maintained unaltered the emission properties of the other [53]. In general, the QD in a stack show different morphologies, compositions, and strains [54]. The top QD usually have larger diameters than the bottom ones. The size asymmetry introduced intentionally would permit to control the type of carrier mediating the tunnel coupling [53] (see section 4.4.2). **Figure 1.8 (a)** shows the energy band diagram of an asymmetric VQDM.

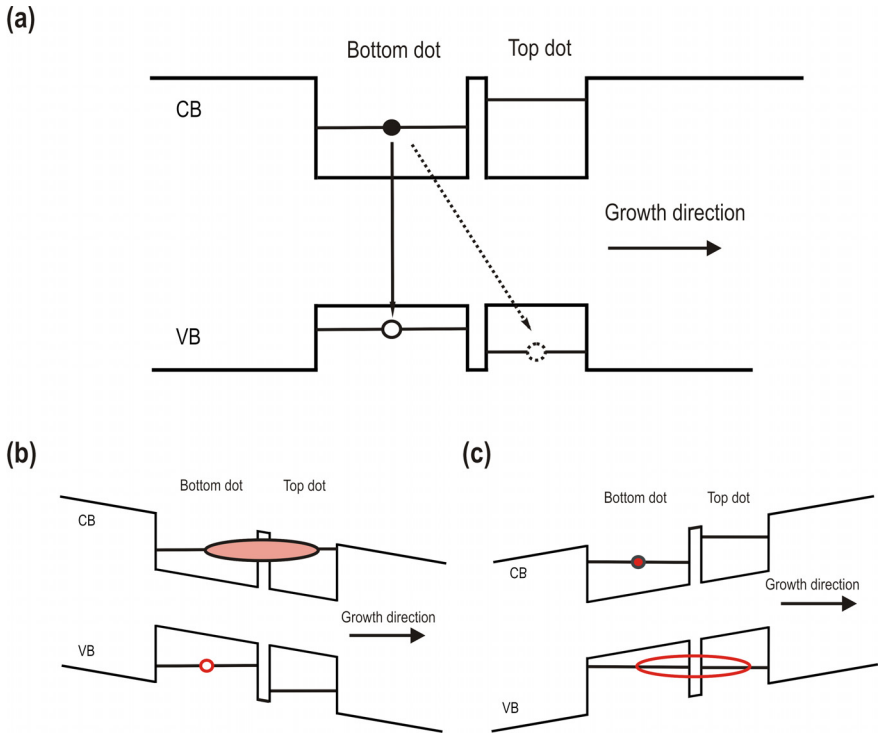

Figure 1.8. (a) Schematic band diagram of an asymmetric QDM. The transition denoted by the continuous arrow indicates the direct exciton and the transition denoted by the dotted arrow indicates the indirect exciton. **(b)** and **(c)** represent the situation when electrons or holes are brought into resonance under positive or negative applied external voltages, respectively (in a n-i Schottky diode) [53].

The energy levels of the two QD are not degenerate, and can be tuned into resonance by a vertical electric field applied along the growth direction. The tunnel coupling between the two QD can be mediated either by electrons, **Figure 1.8 (b)**, or holes, **Figure 1.8 (c)**, depending on the relative size of the two QD and the direction of the applied electric field, which is usually produced by embedding the VQDM in a diode-like structure (see section 4.4.2).

The optical properties of VQDM can be studied by PL spectroscopy. In order to address single VQDM individually, low surface density is required.

Lateral quantum dot molecules (LQDM)

In contrast to VQDM, special growth protocols are required to fabricate LQDM. For this reason, these structures have been less studied [44]. Because of the larger electronic polarizability of QD in the lateral direction, a stronger dependence of the coupling on the actual LQDM geometry is expected compared to VQDM when a lateral electric field is used to tune levels into resonance (see section 4.4.4). Furthermore, the lateral geometry appears more appealing for possible upscaling to a large number of QD. Ideally, also the coupling strength between QD should be tuneable. In the lateral geometry, this may be achieved by positioning a gate electrode between two QD [55,56]. Scanning the relative bias between two electrodes from negative to positive could allow the study of electron and hole-mediated tunnel coupling in the same QDM, which has not been done so far for VQDM.

Since self-assembled growth generally leads to randomly arranged QD, the probability of forming naturally occurring QD that are close enough to each other to display electronic interaction is extremely low, especially when a low QD density is desired. Therefore, special growth protocols are needed to create LQDM in a controlled manner. These growth techniques usually rely on the use of small surface modulations that act as preferential nucleation positions for closely spaced QD forming LQDM [54-56,57,58].

· Quantum rings (Qrings)

The formation [59] and physical properties of ring-like nanostructures have been extensively studied in the past. Due to their specific geometry, Qrings are non-simply connected quantum systems; the hole in the middle provides a capability of trapping a single magnetic flux quanta and offers the opportunity to observe electronic wavefunction phases in magneto-optical experiments, in this sense, the observation of quantum mechanics interference effects such as Aharonov-Bohm-like oscillations has already been obtained [60].

Nanostructures with a ring-like shape were originally obtained in the InAs/GaAs system by molecular beam epitaxy (MBE) in 1997 [61]. In this first example the Qrings were grown in the SK growth mode after partial capping and subsequent annealing.

Recently, another approach based on droplet epitaxy growth technique [62] has emerged as an optimal strategy for obtaining different ring-like complexes [63,65]. In particular, the growth of ring-like structures with optimal uniformity and rotational symmetry have been obtained and well studied in the GaAs/AlGaAs system [63,66].

1.1.3. Drawbacks for application of these nanostructures in new opto-electronic devices

The use of semiconductor nanostructures as active elements in advanced quantum-optical devices has been extensively studied in the last years [12-15, 17-23]. As already commented, semiconductor QD, as a two-level system, have been used in combination with optical resonators, microcavities fabricated around the QD, in order to couple the optical modes to the excitonic states, and that way to study the weak and strong coupling regimes between excitonic and photonic states [17-21]. In the framework of these new technological approximations there are some drawbacks that arise in the use of nanostructures fabricated by a natural self-assembling process. As already commented, SK fabrication method leads to distributions of QD with high optical quality. However, the self-assembled nanostructures are in general randomly distributed in the growth plane due to the stochastic nucleation of the islands on a flat surface. In addition, the difference of the number density of the nanostructures in different regions on the substrate also deteriorates the size homogeneity of the nanostructures and the density/size ratio is normally inter-dependent. Such disadvantages hamper both fundamental studies and device applications of single nanostructures.

In particular, the use of optical microcavities in combination with semiconductor nanostructures demands the fabrication of semiconductor active elements with a precise control in size (emission energy) and location. **Figure 1.9** shows illustrations of microcavities designs as a photonic crystal microcavity (PC microcavity) (**Figure 1.9 (a)**), a micropillar (**Figure 1.9 (b)**) and a microdisk (**Figure 1.9 (c)**) to achieve quantum coupling between a single cavity mode and an embedded QD [67]. The exact location of the interacting nanostructure is indicated by a red dot.

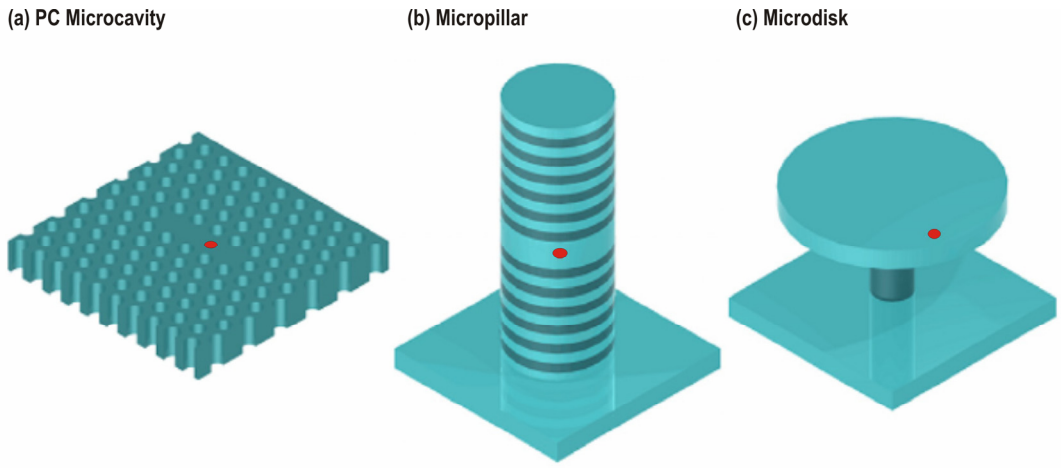

Figure 1.9. Illustrations of three microcavity designs to achieve coupling between a single cavity mode and an embedded quantum dot. (a) Photonic crystal membrane based microcavity, (b) micropillar cavity and (c) microdisk cavity. The location of the interacting quantum dot is indicated by a red dot. (Image taken from reference [67]).

Focusing on the use of PC microcavities, these structures allow for the realization of the smallest mode volume (in the range of $V= 0.7(\lambda/n)^3$) and the highest Q-factors (in the range $>10^7$) for passive structures [68,69]. But the spatial alignment of the semiconductor nanostructure with the mode maximum has to be in the range of <50 nm. Up to now, most of the coupling experiments of QD in PC microcavities are based on an arbitrary spatial overlap of a single QD with the cavity mode maximum, which needs the investigation of hundreds of cavities. To overcome this drawback, methods for pre-positioning of dots are mandatory. The fabrication technology requires then, the formation of nanostructures with simultaneous control in size (emission wavelength) and surface location [70-72]. A first natural approach to this objective is to perform distributions of nanostructures with low enough density that permits to get a certain probability of finding a single active nanostructure within the microcavity. In this approach although some results have already been obtained, the nanostructure localization once it has been buried [72] and the independent control of its emission energy and density [73,74] are still key issues.
A feasible approach to overcome all these inherent constraints of self-assembling processes, is the use of pre-patterned substrates by means of different lithographic techniques [29,40,42,75] where the patterned motives provide preferential sites for the posterior selective nucleation of nanostructures.

Respect to the technological implementation of QDM, promising building blocks of quantum gates [22,47-50], for both practical and fundamental reasons the ability to grow closely spaced QD with a certain control in the number of nanostructures [40], size and location is also needed. In particular, the possibility to obtain symmetric or asymmetric QDM is an essential design property that could provide an opportunity to take advantage of the very different properties of both electrons and holes (see section 4.4.2). Controlling asymmetry requires other processes different to those based on self-assembling techniques. In this sense, the use of pre-patterned substrates and posterior selective growth seems to be a necessary technological approximation.

The epitaxial growth on patterned substrates has also some constraints that will be discussed in more detail in section 2.1.4. Moreover, the lithographic technique use for patterning and the posterior technological processes have to keep the optimal quality of the semiconductor interface to guarantee the selective nucleation of high optical quality nanostructures.
The development of such technological approximations is basically the aim of this thesis and is resumed in the next section.

1.2. Thesis outline

The aim of the work in this thesis is the development of novel technological approximations that by a patterning process and posterior selective epitaxial growth permit to obtain semiconductor nanostructures with control in size, density, location and composition at the same time that their optical

properties are maintained. Such patterning and epitaxial growth approaches are of great technological interest for the fabrication of novel quantum optical devices.
In this direction, this thesis presents the study of two different *ex situ* patterning technologies which take advantage of the ordered pattern of a mask fabricated and the novel use of an *in situ* patterning technique based on droplet epitaxy growth mode.

The outline of the thesis is the following:

Chapter 2 describes both the growth technique of semiconductor nanostructures and the experimental methods used to study them. Molecular beam epitaxy and photoluminescence (PL) set-ups, majority used in this work, are described in detail.

Chapter 3 presents results on the growth of position controlled InAs nanostructures by using two different strategies to fabricate distributions of nanoholes on GaAs substrates. The first technique presented is based on the formation of a monolithically integrated ordered porous alumina mask, by the electrochemical anodization of an aluminum layer epitaxially grown on the GaAs (001) substrate. As a second part in this chapter, the main results concern with a novel method to perform an optimal transfer of a pattern from a mask previously fabricated on a resin layer deposited on the substrate, to the substrate itself. The transfer process of the pattern is based on the ozone selective oxidation of the underlying semiconductor substrate.

Finally, chapter 4 presents results obtained using a novel *in situ* patterning technique based on the droplet epitaxy growth technique developed to form low density nanoholes ($2x10^8$ cm^{-2}) templates on GaAs (001) and InP (001) substrates. Once fabricated, these templates are further used for the formation of different low density III-V semiconductor nanostructures, as InAs QD and InAs QD molecules in lateral and vertical configuration, with a certain control in their size, aspect ratio and composition. Also, by varying the element V pressure used during the patterning process, type II Ga(As)Sb Qrings have been obtained on GaAs (001) substrates.
This chapter concludes presenting results on the localization of the nanostructures after being buried. These last results rely on the development of a specific growth process for the cap layer.

Chapter 5 presents the conclusions of this work.

References

[1] L. Esaki, and R. Tsu, IBM J. Res. Devel. **14**, 61 (1970).
[2] F. C. Frank, and J. H. V. d. Merwe, Proc. R. Soc. London, Ser. A **198**, 205 (1949).
[3] M. Volmer, and A. Weber, Nuclei formation in supersaturated states, Z. Physik. Chem. **119**, 277 (1926).
[4] I. N. Stranski, and L. Krastanow, Sitz. Ver. Akad. Wiss., Math.-naturwiss. Kl. Abt. IIb, 146, 797 (1938).
[5] N. L. D. Bimberg, and M. Grundman, "Quantum Dot Heterostructures" John Willey & Sons, New York, EEUU, (1998).
[6] R. J. Young, Phd "Controlling the fine structure splittingin single InAs quantum dots", University of Cambridge, (2006).
[7] M. Sugawara (ed), "Semiconductors and semimetals" London: Academic, vol. **60** (1999).
[8] J. Sabarinathan, P. Bhattacharya, P-C Yu, S. Krishna, J. Cheng, and D. G. Steel, Appl. Phys. Lett. **81**, 3876 (2002).
[9] D. L. Huffaker, G. Park, Z. Zou, O. B. Shchekin, and D. G. Deppe, Appl. Phys. Lett. **73**, 2564 (1998).
[10] H. Drexler, D. Leonard, W. Hansen, J. P. Kotthaus, and P. M. Petroff, Phys. Rev. Lett. **73**, 2252 (1994).
[11] S. Kiravittaya, A. Rastelli, and O. G. Schmidt, Rep. Prog. Phys. **72**, 046502 (2009).
[12] P. Michler, A. Kiraz, C. Becher, W. V. Schoenfeld, P. M. Petroff, L. Zhang, E. Hu, and A. Imamoglu, Science **290**, 2282 (2000).
[13] M. Pelton, C. Santori, J. Vuckovic, B. Zhang, G. S. Solomon, J. Plant, and Y. Yamamoto, Phys. Rev. Lett. **89**, 233602 (2002).
[14] Z. Yuan, B. E. Kardynal, R. M. Stevenson, A. J. Shields, C. J. Lobo, K. Cooper, N. S. Beattie, D. A. Ritchie, and M. Pepper, Science **295**, 102 (2002).
[15] M. B. Ward, O. Z. Karimov, D. C. Unitt, Z. L. Yuan, P. See, D. G. Gevaux, A. J. Shields, P. Atkinson, and D. A. Ritchie, Appl. Phys. Lett. **86**, 201111 (2005).
[16] D. Bouwmeester, A. Ekert, and A. Zeilinger (eds), "The Physics of Quantum Information" Berlin: Springer, (2000).
[17] J. P. Reithmaier, G. Sek, A. Löffler, C. Hofmann, S. Kuhn, S. Reitzenstein, L. V. Keldysh, V. D. Kulakovskii, T. L. Reinecke, and A. Forchel, Nature **432**, 197 (2004).
[18] T. Yoshie, A. Scherer, J. Hendrickson, G. Khitrova, H. M. Gibbs, G. Rupper, C. Ell, O. B. Shekin, and D. G. Deppe, Nature **432**, 200 (2004).
[19] A. Badolato, K. Hennessy, M. Atatüre, J. Dreiser, E. Hu, P. M. Petroff, and A. Imamoglu, Science **308**, 1158 (2005).
[20] E. Peter, P. Senellart, D. Martrou, A. Lemaitre, J. Hours, J. M. Gerard, and J. Bloch, Phys. Rev. Lett. 95, 067401 (2005).
[21] C. Böckler, S. Reitzenstein, C. Kistner, R. Debusmann, A. Löffler, T. Kida, S. Höfling, A. Forchel, L. Grenouillet, J. Claudon, and J. M. Gérard, Appl. Phys. Lett. **92**, 091107 (2008).
[22] A. Imamoglu, D. D. Awschalom, G. Burkard, D. P. DiVincenzo, D. Loss, M. Sherwin, and A. Small, Phys. Rev. Lett **83**, 4204 (1999).
[23] R. M. Stevenson, R. J. Young, P. Atkinson, K. Cooper, D. A. Ritchie, and A. J. Shields, Nature **439**, 179 (2006).
[24] A. Forchel, R. Steffen, M. Michel, A. Pecher, and T.L. Reinecke, Proceedings of 23rd International Conference on The Physics of Semiconductors, 1285 (1996).
[25] A. Scherer, and H.G. Craighead, Appl. Phys. Lett. **49**, 1284 (1986).
[26] M. Bayer, O. Schilling, A. Forchel, T.L. Reinecke, P.A. Knipp, Ph. Pagnod-Rossiaux, and L. Goldstein, Phys. Rev. B **53**, 15810 (1996).
[27] K. Petter, T. Kipp, Ch. Heyn, D. Heitmann, and C. Schüller, Appl. Phys. Lett. **81**, 592 (2002).
[28] R. Heitz, I. Mukhametzhanov, A. Madhukar, A. Hoffmann, and D. Bimberg, J. of Elect. Mat. **28**, 520 (1999).
[29] P. Atkinson, M. B.Ward, S. P. Bremner, D. Anderson, T. Farrow,G.A.C. Jones, A. J. Shields, and D. A. Ritchie, Jpn. J. Appl. Phys. **45**, 2519 (2006).
[30] H. Heidemeyer, C. Müller, O.G. Schmidt, J. Cryst. Growth **261**, 444 (2004).
[31] T. Ishikawa, T. Nishimura, S. Kohmoto, and K. Asakawa, Appl. Phys. Lett. **76**, 167 (2000).

[32] S. Birudavolu, N. Nuntawong, G. Balakrishnan, Y. C. Xin, S. Huang, S. C. Lee, S. R. J. Brueck, C. P. Hains, and D. L. Huffaker, Appl. Phys. Lett. **85**, 2337 (2004).
[33] H. A. McKay, A. Dehne, J. Y. Lee, and J. M. Millunchicka, Appl. Phys. Lett. **90**, 163109 (2007).
[34] M. Mehta, D. Reuter, A. Melnikov, and A. D. Wieck, and A. Remhof, Appl. Phys. Lett. **91**, 123108 (2007).
[35] Y. Nakamura, O.G. Schmidt, N.Y. Jin-Phillipp, S. Kiravittaya, C. Müller, K. Eberl, H. Gräbeldinger, and H. Schweizer, J. Cryst. Growth **242**, 339 (2002).
[36] P. Alonso-González, L. González, Y. González, D. Fuster, I. Fernández-Martínez, J. Martín-Sánchez, and L. Abelmann, Nanotechnology **18**, 355302 (2007).
[37] P. Alonso-González, M.S. Martín-González, J. Martín-Sánchez, Y. González and L. González, J. Cryst. Growth **294**, 168 (2006).
[38] S. Watanabe, E. Pelucchi, B. Dwir, M. H. Baier, K. Leifer, and E. Kapon, Appl. Phys. Lett. **84**, 2907 (2004).
[39] J. Martín-Sánchez, Y. González, L. González, M. Tello, R. García, D. Granados, J.M. García, and F. Briones, J. Cryst. Growth **284**, 313 (2005).
[40] J. Martín-Sánchez, P. Alonso-González, J. Herranz, Y. González, and L. González, Nanotechnology **20**, 125302 (2009).
[41] P. Alonso-González, B. Alén, D. Fuster, Y. González, and L. González, Appl. Phys. Lett. **91**, 163104 (2007).
[42] P. Alonso-González, D. Fuster, L. González, J. Martín-Sánchez, and Y. González, Appl. Phys. Lett. **93**, 183106 (2008).
[43] Zh. M. Wang, B. L. Liang, K. A. Sablon, and G. J. Salamo, Appl. Phys. Lett. **90**, 113120 (2007).
[44] G.J. Beirne, C. Hermannstädter, L. Wang, A. Rastelli, O. G. Schmidt, and P. Michler, Phys. Rev. Lett. **96**, 137401 (2006).
[45] H. Lee, J. A. Johnson, J. S. Speck, and P. M. Petroff, J. Vac. Sci. Technol. B **18**, 2193 (2000).
[46] L. Wang, A. Rastelli, S. Kiravittaya, M. Benyoucef, and O. G. Schmidt, Adv. Mater. **21**, 1 (2009).
[47] D. Loss, and D. P. Divincenzo, Phys. Rev. A **57**, 120 (1998).
[48] G. Burkard, D. Loss, D. P. Divincenzo, Phys. Rev. B **59**, 2070 (1999).
[49] G. Burkard, A. Imamoglu, Phys. Rev. B **74**, 041307 (2006).
[50] C. Emary, L. J. Sham, Phys. Rev. B **75**, 125317 (2007).
[51] M. Bayer, P. Hawrylak, K. Hinzer, S. Fafard, M. Korkusinski, Z. R. Wasilewski, O. Stern, and A. Forchel, Science **291**, 451 (2001).
[52] G. Ortner, I. Yugova, A. Larionov, G. Baldassarri, M. Bayer, P. Hawrylak, S. Fafard, and Z. Wasilewski, Physica E **26**, 281 (2005).
[53] A. S. Bracker, M. Scheibner, M. F. Doty, E. A. Stinaff, I. V. Ponomarev, J. C. Kim, L. J. Whitman, T. L. Reinecke, and D. Gammon, Appl. Phys. Lett. **89**, 233110 (2006).
[54] O. G. Schmidt, and K. Eberl, Phys. Rev. B **61**, 13721 (2000).
[55] R. Songmuang, S. Kiravittaya, and O. G. Schmidt, Appl. Phys. Lett. **82**, 2892 (2003).
[56] L. Wang, A. Rastelli, S. Kiravittaya, P. Atkinson, F. Ding, C. C. B. Bufon, C. Hermannstädter, M. Witzany, G. J. Beirne, P. Michler, and O. G. Schmidt, New J. Phys. **10**, 045010 (2008).
[57] T. V. Lippen, R. Nötzel, G. J. Hamhuis, and J. H. Wolter, Appl. Phys. Lett. **85**, 118 (2004).
[58] P. Alonso-González, J. Martín-Sánchez, Y. González, B. Alén, D. Fuster and L. González, ACS Crystal Growth and Design **9(5)**, 2525 (2009).
[59] D. Granados, and J. M. García, Appl. Phys. Lett. **82**, 2401 (2003).
[60] N. A. J. M. Kleemans, I. M. A. Bominaar-Silkens, V. M. Fomin, V. N. Gladilin, D. Granados, A. G. Taboada, J. M. García, P. Offermans, U. Zeitler, P. C. M. Christianen, J. C. Maan, J. T. Devreese, and P. M. Koenraad, Phys. Rev. Lett. **99**, 146808 (2007).
[61] J. M. García, G. Medeiros-Ribeiro, K. Schmidt, T. Ngo, J. L. Feng, A. Lorke, J. Kotthaus, and P. M. Petroff, Appl. Phys. Lett. **71**, 2014 (1997).
[62] T. Mano, K. Watanabe, S. Tsukamoto, H. Fujioka, M. Oshima, and N. Koguchi, J. Cryst. Growth **209**, 504 (2000).
[63] T. Mano, T. Kuroda, S. Sanguinetti, T. Ochiai, T. Tateno, J. Kim, T. Noda, M. Kawabe, K. Sakoda, G. Kido, and N. Koguchi, Nano Lett. **5**, 425 (2005).

[64] T. Mano, and N. Koguchi, J. Cryst. Growth **278**, 108 (2005).
[65] P. Alonso-González, L. González, D. Fuster, Y. González, A. G. Taboada, J.M. Ripalda, A. M. Beltrán, D. L. Sales, T. Ben, and S. I. Molina, ACS Cryst. Growth Des. **9(2)**, 1216 (2009).
[66] J. H. Lee, Zh. M. Wang, Z. Y. Abuwaar, N. W. Strom, and G. J. Salamo, Nanotechnology **17**, 3973 (2007).
[67] J. P. Reithmaier, Semicond. Sci. Technol. **23**, 123001 (2008).
[68] Y. Akahane, T. Asano, S. B. Song, and S. Noda, Nature **425**, 944 (2003).
[69] S. B. Song, S. Noda, T. Asano, and Y. Akahane, Nature Mater. **4**, 207 (2005).
[70] K. Hennessy, A. Badolato, M. Wigner, D. Gerace, M. Atatüre, S. Gulde, D. Fält, E. L. Hu, A. Imamoglu, Nature **445**, 896, (2007).
[71] P. M. Intallura, M. B. Ward, O. Z. Karimov, Z. L. Yuan, P. See, A. J. Shields, P. Atkinson and D. A. Ritchie, Appl. Phys. Lett. **91**, 161103 (2007).
[72] K. J. Vahala, Nature **424**, 830 (2003).
[73] H.Z. Song, T. Usuki, Y. Nakata, N. Yokoyama, H. Sasakura and S. Muto, Phys. Rev. B **73**, 115327 (2006).
[74] D. Guimard, H. Lee, M. Nishioka and Y. Arakawa, Appl. Phys. Lett. **92**, 163101 (2008).
[75] J. Martín-Sánchez, G. Muñoz-Matutano, J. Herranz, J. Canet-Ferrer, B. Alén, Y. González, P. Alonso-González, D. Fuster, L. González, J. Martínez-Pastor, and F. Briones, ACS Nano (Accepted) (2009).

II

EXPERIMENTAL TECHNIQUES

2. EXPERIMENTAL TECHNIQUES

This chapter presents an overview of the experimental techniques used in this work for the growth and characterization of the samples. First of all, a brief resume of the growth technique by molecular beam epitaxy is introduced. Next, both kind of characterization techniques, in situ (into the MBE chamber) and ex situ, are presented. As a novel development in this thesis, it is also described in this chapter, section 2.2, the experimental set-up for the ozone selective oxidation of III-V semiconductor substrates. The oxidation performance of a commercial UV-cleaning set-up is also studied for comparison.

2.1. Molecular Beam Epitaxy

Molecular beam epitaxy is a method for epitaxial growth of high purity single crystal films by the reaction of atomic or molecular beams on a heated crystalline substrate in an ultra-high vacuum (UHV) environment (background pressures lower than 10^{-10} mbar) [1].

This growth technique relies on the Gunther´s "three temperatures method" [2], that permitted to obtain stoichiometric polycrystalline thin films of III-V semiconductor compounds. In 1968, J. R. Arthur studied for the first time the kinetics and the structure of the GaAs surface when molecular beams of Ga and As_2 were supplied to the substrate [3]. The posterior advance in UHV techniques made possible in 1975 [1], the growth of high purity GaAs thin films with an excellent morphology.

For the growth of III-V semiconductors, according to the Gunther´s "three temperatures method", when the temperatures of the substrate (T_s), the III-element cell (T_{III}) and the V-element cell (T_V) present the relation $T_V<T_S<T_{III}$, all the atoms of group III that reach the substrate surface condensate with an incorporation ratio of 1. When the amount of V-element reaching the surface is supplied in excess, the possible formation of III-element droplets on the surface is avoided, since the fraction of V-element not incorporated is re-evaporated in a totally compensated process that permits to maintain the stoichiometry of the material grown. This way, under conditions of V-element excess, the compound growth rate is defined by the III-element supply.

Figure 2.1 shows schematically the evaporation process of elements of Groups III and V and n-dopant to form a compound on a monocrystalline substrate.

This process takes place in an UHV chamber that is normally coated inside by liquid N_2 cryopanels that helps to maintain the chamber base pressure in order to get a minimal impurity incorporation during the growth, and is effective for reducing any thermal and chemical cross-talk between the source cells.

The molecular beams of the different materials to grow are obtained from the evaporation of solid elements, incorporated in effusion cells that are directly oriented to the substrate position. These atomic or molecular beams are controlled by the temperature of the cells and, by the incorporation of closure devices, can be quickly interrupted allowing a precise control of the amount of layers deposited.

A system to hold and heat the substrate, an inter-connected pre-growth chamber and a system to transfer the wafers to the growth chamber without breaking its vacuum are also necessary elements for MBE growth.

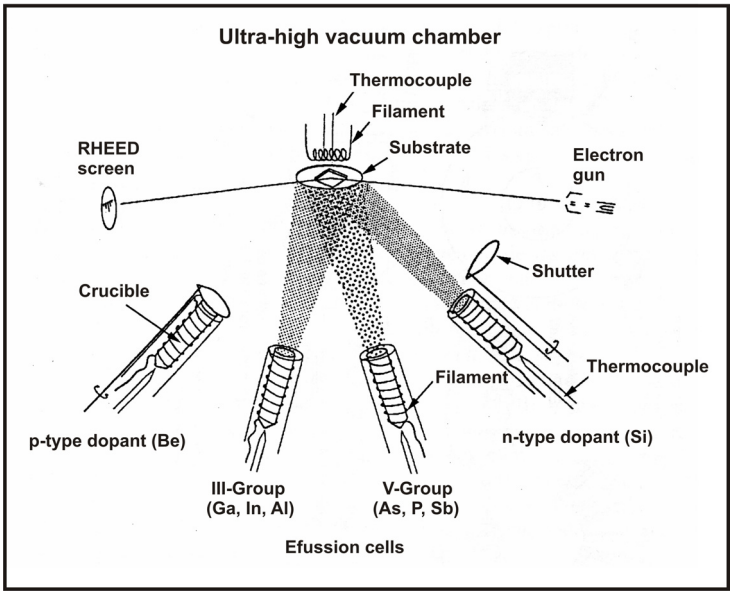

Figure 2.1. Schematic representation of a n-doped III-V semiconductor growth by MBE.

The main advantages of the MBE technique over other epitaxial techniques are:

- Low growth rates (0.2-1.5 μm/h). This way, the thickness of material grown can be controlled with great precision, possibiliting the design of heterostructures with different composition and doping at the atomic monolayer level in a reproducible way.
- A quick interruption of the different molecular beams permitting the growth of abrupt interfaces at atomic level (the shutters open/close times have to be shorter than the time necessary to deposit a monolayer of material).
- The growth temperature is usually not very high (~600ºC in conventional MBE) reducing the elements inter-diffusion at the interfaces.
- Possibility of using in situ characterization techniques compatible with UHV during the growth process.

2.1.1. The MBE facility at IMM

Figure 2.2 (taken from reference [4]) shows a schematic diagram of the MBE equipment (MBE 2 and MBE 3) at the IMM facilities, in which all the samples of this work were grown.

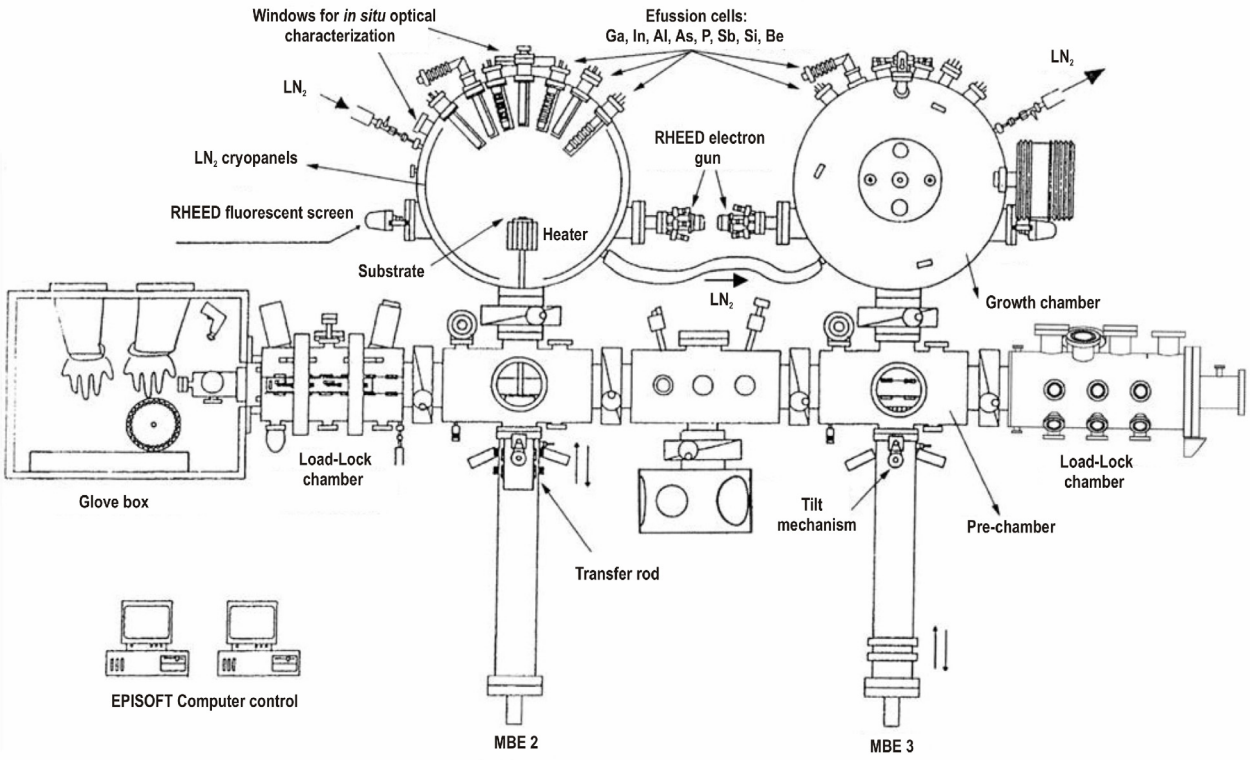

Figure 2.2. Schematic representation of the MBE equipments at IMM. It consists of two inter-connected growth chambers (MBE 2 and MBE 3)

This equipment, designed and built at IMM, basically consists of the following elements:

- Two growth chambers.
- Auxiliary chambers: 2 load-lock chambers, 2 pre-growth chambers, 1 intermediate chamber provided with Auger spectroscopy and a collateral chamber with a scanning tunnel microscopy (STM).
- A sample transfer system.
- Characterization techniques: mass spectroscopy, reflection high-energy electron diffraction (RHEED), reflectance difference (RD), Auger electron spectroscopy (AES) and STM Microscopy.

The base pressure of the growth chambers when the source cells are not heated, is generally as low as $5x10^{-11}$ Torr. For reaching this low pressure, the chambers are pumped by ion pumps and a LN_2 cryopanel surrounds completely the growth environment. There is an ion-gauge in the growth chamber that is attached on a movable arm so it can be situated at the sample position to measure the beam flux incident on the wafer (Beam Equivalent Pressure (BEP)). During the growth of the samples this ion-gauge is kept retracted.

The cells and their respective shutters are mounted on flanges in the posterior part of the system. These cells are surrounded by refrigeration coils in which water runs at a constant temperature. Each shutter is activated by a computer controlled air pressure system. The cells of elements of Group III (Ga, Al, In) and the dopants (n:Si, p:Be) incorporate a Ta filament to heat the pyrolytic boron nitride (PBN) crucible that contains the material and a thermocouple, which is in contact with the bottom of the crucible. Surrounding the crucible, Ta sheets are also arranged to avoid thermal radiation. The reference temperature for the thermocouple measurements is provided by a constant temperature of water refrigeration coils. In this way, the temperature measurements are reproducible for one day to the other.

The arsenic, phosphorous and antimony cells have been designed by F.Briones and built at IMM. All of them incorporate cracking sections that permit to deliver on demand V-element tetramers or V-element dimers. Arsenic and phosphorous cells have valves that permit to close them hermetically with a fast open/close operation (0.1 s). In particular, the As cell has been specially designed and developed in the MBE lab at IMM [5]. It can provide a flux ration, ϕ_{ON}/ϕ_{OFF}, higher than 150 (a value of $\phi_{ON}/\phi_{OFF} \sim 20$ is obtained in conventional arsenic cells), where ϕ is the number of atoms that reach the surface per second and square centimetre. This arsenic cell incorporates also a Ta filament around the mouth of the crucible to measure the temperature and crack the As_4 tetramers into As_2 dimers.

The growth chambers are equipped with an *in situ* characterization RHEED system and a window that permits to attach optical characterization systems (RD). Loading of samples in and out of the system occurs via the use of a load-lock chamber pumped by a turbo-pump system. Before loading, the samples are mounted on a trolley that permits to hold four 3-inch wafers. Transfer of wafers to different parts of the system is carried out moving the trolley by a system of manipulators and rails.

The heater that serves as substrate holder during the growth is attached to a magnetic coupled transfer rod with tilt mechanism. During growth, the pre-growth and growth chambers are communicated, permitting the sample to rotate at rates of 10-35 s per turn to ensure a more uniform epitaxy.

The cells and substrate temperatures, shutters timings and crackers intensities are controlled by a computer programme (EPISOFT). This control permit ON/OFF shutters timings of the cells of ~ 0.1 s.

The signal from the RHEED screens is acquired by a CCD camera and transmitted by a data acquisition system to a computer. This way, the diffraction patterns can be further analyzed to obtain useful information about the growth process.

2.1.2. Growth kinetics

The kinetics of atoms of III and V Groups at the growth front during MBE growth has been studied by modulated molecular beam experiments and models involving the reaction kinetics of Ga atoms with As_2 or As_4 molecules on GaAs (001) substrates have been proposed [6,8].

According to the experimental work by Foxon and Joyce [7,8], the As_4 molecules are initially adsorbed in a mobile precursor state with a low migration energy. Under the presence of two pairs of Ga

atoms, two As_4 molecules dissociate in four As_2 molecules. In this context, two of these As_2 molecules react with a pair of Ga atoms while the two remaining As_2 molecules react between them, giving rise to an As_4 molecule that is desorbed from the surface. These reactions imply an As_4 incorporation coefficient ≤ 0.5.

Figure 2.3 shows schematically the different reactions that take place on a GaAs (001) surface during its exposure to molecular beams of Ga and As_4.

Under conventional MBE conditions, Ga atoms have an incorporation coefficient of 1 up to a substrate temperature of 620ºC; this means that the GaAs growth rate is controlled by the used Ga flux. As atoms can be incorporated if Ga atoms are already adsorbed on the surface. The typical substrate temperature during MBE growth (T_s~ 580ºC) is higher than that of As desorption on GaAs (001) surfaces (T_s~ 550ºC). The growth process can be described by the following reactions:

$$\begin{bmatrix} Ga + As_4 + Ga \rightarrow 2GaAs + As_2 \\ Ga + As_4 + Ga \rightarrow 2GaAs + As_2 \end{bmatrix} + As_4 \uparrow \qquad \textbf{(2.1)}$$

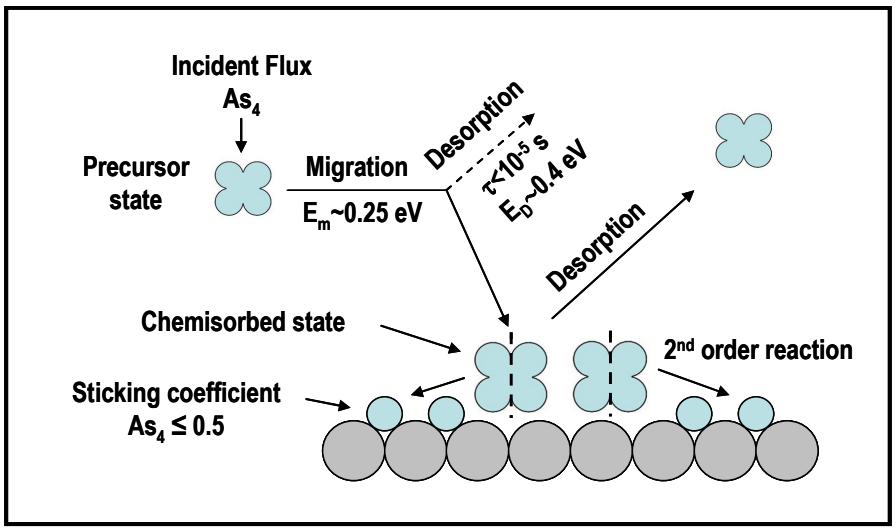

Figure 2.3. Schematic representation of a MBE growth process for Ga and As4, according to the model proposed by Foxon and Joyce [7,8]. (Image taken from reference [15]).

RHEED experiments have been highly beneficial for understanding the MBE growth mechanisms. Next section will describe this experimental *in situ* technique.

2.1.3. In situ characterization techniques

The two *in situ* characterization techniques used in this work (RHEED and RD) will be described in this section. RHEED is the main tool to obtain information of the surface structure and evolution of the

growth front. This technique provides also information about the growth front stoichiometry through the observation of the surface reconstruction and can be used to determine the growth rate, which is a function of the substrate and III-group element cell temperatures.

The RD technique is mainly used to obtain a closer information about the surface stoichiometry (III-group/V-group elements ratio).

Both techniques will be described below.

2.1.3.1. Reflection high-energy electron diffraction (RHEED)

RHEED is an electron diffraction technique which can provide information about the surface structure, cleanliness, smoothness, and growth rate [9].

As shown in **Figure 2.4**, all necessary hardware can be incorporated within the MBE deposition chamber but remote from the growth region, thus allowing operation during deposition. A RHEED system requires an electron source (in the range 0 to 10 KeV in our experimental set-up), a fluorescent detector screen and the sample. The electron beam impinges the substrate at a grazing incidence (typically < 1º) providing a diffraction pattern that is detected onto the fluorescent screen. A video camera located in front of this screen permits to visualize the diffraction pattern on a monitor. This pattern is a representation of the reciprocal lattice of the sample.

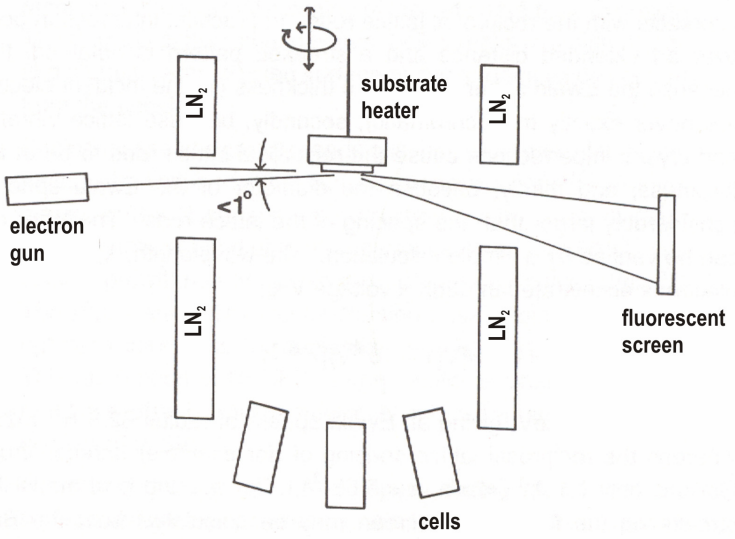

Figure 2.4. Typical RHEED geometry.

The glancing incidence used in RHEED, limits the penetration of the primary electrons to the top few monolayers of the sample under investigation. In consequence, a clean flat crystal surface essentially acts as a two dimensional grating. The reciprocal lattice of such a grating consists of an array of rods perpendicular to the real surface, because the real lattice spacing is effectively zero in this direction.

Figure 2.5 shows a schematic representation of the reciprocal lattice from the surface together with the Ewald sphere of the incident electrons [10]. As a consequence of the Laue scattering condition, constructive interference occurs wherever the Ewald sphere intersects with the reciprocal lattice rods. In practice, intersection occurs over an extended distance and then, a streaked pattern is obtained, firstly because the Ewald sphere is of finite thickness (as the incident electrons are never exactly monochromatic); secondly, because lattice vibrations and crystal imperfections cause the reciprocal lattice rods to be of finite width; and thirdly, because the diameter of the Ewald sphere is considerably larger than the spacing of the lattice rods [9].

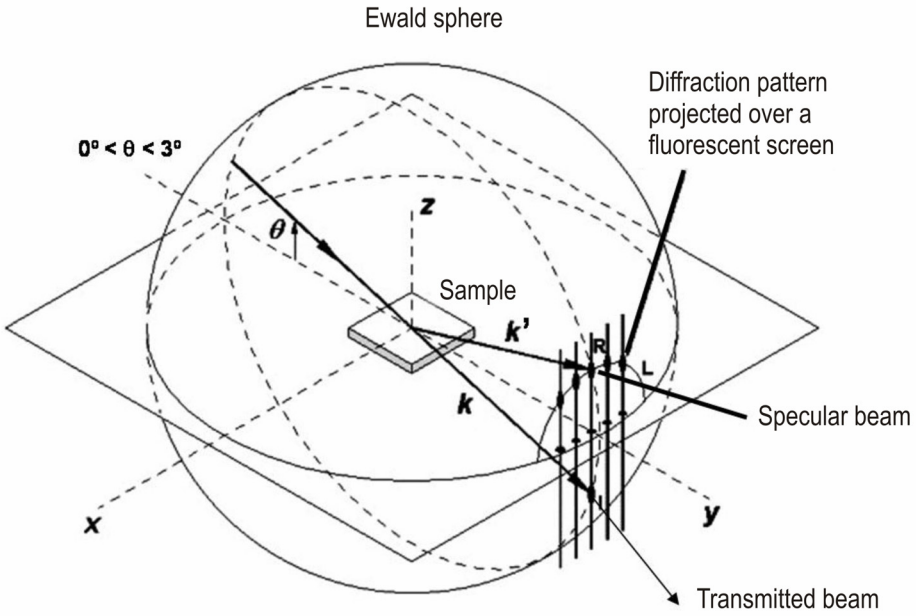

Figure 2.5. Schematic representation of the diffraction pattern formation over a fluorescent screen for a high energy electron beam at glancing incident on the sample surface. (Taken and modified from reference [10]).

As already advanced, RHEED is particularly useful in MBE because permits to determine the surface reconstruction, a re-ordering of the outmost atomic layer of a crystal to reduce the energy of the free surface. The reconstructions that a given surface can support during growth can only be maintained over a limited range of flux ratios and substrate temperatures at a given growth rate. Thus the surface reconstruction is extremely useful as an equipment-independent monitor of the MBE growth conditions. For example, the most ordinary GaAs (001) surface under MBE growth conditions is a (2x4) reconstruction, in which the periodicity of the atomic positions is reduced in the reciprocal space (larger atomic inter-distance in the real space) along two orthogonal directions [*110*] by a factor of two and four respectively. This increase in the real space unit cell, induces the appearance of new streaks in the diffraction pattern that are located in between those corresponding to the bulk material. The observation of the RHEED diagram at different azimuths, permits to determine the surface reconstruction in real time

during the growth. In absence of growth, the surface reconstructions are perfectly determined as a function of the As pressure (in case of GaAs) and substrate temperature. From the RHEED diagram at certain experimental conditions, is also possible to derive, in a qualitative way, the surface stoichiometry during the growth.

If any surface asperities or 3D nuclei are present, as in the case of quantum dots, the incident electron beam is usually diffracted into a series of discrete spots instead of a streaked RHEED pattern. The shape and intensity of these diffraction spots depend on the shape and distribution of the diffracting elements [11]. If these nuclei on the surface present well-defined facets, the diffraction pattern incorporates additional streaks that permit their identification [12]. On the other hand, when the surface has an amorphous structure, as in the case of the native oxide, a diffuse diffraction pattern is obtained.

Depending on the growth conditions, the specular beam (I_{00}) changes periodically or remains constant with time. As I_{00} is sensitive to the surface morphology, the behaviour observed for the I_{00} evolution with growth time can be related to the morphology evolution of the growth front. In this sense, three different MBE growth mechanisms can be observed:

· Layer-by-layer

Layer-by-layer (Frank-van der Merwe) growth occurs when the growth process is carried out on an ideal substrate (a contaminants and defects-free plane substrate) at optimal MBE conditions: i) $T_s \sim$ 580ºC permitting the atoms of group III to have enough migration length; ii) $\phi_{As4}/\phi_{Ga} \sim 10$, providing a (2x4) As-stabilized surface. The As_4 flux is high enough to counteract its thermal desorption and to supply, at the same time, the necessary amount of material to maintain the stoichiometry of the surface. At these growth conditions, on an ideal substrate, atoms of group III have sufficient energy to migrate on the surface, permitting the reaction given in equation 2.1. The as-formed nuclei are now, preferential nucleation centres for new atoms of group III reaching the surface, which extends the formed 2D islands up to the formation of a monolayer, recovering that way, the starting surface configuration.

In this growth mode, a RHEED specular beam intensity oscillation is well-observed.

· Step propagation

In the case of having a surface with a regular density of steps, the growth, at the same conditions as commented in the previous case, is preferential at the step edges, which originates a progressive propagation of such surface irregularities.

In this growth mode, no RHEED specular beam intensity oscillations are observed [13].

· **3D growth**

If the substrate temperature is low or the relation ϕ_{As4}/ϕ_{Ga} is not appropriate, the mobility of atoms of group III on the surface diminishes and a 3D growth initiates. The degradation of the surface is observed in the RHEED diagram by the apparition of diffuse spots. It has to be notice that this growth mode could also occur, even at optimal growth conditions, if the starting surface presents contaminants, a high density of defects or a very rough morphology, since, all these features act as preferential nucleation centres.

An important application of RHEED technique is that it permits, at MBE layer-by-layer growth conditions, to calibrate in a very accurate way the growth rates of the growing compounds. As already commented the RHEED oscillations are much more appreciable in the specular beam due to the fact that the surface reflectivity is very sensitive to the surface morphology and stoichiometry [14,15]. The intensity and period of these oscillations are directly related to the used growth conditions; in particular, the period is exactly the necessary time to grow a monolayer of material. In the case of GaAs (001), a monolayer consists of a layer of Ga atoms and a layer of As atoms, and it has a thickness of 0.28266 nm, corresponding to a/2 where a, is the GaAs lattice parameter. **Figure 2.6** (taken from reference [16]), shows the surface morphology evolution during a growth process together with the resulting specular beam intensity oscillations.

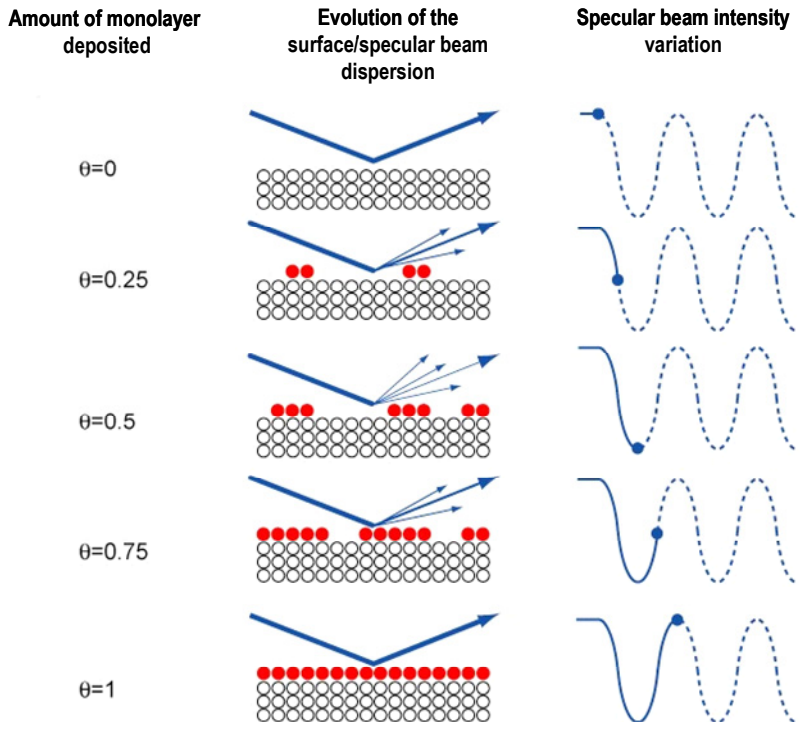

Figure 2.6. Schematic representation of a layer by layer growth process and the evolution of the specular beam intensity. (Image taken and modified from reference [15]).

At the initial stage, the substrate surface is totally flat obtaining a maximum of the specular beam intensity. Continuing the growth, as new material is deposited, 2D islands appear which diminishes the oscillation intensity. The minimum of intensity is obtained when the density of islands is maximum, that usually takes place when approximately ½ monolayer is grown (θ= 0.5 in **Figure 2.6**). As the growth continues, the surface starts to flatten until the completion of the monolayer, obtaining that way, a new maximum of the specular beam intensity (θ= 1 in **Figure 2.6**). By this process, monitoring the specular beam oscillations and measuring the corresponding period, the material growth rate can be accurately calibrated.

Figure 2.7 shows the specular beam intensity oscillations obtained along the GaAs [*110*] direction during its growth at T_s= 580ºC and $BEPAs_4$= $2x10^{-6}$ Torr. In this case, the resulting GaAs growth rate is 1 ML/s. The observed dumping of intensity with time is caused by phase differences in the growth kinetics at different locations on the sample [17].

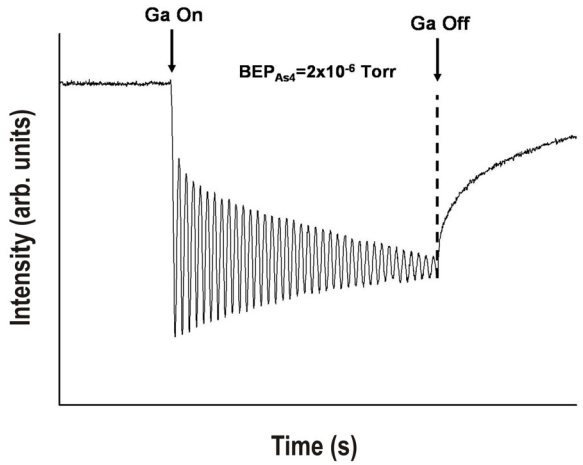

Figure 2.7. Specular beam oscillations corresponding to the growth of a GaAs layer at T_S= 580ºC and $BEPAs_4$= $2x10^{-6}$ Torr.

The MBE machines at IMM use electron guns with a beam acceleration voltage of 10 KeV and 1 mm-wide diameter. In this system, the incidence angle can be varied by using a magnetic field that is generated by copper coils attached to the chamber.

Figure 2.8 shows the diffraction patterns corresponding to a (2x4) surface reconstruction on a GaAs (001) surface along the GaAs [*110*] (**Figure 2.8 (a)**) and [*1-10*] (**Figure 2.8 (b)**) directions. **Figure 2.8 (c)** shows a characteristic 3D diffraction pattern along the GaAs [*1-10*] direction corresponding to the formation of InAs quantum dots on a GaAs (001) surface. In this last image, it can be observed that the typical 3D spots acquire a V-shape that is called *chevron*. This effect indicates that the quantum dots are terminated by facets inclined by only a small angle with respect to the substrate plane so that the electrons, diffracted from these facets, can be observed on the screen [18]. On the other hand, the intensity at the formed spots is proportional to the quantum dot volume [19].

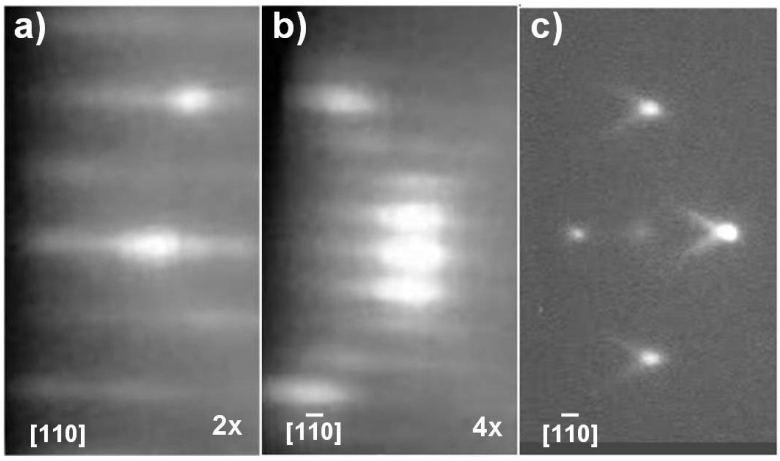

Figure 2.8. RHEED diffraction patterns corresponding to a (2x4) surface reconstruction on a GaAs (001) surface along [110] direction **(a)** and [1-10] direction **(b)**. **(c)** RHHED pattern along the [1-10] direction of a GaAs (001) surface when InAs QD are grown. (Image taken from reference [15])

In the following subsections a detailed description of the main measurement and calibration routines carried out using this technique is presented. In general, this technique can be used to obtain relevant growth parameters that can be transferred to different MBE equipments as equipment-independent measurements.

For the samples grown in this work, an accurate calibration of GaAs and InAs growth rates are mandatory.

· **Growth rate**

For GaAs, the growth rate, measured through the RHEED specular beam intensity oscillations period, as previously commented, is an optimal procedure. This way of measuring the growth rate is quite universal, as compared to the measurement of the III-element flux, which depends on the ion gauge ionization efficiency and the specific geometry of the system.

For InAs, the difference of lattice parameter, a= 6.06 Å, to GaAs, a= 5.65 Å, is 7%, which prevents the InAs to grow indefinitely flat on GaAs substrates and therefore, to measure directly the InAs growth rate by the RHEED oscillations period. For the calibration of InAs, two different procedures can be followed. On one hand, it could be calibrated by growing an InGaAs layer at low InAs growth rates (<0.1 ML/s) and at a fixed GaAs growth rate (~1 ML/s). This way it could be obtained an InGaAs layer with a lattice parameter closer to the GaAs substrate, which permits the growth of thicker flat layers with their corresponding optimal specular beam oscillations. From this InGaAs growth rate, and known the previously calibrated GaAs growth rate, it can be directly derived the InAs growth rate.

InAs growth rate can also be obtained by measuring the interval of time necessary to form InAs quantum dots (2D→3D transition in the RHEED diagram) on GaAs (001) surfaces, which corresponds, as previously calibrated, to an InAs critical thickness of ~ 1.7 ML at BEP(As_4)= 2x10^{-6} Torr and T_s= 510ºC.

· As flux on GaAs (001) surfaces

RHEED can also be used for equipment-independent measurements of the arsenic flux supplied to the growth front. It is based on the As incorporation rate (ML/s) on Ga-saturated surfaces as a function of the ion gauge BEP. To do this, it is necessary to measure the RHEED specular beam oscillations produced when an As beam is supplied on a Ga-rich GaAs (001) surface (T_s= 500ºC) after depositing several Ga monolayers. This way, the As_4 incorporation kinetics on a GaAs (001) surface is modified in such a way that all the As atoms incorporate to the surface forming GaAs. The number of specular beam oscillations obtained is determined by the number of Ga monolayers previously deposited. The period of these oscillations is a direct measurement of the As-atoms monolayers per second (ML/s) that reach the surface for a given BEP(As_4) ion gauge reading.

· Substrate temperature

In order to measure the substrate temperature in a reproducible way, with independence of the used experimental set-up, it is performed a protocol based on changes of the GaAs (001) surface reconstruction, well-measured by RHEED, with the substrate temperature and under different As_4 flux (static conditions) or in absence of arsenic flux [20]. This kind of protocols relies on the fact that a change of surface reconstruction is much more sensitive to the substrate temperature than to the V-element flux [9]. This way, varying T_s at a fixed BEP(As_4) and observing any change in the RHEED pattern, it is possible to establish, from a surface reconstructions diagram as a function of T_s and BEP(As_4), an accurate correspondence between the thermo-couple temperature measurement and the actual surface temperature value for such a RHEED transition [21].

In particular, in this work, for the substrate temperature calibration, two different pairs of temperature values ($T_{thermocouple}$, T_{real}) corresponding to two perfectly defined RHEED transitions were used:

- the GaAs (001) native oxide desorption that corresponds to T_{real}= 600ºC [22] and

- the surface reconstruction transition (2x4) $\rightarrow$ c(4x4) under an arsenic flux equivalent to 2 ML/s (BEP(As_4)= 2x10^{-6} Torr in our set-up) that corresponds to a T_{real}= 510ºC [23].

With these two temperatures and assuming a linear interpolation, a ($T_{thermocouple}$-T_{real}) temperature calibration in the range of temperatures 450ºC – 600ºC can be obtained.

2.1.3.2. Reflectance Difference (RD)

In this work we have used reflectance difference (RD) measurements to monitor the surface stoichiometry of the growth front. Reflectance difference spectroscopy (RDS) or reflectance anisotropy spectroscopy (RAS) is a technique developed in 1985 [24,25] and based on the measurement of the optical reflectance anisotropy of a surface along two orthogonal crystallographic axis, typically [*110*] and [*1-10*] directions on (001) surfaces of III-V semiconductors. In bulk isotropic materials, as semiconductors, this optical anisotropy comes from the surface, specifically, from the lack of symmetry coming from the atoms re-organization of each characteristic surface reconstruction. The spectra measured by this technique permits then, the identification of the different surface reconstructions during the growth process [26]. Depending on the incident light wavelength, the optical anisotropy observed in the RD signal ($R_{[110]} - R_{[1\text{-}10]}$) is related to different absorption [27]. In particular, at photon energies of 1.8 eV, it is related to the absorption of dimers of elements of Group III, formed on a (001) semiconductor surface [28]. Thus, if a He-Ne laser is used as light emitter (emission at 1.96 eV), variations in the RD signal will correspond to the variation of the population of dimers of elements of Group III on the surface during the growth process.

The experimental set-up of this technique, developed at IMM, is shown in **Figure 2.9**. Light from the He-Ne laser is linearly polarized and the angle of incidence is set at 45º respect to the GaAs (001) [*110*] and [*1-10*] directions. This way, once separated by a Wollaston prism, each of the polarizations along [*110*] and [*1-10*] of the reflected light on the sample, are measured by the use of two photodiodes. The signal from these photodiodes is introduced in a differential amplifier, obtaining that way, the relative difference of both signals. On III-V semiconductor surfaces, the RD values are smaller than 1% of the total surface reflectance. Although this is a small value, the experimental set-up shown in **Figure 2.9** provides an excellent signal to noise relation and a modulation of the incident beam is not necessary.

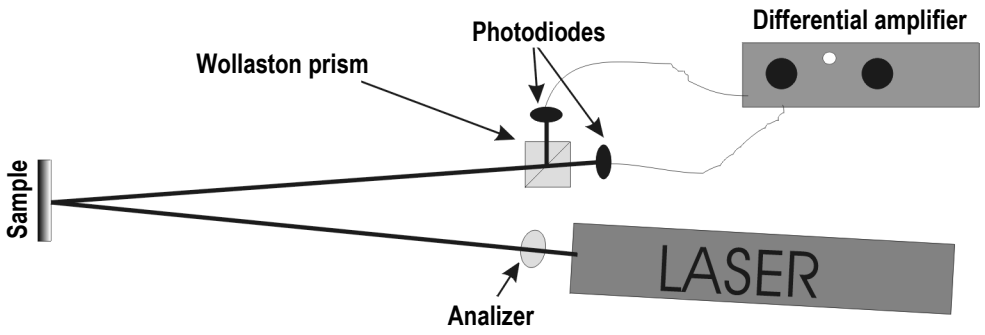

Figure 2.9. Schematic representation of the reflectance difference set-up at an energy of 1.96 eV (He-Ne laser emission). (Image taken from reference [4]).

RD technique is specially useful for controlling the surface stoichiometry during atomic layer molecular beam epitaxy (ALMBE) growth process [29,30]. With this ALMBE growth technique, the continuous supply of III-V materials is replaced by an alternating protocol or, in a similar way, by keeping constant the flux of element of group III while the element of group V is pulsed periodically in coincidence with the completion of a monolayer of element of group III. The amount of atoms of group V can be controlled by the duration of the pulse, permitting the growth of the III-V compound with control in the surface stoichiometry. This MBE alternating growth protocol permits to obtain a 2D growth in substrate temperature and lattice mismatch conditions that would be inaccessible by conventional MBE. During ALMBE growth, the RD signal oscillations, related to the transition between a surface saturated in element of Group III (when the flux of element of Group V is interrupted) and a surface rich in element of Group V (when the flux of element of Group V is supplied), are measured and the amplitude of them is related to the surface saturation of each supplied element. Therefore, by controlling the amplitude of these RD oscillations, the conditions for the ALMBE growth can be optimized as desire.

In this work, the ALMBE conditions were optimized for an optimal 2D GaAs growth on patterned substrates (described in more detail in the experimental sections of chapter 3) and modified for a controlled formation of low density nanoholes templates on GaAs (001) and InP (001) surfaces (**Figure 4.4** and **Figure 4.5** in chapter 4).

2.1.4. Selective growth of III-V semiconductor nanostructures on patterned substrates by MBE

This section is devoted to describe the main relevant aspects to take into account in the selective epitaxial growth of III-V semiconductor nanostructures on patterned substrates. The role of the chemical potential as driving force for selective growth is also presented.

As already commented in chapter 1, the integration of QD as active elements in new quantum optoelectronic devices requires a precise control in their shape, size and location over the substrate. In this direction, different strategies have been followed in the last years with promising results. One of them is the use of patterned substrates.

· Preparation of the pattern

When using a prestructured surface, the technological processes to carry out have to be compatible with the preservation of such a surface. In this direction, the following restrictions have to be considered:

- *Substrate temperature*: in order to preserve the pattern of the substrate, the maximum substrate temperature should not overcome the temperature for which surface atom migration becomes relevant [31].

- *Buffer layer thickness*: due to the presence of non-radiative centres on the patterned surface, it is necessary to separate the nanostructures from this interface by the growth of buffer layers of a few monolayers thick. The growth conditions of this buffer layer have to be adapted to avoid preferential growth into the nanohole and therefore, its evolution towards a flat surface. This way, the buffer layer thickness is limited and its value is conditioned by the used epitaxial growth conditions [32].

· **Driving force for selective growth: chemical potential** [33]

When crystal growth is carried out on a nanostructured surface, the formation and positioning of the nanostructures are naturally determined by the minimization of the total free energy of the surface. This energy involves basically two terms. First, the surface and interface energies of the substrate and growing layer, together with their anisotropies that are in the origin of facetting. The second is the elastic energy stored in the bulk of the objects and neighbouring media (substrate, deposited film, etc.). The place where the growth takes place depends on the relative values of these two physical magnitudes. The surface chemical potential can be expressed as

$$\mu = \frac{\partial}{\partial N}(F + PV)\Big|_{T,P} \qquad \textbf{Equation 2.1}$$

where F is the surface free energy and N the number of particles in the system of volume V and pressure P. Although μ is an equilibrium thermodynamic quantity, we use it here referred to the case of local equilibrium in order to apply it to the case of real growth conditions.

The atom difussion on the surface is driven by the gradient of the chemical potential. The atomic surface flux j is given by the Nernst-Einstein relation

$$j = -\frac{nD}{k_B T}\frac{\partial \mu}{\partial s} \qquad \textbf{Equation 2.2}$$

where n is the adatom density, D is the surface diffusion coefficient and ∂s is an infinitesimal length.

Following the work by Herring [34] and Mullins [35] and considering an unidimensional surface described by a single variable x, the chemical potential can be described as

$$\mu(x) = \mu_0 + \Omega_0 \gamma K(x) + \Omega_0 E_s(x) \qquad \textbf{Equation 2.3}$$

where μ_0 is the chemical potential of the surface plane, Ω_0 is the atomic volume, γ is the surface free energy (which depends on the orientation) and $K(x)$ is the curvature of the surface (negative for a concave morphology). The function $E_s(x)$ is the local energy due to the surface stress.

This simplified model represented in **Equation 2.3** shows that for the growth of a layer of the same composition of the substrate:

- The surface curvature term favours adatom diffusion towards the bottom of concave morphological features, such as holes, channels and so on;

- The elastic term favours growth in convex regions, such as ridges, peaks and so on, where there is greater release of elastic energy.

Epitaxial growth of an element differing from the substrate (heteroepitaxy) also depends on these two terms (see section 4.7). The elastic term must in this case account for the lattice mismatch between the elements [36]. Hence, the critical thickness at which islands begin to form in the SK transition will be more quickly reached at specific locations in a pattern. One can thus obtain long-range ordering in the dot positions depending directly on the pattern regularity.

· InAs deposition on GaAs (001) patterned substrates

For the special case of InAs deposition on GaAs (001) patterned substrates, system mainly used in this work, there are some growth parameters that has to be properly chosen to obtain an optimal selective epitaxial growth. In particular, it can be found in the literature several works that study in detail the influence of the substrate temperature [37,38], the In growth rate [39,40] and the As pressure [41-43] in the formation of InAs QD.

Concerning the dependence of the InAs growth kinetics with the substrate temperature, it has been found that the In diffusion on GaAs (001) surfaces increases with this growth parameter yielding a decrease in the density of formed QD together with an increase in their size [38]. On the other hand, it has also been observed experimentally that the InAs desorption from the surface increases with the substrate temperature for certain growth conditions [41]. Moreover, an increase of temperature also implies an enhancement of atoms interdiffusion between In deposited and Ga from the substrate and In segregation

processes during the capping growth with GaAs [44,45]. Thus, the control of this parameter is important in order to obtain QD of a given size and composition (see section 4.4.4).

Concerning the In growth rate, different works have demonstrated that a decrease in the value of this parameter leads to an increase of the In diffusion length [40,46]. Alloing et. al. [46] have shown that is possible to reduce the density of QD from $3x10^{10}$ cm^{-2} to $2x10^{8}$ cm^{-2} when the In growth rate is reduced from 0.16 ML/s to 0.0012 ML/s. The reason underlying this effect is that low growth rates are closer to the thermodynamic equilibrium conditions and then the importance of kinetic effects is minimized [47]. On the other hand, Heyn et. al. [39,48] have also shown that low In growth rates at a given substrate temperature lead to an increase of the interdifussion processes between In deposited and Ga atoms from the surface.

Another parameter that influences the In diffusion length on GaAs (001) substrates is the As pressure used during InAs deposition. In this direction, it has been demonstrated that lower As pressures lead to a decrease in the QD density and an increase in their size [49,50].

2.2. Ozone selective oxidation set-up

In this section, it is presented the calibration of the experimental set-up assembled in this work for the ozone selective oxidation of III-V semiconductor surfaces. As a comparison, the calibration of a commercial UVO-CLEANER® set-up is also studied.

The experimental technique here presented, is based on the selective oxidation of GaAs and InP substrates by means of their interaction with a reacting ozone atmosphere [51]. As previously commented in the introduction of this thesis, the aim of this novel process is to provide selective nucleation centres, as concave pits, that permit to grow ordered configurations of QD by further InAs deposition. The nucleation results of this technological approximation are shown in chapter 3.

The ozone is produced by the irradiation with UV light, produced by a discharge low-pressure mercury lamp (wavelengths λ_1= 184.9 nm and λ_2= 253.7 nm), of an open-air container. The 184.9 wavelength is absorbed by oxygen, and leads to the generation of ozone (the energy required to dissociate an O_2 molecule into two ground state O atoms corresponds to 245.4 nm) [52]. The 253.7 nm radiation is not absorbed by oxygen; it therefore does not contribute to ozone generation. However, it is absorbed by most hydrocarbons and also by ozone. The absorption by ozone is principally responsible for the destruction of ozone in the UV box (λ_2 is called "*ozone killer*"). Therefore, when both wavelengths are present, ozone is continuously being formed and destroyed. An intermediate product of both the formation and destruction processes is atomic oxygen, which is a very strong oxidizing agent.
The different processes involved are shown in **Figure 2.10**: [53]

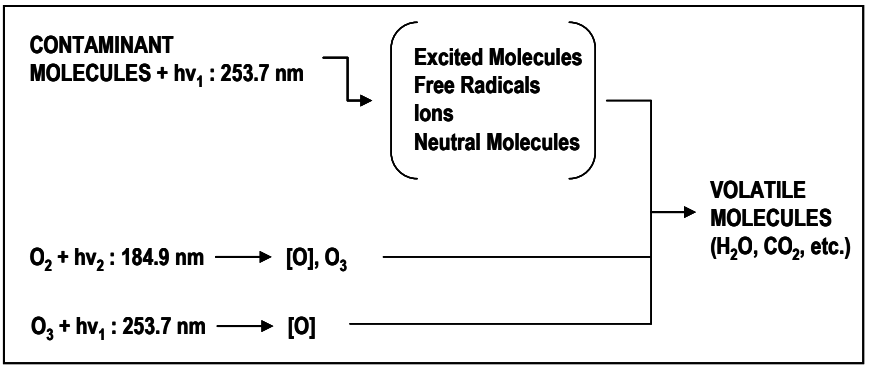

Figure 2.10. Processes involved in an open-air system when it is irradiated by UV light with wavelenghts λ1= 184.9 nm and λ2= 253.7 nm.

Once the ozone is produced, it reacts with the GaAs surface producing the oxides Ga_2O_3, As_2O_5 and As_2O_3 [54].

For the calibration of the experimental set-up as a function of the light exposure time on GaAs and InP substrates, we fabricated a metallic mask on these substrates by conventional photolithography (squares and circles opened to the substrate ranging from 1 μm to 5 μm in diameter and side, respectively). By the selective oxidation and posterior oxide etching process of the semiconductor substrate through these apertures, an accurate oxidizing performance of the lamp was performed. In particular, oxidation processes with durations ranging from 1 min to 30 min were carried out. For each oxidation time intervals the process was repeated 5 times for averaging. Citric acid dips (t= 60 s, dissolution 1 M) were carried out, each time, in order to remove the as-formed oxide.

The oxide thicknesses obtained for the different time intervals were measured by AFM as the average difference between the initial and final depth of the opened windows after the oxidation-etching process.

2.2.1. Home-made oxidation set-up

Figure 2.11 shows an image of a home-made oxidation set-up. It consists of an aluminium box where it has been located a low pressure Hg discharge lamp (output power of 4 W). The tube of the lamp consisted of a cylindrical fused quartz (10 cm in length and 2 cm in diameter) which transmits both the 253.7 and 184.9 nm lines. A Ta sheet has been welded as the sample holder at a distance of 1 cm from the lamp. Below this image the lamp 220V-circuit is also shown.

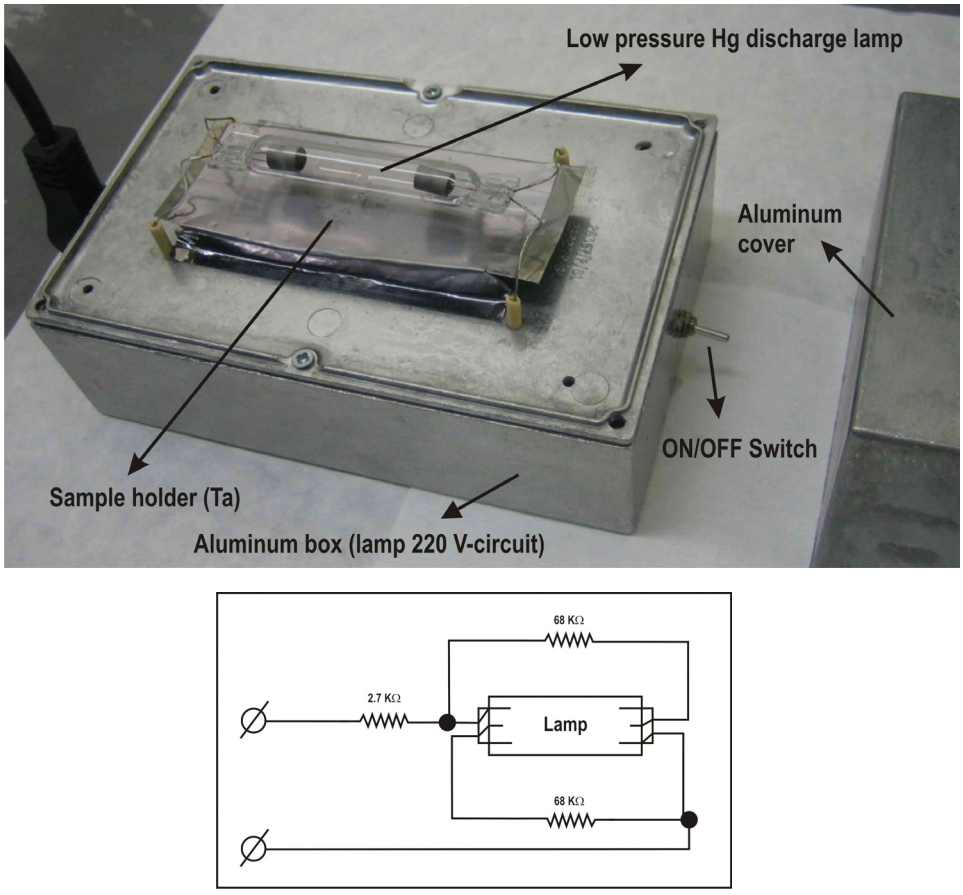

Figure 2.11. Image of the home-made UV-ozone selective oxidation set-up used in this work. Below the image the lamp 220V-circuit is also shown.

Figure 2.12 shows the calibration curve obtained for GaAs (red squares) and InP (black triangles) substrates.

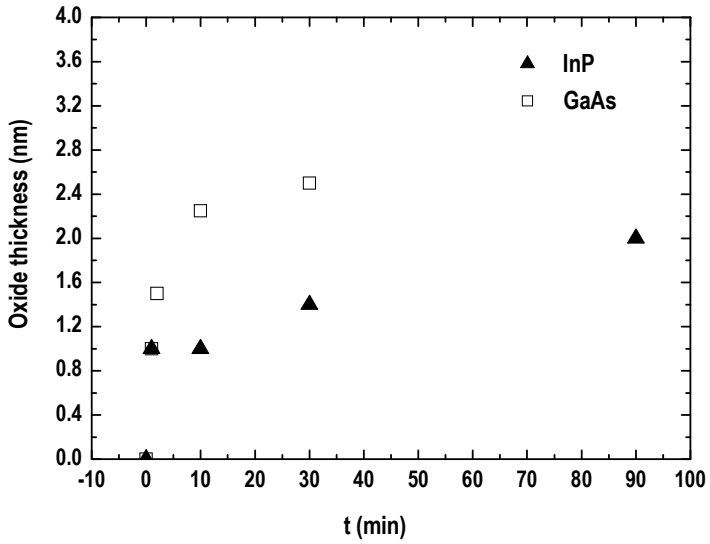

Figure 2.12. Thickness of the oxide as a function of the exposure time on GaAs (001) and InP (001) surfaces.

The results obtained show an expected logarithmic behaviour with a time of 30 min for the oxide saturation in GaAs. Notice that with 1 min of exposure a 1 nm-thick oxide is obtained on both materials. However, the InP oxide thickness seems to reach a smaller saturation size.

2.2.2. Commercial UV-cleaning set-up (UVO-CLEANER® Model 42-220)

The experiments presented in this thesis related to the selective oxidation of III-V semiconductors have been obtained by the use of a home-made ozone producer set-up. In order to compare with a commercial set-up, designed for removing organic contaminants from surfaces, is presented in this section. (This work was carried out at the semiconductors group of the Cavendish Laboratories at the University of Cambridge).

In particular, an UVO-CLEANER® Model 42-220 (**Figure 2.13**) was used for oxidizing GaAs substrates in a controlled way. It consists of an encapsulated stainless steel box with a low pressure Hg vapour grid with an output of 28 W/cm from 6 mm distance to the sample holder [55].

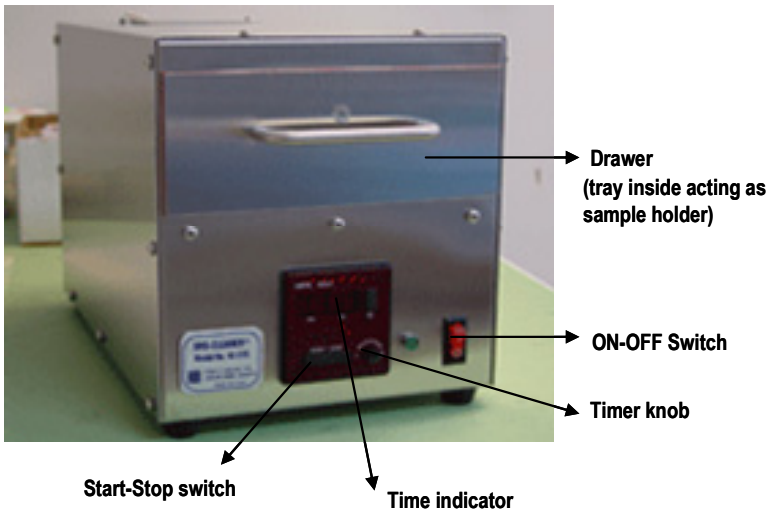

Figure 2.13. Image of a commercial UVO cleaner set-up

For the oxide growth calibration, the exposure time intervals used were 0 s (to measure the thickness of the native oxide),10 s, 60 s and 120 s. The results obtained (**Figure 2.14**) show again an expected logarithmic behaviour where after a 60 s oxidation step the oxide thickness already saturates with a mean value of 10.6 nm. It has to be noticed, as a comparison to the home-made lamp, that after only 10 s of oxidation time, a 5.4 nm-thick oxide is already formed (**Figure 2.15**) with this set-up.

The square mean roughness (rms) of the GaAs surface after this oxidation-etching process is 1.2 nm. It has to be taken into account that no specific cleaning processes were performed in these samples to avoid such a rough surface.

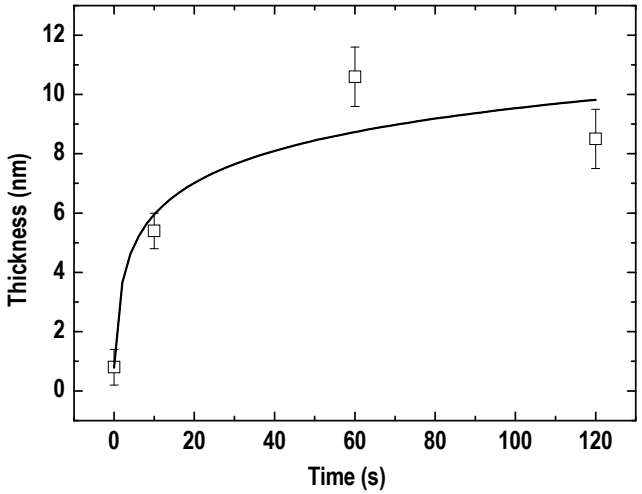

Figure 2.14. Set-up calibration curve for different exposure time intervals. At 60 s, the saturation regimen is already reached, resulting in the formation of a 10nm thick GaAs oxide.

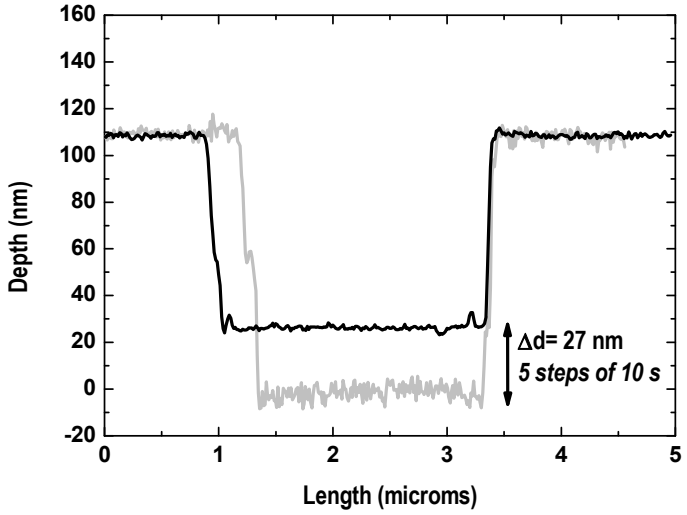

Figure 2.15. AFM profiles of a mask aperture, before (black line) and after (red line), a 5-step 10s-oxidation-etching process.

According to these results, it can be derived that our home-made set-up can provide, probably due to the use of a unique and less powerful lamp, a more controlled oxidation process in the range of depths 1-10 nm. However, if nanoholes deeper than 10 nm are necessary, the commercial set-up is more optimal since, the oxidation/etching process is limited to a single technological step.

2.3. Atomic force microscopy (AFM)

Atomic force microscopy (AFM) is a technique that allows to obtain topographic images of all kind of materials (metals, insulators, semiconductors, biological species...etc) with a very high resolution

[56,57]. It is based on the interaction forces that arise between atoms in a nanometric tip and a surface when the tip is approached slowly towards the surface.

Basically, this topographic technique consists in scanning across the sample surface a tip of nanometric size, located in the apex of a micro-cantilever, maintaining a constant tip-sample interaction (**Figure 2.16**). To do this, a laser spot is reflected off the back-side of the cantilever onto a four-segment photo-diode. The surface topography is obtained from the cantilever deflexion variations that permit to maintain constant the tip-surface interaction. These variations are detected by the photo-diode. AFM can generally measure the vertical and horizontal deflection of the cantilever. To do this, the signal from the four-segment photo-diode can be configured in two different modes depending on the kind of information to measure. If we want to measure vertical displacements (micro-cantilever deflexion) of the laser beam, the differential signal between the upper and lower parts of the photo-diode is carried out. If, on the contrary, we are interested in measuring lateral displacements (torsional cantilever deflections), the differential signal between the left and right parts of the photo-diode will be carried out. In this work, we have always carried out topographic measurements, so, the vertical deflexion of the cantilever was always used.

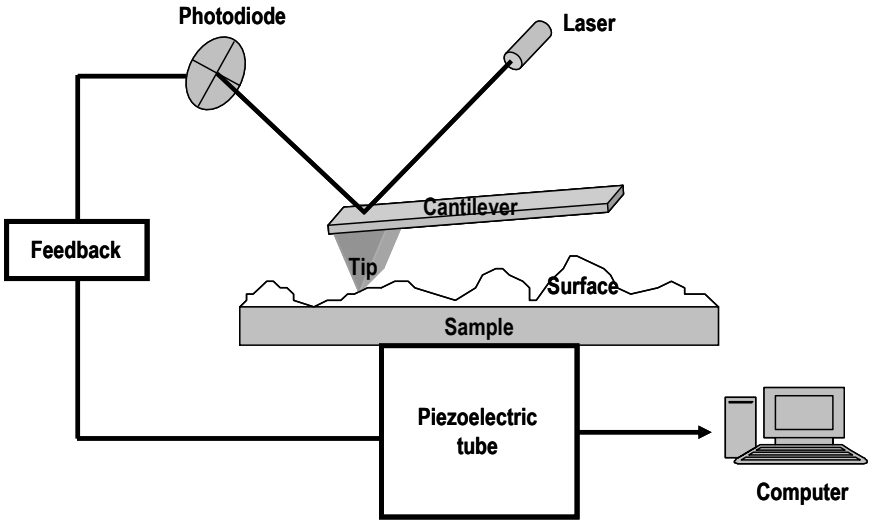

Figure 2.16. Schematic representation of an AFM system operation (image taken from reference [15]).

Previously to approach the tip to the surface, the set-up is aligned by centring the reflected laser beam at the photo-diode. This way, the initial differential signal will be zero (**Figure 2.16**). At this moment, the tip is approached towards the sample. As the surface-tip distance becomes small, then the tip feels the interaction with the sample and the cantilever is deflected, which is detected by a signal variation in the photo-diode. This static cantilever deflexion will be the set-point value that will be maintained constant during the imaging process by a feedback mechanism (contact mode [58]). Usually, the feedback mechanism acts on a piezoelectric tube where the sample is mounted, that can move the sample in vertical direction for maintaining a constant force, and in lateral directions for scanning the sample. For

maintaining constant the set-point during scanning, different voltages are applied to the piezoelectric in order to approach or withdraw the sample depending on the surface roughness. These voltage values are translated into nanometers by a control software, establishing a 3D map of the surface topography.

The AFM can be operated in a number of modes, depending on the application. In general, possible imaging modes are divided into static (contact mode, previously described) and a variety of dynamic (or non-contact) modes where the cantilever is vibrated. In the dynamic mode, the cantilever is externally driven to oscillate at, or close, to its fundamental resonance frequency or a harmonic. The oscillation amplitude, phase and resonance frequency are modified by tip-sample interaction forces; these changes in oscillation with respect to the external reference oscillation provide information about different sample's characteristics. Schemes for dynamic mode operation include frequency modulation [59] and the more common and mainly used in this work, amplitude modulation [60] or more specifically tapping mode.

In the tapping mode a small piezoelectric element mounted in the AFM tip holder drives the cantilever to oscillate up and down at near its resonance frequency. The amplitude of this oscillation is greater than 10 nm, typically 100 to 200 nm. The amplitude of the oscillation decreases as the tip gets closer to the sample due to the interaction of forces (Van der Waals force or dipole-dipole interaction, electrostatic forces,...etc) acting on the cantilever. An electronic servo acts to the piezoelectric actuator to control the height of the cantilever above the sample. The servo adjusts the height to maintain a set cantilever oscillation amplitude (set-point in tapping mode) as the cantilever is scanned over the sample. A tapping AFM image is therefore produced by imaging the force of the oscillating approaches of the tip with the sample surface. This mode is an improvement over conventional contact AFM, in which the cantilever just drags across the surface at constant force and can result in surface damage [61,62]. Due to the requirement of further MBE regrowth processes in the patterned samples of this work, AFM tapping mode was the operation mode mainly used.

· Experimental set-up

Figure 2.17 shows an image of the AFM system used in this work fabricated by Nanotec [63]. Basically, this system consists of:

- The AFM head: it contains a four-segment photo-diode, a laser, prisms for fine adjustment of the laser on the photodiode and the chip (or AFM tip holder) holder. A small piezoelectric element is mounted on this chip to excite the oscillation of the cantilever (voltages up to 10 V and frequencies in the range 1 Hz – 2 MHz). By the use of micrometric screws, lateral XY tip displacements up to 6 mm over the sample are also possible.

- A piezoelectric tube: this element is divided in four longitudinal segments. When voltage is applied, it permits to make XYZ lateral displacements of the sample [64]. Its concentric tubular design minimizes the thermal drift. The maximum horizontal (XY) and vertical ranges (Z) are 70 μm x 70 μm and 12 μm, respectively. The resolution is 3.7 Å in horizontal direction and 0.3 Å in vertical direction. The scanning frequencies range between 0.001 Hz and 800 Hz.

- A chassis: it consists of a basis of 30 x 30 cm over which the AFM chassis is mounted. Between the table and the chassis there is an allocated place for the scanner and its connections.

- An anti-vibration table: it avoids any mechanical vibration.

- A control system (electronics): it controls the input/output signals. It is operated by using a Nanotec (WSxM) software [63].

- An optical microscope with an incorporated CCD camera: it allows for the spatial XY localization of motifs on patterned surfaces.

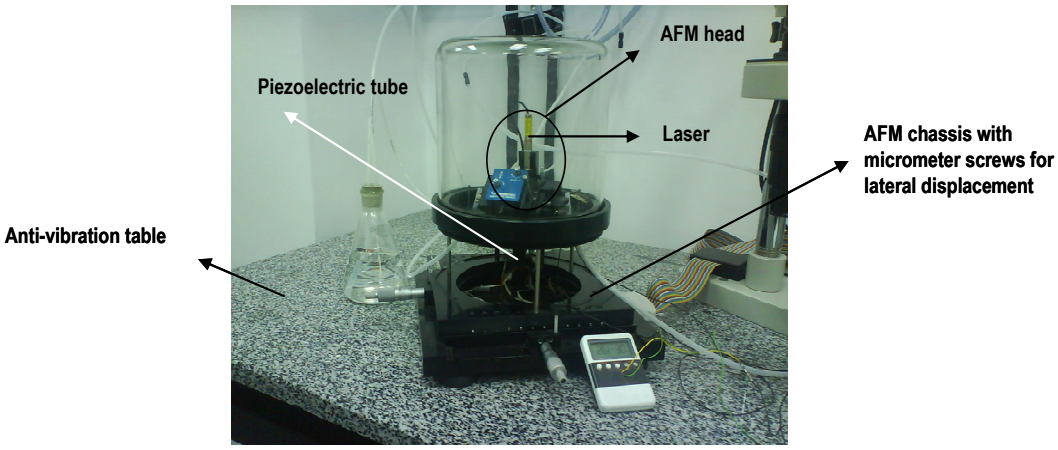

Figure 2.17. Image of the AFM system used in this work.

2.4. Photoluminiscence (PL)

The optical properties of the semiconductor nanostructures fabricated in this work have mainly been studied by means of photoluminescence (PL) measurements. This technique basically consists in obtaining the sample emission of light after being irradiated with light normally produced by a laser. When

the excitation light beam has a photon energy above the semiconductor bandgap energy, electrons from the valence band are promoted to the conduction band. The valence band is left with unoccupied states or holes. The photo-generated electron-hole pairs will recombine after relaxing their kinetics energy by the emission of phonons.

The PL signal can provide information about the structure of energy levels in the sample. It has to be noticed that the information obtained by this technique comes from a depth that approximately corresponds to the excitation light absorption in the material, where the electron-hole pairs are generated.

The PL results shown in this work were carried out at IMM. **Figure 2.18** shows a schematic representation of the PL experimental set-up. A frequency-doubled Nd:YAG laser or a diode laser, λ_{exc}= 532 nm and λ_{exc}= 808 nm respectively, is focused onto the sample surface with a spot diameter of ~ 200 μm. The luminescence emitted from the sample is then focussed by two lenses into the spectrometer (220 mm focal length), at normal incidence. A laser blocking filter is also inserted between the sample and the spectrometer to block any undesired light at the laser wavelength.

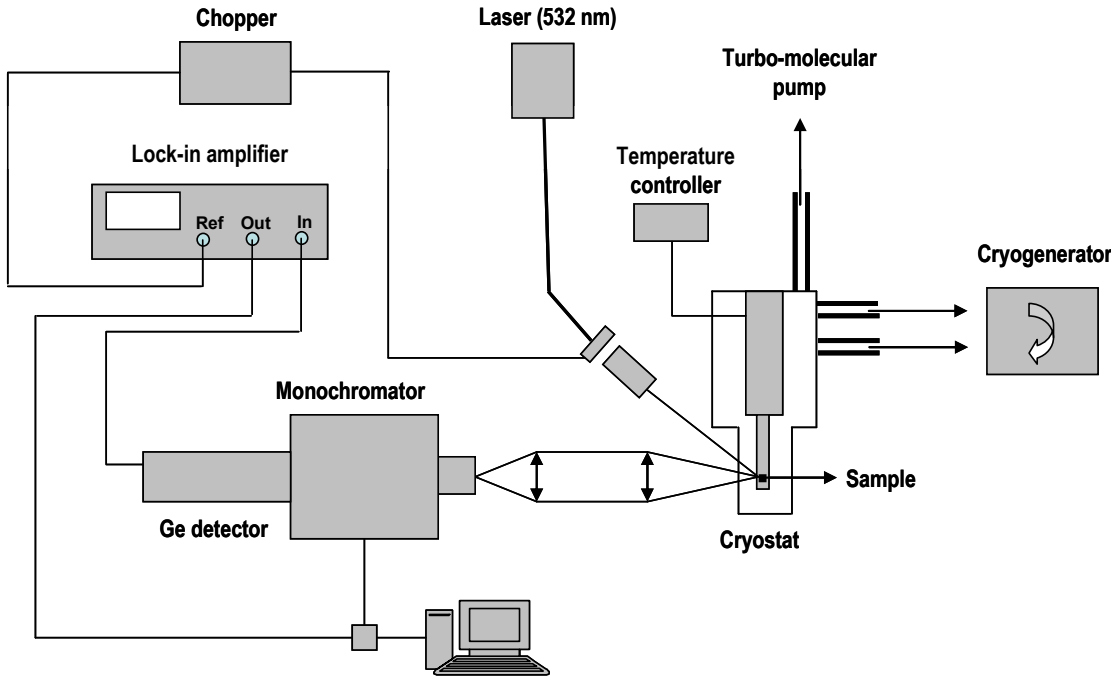

Figure 2.18. Schematic representation of the PL set-up used in this work.

The laser beam is modulated, using a chopper at a frequency of 170 Hz. This frequency is set as a reference into a lock-in amplifier, which permits to recover signals from the sample in the presence of a noisy background. The sample is mounted on a helium continuous flow cold finger cryostat connected to a turbomolecular pump that provides a vacuum of 10^{-6} Torr. For controlling the sample temperature, a Pt-100 resistance is located at the cold finger and connected to an external controller. This way, the temperature can be accurately fixed from 20K to 300K.

The PL spectra is recorded by using a LN_2 cooled Germanium (Ge) detector. It consists of a photo-multiplier tube formed by a Ge crystal at which a high voltage is applied. This detector shows a great sensibility from 800 nm to 1700 nm (1.55 eV – 0.73 eV) suitable to characterize InAs QD on GaAs substrates (typical emission at 1100 nm). The detector generates an output voltage for each detection wavelength, proportional to the recorded intensity. This signal is finally introduced into the lock-in amplifier that permits to obtain the spectra from the sample with a great signal to noise relation.

2.5. X-rays diffraction

X-rays diffraction is a non-destructive analytical technique that reveals information about the crystallographic structure, chemical composition and physical properties of materials and thin films. It can also provide information about the composition, thickness and strain [65] of different layers in a sample. The technique is based on observing the scattered intensity of an X-ray beam hitting a sample as a function of incident and scattered angle and wavelength or energy. The X-rays diffraction spectra depends on several factors as the crystalline structure of the materials, their composition and thickness. These parameters are obtained by fitting the experimental spectra to a model developed by dynamic diffraction theory.

In this work, X-rays diffraction has been mainly used for studying the crystalline structure of Al layers epitaxially grown on III-V semiconductor substrates. For this purpose, it has been used a four-circle X-ray diffraction system with high-resolution optics: a Philips Xpert MRD. The measurements were performed using the $CuK\alpha_1$ radiation (λ= 0.15405nm). As primary optics it was used a 4-crystal Ge (220) monochromator that provides an intense, highly collimated beam (angular divergence of 15”). As secondary optics, a proportional counter detector without any receiving slit providing an angular aperture of 3.5º, was used.

Figure 2.19 shows a schematic diagram of the used X-ray diffraction system at IMM.

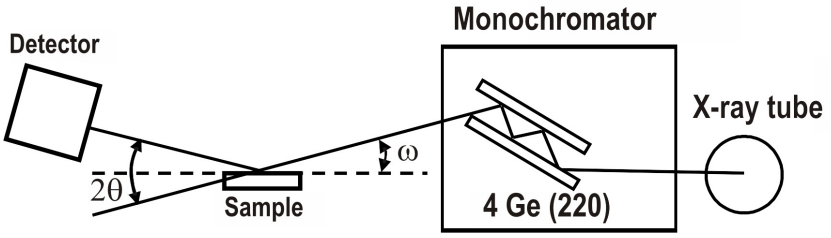

Figure 2.19. Schematic representation of the X-rays diffractometer (Philips Xpert MRD).

References

[1] A.Y. Cho, and J.R. Arthur, Prog. Solid Satate Chem. **10**, 157 (1975).
[2] K.G. Günther, Z. Naturforsch. **13a**, 1081 (1958).
[3] J.R. Jr. Arthur, J. Appl. Phys. **39**, 4039 (1968).
[4] "Phd thesis: Crecimiento y caracterización de hilos cuánticos de Arseniuro de Indio sobre substratos de Fosfuro de Indio (InAs/InP)", D. Fuster, Universidad de Valencia (2005).
[5] "Phd thesis: Epitaxia por haces moleculares (MBE) de heteroestructuras semiconductoras III-V con fuerte desajuste de parámetros de red", A. Ruiz, Universidad Complutense de Madrid (1989).
[6] T.C. Foxon, M.R. Boundry, and B.A. joyce, Surface Science **44**, 69 (1974).
[7] C.T. Foxon, and B.A. Joyce, Surface Science **50**, 434 (1975).
[8] C.T. Foxon, and B.A. Joyce, Surface Science **64**, 293 (1977).
[9] "Molecular Beam Epitaxy, Applications to Key Materials" Noyes Publications, R. F. C. Farrow (1995).
[10] http://www.las.inpe.br/~cesar/Infrared/rheed.htm.
[11] M.G. Lagally, D.E. Savage, and H.G. Tringides, P.K. Larsen and D.J. Dobson, Eds. Plenum Press. NATO ASI Series B **188**, 139 (1988).
[12] B.A. Joyce, J.H. Neave, P.J. Dobson and P.K. Larsen, Phys. Rev. B **29**, 814 (1984).
[13] J.H. Neave, P.J. Dobson, and B.A. Joyce, Appl. Phys. Lett. **47**, 100 (1985).
[14] J.H. Neave, B.A. Joyce, P.J. Dobson, and N. Norton, Appl. Phys. A **31**, 1 (1983).
[15] J.M. Van Hove, C.S. Lent, P.R. Pukite, and P.I. Cohen, J. Vac. Sci. Technol. B **1**, 741 (1983).
[16] "Phd thesis: Crecimiento selectivo de InAs sobre substratos grabados de GaAs (001) mediante litografía de oxidación local de AFM", Javier Martín-Sánchez, Universidad Autónoma de Madrid (2009).
[17] F. Briones, D. Golmayo, L. González, and A. Ruiz, J. Cryst. Growth **81**, 19 (1987).
[18] A. Feltrin, and A. Freundlich, J. Cryst. Growth **301**, 38 (2007).
[19] Ch. Heyn, and W. Hansen, J. Cryst. Growth **251**, 218 (2003).
[20] V.P. LaBella, D.W. Bullock, C. Emery, Z. Ding, and P.M. Thibado, Appl. Phys. Lett. **79**, 3065 (2001).
[21] A.S. Bracker, M.J. Yang, B.R. Bennett, J.C. Culbertson, and W.J. Moore, J. Cryst. Growth **220**, 384 (2000).
[22] Y. Asaoka, J. Cryst. Growth **251**, 40 (2003).
[23] J. Zhou, Q. Xue, H. Chaya, T. Hashizume, and T. Sakurai, Appl. Phys. Lett. 64, 584 (1994).
[24] D. E. Aspnes y A. A. Studna, Phys. Rev. Lett. **54**, 1956 (1985).
[25] D. E. Aspnes, J. P. Harbison, A. A. Studna y L. T. Florez, Phys. Rev. Lett. **59**, 1687 (1987).
[26] I. Kamiya, D. E. Aspnes, L. T. Florez y J. P. Harbison, Phys. Rev. B **46**, 15894 (1992).
[27] D. E. Aspnes, Y. C. Chang, A. A. Studna, L. T. Florez, H. H. Farrell y J. P. Harbison, Phys. Rev. Lett. **64**, 192 (1990).
[28] P. A. Postigo, T. Utzmeier, G. Armelles y F. Briones, J. Cryst. Growth **175-176**, 298 (1997).
[29] F. Briones, L. González y A. Ruiz, Appl. Phys. A **49**, 729 (1989).
[30] F. Briones y A. Ruiz, J. Cryst. Growth **111**, 194 (1991).
[31] S. Kiravittaya, H. Heidemeyer, and O. G. Schmidt, Physica E **23**, 253 (2004).
[32] J. Martín-Sánchez, Y. González, P. Alonso-González, and L. González, J. Crystal Growth **310**, 46768 (2008).
[33] M. Hanbücken, J. Eymery, and S. Rousset, "Growth of organized nano-objects on pre-patterned surfaces" Ed. Springer (2007).
[34] C. Herring, J. Appl. Phys. **21**, 437 (1950).
[35] W. W. Mullins, J. Appl. Phys. **28**, 333 (1957).
[36] B. Yang, F. Liu, M. G. Lagally, Phys. Rev. Lett. **92**, 025502 (2004).
[37] Ch. Heyn, Phys Rev. B 64, 165306 (2001).
[38] M. Yakimov, V. Tokranov, G. Agnallo, J. van Eisden, and S. Oktyabrsky, J. Vac. Sci. Technol. B **23**, 1221 (2005).
[39] Ch. Heyn, A. Schramm, T. Kipp, and W. Hansen, J. Cryst. Growth **301**, 692 (2007).
[40] P. B. Joyce, T. J. Krzyzewski, G. R. Bell, T. S. Jones, S. Malik, D. Childs, and R. Murray, Phys. Rev. B **62**, 10891 (2000).
[41] Ch. Heyn, and W. Hansen, J. Cryst. Growth **251**, 218 (2003).
[42] L. Chu, M. Arzberger, G. Böhm, and G. Abstreiter, J. Appl. Phys. **85**, 2355 (1999).

[43] B. J. Riel, K. Hinzer, S. Moisa, J. Fraser, P. Finnie, P. Piercy, S. Fafard, and Z. R. Wasilewski, J. Cryst. Growth **236**, 145 (2002).
[44] Ch. Heyn, and W. Hansen, J. Cryst. Growth **251**, 140 (2003).
[45] J.M. García, J.P. Silveira and F. Briones Appl. Phys. Lett **77**, 409 (2000).
[46] B. Alloing, C. Zinoni, V. Zwiller, L. H. Li, C. Monat, M. Gobet, G. Buchs, A. Fiore, E. Pelucchi, and E. Kapon, Appl. Phys. Lett. 86, 101908 (2005).
[47] G. Constantini, C. Manzano, R. Songmuang, O. G. Schmidt, and K. Kern, Appl. Phys. Lett. **82**, 3194 (2003).
[48] Ch. Heyn, A. Bolza, T. Maltezopoulos, R. L. Johnson, and W. Hansen, J. Cryst. Growth **278**, 46 (2005).
[49] H. Yasuda, F. Matsukura, Y. Ohno, and H. Ohno, Appl. Surf. Sci. **166**, 413 (2000).
[50] K. Yamaguchi, K. Yujobo, and T. Kaizu, Jpn. J. Appl. Phys. **39**, L1245 (2000).
[51] P. Alonso-González, L. González, Y. González, D. Fuster, I. Fernández-Martínez, J. Martín-Sánchez, and L. Abelmann, Nanotechnology **18**, 355302 (2007).

[52] J. R. Vig, J. Vac. Sci. Technol. A **3**, 1027 (1984).

[53] *http://www.jelight.com/uvo-ozone-cleaning.php*.

[54] J. R. McNesby, and H. Okabe, Adv. Photochem. **3**, 166 (1964).

[55] *http://www.jelight.com/images/manuals/uvo-cleaner/42-220-60.pdf*.

[56] F. Ohnesorge, and G. Binnig, Science **260**, 1451 (1993).
[57] F.J. Giessibl, Science **267**, 68 (1995).
[58] G. Binnig, C.F. Quate, and Ch. Gerber, Phys. Rev. Lett. **56**, 930 (1986).
[59] T. R. Albrecht, P. Grtitter, D. Horne, and D. Rugar, J. Appl. Phys. **69**, 668 (1991).
[60] Y. Martin, C.C. Williams, and H.K. Wickramasinghe, J. Appl. Phys. **61**, 4723 (1987).
[61] J. Tamayo, and R. García, Langmuir **12**, 4430 (1996).
[62] A. San Paulo, and R. García, Biophysical Journal **78**, 1599 (2000).
[63] I. Horcas, R. Fernández, J. M. Gómez-Rodríguez, and J. Colchero, Rev. Sci. Instrum. **78**, 013705 (2007).
[64] S. Vieira, IBM J. Res. Develop. **30**, 553 (1986).
[65] D. K. Bowen y B. K. Tanner, Taylor & Francis Ltd, London, (1998).

III

EX SITU PATTERNING TECHNOLOGIES

3. *EX SITU* PATTERNING TECHNOLOGIES

This chapter presents two technological approaches to achieve the growth of position controlled InAs nanostructures by using different strategies to fabricate distributions of nanoholes on GaAs substrates. The first technique presented is based on the formation of a monolithically integrated ordered porous alumina mask, by the anodic anodization of an aluminum layer epitaxially grown on the GaAs (001) substrate. As it will be shown, by continuing the anodization process of the aluminum layer up to the semiconductor substrate, nanoholes with a certain hexagonal lateral ordering are obtained for further InAs selective growth. As a second part in this chapter, it is presented a novel method to perform an optimal transfer of a pattern, previously performed on a resin layer deposited on the substrate. The transfer process of the pattern is based on the selective oxidation of the underlying semiconductor substrate. In particular, it will be shown that the different technological processes carried out for this transfer and for the posterior InAs overgrowth, are good enough for nucleating spatially ordered QD with excellent optical properties.

3.1. Selective growth of InAs QD on GaAs (001) substrates by the formation of alumina masks monolithically integrated on the substrate

In this section it is presented a technological process for the selective growth of InAs QD into GaAs nanoholes fabricated by the transfer of an ordered pattern previously obtained on an alumina mask. This process relies on the use of an Al layer, epitaxially grown on GaAs (001) substrates by molecular beam epitaxy (MBE), as starting point for further porous alumina fabrication. This way, by the electrochemical anodization of this Al layer, a GaAs substrate with a monolithically integrated nanoporous alumina mask is obtained. By continuing the anodization process a few nanometers through the GaAs substrate and removing the nano-channel alumina (NCA) mask selectively, a large area of ordered nanoholes on the GaAs substrate is finally obtained. This experimental procedure is schematically summarized in **Figure 3.1**.

The natural advantage of this procedure is that the technological processes necessary to fix an alumina mask on top of GaAs are suppressed, and consequently, the related GaAs surface contamination avoided. The results presented in this section will show that after InAs deposition, QD are only formed inside the nanoholes and not randomly across the surface, demonstrating that this patterning technology allows obtaining an optimal preferential nucleation of InAs material into previously fabricated GaAs nanoholes.

The section is divided as follows: in a first part a detailed introduction to the anodization process of Al layers is presented. Then, the experimental procedure for obtaining epitaxial Al layers on GaAs substrates by MBE growth and its posterior electro-chemical anodic anodization process is studied. Finally, the different pre-growth treatments of the sample for obtaining a contaminants free GaAs surface after removal of the alumina mask, and the final InAs QD selective nucleation on the pattern are described.

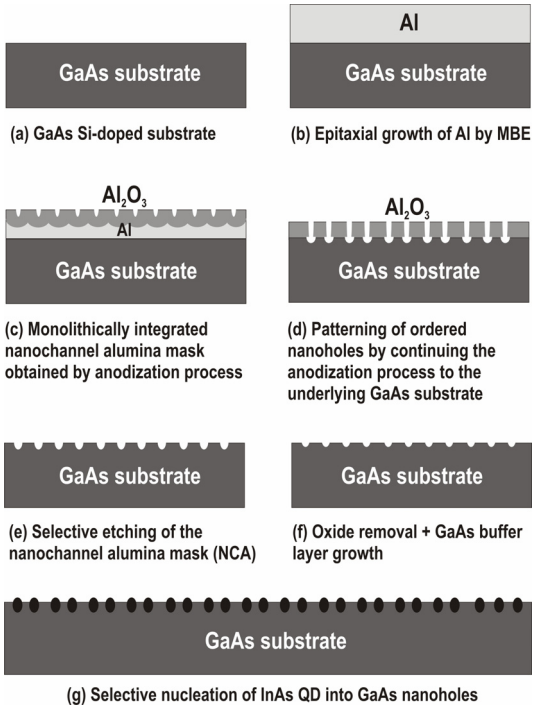

Figure 3.1. Scheme of the fabrication process of a two-dimensional array of ordered InAs/GaAs(001) quantum dots developed in this work.

3.1.1. Aluminum anodization

· Introduction and state of the art

The electrochemical oxidation of Al started to be used in the beginning of the last century. In particular, the anodic treatment of Al was intensively investigated in the past for obtaining protective and decorative films on its surface [1,2]. In general, depending on the experimental conditions, for example, the kind of electrolyte, different types of anodic alumina films can be formed. As a special case, it is well known that by using sulphuric, oxalic or phosphoric acids as electrolytes in the anodization process of thin layers of Al, under certain conditions, oxidation and dissolution of aluminum leads to the formation of pores [3]; otherwise, barrier type films are formed (**Figure 3.2**).

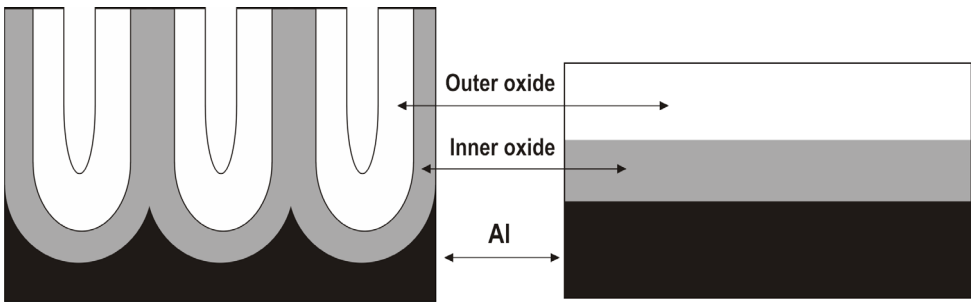

Figure 3.2. Schematic diagram for the alumina structure in a porous (left) and a barrier (right) layer. It consists of an inner oxide of high purity alumina (gray area in the figure) and an outer oxide layer (white area in the figure) comprised of alumina which has incorporated anions.

Pores tend to form a self-assembled honey-comb structure with short range order over certain ranges of anodization potential and electrolyte pH. In the case of nanopores formation, a natural use of these layers as membranes suitable for fabricating patterns on different substrates was immediately investigated [4-6]. However, at the initial stages of this technological approximation, the as-formed alumina films presented not well-ordered pores with a wide diameter distribution and a numerous presence of defects over the surface. In this sense, a breakthrough discovery in the preparation of self-ordered 2D polydomain porous alumina structures, with a very narrow distribution and the nanochannels fairly parallel to each other and perpendicular to the starting Al surface, was obtained by Masuda and Fukuda in 1995 [7,8]. The original process developed for these researchers was based on a two-step anodization process of an Al foil, (see next sections) resulting in porous alumina membranes that subsequently were used as masks for further formation of metal nanodot arrays on Si substrates by electron beam evaporation [9]. Within this approach, new applications have been proposed by exploiting the formation of porous alumina layers on large areas with a narrow pore size distribution. For example, using porous alumina masks, the fabrication of new inorganic templates has been used as a mask in the electrodeposition of nanowires or nanotubes arrays with a uniform control of diameter and high aspect ratios [10-16]. In the same way, nanodots arrays of different metals [17-20] and semiconductors [21-29] have been obtained on several substrates by this template-synthesis method. Also, by combining the anodization process with novel nanoimprint technologies monodomain porous alumina structures have already been obtained on thick Al foils [30,31].

Altogether, this collection of results has revealed the technology based on the anodization of Al layers by the formation of NCA masks for further definition of a nanopattern, as a cost-effective and highly manufacturability approach compared to nanolithography. However, as it will be presented in this chapter, for the special case of using semiconductor substrates, the transfer mechanism to the underlying substrate of a regular pattern obtained in a thin alumina layer, has to be improved for an optimal technological application.

· Al anodization process

It is well known that aluminum and its alloys present a high reactivity under an oxygen atmosphere, which naturally originates a thin (a few nanometers) and continuous native oxide all over the surface. This oxide layer mainly consists of amorphous alumina (Al_2O_3) and acts as a natural protection under different external atmospheric agents [1,2]. Studying in detail this reaction, the thermodynamics [31] for this process is as follows:

$$2Al(s) + \frac{3}{2}O_2(g) \rightarrow Al_2O_3(s)\ ;\ \Delta G^\circ = -1582 kJ/mol$$

$$2Al(s) + 3H_2O(l) \rightarrow Al_2O_3(s) + 3H_2(g)\ ;\ \Delta G^\circ = -871 kJ/mol$$

The large Gibb´s free energy changes resulting of these reactions explain the spontaneous reaction leading to the formation of aluminum oxide when a layer of aluminum is exposed to air.
When aluminum is electrochemically anodized, an oxide grows at an anode electrode [32], while hydrogen evolves at the cathode (**Figure 3.3**).

$$2Al(s) + 3H_2O(l) = Al_2O_3(s) + 6H^+ + 6e^- \qquad anode$$
$$6H^+ + 6e^- = 3H_2(g) \qquad cathode$$

From the Nernst equation:

$$U = U_0 - \left(\frac{RT}{zF}\right)\ln\left(\frac{[red]}{[ox]}\right)$$

where R is the universal gas constant, T is the absolute temperature in Kelvin, *z* is the charge number of the electrode reaction, U_0 is the standard reduction potential and F is the Faraday constant (96.500 Coulomb/mole). The electrode reduction potential U at the anode can be written as:

$$U = -1.550 - 0.0591\,pH$$

This explains that the reaction at the anode electrode, at the Al layer in our case, thermodynamically depends on the pH value, which is determined by electrolyte and temperature (this is true for weak acids).

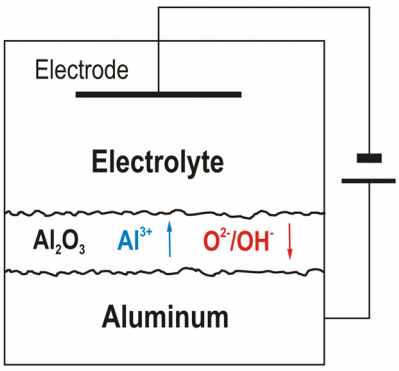

Figure 3.3. Schematic diagram of the Al anodization process.

Related to the kinetics in this process, the current density passing across the oxide film can be written as [32,33]:

$$j = j_a + j_c + j_e$$

where j_a, j_c and j_e are the anion, cation and electron current density contributions, respectively. Since the electronic conductivity in the aluminum oxide is very low, the ionic current density ($j_i = j_a + j_c$) is the

predominant mode to transport the charges. The relationship between the ionic current, j_i, and the electric field, *E*, can be expressed in terms of the Guntherschultze-Betz equation:

$$j_i = j_0 \exp(\beta E)$$

where both j_0 and β are temperature- and metal-dependent parameters.

As it will be commented hereinafter, the effect of maintaining constant the total current density, j_i, or the applied potential, U, in the anodization process seems to be a critical point to obtain a good patterning result on the underlying GaAs substrate.

· Porous alumina structure and formation mechanisms

As it was previously commented, if the electrolyte used in the anodization process partially dissolves the alumina, porous all over the surface are formed. The structure of the nanopores obtained when sulphuric, phosphoric, chromic or oxalic acids are used as electrolytes, has been well studied in the literature [8,34,35]. The structure for the porous type alumina is shown schematically in **Figure 3.2**. It consists of an inner oxide of high purity alumina (grey area in the figure) and an outer oxide layer (white area in the figure) comprised of alumina that contains characteristic anions from the electrolyte (during the electrolytic process not only oxygen ions are incorporated to the formation of the porous) [36,37]. These acid anions are not homogeneously incorporated to the porous alumina forming the outer oxide layer. The nomenclature of the inner and the outer oxide are naturally determined in terms of the interfaces. As it is represented in **Figure 3.2**, the inner oxide is adjacent to the oxide/metal interface, while the outer oxide is adjacent to the electrolyte/oxide interface. The structure for a barrier-type alumina without pores is also represented in this figure for comparison.

Related to the formation mechanisms of these nanopores, a totally convincing explanation has not yet been stated. In the following, the most accepted mechanism is explained by studying the typical current density curve obtained during the Al anodization process. **Figure 3.4** shows a schematic diagram for the current density curve when pore or barrier alumina layers are formed at a constant applied potential. In this figure, j_b and j_p, indicate the current density for the barrier film and the porous film formation, respectively.

As it can be clearly observed, it can be distinguished four different current density transients, that are associated to the different stages observed in the formation of nanopores in an alumina layer [33,38]. At the beginning of the anodization process, the current density j_p, decreases rapidly (regime 1 in **Figure 3.4**), which is associated to the initial formation of a non-porous alumina barrier film consisting of a non-conductive oxide that covers the entire surface of the aluminum. At this point, due to the initial roughness of the Al surface and the difference in cell parameter between Al and Al_2O_3, the electric field is locally focused on that randomly located surface fluctuations that present a convex profile as pits or valleys (regime 2 in **Figure 3.4**).

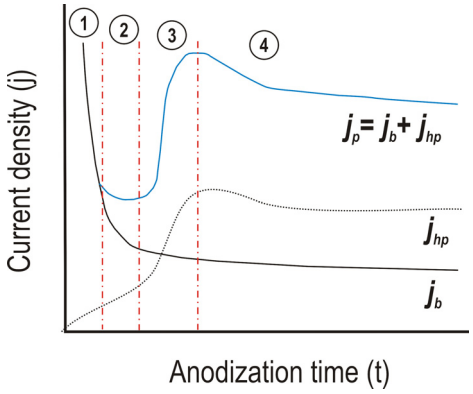

Figure 3.4. Schematic diagram of the current density curve during the initial alumina growth (<1h) at constant voltage. j_b and j_p indicate the current density for the barrier film and the porous film formation, respectively. j_{hp} represents a hypothetic current density, which is the difference between j_p and j_b.

This situation is also displayed schematically in **Figure 3.5 (b)**.

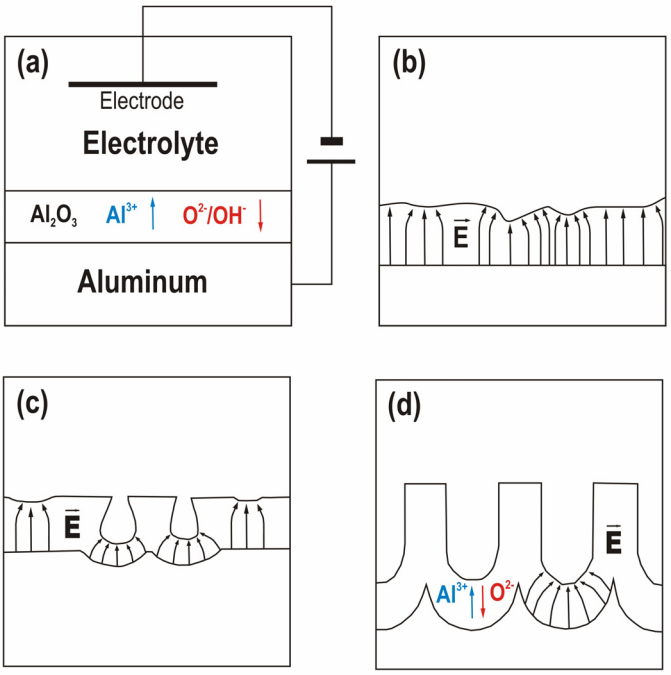

Figure 3.5. Schematic diagram of the pore formation at the beginning of the anodization. **(a)** Formation of a barrier oxide on the entire area. **(b)** The electric field is locally focused on that randomly located surface fluctuations that present a convex profile. **(c)** Creation of pores by field-enhanced or/and temperature-enhanced dissolution. **(d)** Stable pore growth.

This way, these oxide areas will present a field-enhanced and/or temperature-enhanced (local Joule effect) effect that induces an increased of the acid dissolution action [39,40] and then, the formation of nanopores at that location (**Figure 3.5 (c)**) [41]. Owing to this local solvent action, the system resistance diminishes, inducing that way an increase in the current density (regime 3 in **Figure 3.4**). This increase will finish in a maximum that has been interpreted as the moment at which the amount of oxide produced at the oxide/metal interface (inner oxide) reaches the same value to that, chemically etched, at the bottom of

the pits or valleys. From this moment, the thickness of the oxide at the bottom of the pore remains constant during the rest of the process. At those locations where the reacting action of the acid dissolution is not locally enhanced (flat regions in-between the valleys), the oxide growth rate will remain higher than the dissolution rate giving way to the formation of the alumina oxide that surrounds the pores.

Finally, a regime 4 in **Figure 3.4** accounts for a slight decrease of the current density that finally stabilizes in a constant value. It is proposed that is in this regime when the nanopores tend to organize in a hexagonal close-packed (HCP) lattice due to a surface homogenization of the electric field and a minimization of the mechanical stress among the pores [42,43]. This last process, described in more detail in the next section, is produced by the oxide volumetric expansion since the atomic density of Al forming Al_2O_3 is a factor of two lower than in the case of forming metallic Al (**Figure 3.5 (d)**). At this stage, pores grow in a stable manner. However, it is very often observed that during this stable pore growth, the current density continues to decrease slightly. This is due to diffusion limits in the chemical species involved in the formation of very long pores [38].

The term j_{hp} in **Figure 3.4** represents a hypothetic current density difference between j_p and j_b. According to this, it can be considered the current density j_p as the sum of j_b and j_{hp}, which means the pure current density for creating pores. j_b is determined by the applied potential in terms of the anodizing ratio, while j_{hp} depends also on the electrolyte and the temperature.

· Self-ordered porous alumina

Through a careful literature review it can be noticed that self-ordered porous alumina structures can only be obtained under specific conditions. For example, as seen in **Figure 3.6**, structures with pore spacing of 50, 65, 100, 420 and 500 nm are fabricated at 19 V and 25 V in sulphuric acid, at 40 V in oxalic acid, and at 160 V and 195 V in phosphoric acid, respectively [8,34,35].

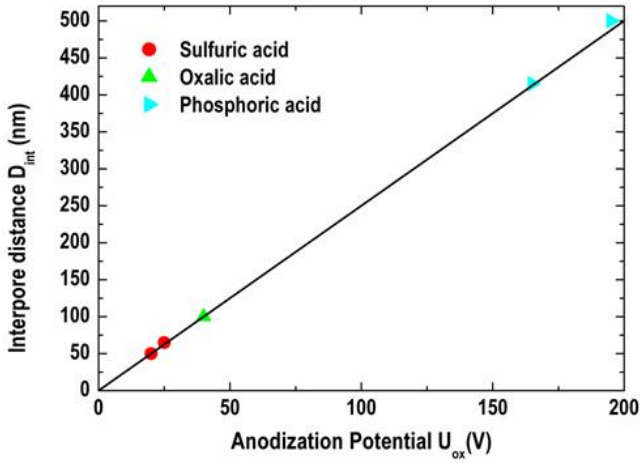

Figure 3.6. Interpore distance as a function of the applied potential. The different symbols show the results obtained in the literature by using sulfuric acid], oxalic acid and phosphoric acid]. The line is a fit to the data with a proportional constant k = 2.5 nm/V.

For this reason throughout this section the different parameter influencing self-ordering are studied in detail. To do this, it is important to introduce first the experimental setup used in this work. **Figure 3.7** shows a schematic diagram of the apparatus for electrochemical experiments. The electrochemical cell consists of a two-electrode system, i.e., platinum (Pt) gauze is used as the counter electrode and the Al layer on the sample as the working electrode. The Al layer is fixed to a W foil and covered by non-conducting paint that permits to expose only the Al surface to the solution. To stir the electrolyte, a motor-controlled agitator is used. For cooling the apparatus, a Peltier element is employed. The temperature is fixed at 0.3ºC. The process is monitored by a computer connected multimeter.

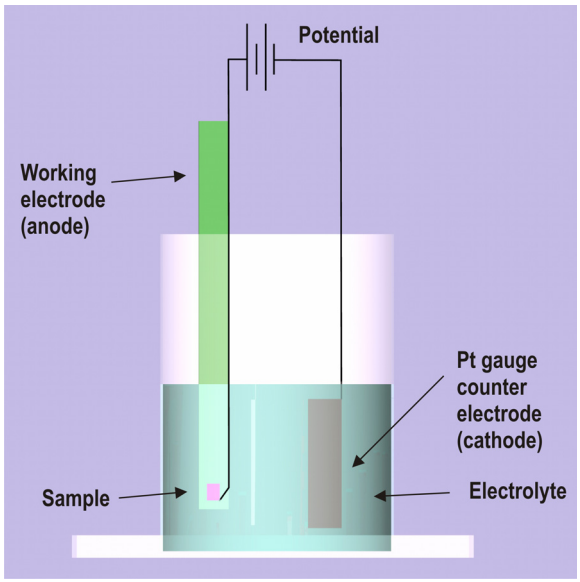

Figure 3.7. Schematic diagram of the set-up used for the anodization of epitaxial Al layers.

· Anodization parameters influencing self-ordering

Related to the anodization process, the main parameters influencing the final ordering of the nanopores are the applied potential, the type and concentration of the electrolyte and the electrolyte temperature and stirring during anodization. Related to the material properties, the density of impurities and the surface roughness in the Al layer are key parameters for an optimal nanopores formation and final self-ordering. The importance of all these parameters is described in detail hereinafter:

- *Anodization Potential*

One of the most important factors to adjust the final self-assembly of porous alumina, is the applied potential U. As previously shown in **Figure 3.6**, the interpore distance, D_{int}, is linearly proportional to the applied potential, $D_{int} = kU$, with a proportionality constant k of approximately $2.5 \leq k\ (nm/V) \leq 2.8$ [35,46].

Additionally, the thickness of the barrier layer can be approximately estimated as half of the interpore distance (D_{int}= $2D_B$, where D_B is the barrier-layer thickness).

- *Type and concentration of the electrolyte*

The type and the concentration of the electrolyte for a given potential has to be properly selected to obtain a self-ordered pore growth. In other words, the choice of the type of electrolyte is restricted. Usually, the anodization of aluminium is carried out in sulphuric acid at low potential ranges (5~40 V) [34], oxalic acid is used for medium potential ranges (30~120 V) [23,25,35] and phosphoric acid for high potential ranges (80~200 V) [8]. This restriction is due to the conductivity and pH value of the electrolyte. For example, if aluminum is anodized in sulphuric acid at a high potential (note that sulphuric acid has a very high conductivity), a breakdown of the oxide layer takes place very often. In addition, the pH value of the electrolyte determines the size of the pores (the lower the pH value, the lower the potential threshold for field-enhanced dissolution at the pore tip). This leads to a smaller size of the pores. In particular, large pore diameters are formed by using the phosphoric acid, and small pore diameter are obtained by using sulphuric acid [36]. **Table 3.1** resumes the nominal diameters and interpore distances for different electrolytes.

Electrolyte	Interpore distance D_{int}	Inner wall thickness D_{inner}	Pore diameter D_p(=2r)
H_2SO_4	66.3 nm	7.2 nm	24 nm
$(COOH)_2$	105 nm	9.1 nm	31 nm
H_3PO_4	501 nm	54 nm	158.4 nm

Table 3.1. Nominal interpore distances and diameters for different electrolytes.

- *Electrolyte temperature*

During the anodization, the temperature should be kept lower than room temperature (RT) to prevent the formed oxide structure from being dissolved in acidic electrolytes. For example, anodization at 40 V in oxalic acid is performed at 5~18ºC and at 0~2ºC in the case of anodization at 195 V in phosphoric acid. A second reason to keep the temperature as low as possible is to avoid a local heating at the bottom of the pores during the course of anodization (specially, in the case of anodization at a high potential). The local heat caused by an inhomogeneous electric field distribution at the bottom, leads to local electrical breakdown of the oxide. In fact, cracks and bursts of the oxide film are generated if porous alumina is formed without control of temperature. If the temperature is too low (just below zero degree) and diluted

electrolytes are used, the electrolyte may freeze. In addition, the speed of the growth of porous alumina is affected by the temperature; the lower the temperature, the lower the growth rate.

- *Electrolyte stirring*

For a homogeneous pH and temperature of the solution it is important to stir the electrolyte during anodization; otherwise, some regions would be overheated promoting a local electrical breakdown of the oxide as commented above. On the other hand, this stirring should also be strong enough for removing the hydrogen bubbles originated during the process, allowing a homogeneous ion diffusion along the pores channels [42].

A careful control of all these parameters allows the fabrication of nanopores with diameters as low as 10 nm and distance between nanopores as high as 200 nm, over regions of several micrometers [43].

· The mechanical stress model

As previously commented, it has been proposed a mechanical stress model to explain the formation of hexagonally-ordered pore arrays [35,42]. In this sense, the following factors are considered:

1.- The oxidation takes place at the entire metal/oxide interface mainly by the migration into the metal of oxygen containing ions (O^{2-} or OH^{-}) from the electrolyte.

2.- The dissolution and thinning of the oxide layer is mainly due to the hydration reaction of the formed oxide layer.

3.- In the case of barrier oxide growth without pore formation, all Al^{3+} ions reaching the electrolyte/oxide interface contribute to oxide formation. On the other hand, porous alumina is formed when Al^{3+} ions drift through the oxide layer. Some of them are ejected into the electrolyte without contributing to the oxide formation.

4.- Pores grow perpendicularly to the surface when the field-enhanced dissolution of the oxide at the electrolyte/oxide interface is equilibrated with oxide growth at the oxide/metal interface.

5.- The formed alumina is assumed to be amorphous Al_2O_3. Therefore, the atomic density of aluminium in alumina is by a factor of 2 lower than in metallic aluminium. This means that the volume of the anodized alumina expands to about twice the original volume of the aluminum matrix.

6. This volume expansion leads to a compressive stress in the Al_2O_3 layer during the oxide formation in the oxide/metal interface. The corresponding expansion in the vertical direction pushes the pore walls upwards.

According to these studies, the degree of the volume expansion of aluminum, the volume expansion coefficient ξ, varies with the applied potential and determines either the formation of self-ordered pores or the formation of disordered pores. If the stress is maximum (corresponding to a $\xi_{max} \sim 2$), no pores are generated. If the stress is too small ($\xi < 1.2$), the force promoting ordering is too small, and a disordered porous alumina array is formed. In the case of moderate promoting forces ($\xi \sim 1.2$), ordered pore growth occurs. If $1.3 < \xi < \xi_{max}$, the size of domains of self-ordered porous alumina decreases and finally disappear due to the strong repulsive interactions. From this model, it can be concluded that self-ordered porous alumina is best formed when the volume expansion coefficient is $\xi \approx 1.2$.

It is noticeable that in the case of using sulphuric acid as electrolyte, a novel recent work [43] has shown the possibility to obtain large-area highly ordered nanoporous alumina films, through a single-step high-field anodization process. In this sense, as previously commented, the expansion force increases with electric field, due to the high-speed formation of alumina at the semi-spherical pore tips under high potential and high current density. It is proposed in this work that this strong repulsive or expansion force under high field (40-70 V) can be used in a controlled way to limit the transverse growth of alumina cells and force them to adopt the mostly closed geometric space arrangement, i.e., the ideally hexagonal arrays, thus producing highly ordered NCA films over large areas.

· Self-ordered alumina by a 2-step anodization process

Figure 3.8 shows a schematic diagram of the different processes normally carried out for the fabrication of an optimal porous alumina layer. It consists in a two step anodization process, firstly used by Masuda et. al. [7,8], that permits to obtain a much better homogeneity of the formed nanopores as well as their final lateral distribution.

Figure 3.8 (a) shows the Al layer as the starting point. At this initial stage the Al is normally electropolished and/or annealed to reduce the surface roughness and to obtain large single crystalline grains, respectively. As a matter of fact, normally, electropolishing is a prerequisite for the formation of self-ordered porous alumina with large domain size while the larger the grains, the larger the domains of self-ordered porous alumina finally obtained. It can be advanced here that, as a difference from other works using this technological process, the metallic layer used in our work is epitaxially grown by MBE which permits, as it will be presented in the next sections, to obtain an initial very flat Al surface with a main crystalline orientation without the use of any other external technological process.

Figure 3.8 (b) shows the pores that are obtained after an initial anodization process. They present a large diameter distribution and a random location on the surface. However, if long anodization processes are

used, self-organization occurs due to the repulsive forces between neighbouring pores. As a result, hexagonally close-packed arrays of nanopores reaching the aluminum substrate. At this point, the porous alumina film is selectively dissolved in a solution containing chromic acid [47] preserving the underlying Al film. Patterns that are replicas of the hexagonal pore array are preserved on the fresh aluminium surface, **Figure 3.8 (c)**. This allows the preparation of nanopores with a high regularity by a subsequent second anodization process, in which each initial valley on the Al will act as new starting location for further nanopores formation. It is important this second step to be carried out under the same conditions (potential, temperature, type and concentration of the electrolyte) as the first anodization (**Figure 3.8 (d)**) process.

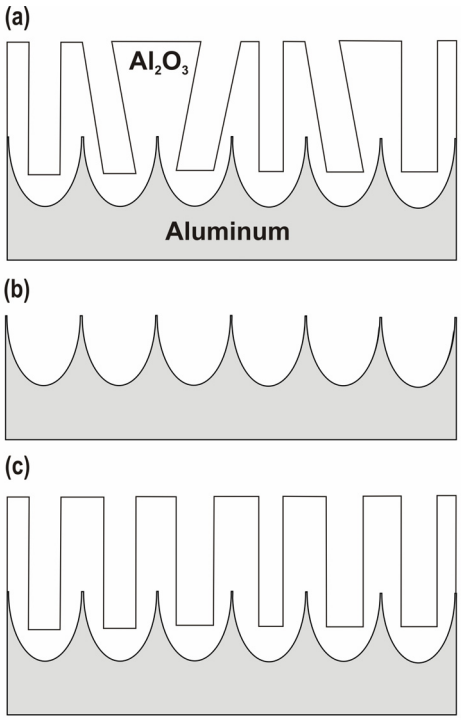

Figure 3.8. Schematic diagram of a two-step anodization process. **(a)** First anodization process. **(b)** Al surface after removal of the resulting alumina layer. **(c)** The homogeneity of the nanopores is clearly enhanced after a second anodization process is performed.

The experimental results obtained in our case, following these processes, are presented in section 3.1.3.

3.1.2. Epitaxial growth of aluminum by MBE

As previously commented, the novelty of the patterning process to carry out in this work relies on the use of an Al layer, epitaxially grown on GaAs (001) substrates by MBE, as starting point for further porous alumina fabrication. This way, by the electro-chemical anodization of this Al layer, a GaAs substrate with a monolithically integrated nanoporous alumina mask is obtained for further GaAs patterning processes. The natural advantage of this procedure is that the technological processes

necessary to fix an alumina mask on top of GaAs are suppressed and consequently the related GaAs surface contamination avoided.

In this direction, this new section presents an overview of the different works published in the literature for obtaining crystalline Al layers on semiconductor substrates by MBE. Schematic diagrams of the unit cells for the different phases observed for these Al layers are also shown.

The growth of Al under optimal conditions on a semiconductor surface was initially problematic because of the extreme reactivity of this metal. However, with the advent of advanced growth techniques such as MBE, it became possible to prepare oxide-free interfaces and thus, since both semiconductor and metal, could be grown in an *in situ* context to alleviate most of the problems associated with surface preparation prior to metallization. In this sense, the growth of epitaxial Al layers on semiconductor surfaces was initially performed by R. Ludeke et. al. at IBM in the 70´s [48], and improved more recently, by A. Y. Cho et.al., with the aim of fabricating optimal Schottky-barrier diodes [49,50]. From these original papers and posterior works on AlAs substrates [51] it can be derived that the type of semiconductor surface at the atomic level (either As-stabilized or Ga-stabilized GaAs (001) surfaces) strongly influence on the orientation of the epitaxially grown Al layer. So, Al layers can be obtained in the main (001), (110) and (110)R orientations. More recent works have also referred to the growth of Al in the (111) orientation [52]. This variety of configurations are related to the nature of the Al/GaAs interface, where the intermixing between Al and Ga, and the diffusion of As into Al layers, occur as a result of the high reactivity of Al.
Figure 3.9 and **Figure 3.10** show schematically the Al (001) and (110) orientations on a GaAs unit cell. Also 3D drawings of these orientations are shown to clarify these structures.

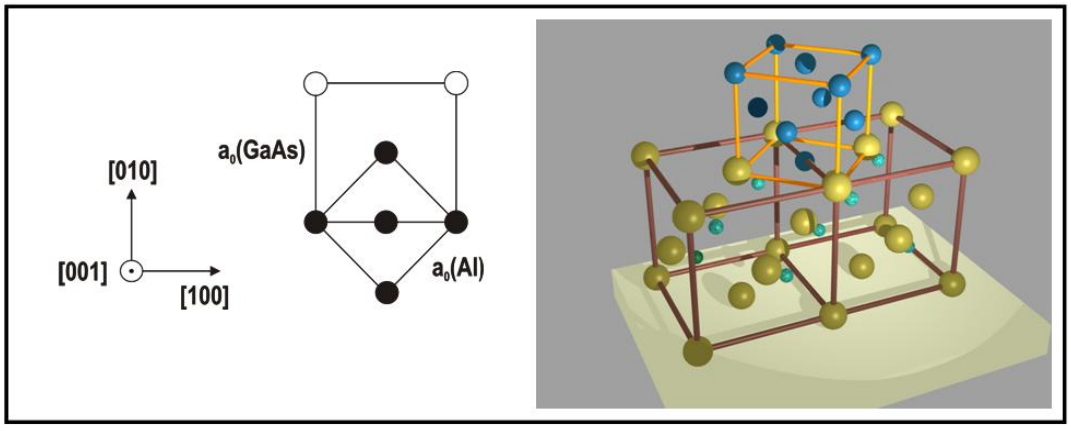

Figure 3.9. Primitive cell of (001) Al crystal orientation on a GaAs (001) substrate.

It can be clearly observed in **Figure 3.9** that the (001) Al orientation is in principle, an energetically more favourable situation since Al, that presents a face centred cubic (fcc) structure with a lattice constant of 4.0496 Å and GaAs, that is also fcc (zinc-blenda structure) with a lattice constant of 5.6532 Å, can be closely lattice matched by a simply rotation of 45º of the Al cell on the [*001*] axis. In this sense, T. Yao et.

al. [53,54] proposed also a model for the initial development of the (110) or (110)R Al orientations (**Figure 3.10**) on AlGaAs surfaces formed, as already commented, by the diffusion of Al into the GaAs substrate. According to this model, the formation of Al (110)-type orientation would be favoured when Al atoms are deposited on As-stabilized AlAs surfaces, as Al atoms could initially occupy Al sites on the AlAs surface due to a tetrahedral covalent bonding between Al adatoms and As on the surface.

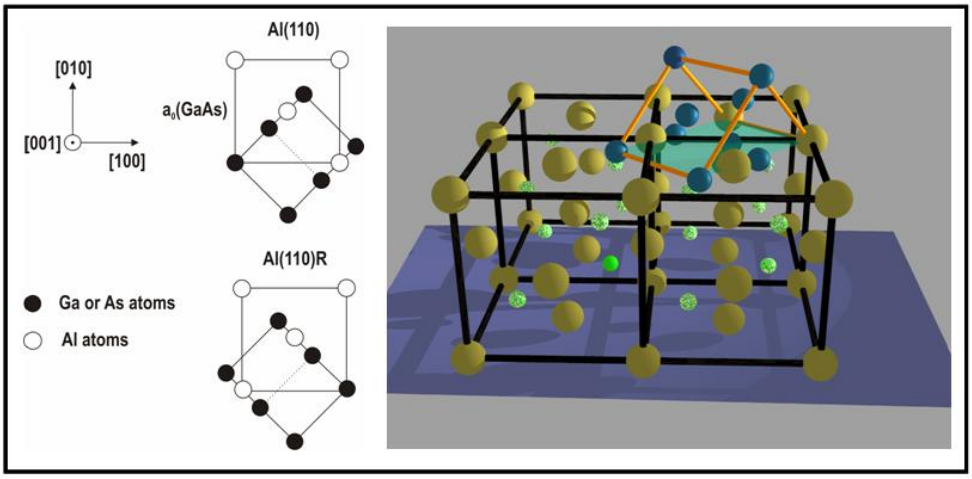

Figure 3.10. Primitive cell of (110) Al crystal orientation on a GaAs (001) substrate.

It is also important to mention that the typical substrate temperature used during the growth of all these metal orientations is close to RT. This effect is in principle induced by the low activation barrier energy for surface migration produced by the small metal-metal (e.g., Al-Al) bond strength. As above commented, the kind of starting surface plays a key role in the final orientation of the Al epitaxial layer and, most probably, the final Al layer will show a mixture of orientations. However, this may not be a problem, as the most important parameter for using the Al layer for further electrochemical anodization process is its morphology.

3.1.3. Experimental and results

The aim of the work here presented is to produce ordered arrays of QD nucleated on substrates that provide specific nucleation sites for InAs material. With this purpose it has been developed a process to pattern a GaAs (001) substrate based on the electrochemical anodization of an epitaxially grown Al layer on the GaAs substrate. This lithographic process and the results obtained for InAs QD grown on the patterned substrate will be described in this section.

The patterning of the substrate is obtained, as previously commented, by using a monolithically integrated nanochannel alumina mask that transfers its self-ordering to the underlying GaAs (001) substrate by continuing the anodization process once the semiconductor surface is reached. After patterning, the GaAs substrate follows a low temperature process for surface preparation before epitaxial growth for QD

formation. As a final result, it will be shown that the nanoholes act as preferential nucleation sites for InAs nucleation, with a filling factor close to unity, while the QD formation on the surface region between the patterned holes is completely suppressed.

· Aluminum growth on a GaAs(001) substrate by MBE

The process performed in this work for Al epitaxial growth starts with the growth of a 500 nm-thick Si-doped ($1x10^{18}$ cm^{-3}) GaAs buffer layer on a GaAs (001) Si-doped substrate by MBE at a growth temperature T_s= 580ºC (**Figure 3.1(a)**). After this buffer layer growth, the samples are cooled down from 580ºC to RT, with a chamber base pressure of P= $6x10^{-9}$ mbar. During this process, the GaAs surface always maintained a well-defined As-rich GaAs (2x4) surface reconstruction. The epitaxial Al layer is grown on this GaAs (2x4) surface at RT. In particular, the first 7 nm of Al layer are grown at low growth rate in order to observe in detail the first stages of the growth process. In this sense, a low enough growth rate corresponding to 0.1 ML/s of AlAs on GaAs (001) is used, as previously measured by RHEED oscillations. The rest of the Al layer is grown at a growth rate corresponding to r_g (AlAs)= 1.68 ML/s (**Figure 3.1(b)**).

The Al layers were studied both *in situ* with RHEED and by X-ray diffraction after their removal from the growth system. In particular, **Figure 3.11** shows the Al layer preferential orientations observed in the θ/2θ X-ray diffractogram. Besides the GaAs substrate related reflections, two other peaks that correspond to the Al (001) and (110) crystal orientations are observed (schematic diagrams in **Figures 3.9** and **3.10**). Considering the structural factors of these two reflections, the amount of material showing Al (001) orientation in the epitaxial Al layer is about 300 times lower than Al (110) structure.

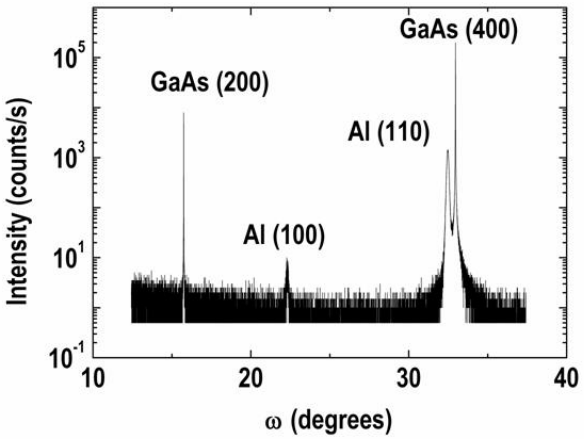

Figure 3.11. θ/2θ double crystal X-ray diffractogram of Al epitaxial layer grown on GaAs (001) substrate, showing diffraction peaks corresponding to (110) and (001) Al crystal orientations.

These results are consistent with the RHEED diagram observed at the initial stages of the Al growth, which also showed a mixture of two crystalline orientations. In fact, at the onset of the Al layer growth, a spotty pattern consisting in the superposition of two different lattice parameters which can be related to the two crystalline orientations mentioned above was observed (**Figure 3.12**). As the growth continued, streaks in the RHEED diagram along the GaAs [*1-10*] direction, with the same separation as the GaAs (001) lattice (4 Å), appeared, **Figure 3.13** . Along the GaAs [*110*] direction, the Al layer RHEED diagram showed also streaks, but with a larger separation corresponding to a lattice parameter of 2.86 Å. A surface reconstruction of this Al phase seems to appear also, close to the zero-order streak pattern [51] (**Figure 3.14**).

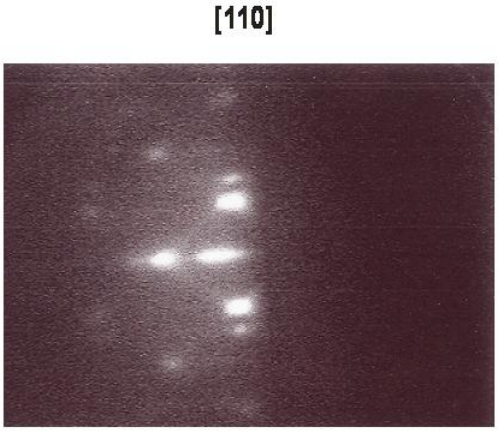

Figure 3.12. A mixture of two Al crystal orientations is observed, at the first stages of the Al growth, in the RHEED diagram along the GaAs [110] direction.

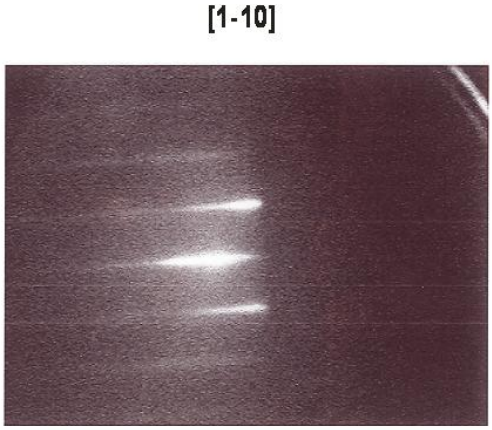

Figure 3.13. RHEED diagram during Al growth along the GaAs[1-10] direction. Streaks showing the same separation as the GaAs(001) lattice (4 Å), appeared.

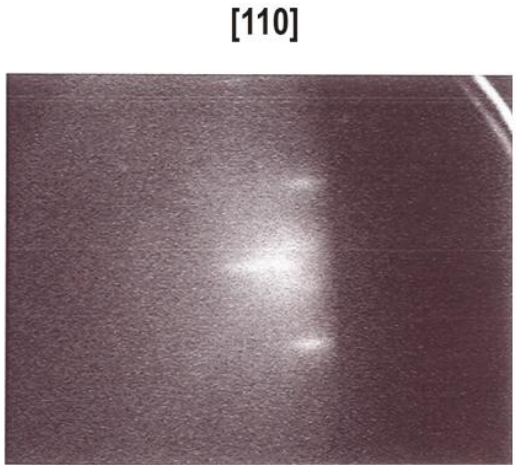

Figure 3.14. RHEED diagram during Al growth along the GaAs[110] direction. Streaks showing a periodicity, corresponding to a lattice parameter of 2.86 Å, are observed. Also a surface reconstruction of this Al phase is observed close to the zero-order streak pattern.

From these results, it can be derived that the Al layer obtained has a main (110)R orientation [50], see **Figure 3.10**. These RHEED patterns were observed after an amount of Al equivalent to 110 nm of AlAs on GaAs (001) was deposited. According to the X-ray results, this thickness would correspond to a 40 nm-thick Al (110)R layer. Thus, RHEED and X-ray diffraction results indicate the presence of a preferential Al (110)R orientation, although in a region close to the GaAs interface there is a coexistence of two orientations: Al (001) and Al (110)R. Using these results, a total thickness of the Al layer of 885 nm can be estimated.

The topography of the as-grown Al layer was studied by AFM as shown in **Figure 3.15**. It shows a directional roughness along the [*1-10*] direction of the GaAs substrate with an rms= 1.51 nm. As previously commented, the topography of the As surface has a certain influence on the posterior Al layer anodization process (see next section).

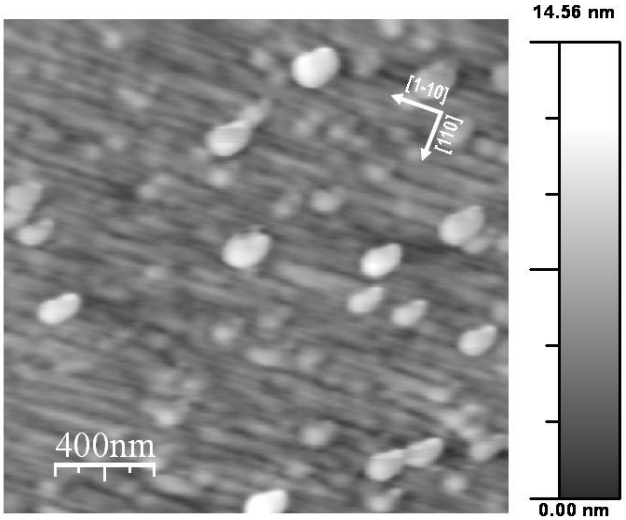

Figure 3.15. AFM image (2µm x 2µm) of the resulting epitaxial Al layer. A directional roughness along the [1-10] direction of the GaAs substrate is clearly observed.

· Al layer anodic oxidation

Once the Al/GaAs sample was taken out from the MBE chamber and carried into the electro-chemical setup, the NCA mask fabrication process was initiated. This process consisted, in a first stage, in the synthesis of ordered nanoporous alumina by electrochemical anodization of the Al layer and, in a final step, in the transfer of the self-organized pattern of the mask to the GaAs substrate. (The assembling of the electro-chemical setup, **Figure 3.7**, and the work here presented involving any electro-chemical process has been carried out at IMM by Dra. Marisol Martín González).

The electro-chemical process consists in a two step Al anodization process [9] carried out in a two electrode cell using a regulated dc power supply. The sample is anodized in a 0.3 M oxalic acid at 40 V and temperature T= 0.3ºC while the electrolyte is mechanically stirred. As previously described, platinum gauze is used as a counter electrode (cathode) and the sample edges were covered by insulating paint. The first anodization process is stopped after the formation of 466 nm of alumina. At this moment, the alumina layer is selectively removed by immersing in 4 vol % CrO_3 + 10 vol % H_3PO_4 at 70ºC for 5 min. The periodic concave features shown at the Al surface after removal of this first alumina layer (**Figure 3.1 (c)**), are used as seeds for further formation of ordered pores at a second anodization step.
As commented in the last section, the topography of the Al layer (**Figure 3.15**) influences on the anodization process since the nanopores formed after the first anodization step are inside valleys formed along the [*1-10*] direction (**Figure 3.16 (a)**).

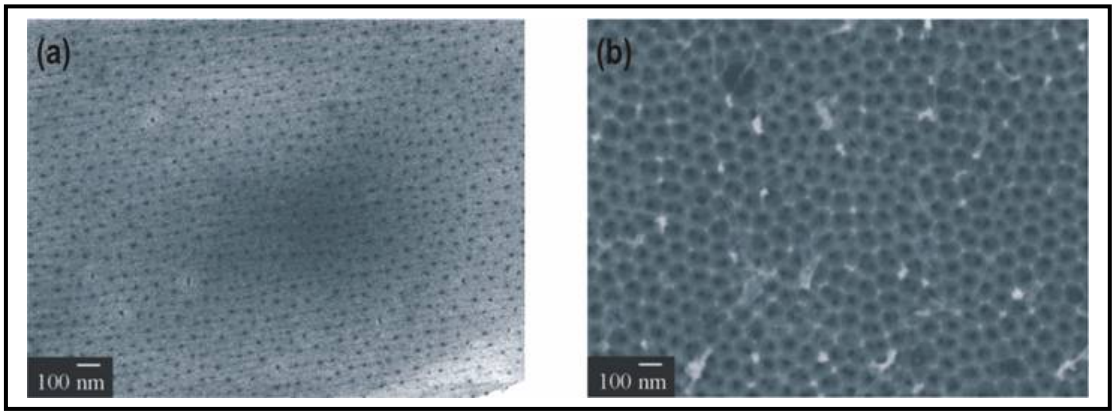

Figure 3.16. SEM images of nanoporous alumina layer surface fabricated on Al/GaAs(001) at different stages of the fabrication process. **(a)** After a first anodization step. **(b)** After a second anodization step. It is observed a clear improvement in the pore spatial ordering on the alumina surface after this final process.

Together with the alignment of the nanopores along the main roughness direction of the Al layer, it is also observed a local incipient hexagonal periodicity. This is a surprising result taking into account that using this approach, the anodization process was carried out during a short time (~ 13 min) and only a thickness of 466 nm of Al has been attacked, instead of the tens of microns that normally are anodized during a first anodization step when Al bulk is used as source material for fabrication of NCA templates [55].

In order to improve the final periodicity of the alumina pattern, a second anodization step is carried out under the same conditions previously used [9]. In **Figure 3.16 (b)** SEM images of the nanoporous alumina pattern obtained after this second anodization step are shown. It is clearly observed an improvement in the order of the nanoporous alumina membrane obtained after this second step. In this case, the holes obtained show an interpore distance of about 100 nm in perfect agreement with previous experiments [35], using 0.3 M oxalic acid as electrolyte in the electro-chemical process.

· Transfer of the alumina pattern to the GaAs surface

In order to use the alumina pattern as a template for growing ordered InAs QD, the anodization process has to continue up to the GaAs surface. This critical point is recognizable during the process by means of a colour change in the surface of the sample and a sharp increase of the current intensity in the chronoamperometry, as shown in **Figure 3.17**. Maintaining this situation during approximately 60 s, the GaAs surface under the alumina nanoholes is attacked permitting that way the transfer of the alumina self-ordered lateral arrangement to the substrate (**Figure 3.1 (d)**). The porous alumina fabricated by this process is finally selectively etched away by a few seconds dip in a 49% dissolution of fluorhidric acid (**Figure 3.1 (e)**).

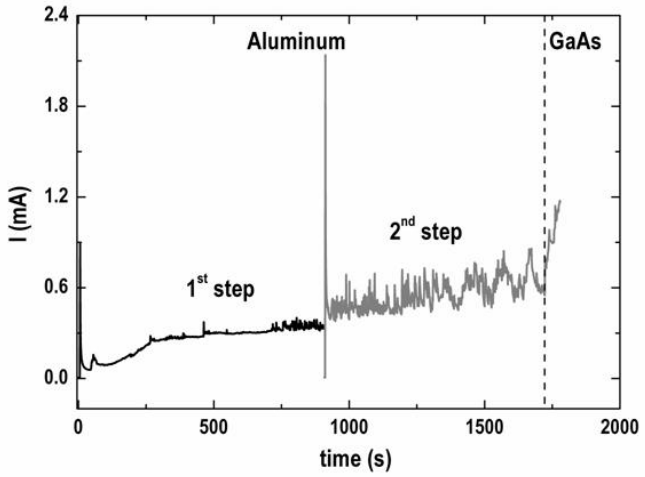

Figure 3.17. Cronoamperometry showing the differences in the current density between the 1st and 2nd anodization steps. Between both steps a selective dissolution of the porous alumina is performed. A drastic slope change in the intensity is observed when the semiconductor surface is reached (marked with a dotted vertical line).

As expected, the result of the above described process is that the GaAs substrate is patterned. **Figure 3.18** shows AFM images of both, the alumina surface after a double step process (**Figure 3.18 (a,c)**) and the corresponding GaAs surface once the nanoporous alumina layer is selectively removed (**Figure 3.18 (b,d)**).

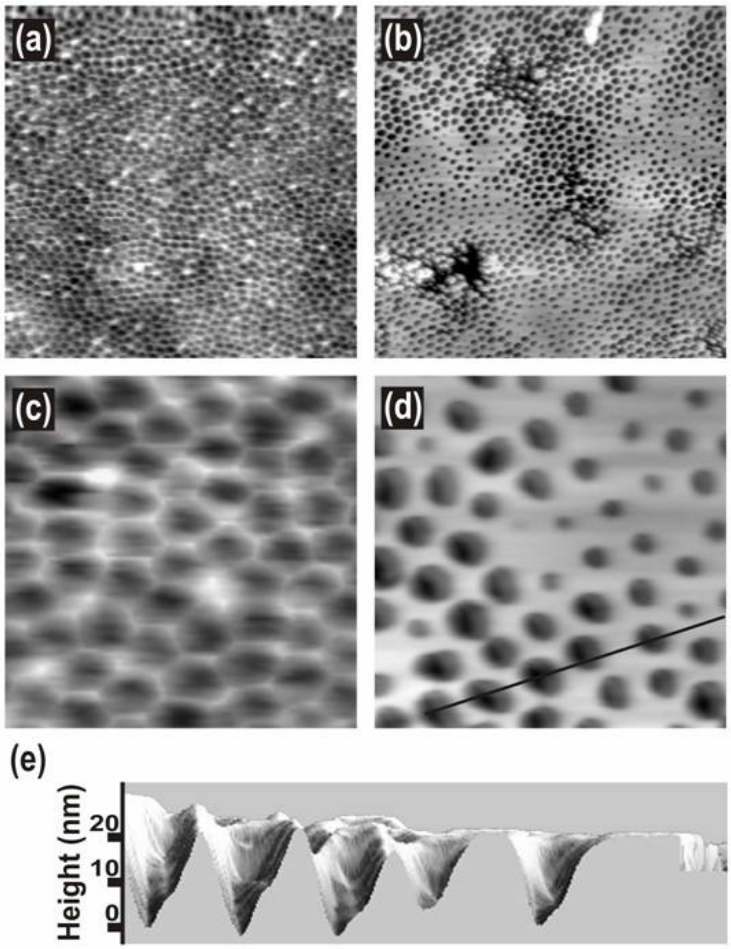

Figure 3.18. AFM images of the alumina surface after a two steps anodization process **(a,c)**, and the patterned GaAs surface that results after removal of the alumina layer **(b,d)**. **(e)** Profile along the line drawn on **(d)**.

Although the alumina pattern seems to be quite homogeneous across large areas of the surface, the homogeneity of the distribution of nanoholes that results at the GaAs surface is not as nice. The patterned surface shows flat areas without holes where apparently the GaAs anodization process has not taken place, or large hollows where it seems that closely formed nanoholes have collapsed. The differences observed between the alumina mask and the patterned GaAs substrate are related to the process of alumina nanoholes formation during the aluminum anodization: first of all, there is a time delay in the nucleation of different pores across the surface, and second, some of the pores grow more perpendicular to the GaAs surface than others. This means that the total thickness of the porous alumina film is not the same for all the pores. For these reasons, at a certain time, some of the pores reach the GaAs surface and start to widen while others have not reached the GaAs surface, resulting in the morphology shown in **Figure 3.18 (b,d)**.

In the regions where there has been an efficient transfer of the alumina pattern (**Figure 3.18 (d)**), the density of holes at the GaAs substrate, $5x10^9$ cm^{-2}, coincides with that of the alumina layer (**Figure 3.18 (c)**). The depth of the holes patterned on the GaAs substrate range from 10 to 20 nm, as observed in the

AFM profile (**Figure 3.18 (d)**). This profile also shows that certain facets seem to originate inside the holes during the GaAs anodization process.

· InAs/GaAs QD formation

Next experimental step is the growth of InAs QD on the obtained GaAs patterned surface. As previously commented in section 2.1.4, an optimal epitaxial growth process has to be performed at a low enough temperature in order to inhibit any pattern smoothing. To do this, the sample is introduced again in the MBE chamber together with a non-patterned epitaxial GaAs as a reference. Before the deposition of InAs for QD formation, native oxide and other contaminants of the surface are removed by exposing the GaAs surface of the substrates (reference and patterned) during 5 min to an atomic hydrogen flux [56] with a hydrogen pressure of $P(H_2)= 10^{-5}$ mbar at a substrate temperature $T_s= 450ºC$.

After the oxide removal, a 6.8 nm thick GaAs buffer layer is grown at a low enough temperature ($T_s= 490ºC$) by ALMBE technique [57] (**Figure 3.1 (d)**). The thickness of the buffer layer was chosen as a compromise for separating the QD from the unavoidable defects of the interface with the substrate, and at the same time, to guarantee the pattern profile. During the growth of this thin buffer layer, the RHEED pattern observed on the flat reference sample corresponded to a 2D growth process, meaning that the oxide removal process effectively removed impurities at the surface.

In the case of the patterned sample, the AFM image (**Figure 3.19**) of the surface that results after this buffer layer growth, shows a total preservation of the pattern and similar to that observed in **Figure 3.18 (d)**, smooth regions between holes.

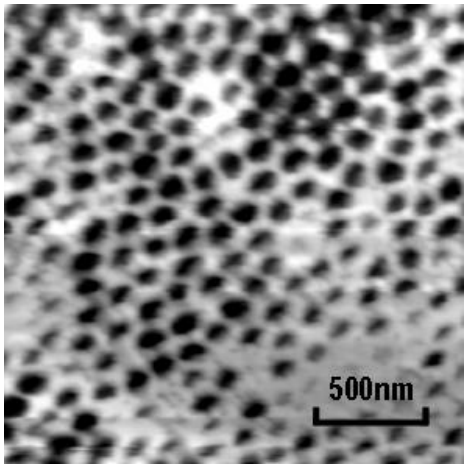

Figure 3.19. AFM image (2μm x 2μm) of the patterned GaAs surface after growing a GaAs buffer layer of 24ML by ALMBE.

The formation of InAs QD is carried out by growing InAs material up to the critical thickness ($\theta_c= 1.7$ ML), as observed by a 2D-3D change in the RHEED diagram of the reference sample (without pattern)

at T_s= 490ºC. For InAs deposition, it is used a growth sequence consisting in 0.1 ML of InAs deposition at a growth rate of 0.07 ML/s followed by a pause of 2 s under As_2 flux ($BEPAs_2$= $2x10^{-6}$ Torr). AFM images of the patterned surface after InAs deposition (**Figure 3.20**) show that the nanoholes act as preferential nucleation centre for InAs with the total absence of QD formed outside them. Thus, apart from the patterned nanoholes, there are not any other preferential nucleation centres for InAs QD formation.

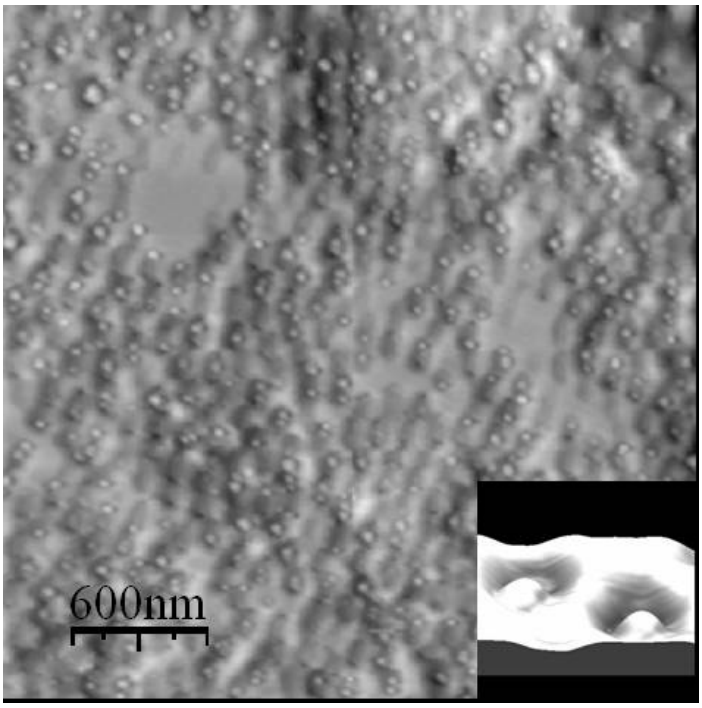

Figure 3.20. AFM image obtained after the deposition of 1.7 ML of InAs on the GaAs patterned substrate. A derivative image is shown to emphasize the morphology features. It can be observed that most of the GaAs nanoholes are occupied by an InAs QD and no nanostructures are formed elsewhere. At the bottom inset a 3D image of a QD into a nanohole is shown.

Observing the **Figure 3.20** it can be noticed that there is a certain distribution in the QD size. Considering the large non-uniformities of the patterned motifs shown in **Figure 3.18 (d)** (it is observed a standard deviation (SD) of 26% centred at a mean diameter of 89 nm), it is quite plausible to establish a correlation between the dispersion in the nanoholes size and the resulting distribution of QD size. In this respect it could be fixed an upper limit for the QD size uniformity corresponding to the nanoholes size dispersion. This value is larger than that obtained in the QD distribution of the reference sample (SD of 12 % at a mean diameter of 50 nm). These results show that, although the process carried out demonstrates selective nucleation of QD, the characteristics of the patterned surface must be improved in order to achieve a highly uniform distribution of QD formed at specific sites. In this sense, it seems that the non-uniform depth of the alumina pores hinders the simultaneous transfer of the pattern across the surface, with a final result of a non homogeneous distribution of the nanoholes. Fortunately, these are not intrinsic problems associated to the porous anodic alumina templates, but can be overcome by following different

approaches. In particular, different works have recently proposed the alternative of using the ionic current density passing across the oxide layer as a constant parameter instead of the applied potential, to perform a more controlled anodization process [57].

3.1.4. Conclusions

A process for obtaining large area site-controlled InAs QD in pre-patterned GaAs (001) surface has been proposed. The patterned GaAs surface has been produced by transferring to a GaAs substrate, the pattern produced on a porous alumina layer fabricated from a monocrystalline Al layer epitaxially grown by MBE.

The results obtained demonstrate that the geometry of the nanoholes in an alumina membrane can be directly transferred to a GaAs substrate. In this sense, the monolithically integrated Al layer acts as a good mask preserving the cleanliness and smoothness of the GaAs (001) substrate, during the processes followed for GaAs patterning. The subsequent process of surface preparation for epitaxial growth preserves the pattern optimally, producing clean and smooth surface regions between nanoholes. As a consequence of this, InAs QD were only formed inside the nanoholes, showing that patterns obtained by GaAs anodization act as preferential sites for further InAs growth.

3.2. Ordered InAs QD on GaAs (001) substrates by transferring a pattern previously designed by Laser Interference Lithography (LIL) on a resin layer

In this section it is presented a technological process that permits the selective growth of ordered InAs QD on GaAs substrates by an optimal transfer of a pattern fabricated on a resin layer. In particular, it is developed a novel method that by the ozone selective oxidation of an underlying semiconductor substrate, has permitted to transfer, with nanometer resolution, a pattern fabricated by Laser Interference Lithography (LIL). The experimental procedure is schematically summarized in **Figure 3.21**.

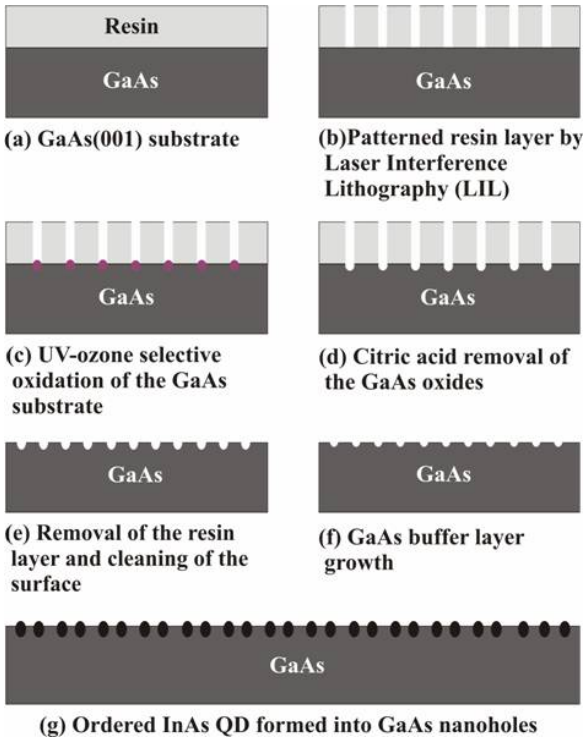

Figure 3.21. Scheme of the fabrication process of a two-dimensional array of ordered InAs/GaAs(001) quantum dots developed in this work.

As it was introduced in section 2.2.1 of chapter 2, the combination of selective UV-ozone cleaning/oxidation process and chemical etching, permits the definition of concave pits, with excellent control of depth, on III-V semiconductor substrates. As it will be shown throughout this section, the different technological processes carried out for the transfer of the LIL pattern and the posterior *in situ* pre-growth treatments of the sample, are good enough to achieve selective nucleation of spatially ordered QD with an optical quality, similar to that of QD formed by a self-assembling process. This effect has important technological consequences, since it would permit the use of these ordered QD from the first layer of nanostructures without the need of stacking QD or the growth of thick buffer layers to separate them from the patterned surface, that eventually smooth the patterned profile.

The section is divided as follows: in a first part, a detailed introduction to the LIL technique is presented. Followed, the experimental part for obtaining an optimal transfer of the LIL pattern is studied. Finally, the pre-growth sample treatments for getting rid of the different residues generated in the process leaving a contaminants-free GaAs substrate, suitable for the posterior InAs QD selective nucleation on the pattern, are described.

3.2.1. Laser interference lithography technique

Laser Interference Lithography is a mask-less lithographic technique in which a photosensitive resist is exposed to an interference light pattern, produced by two coherent laser beams. This lift-off lithographic technique has the capability of generating patterned structures over large areas [58-61] in typical exposure times shorter than 1 min. The method has been used for many years as a tool for fabricating submicron gratings for application in integrated optics [62,63]. In recent years Interference Lithography has attracted great attention for a wide variety of applications [64], amongst others: field emission displays [65], antireflection-structures and polarization elements [66], photonic crystals [67], masks for nanoimprint and X-ray lithography [68,69] and patterned magnetic media [70,71]. Its capability for patterning large areas is clearly demonstrated by the fabrication of 50 x 50 cm^2 areas of submicron dots [72].

In the following, the well-known principle of interference, is described in order to establish the patterning resolution of this technique.

· Principle of interference

Assumed two planar waves, denoted by $\vec{k}_1$ and $\vec{k}_2$ which are incident to a surface under an angle θ with respect to the $\hat{z}$ direction (perpendicular to the surface plane) in different azimuths (**Figure 3.22**).

$$\vec{k}_1 = k(\hat{x}\sin\theta, \hat{z}\cos\theta) \text{ and } \vec{k}_2 = k(-\hat{x}\sin\theta, \hat{z}\cos\theta) \quad \textbf{(3.1)}$$

From (3.1) it is obtained that $\left|\vec{k}_1\right| = \left|\vec{k}_2\right| = k$, where k is the wave number which is related to the wavelength of the radiation source, $k = 2\pi/\lambda$. Both light beams are added at a certain $\vec{r} = x\hat{x} + z\hat{z}$ position of the surface. The intensity of the light at that point can be expressed as:

$$I(\vec{r}) \propto \left|\exp(i\vec{k}_1\cdot\vec{r}) + \exp(i\vec{k}_2\cdot\vec{r})\right|^2 = 4\cos^2\left(\frac{1}{2}(\vec{k}_1 - \vec{k}_2)\cdot\vec{r}\right) \quad \textbf{(3.2)}$$

After calculating the inner product, it is obtained the following expression for the intensity pattern along the substrate in the $\vec{x}$ direction:

$$I(\hat{x}) \propto \cos^2(kx\sin\theta) \tag{3.3}$$

that means that the intervals of light are a periodic function, with period $kx\sin\theta = \frac{\pi}{2}$. The minimal resolvable feature size Δx, which corresponds to the distance between intensity maximum and an adjacent minimum, can be found with help of the following relation:

$$k\Delta x\sin\theta = \frac{\pi}{2} \tag{3.4}$$

So, the minimal resolvable feature can be expressed as

$$\Delta x = \frac{\pi}{2k\sin\theta} = \frac{\pi}{2(\frac{2\pi}{\lambda}\sin\theta)} = \frac{\lambda}{4\sin\theta} \tag{3.5}$$

Finally, the period Λ of the created pattern (distance between two adjacent maxima) is two times Δx:

$$\Lambda = \frac{\lambda}{2\sin\theta} \tag{3.6}$$

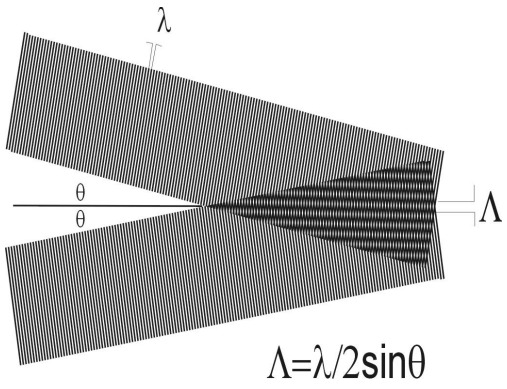

Figure 3.22. Laser interference lithography principle

As seen from the last expression, the minimum achievable periodicity is ideally that corresponding to half the wavelength of the radiation source,

$$\Lambda_{\min} = \frac{\lambda}{2} \tag{3.7}$$

From the last two expressions it is concluded that the smaller the wavelength used, the smaller the produced patterns will be. According to the equation (3.6), **Figure 3.23** shows the pattern periodicity as a

function of the angle of incidence for a fixed wavelength (λ= 266nm). By changing the angle θ, the periodicity Λ can be easily adjusted from almost 1 μm down to 150 nm.

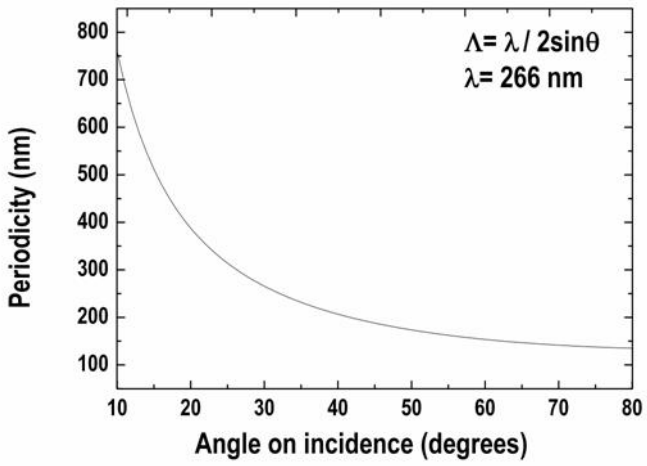

Figure 3.23. Line pattern periodicity (nm) as a function of the angle of incidence respect to the normal of the surface for a fixed wavelength λ = 266 nm. For all practical purposes periodicities ranging from almost 1 μm down to 150 nm can be achieved in the laser interference setup at the MESA+Institute.

In the following section, the laser interference setup used in this work at the SMI, MESA+Institute of Nanotechnology facilities is presented.

· The Lloyd´s Mirror Interferometer

Different kinds of experimental arrays based on either reflective or diffractive optics elements have been proposed in order to produce structures by means of Interference Lithography. In particular, in this work it was used a reflective optics based interferometer called the Lloyd´s Mirror (**Figure 3.24**). It basically consists of a mirror placed perpendicular to the sample holder. An expanded beam illuminates both, the mirror and the sample. Part of the light is reflected on the mirror and interferes with the portion of the beam that is directly illuminating the sample (**Figure 3.22**). The periodicity of the produced pattern can be changed by rotating the whole array (mirror and sample holder). As a difference to other interferometers, in the case of the Lloyd´s mirror, there is only one laser beam which is expanded and spatially filtered by an array of lens(es) and a pinhole. This intrinsic property gives an advantage for this system, since it has less moving parts than other setups based on dual beam interferometers[1] and, therefore, less influence of vibrations during the exposure time. As commented, the Lloyd´s Mirror interferometer only requires a simple rotation of the system sample-holder and mirror-array in order to change the periodicity of the produced interference pattern. In this set-up, arrays of dots (in the case of

[1] The dual beam interferometer makes also use of reflective optics as a means to produce interference patterns. A beam of light is directed onto a beam splitter where it is divided into two branches of almost the same intensity. Each branch is directed to a mirror whose configuration is in such a position and angle that they reflect the beams in a way that they intersect each other, at the surface of the sample to be patterned.

using positive photoresist) or nanoholes (negative photoresist) can simply be fabricated by a second exposure after rotating the substrate over 90º (see different distributions of motifs in **Figure 3.25**).

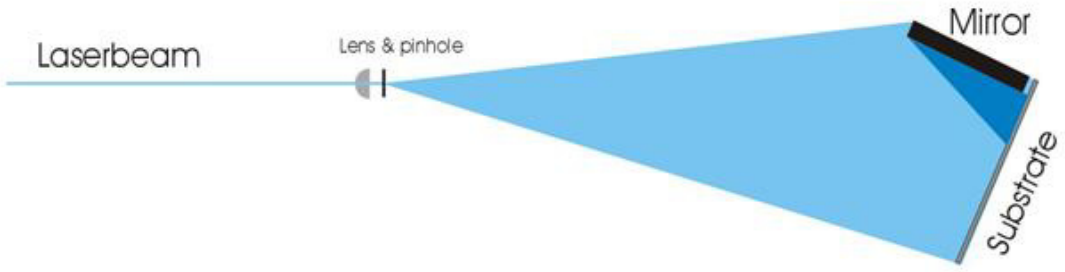

Figure 3.24. Lloyd´s mirror laser interference lithography set-up.

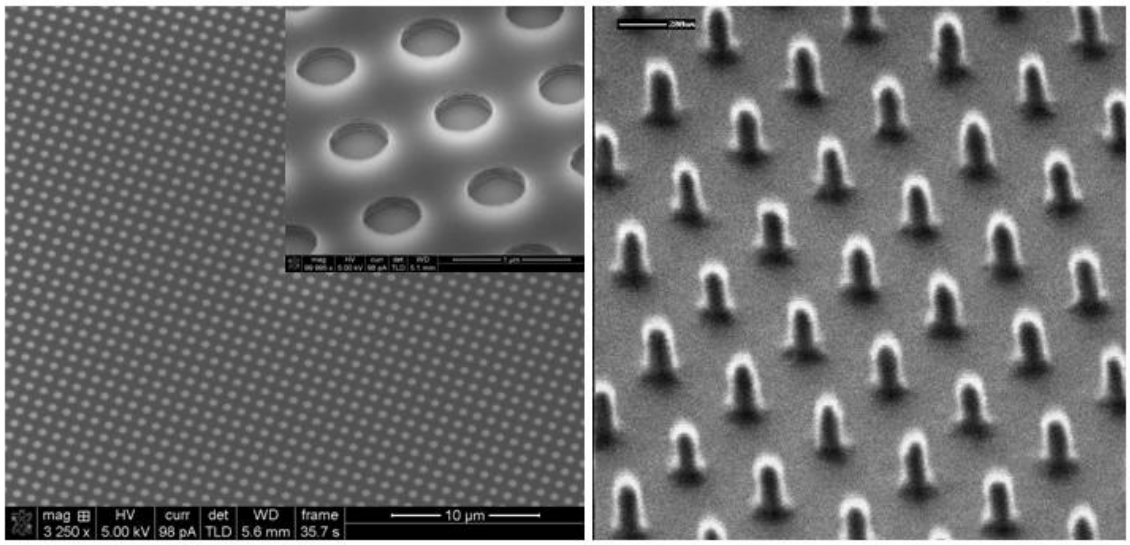

Figure 3.25. Square distributions of holes and dots fabricated by laser interference lithography [images taken from the SMI, MESA+Institute of Nanotechnology, University of Twente].

The patterned area is determined by the diameter of the laser beam and the size of the mirror. With the setup used in this work, highly regular patterns can be produced over areas of about 2 cm x 2 cm.

In a more detailed way, **Table 3.2** resumes the main general characteristics of the LIL setup used in this work.

Laser	Nd:YAG de 1064 nm, 200mW + 2 frequency multipliers.
Exposure time	A few seconds
Photoresins	Olin 907/12 diluted in 3-ethoxypropionate (positive). Methyl 3-methoxypropionate TI 09xr and MaN2403 MicroResist (negative)
Resin preparation	Spin at 4000 RPM during 20 s. Bake out during 15 min at 95ºC
Surface cleaning	Acetone. Developer MF 319 (Microposit). Remover mr-REM 660 (Microresist). HF
Motif minimum diameter	60 nm
Motif maximum diameter	300 nm
Minimum periodicity	150 nm
Maximum periodicity	1000 nm
Maximum working area	2x2 cm
Period vs. Motif diameter	Period/3 ≈ Motif diameter
Period vs. Laser wavelength	Minimum period = laser wavelength / 2
Motifs distributions	Square (2 exposures after rotating 90º). Triangular (2 expossures after rotating 60º)
Motifs	Lines (1 exposure). Circles (2 exposures at 90º or 3 at 60º). Squares (2 exposures at 60º)
Other charateristics	It is possible to fabricate patterned arrays on very rough surfaces (rms ~ 1µm)
Inconvenients	The setup is very sensitive to mechanical vibrations. It is very difficult to fabricate motifs other than line, squares or circles.

Table 3.2: Main general characteristics of the laser interference lithography set-up used in this work

3.2.2. Experimental and results

As in previous exposed results (section 3.1.3), the aim of the work here presented is to produce large areas of ordered distributions of QD with high optical quality. In this section, a new approach based on LIL nanolithography will be described. The process followed implies a new development in the use of ozone selective oxidation to transfer a pattern previously fabricated on a resin layer to the underlying substrate.

· LIL patterns on GaAs substrates

The experimental procedure starts using a 500 nm-thick undoped epitaxial GaAs layer grown by MBE, on a commercial epi-ready GaAs (001) substrate (from this point on, epitaxial substrate). On top of this epitaxial substrate, a direct negative resist (MaN2403, MicroResist Technology, Berlin/Germany) is spin-coated followed by a bake-out process for nanoholes formation. The initial photoresist thickness is

215 nm, which decreases somewhat after bake-out. The exposure of the photoresist is carried out with the laser interference setup previously described in section 3.2.1 [73]. In this setup, a 266 nm quadrupled Nd:YAG laser beam is projected onto a Lloyd's mirror interferometer and the resulting periodic fringe interference pattern with a periodicity of 300 nm is used for the exposure. By rotating the sample at an angle of 90º and performing a second exposure, it is obtained after development, an array of holes aligned in a square pattern. In this sense, **Figure 3.26 (a)** shows the AFM image of a typical hole array as starting pattern configuration. In this case, the diameter of the circular windows is 220±20 nm and their average depth (see profile at the right of the figure) is 200 nm that fairly corresponds to the previously deposited resist thickness. The centre to centre distance between contiguous holes is 300±10 nm, which is in good agreement with the settings above described for the LIL setup.

(I want to notice at this point that all the work presented in this chapter related to the fabrication of patterns by LIL on GaAs substrates, was entirely made by Mr. H. Kelderman in the group of Prof. L. Abelmann at SMI, MESA+Institute of Nanotechnology, University of Twente).

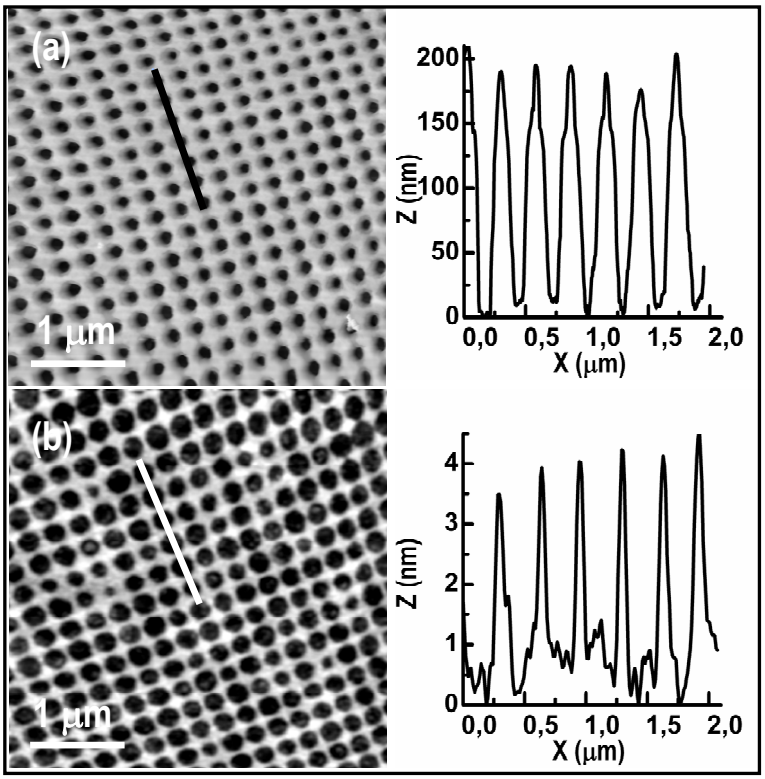

Figure 3.26. AFM images (5μm x 5μm) of **(a)** the initial patterned surface fabricated by LIL with opened nanoholes over a resin layer and **(b)** the GaAs etched surface after four oxidation/oxide dissolution cycles. A profile along the line drawn on the respective figures is shown on the right.

· Ozone selective oxidation

Next experimental step is to transfer the pattern shown in **Figure 3.26 (a)** fabricated by LIL, to the GaAs substrate. For that purpose it has been developed a process that consists in the oxidation of the bare GaAs nanoholes by exposing the sample to ozone. After that, the GaAs oxides are chemically removed by a selective etching, leaving small nanoholes at the GaAs surface. The repetition of oxidation/oxide removal process, results in an accurate transfer of the pattern to the substrate (see section 2.2.1).

The oxidation process consists in the exposure of the GaAs substrate to UV light with a wavelength λ= 184.9 nm produced in a low-pressure Hg discharge lamp in open air conditions. As previously described, in this situation, atomic oxygen and ozone are simultaneously produced upon interaction of the UV light with the oxygen present at the air atmosphere [76]. The ozone reacts with the GaAs surface producing Ga_2O_3, As_2O_5 and As_2O_3 [74]. After this ozone exposure, the bottom of the holes is now oxidized GaAs that can be chemically removed by dipping the sample in 1 M citric acid dissolution during 60 s. The combination of oxide formation/oxide dissolution leaves atomically smooth GaAs surface, as characterized by AFM. Previous calibrations of the experimental set up (see section 2.2.1 in chapter 2) show that 1 nm of the GaAs substrate is removed per oxidation/oxide dissolution cycle, for an ozone exposition of 60 s. By repeating this process nanoholes can be produced in the GaAs substrate tuning their depth in an extremely accurate way.

The GaAs patterned substrate is obtained after getting rid of the resin existing between the nanoholes. In particular, the resin is selectively removed by a proper mix of developer MF 319 (Mcroposit), remover mr-REM 660 (microResist) and HF. Oxygen plasma is also used to guarantee surface cleanliness.

Figure 3.26 (b) shows the GaAs surface after four oxidation/oxide dissolution cycles. The average diameter of the obtained patterned holes is 280±30 nm and 4±0.5 nm in depth. Comparing with the original apertures on the resin layer (**Figure 3.26 (a)**), the final holes transferred to the GaAs substrate are wider, while the distance between the holes is totally preserved (290±10 nm). The surface between holes is very smooth (see profile at the right of the figure) with a peak to peak roughness of 0.6 nm. As regards the morphology at the bottom of the holes, it presents a higher, although still low, roughness of 1 nm.

· InAs/GaAs QD formation

Once the patterned GaAs substrates are obtained, the samples are loaded in the MBE chamber. As usual, previously to the growth of InAs QD, the patterned surface has to be treated in order to remove native oxides and other possible residual contaminants. As previously commented (see section 2.1.4), this process has to be carried out at a low enough substrate temperature, as close as possible to T_s < 500ºC for GaAs, in order to avoid the degradation or smoothing of the pattern. In this case, the sample, introduced in the chamber together with a non-patterned GaAs epitaxial substrate as a reference, is

treated by exposing to an atomic hydrogen flux with a pressure of $P(H_2)= 10^{-5}$ mbar at a substrate temperature of $T_s= 450ºC$. During this process the As cell is maintained opened with a $BEPAs_4= 2x10^{-6}$ mbar. The RHEED diagram shows a clear 2x periodicity along [*1-10*] direction on the reference sample after the first minute of H/As exposure. The process is maintained during 20 min in order to eliminate any possible residual organic contaminants from the resin on the patterned sample.

Trying to keep most of the growth process at $T_s < 500ºC$, after the oxide removal process, a 6.8 nm thick GaAs buffer layer is grown at $T_s= 450ºC$ by ALMBE technique [56].

The final formation of InAs QD is carried out by depositing at $T_s= 510ºC$ InAs up to the critical thickness ($\theta_c= 1.7$ ML), as observed by a 2D-3D change in the RHEED diagram of the reference sample (without pattern). InAs is grown following a growth sequence consisting of 0.1 monolayers (ML) of InAs deposition at a growth rate of 0.05 ML/s followed by a pause of 2 s under As_2 flux. As previously described, the different parameters involved in the epitaxial growth process are optimized to ensure the atomic flatness of the interface and the highest optical quality of the QD [77].

For PL investigation, the InAs QD are capped in this case by a 15 nm-thick GaAs layer. For AFM characterization, after the GaAs cap layer, 1.7 ML of InAs were again deposited for QD formation on the surface.

Figure 3.27 shows comparative AFM images of the superficial InAs QD grown on patterned and non-patterned substrates (**Figure 3.27 (a)** and **(b)** respectively), for samples containing buried QD (for PL characterization) and QD at the surface.

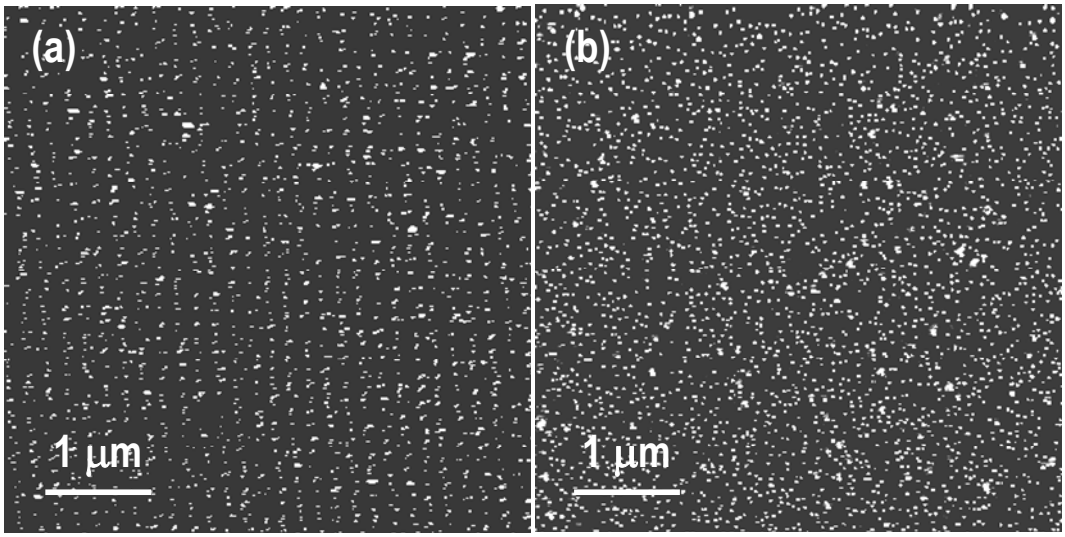

Figure 3.27. AFM image (10μm x 10μm) of **(a)** square superficial QD distribution grown on a selective etched GaAs substrate and **(b)** QD grown on the non-patterned reference sample.

On the patterned substrate, **Figure 3.27 (a)**, a square configuration of ordered QD is clearly observed. The spatial distribution of the buried QD seems to be perfectly replicated onto the QD grown at the surface following the initial pattern ordering (**Figure 3.26 (b)**). On the other hand, the AFM image of the reference sample (**Figure 3.27 (b)**) shows a typical random nucleation of QD. It can be also observed that, due to imperfections in the LIL process, some peripheral parts of the initial pattern presents an eventual overlapping of the holes along the GaAs [*1-10*] direction (**Figure 3.28 (a)**). Related to this geometry of the initial pattern, linear configurations of QD are obtained (**Figure 3.28 (b)**). The features of the pattern will probably be magnified during the 6.8 nm thick GaAs buffer layer growth, due to the enhanced Ga diffusion along the GaAs [*1-10*] direction.

The average base diameter and height of QD in both, square and linear configuration, are 69±10 nm and 18±5 nm respectively. The QD on the reference sample present a similar diameter of 67±10 nm and height of 17±5 nm. The density of QD in the patterned and the reference samples is 1.9×10^9 cm^{-2} and 2.5×10^9 cm^{-2} respectively.

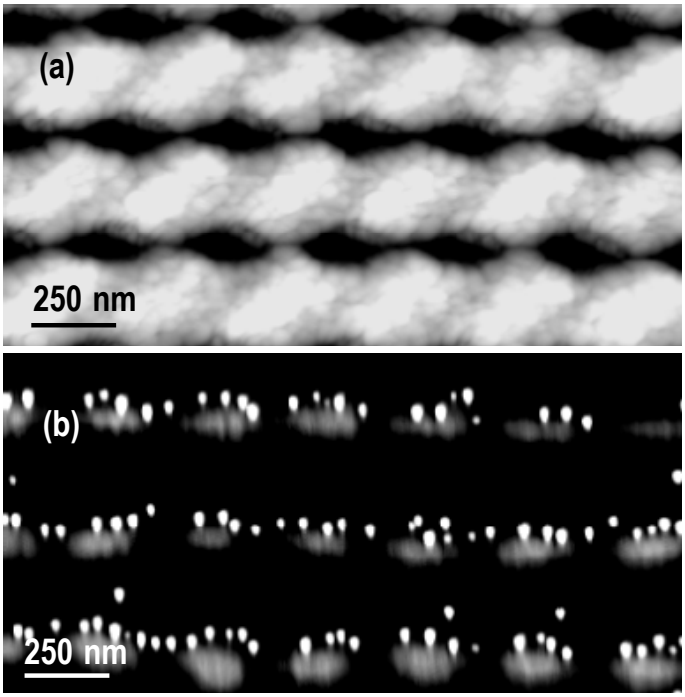

Figure 3.28. AFM images (2μm x 1μm) of **(a)** the starting resin pattern fabricated by LIL showing overlapping of the holes along [1-10] direction and **(b)** aligned QD grown on the resulting GaAs patterned substrate.

Figure 3.29 shows the normalized 20 K PL spectra for InAs QD grown on the patterned substrate (dotted line) and on the reference sample (continuous line). QD distribution of these samples is shown in **Figure 3.27**. Both, the emission energy and linewidth of the main PL peak (E_p= 1.2, 1.18 eV, FWHM= 43, 44 meV for the patterned and reference sample respectively), are very similar. In the ordered QD PL spectrum,

another peak of less intensity at lower energies is observed. It is excluded that these two PL peaks correspond to ground and excited states of the QD since the relative intensity remains constant with the excitation power. The appearance of two PL peaks might be related to a bimodal size distribution in the QD [78] of the patterned sample. Nevertheless, it remains unclear why the low energy PL peak is not observed in the reference sample, taking into account that the size distribution of QD on both, patterned and non-patterned substrates, is very similar.

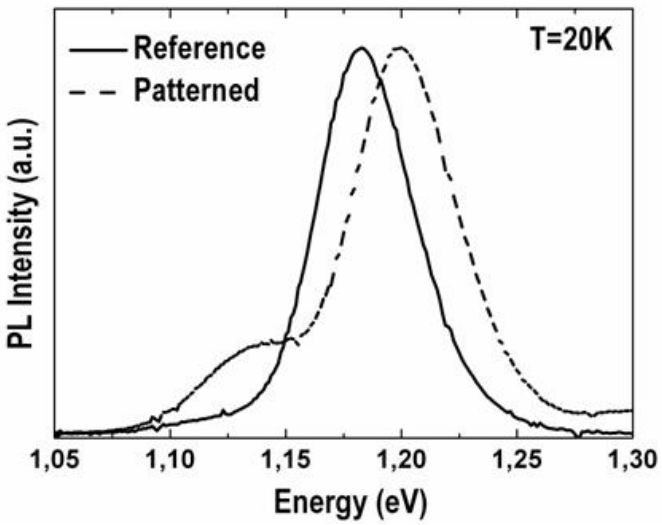

Figure 3.29. Comparison of the normalized 20 K PL spectra of the ordered InAs QD array (dotted line) and the simultaneously grown reference sample (continuous line). The emission energy and the linewidth of the main PL peak are Ep = 1.2 and 1.18 eV, FWHM = 43 and 44 meV respectively.

These results show that after the whole technological process for patterning the GaAs substrates and further growth of an extremely thin GaAs buffer layer (6.8 nm), it has been obtained a patterned substrate with the same characteristics of flatness and cleanliness of an unprocessed substrate. Instead of the random distribution of self-assembled QD on flat surfaces, the patterned substrates impose an ordering of the QD layout. In turn, improvements in size uniformity in the initial patterning could be critical for the degree of ordering achieved in the final QD distributions

3.2.3. Conclusions

In this section it has been demonstrated that ordered QD with the same optical quality as shown by random self-assembled QD, can be obtained without the need of stacking a number of QD layers to separate the active QD far from the patterned substrate. To achieve this, a fabrication process based on a novel combination of ozone oxidation/oxide etching by citric acid has been developed in order to transfer to the GaAs substrate a certain pattern, previously designed by LIL. In particular, by repeating the

oxidation/oxide dissolution process, the resin pattern is transferred to the semiconductor substrate originating arrays of nanoholes that can be tuned in depth with nanometer resolution. Upon further epitaxial growth, ordered QD distributions have been obtained at a short distance of 6.8 nm to the patterned substrate with a PL emission similar to that obtained on self-assembled QD grown on un-processed substrates.

It is important to emphasize that once demonstrated for the case of patterning by LIL lithography, this process can be extended to any other lithographic technique.

3.3. Summary and conclusions

In this chapter results on the selective growth of InAs QD by using different nanoholes templates on GaAs substrates have been presented. In particular, two technological processes based on the use of patterned layers have been developed to perform ordered distributions of nanoholes on an epitaxial GaAs (001) substrate.

· In a first approach, a mask based on a nanoporous alumina layer was fabricated by the electrochemical anodization of an epitaxial 1 μm-thick Al layer, previously grown by MBE at RT. In particular, by continuing the formation mechanism of this nano-channel alumina mask a few nanometers in the GaAs substrate, a large area distribution of nanoholes on the substrate was finally obtained.
The main conclusions derived from this process are the following:

- The epitaxial growth of a 1 μm-thick Al layer on GaAs (001) substrates by MBE, results in a very flat (rms= 1.51 nm) (110) monocrystalline layer.

- The anodic oxidation of a so thin Al layer, already yields an alumina surface with ordered nanoholes suitable to be transferred to an underlying GaAs substrate.

- The Al layer acts as a good mask preserving the flatness and cleanliness of the substrate once the formed alumina is removed.

- The pregrowth sample treatment with atomic H and the posterior GaAs buffer layer growth at low substrate temperature, yield an optimal surface suitable for further InAs QD formation.

- All InAs QD formed, nucleate into the nanoholes.

· In a second approach, a novel combination of ozone oxidation/oxide etching process was developed to transfer to a GaAs substrate the order of a patterned resin layer, previously designed by laser interference lithography (LIL). This process can be extended to any other lithographic technique.
The main conclusions derived from this work can be summarized as follows:

- A novel ozone oxidation / citric acid oxide etching process allows transferring a pattern designed by an external lithographic technique with nanometric resolution.

- The different *ex situ* (oxygen plasma, developer, remover and HF dips) and *in situ* (atomic H irradiation) pregrowth preparation processes of the patterned substrate and the posterior GaAs buffer layer growth at low substrate temperature, yield an optimal semiconductor surface suitable for further selective formation of InAs QD.

- The nucleation, and therefore, the QD distribution on a GaAs surface is imposed by the pattern transferred from the resin layer.

- The most important, the PL emission from the QD ordered by this technological process is similar in intensity to those formed by a self-assembled process on a reference sample.

References

[1] F. Keller, and J. D. Edwards, Metal Progress **54**, 35-41 and 195 (1948).
[2] H. P. Godard, Mater. Perf. **3**, 9 (1981).
[3] C. R. Martin, Science **266**, 1961 (1994).
[4] K. Itaya, S. Sugawara, K. Arai, and S. Saito, J. of Chemical Eng. of Japan **17**, 514 (1984).
[5] A. T. Shawaqfeh, and R. E. Baltus, J. of Membrane Science **157**, 147 (1999).
[6] T. Kyotani, W. H. Xu, Y. Yokoyama, J. Inahara, H. Touhara, and A. Tomita, J. of Membrane Science **196**, 231 (2002).
[7] H. Masuda, and K. Fukuda, Science **268**, 1466 (1995).
[8] H. Masuda, K. Yada, and A. Osaka, Jpn. J. Appl. Phys. **37**, L1340 (1998).
[9] H. Masuda, and M. Satoh, Jpn. J. Appl. Phys. **35**, L126 (1996).
[10] S. K. Hwang, J. Lee, S. H. Jeong, P. S. Lee, and K. H. Lee, Nanotechnology **16**, 850 (2005).
[11] K. Nielsch, F. Müller, A. P. Li, and U. Gösele, Adv. Mater. **12**, 582 (2000).
[12] S. Shingubara, J. of Nanoparticle Research **5**, 17 (2003).
[13] G. Sauer, G. Brehm, S. Schneider, K. Nielsch, R. B. Wehrspohn, J. Choi, H. Hofmeister, and U. Gösele, J. Appl. Phys. **2**, 3243 (2002).
[14] M. Steinhart, J. H. Wendorff, A. Greiner, R. B. Wehrspohn, K. Nielsch, J. Schilling, J. Choi, and U. Gösele, Science **296**, 1997 (2002).
[15] G. Che, B. B. Lakshmi, C. R. Martin, E. R. Fisher, and R. S. Ruoff, Chemistry of Materials **10**, 260 (1998).
[16] G. Che, B. B. Lakshmi, E. R. Fisher, and C. R. Martin, Nature **393**, 346 (1998).
[17] R. Zhu, Y. T. Pang, Y. S. Feng, G. H. Fu, Y. Li, and L. D. Zhang, Chem. Phys. Lett. **368**, 696 (2003).
[18] T. Gao, J. C. Fan, G. W. Meng, Z. Q. Chu, L. D. Zhang, Thin Solid Films **401**, 102 (2001).
[19] S. Shingubara, Y. Murakami, K. Morimoto, and T. Takahagi, Surf. Sci. **532**, 317 (2003).

[20] P. L. Chen, C. T. Kuo, T. G. Tsai, B. W. Wu, C. C. Hsu, and F. M. Pan, Appl. Phys. Lett. **82**, 2796 (2003).
[21] R. S. Guico, M. Tzolov, W. Guo, S. G. Cloutier, R. Beresford, and J. Xu, J. Vac. Sci. Technol. B **25(3)**, 1093 (2007).
[22] Y. Song, M. Zheng, and L. Ma, Nanotechnology **18**, 415302 (2007).
[23] P. Alonso-González, M. S. Martín-González, J. Martín-Sánchez, Y. González, and L. González, J. Cryst. Growth **294**, 168 (2006).
[24] X. L. Che, L. Li, F. Q. Liu, X. Q. Huang, and Z. G. Wang, Appl. Phys. Lett. **88**, 263107 (2006).
[25] K. Meneou, K. Y. Cheng, Z. H. Zhang, C. L. Tsai, C. F. Xu, and K. C. Hsieh, Appl. Phys. Lett. **86**, 153114 (2005).
[26] X. Mei, M. Blumin, D. Kim, Z. Wu, and H. E. Ruda, J. Cryst. Growth **251**, 253 (2003).
[27] X. Mei, D. Kim, and H. E. Ruda, Appl. Phys. Lett. **81**, 361 (2002).
[28] M. Nakao, S. Oku, T. Tamaura, K. Yasui, and H. Masuda, Jpn. J. Appl. Phys. **38**, 1052 (1999).
[29] H. Föll, S. Langa, J. Carstensen, M. Christophersen, and I. M. Tiginyanu, Adv. Mater. **15**, 183 (2003).
[30] H. Masuda, H. Yamada, M. Satoh, H. Asoh, M. Nakao, and T. Tamamura, Appl. Phys. Lett. **71**, 2770 (1997).
[31] J. Choi, Y. Park, and A. Scherer, Nanotechnology **16**, 1655 (2005).
[32] A. J. Bard (Ed), Encyclopedia of electrochemistry of the elements, vol:**6** New York and Basel: Marcel Dekker, (1973).
[33] J. W. Diggle, T. C. Downie, and C. W. Coulding, Chemical Review **69**, 365 (1969).
[34] H. Masuda, F. Hasegwa, and S. Ono, J. Electroch. Soc. **144**, 127 (1997).
[35] A. P. Li, F. Müller, A. Birner, K. Nielsch, and U. Gösele, J. Appl. Phys. **84**, 6023 (1998).
[36] K. Nielsch, J. Choi, K. Schwirn, R. B.Wehrspohn, and U. Gösele, Nano Letters. **2**, 677 (2002).
[37] H. Habazaki, K. Shimizu, P. Skeldon, G. E. Thompson, G. C. Wood, and X. Zhou, Corrosion Science **39**, 731 (1997).
[38] R. B. Wehrspohn and A. P. Li, K. Nielsch and F. Müller and W. Erfurth and U. Gösele (editors: K. R. Hebert and R. S. Lillard and B. R. Mac Dougall), *Highly ordered alumina films: pore growth and applications (Oxide Films in The Electrochemical Society Proceeding Series)*, vol. PV **2000-4**, 271. Pennington, NJ: Marcel Dekker (2000).
[39] D. Oner, and T. J. McCarthy, Langmuir **16**, 7777 (2000).
[40] A. B. D. Cassie, and S. Baxter, Trans. Faraday Soc. **40**, 546 (1944).
[41] V. P. Parkhutik and V. I. Shershulsky, J. Physics D – Appl. Phys. **25**, 1258 (1992).
[42] O. Jessensky, F. Müller, and U. Gösele, Appl. Phys. Lett. **72**, 1173 (1998).
[43] S. Z. Chu, K. Wada, S. Inoue, M. Isogai, and A. Yasumori, Adv. Mater. **17**, 2115 (2005).
[44] O. Jessensky, F. Müller, and U. Gösele, J. Electroch. Soc. **145**, 3735 (1998).
[45] K. Nielsch, J. Choi, K. Schwirn, R. B. Wehrspohn, and U. Gösele, Nano Lett. **2**, 677 (2002).
[46] F. Keller, M. S. Hunter, and D. L. Robinson, J. Electroch. Soc. **100**, 411 (1953).
[47] G. C. Schwartz and V. Platter, J. Electroch. Soc. **122**, 1508 (1975).
[48] R. Ludeke, L. L. Chang, and L. Esaki, Appl. Phys. Lett. **23**, 201 (1973).
[49] A. Y. Cho, and P. D. Dernier, J. Appl. Phys. **49**, 3328 (1978).
[50] M. Missous, W. S. Truscott, and K. E. Singer, J. Appl. Phys. **68**, 2239 (1990).
[51] N. Maeda, M. Kawashima, and Y. Horikoshi, J. Appl. Phys. **74**, 4461 (1993).
[52] J. E. Oh, P. K. Bhattacharya, J. Singh, W. Dospassos, R. Clarke, N. Mesteres, R. Merlin, K. H. Chang, and R. Gibala, Surf. Sci. **228**, 16 (1990).
[53] T. Yao, H. Nakahara, H. Matsuhata, and Y. Okada, J. Cryst. Growth **111**, 221 (1991).
[54] H. Nakahara, H. Matsuhata, and Y. Okada, Appl. Phys. Lett. **58**, 1970 (1991).
[55] A. L. Prieto, M. S. Sander, M. S. Martín-González, R. Gronsky, T. Sands, and A. M. Stacy J. Am. Chem. Soc. **123**, 7160 (2001).
[56] Martín-Sánchez J, González Y, González L, Tello M, García R, Granados D, García J. M and F. Briones J. Crystal Growth **284**, 313 (2005).
[57] F. Briones, L. González, and A. Ruiz, Appl. Phys. A, **49**, 729 (1989).
[58] T. A. Savas, M. L. Schattenburg, J. M. Carter, and H. I. Smith, J. Vac. Sci. Technol. B **14**, 4167 (1996).
[59] K. Nagai, K. Utaka, T. Ohira, T. Segawa, and M. Nakao, Jpn. J. Appl. Phys. **41**, 1085 (2002).

[60] M. Farhoud, J. Ferrera, A. J. Lochtefeld, T. E. Murphy, M. L. Schattenburg, J. Carter, C. A. Ross, and H. I. Smith, J. Vac. Sci. Technol. B **17**, 3182 (1999).
[61] J. Y. Decker, A. Fernandez, and D. W. Sweeney, J. Vac. Sci. Technol. B **15**, 1949 (1997).
[62] L. F. Johnson, G. W. Kammlott, and K. A. Ingersoll, Appl. Opt. **17**, 1165 (1978).
[63] E. H. Anderson, C. M. Horwitz, and H. I. Smith, Appl. Phys. Lett. **43**, 874 (1983).
[64] J. C. Lodder, J. Magn. Magn. Mater **272**, 1692 (2004).
[65] A. Fernández, H. T. Nguyen, J. A. Britten, R. D. Boyd, M. D. Perry, and D. R. Kania, J. Vac. Sci. Technol. B **15**, 729 (1997).
[66] R. C. Enger, and S. K. Case, Appl. Opt. **22**, 3220 (1983).
[67] V. Berger, O. Gauthier-Lafaye, and E. Costard, Electon. Lett. **33**, 425 (1997).
[68] W. Wu, B.Cui, X. Sun, W. Zhang, L. Zhuang, L. Kong, and S. Y. Chou, J. Vac. Sci. Technol. B **16**, 3825 (1998).
[69] M. L. Schattenburg, C. R. Canizares, D. Dewey, K. A. Flanagan, M. Hamnett, A. M. Levine, K. S. K. Lum, R. Manikkalingam, T. H. Markert, and H. I. Smith, Opt. Eng. **30**, 1590 (1991).
[70] A. Fernandez, P. J. Bedrossian, S. L. Baker, S. P. Vernon, and D. R. Kania, IEEE Trans. Magn. **32**, 4472 (1996).
[71] M. Farhoud, M. Hwang, H. I. Smith, M. L. Schattenburg, J. M. Bae, K. Youcef-Toumi, and C. A. Ross, IEEE Trans. Magn. **34**, 1087 (1998).
[72] J. P. Spallas, R. D. Boyd, J. A. Britten, A. Fernandez, A. M. Hawryluk, M. D. Perry, and D. R. Kania, J. Vac. Sci. Technol. B **14**, 2005 (1996).
[73] R. Murillo-Vallejo, H.A.G.M. Van Wolferen, L. Abelmann, and J. C. Lodder, Microelectronic Eng. **78**, 260 (2005).
[74] J. R. McNesby, and H. Okabe Advances in Photochemistry **3,** 166 (1964).
[75] Z. H. Lu, B. Bryskiewicz, J. McCaffrey, Z. Wasilewski, and M. J. Graham J. Vac. Sci.Technol. B **11(6),** 2033 (1993).
[76] J. R. Vig, J. Vac. Sci.Technol, A **3(3)**, 1027 (1984).
[77] J. Martín-Sánchez, Y. González, P. Alonso-González, and L. González, J. Cryst. Growth **310**, 4676 (2008).
[78] Zhang Y.C, Huang C. J, Liu F. Q, Xu B, Wu J, Chen Y. H, Ding D, Jiang W. H, Jiang X. L, Ye X. L and Z. G Wang J. Appl. Phys. **90**, 1973 (2001).

IV

IN SITU PATTERNING TECHNIQUE BY DROPLET EPITAXY

4. IN SITU PATTERNING TECHNIQUE BY DROPLET EPITAXY

In the previous chapter, two different *ex situ* technological approaches were explored with the aim of growing position controlled InAs QD. In this new chapter, a novel *in situ* patterning technique based on the droplet epitaxy growth technique is studied to form low density nanoholes ($2x10^8$ cm^{-2}) templates on GaAs(001) and InP(001) substrates. Once fabricated, these templates are further used for the formation of different low density III-V semiconductor nanostructures, as InAs QD and InAs QD molecules in lateral and vertical configuration, with a certain control of their size, aspect ratio and composition. Also, by varying the element V pressure used during the patterning process, type II Ga(As)Sb Qrings have been obtained on GaAs(001) substrates. The nanostructures density obtained by this patterning technique has permitted, as it will be shown, a precise study of the single optical properties in the cases of InAs QD and lateral QD pairs.

Finally, results on the localization of the nanostructures after being buried will be shown. These results rely on the development of a specific growth process for the cap layer.

4.1. Introduction to droplet epitaxy growth technique

Droplet epitaxy (DE) was first used as an epitaxy growth technique at the beginning of the nineties by Koguchi and Ishige [1-3]. It was initially proposed as a new MBE method for the fabrication of III-V semiconductor microcrystals on II-VI semiconductor substrates with a nearly equal lattice constant. In this sense, it came to fill the gap that Stranski-Krastanow growth mode presents in the formation of lattice-matched semiconductor nanostructures. It basically consists in the deposition of atoms of Group-III element on the surface under the absence of the supply of Group-V element, creating liquid metal droplets. The formation mechanism of group-III metal droplets such as Ga, Al and In is explained by the Volmer-Weber growth mode [4], in which the bonding energy between incoming Group-III adatoms is much higher than the bonding energy between the surface and the adatoms. The as-formed droplets are then subsequently exposed to an atmosphere of Group-V element that induces their crystallization into III-V semiconductor QD. As already said, although this technique has been mainly applied to lattice-matched compound-semiconductor systems [2,3,5-10] (droplet homoepitaxy), the growth of nanostructures in lattice-mismatched compound-semiconductor systems has also been obtained [11-14] (droplet heteroepitaxy). Recent demonstrations of droplet epitaxy versatility have included InAs QD [15-26], GaAs QD [27-37], coupled QD [38-45], GaAs Qrings [46-55] and Qrings complexes [47,56-60].

In most of the experiments related to Ga droplets formation, the effect of the substrate temperature during crystallization permits to differentiate between low T_s (200-300ºC) and high T_s (~500ºC) DE growth processes.

At low temperature DE, the gallium droplets crystallize into QD, single-ring and concentric Qring complexes under high (~10^{-4} Torr) [6,61], medium (~$8x10^{-6}$ Torr) [56] and low (~$2x10^{-6}$ Torr) [56] arsenic pressure, respectively (**Figure 4.1 (a), (b)** and **(c)**). These nanostructures formed at a relative low substrate temperature (~200-300ºC) usually show a lower optical quality than those spontaneously formed by a self-assembling process. However, by performing a rapid thermal annealing process after growth, photopumped laser action [28], single-photon correlation measurements [32] and Purcell effect of exciton emission by the use of optical microcavities [35] have been demonstrated using these nanostructures.

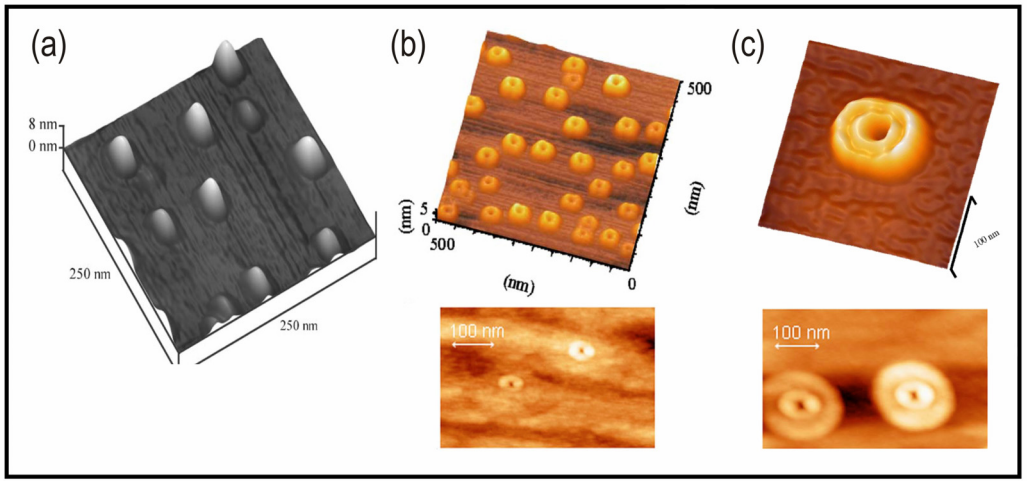

Figure 4.1. Semiconductor nanostructures fabricated by droplet epitaxy growth technique. (Images taken from references 46, 56 and 58).

On the other hand, at high substrate temperature (~500ºC), DE has emerged as a very useful tool to fabricate deep nanoholes on GaAs surfaces. This mechanism has been recently coined by Wang et. al. as a "*nanodrilling process*" [62]. It deals with the fact that at ~500ºC the initially deposited Ga droplets transform into single Qrings with a hole inside that penetrates into the substrate. This effect reveals a selective etching process at the substrate interface that can be controlled to fabricate nanoholes with a relative control of diameter and depth [63] (**Figure 4.2**).

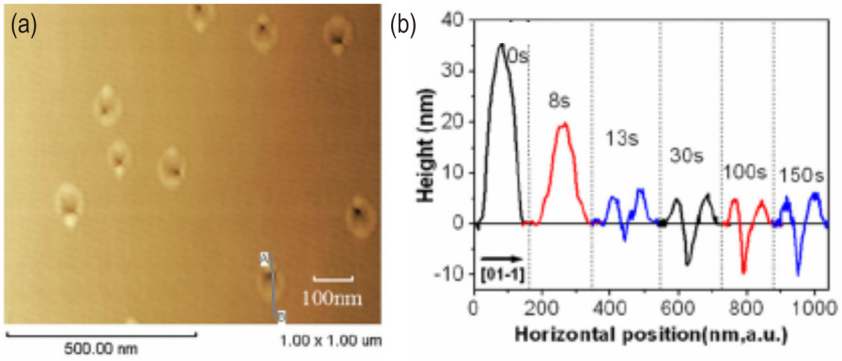

Figure 4.2. (a) AFM image of Ga droplets annealed in As4 ambient (~1×10−6 Torr) at 480ºC for 100 s. **(b)** Cross-sectional profiles of a single Ga Droplet along the [1-10] GaAs direction for different annealing times. (Image taken from reference 63).

In this thesis, results on the fabrication of nanostructures by DE at both, low and high substrate temperature, will be presented. In particular, low T_s DE was used to form for the first time, low density type II Ga(As)Sb Qrings by "*antimonization"* of Ga droplets while high T_s DE, was used to perform random distributions of GaAs and InP nanoholes for posterior selective nucleation of size-controlled InAs QD. An important intrinsic advantage of this last application of droplet epitaxy technique, is that it can provide nanotemplates for QD formation without the need of growing thick buffer layers for avoiding the influence of residual contamination from the fabrication process on the optical properties of the nanostructures. Additionally, by the use of high substrate temperatures for both the formation of the nanoholes and deposition of InAs, the optical quality of the material is preserved. This result, together with the fact that the nanostructures obtained replicates the low density of the formed nanoholes, $2x10^8 cm^{-2}$, makes this DE growing technique, as an optimal strategy for the design of active elements suitable for their implementation in new generation quantum optics devices.

In the next section, the formation mechanisms proposed in the literature for the fabrication of different nanostructures by DE technique is resumed.

4.2. Formation mechanisms of nanostructures by droplet epitaxy

In the following, the model proposed for the transformation of Ga droplets into GaAs nanostructures, which is the best-studied system, will be shown.

It has been demonstrated that the substrate temperature and arsenic flux density employed during annealing, or *arsenization* of Ga droplets are key parameters that determine their final morphology [63,64]. Under the condition of low T_s (180ºC) and high arsenic pressure (PAs_4= $2x10^{-4}$ Torr), Ga droplets tend to form GaAs QD [10] (**Figure 4.1 (a)**). These growth conditions were firstly used in the DE technique by Koguchi et. al. in the nineties [2,3,6]. The formation of QD in this case was ascribed to the fact that low substrate temperature and high arsenic pressure can significantly reduce the diffusion of Ga atoms [65-67]. Furthermore, it is expected that high arsenic pressure will also induce a high crystallization rate of Ga atoms. Thus, these two mechanisms, limited Ga diffusion and fast crystallization, cause that Ga droplets crystallize before the Ga atoms can diffuse out of the droplets. If in this scenario, the arsenic pressure is decreased, the Ga diffusion increases [67] implying then, a reduction of the crystallization rate. This fact would cause the diffusion of Ga atoms out of the droplets and therefore, the crystallization into Qring structures [47,60] (**Figure 4.1 (b)** and **(c)**). According to the literature involving this crystallization effect, the interior of these Qrings is shallow and no apparent holes at the flat surface level are formed, which can be attributed to the low dissolution rate of the underneath GaAs surface by the Ga droplets at low substrate temperature. Accordance with reference [65], the diffusion coefficient of As in Ga droplets is as low as 10^{-15} cm^2 s^{-1} at 200ºC. Hence, the dissolution of GaAs by Ga droplets is not significant at these temperatures. On the other hand, it is well documented that, at a high substrate temperature of 500ºC,

GaAs is unstable under Ga-rich conditions and As desorption could occur [68]. In this case, in the absence of As supply, the interface region with the GaAs substrate will dissolve into Ga and As. As illustrated in **Figure 4.3 (a)** the As atoms may diffuse through the Ga droplet, escaping into the vacuum chamber or incorporating to the boundary area of the Ga droplet forming GaAs again with Ga atoms from the droplet (the diffusion of Ga is also significantly enhanced at this temperature). This is the reason that GaAs lobes also form around the nanoholes (**Figure 4.3 (c)**) even before any supply of As. The remaining Ga atoms at the interface region after As desorption, merge into the Ga droplet. As this process continues, there are more GaAs underneath the droplet dissolving, more Ga atoms from the GaAs substrate joining the Ga droplet, and more As atoms diffusing to the boundary region to form GaAs again. The Ga droplet acts then, as a *"nanodrill"* etching into the GaAs surface to give rise to nanoholes. It is clear to see that this mechanism is, in the absence of As supply, a self-assisted process. Obviously, this nanodrill effect is strongly affected by the supply of As. As soon as an As flux is applied, the Ga droplet crystallization becomes the dominant growth mechanism since it is much faster than the nanodrill process.

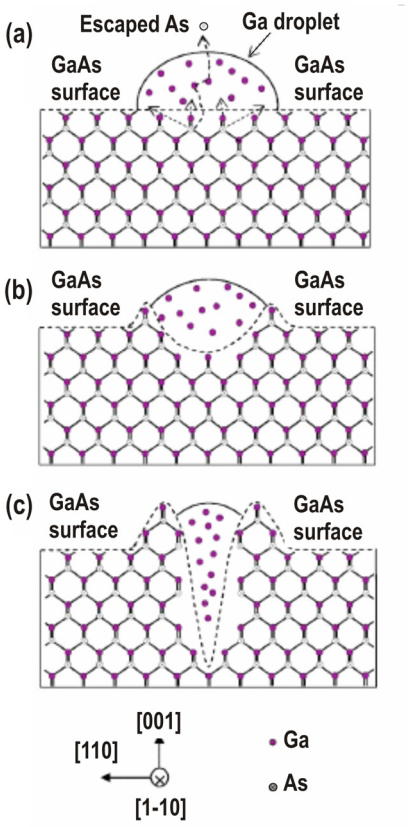

Figure 4.3. Schematic illustration of the proposed model for the Ga "nanodrill" process. (Image taken and modified from reference 62)

It can be highlighted that this etching of the GaAs surface is a selective process, in the sense that the diffusion rate of arsenic is highly increased only at the interface with a metallic environment, in this case a Ga droplet. As a final result, nanostructures are produced at the GaAs surface. This effect has a high potential when used as a nanolitographic toll for controlling both the spatial position and size of the nanostructures. For example, the localization of the nanostructure could be achieved by the use of a

controlled deposition of Ga droplets by, for example, a dip-pen technique [69] or similar, while the control of size could be obtained by the growth of certain epitaxial layers that at a chosen distance to the surface, would stop the dissolution process [63]. Hence, by this process, nanoholes with control in spatial position, diameter and depth could be achieved. The tuning of these parameters are referred to the Ga droplet formation and their effect to the underneath substrates. Alternately, as presented in the next section, another tuning approach has been performed in this thesis by using randomly located low density GaAs nanoholes (self-assembling process), fabricated by a *nanodrilling process* with a fixed depth, to form by their filling with InAs material, QD with a certain control in size (energy emission) and configuration (single QD or QD molecules).

As an innovation in the subject of patterning fabrication by droplet epitaxy, results on the formation of novel nanoholes templates by depositing In droplets on InP(001) substrates are also presented in this work. According to the similar results obtained for this material, the nanoholes formation mechanism on InP seems to be perfectly compatible with the above commented in the case of using GaAs substrates.

4.3. Nanoholes templates on GaAs(001) and InP(001) substrates

The fabrication procedure and experimental conditions for the fabrication of nanoholes on GaAs(001) and InP(001) substrates, are presented with detail in the next section. Typical templates of nanoholes obtained in this work are also shown with their corresponding dimensions.

4.3.1. GaAs nanoholes template

The experimental procedure performed in this work to the fabrication of nanoholes templates on GaAs(001) substrates by droplet epitaxy is described below.

First of all, the starting GaAs surface is initially flattened by the growth of a 0.5 μm-thick undoped buffer layer at T_s= 580ºC by MBE. Once obtained an optimal GaAs surface (rms= 0.24 nm), the substrate temperature T_s is decreased to 500ºC and the nanoholes template formation is performed. To do this, the Ga shutter is firstly opened during 10 s with the Ga cell providing a flux equivalent to the growth of GaAs at 1 ML/s. During this time, the arsenic cell is also periodically opened during 0.2 s every 0.8 s. The beam equivalent pressure of As_4 is fixed during the process to $5x10^{-7}$ Torr. This process results in Ga droplets spread all over the surface with a density of $2x10^8$ cm^{-2}. At this moment, the RHEED diagram shows the GaAs (2x4) surface reconstruction with incipient chevrons indicating the presence of droplets on the surface. The RD spectrum of this process is shown in **Figure 4.4 (a)**.

Finally, for a controlled stop of the *nanodrilling* process, the sample is kept during 6 min at the same substrate temperature and As_4 pressure of $BEPAs_4$= $5x10^{-7}$ Torr.

At this stage, nanoholes with a density of $2x10^{-8}$ cm^{-2} and showing an elongated structure along the GaAs [*110*] direction, with asymmetric surface side lobes are formed (**Figure 4.4 (b)**). The nanoholes mean dimensions are h= 4.4±0.7 nm for the nanoholes depth (**Figure 4.4 (c)**) and a bimodal distribution, measured by two Gaussian line-shape fit, centred at D_1= 95±5 nm and D_2= 110±9 nm for the nanoholes diameter (**Figure 4.4 (d)**). These results suggest an initial Ga droplet bimodal distribution that develops into nanoholes with similar depths but a clear bimodal distribution of diameters. On the other hand, the elongated shape along [*1-10*] is probably originated by the higher Ga diffusion in that direction at the used experimental conditions. The asymmetric side lobes are typically 5 and 4 nm in height respectively. The formation of such a structure in which along [*110*] direction well-defined side walls are originated, will play an important role, as shown in section 4.4.3, to the formation of QD pairs structures.

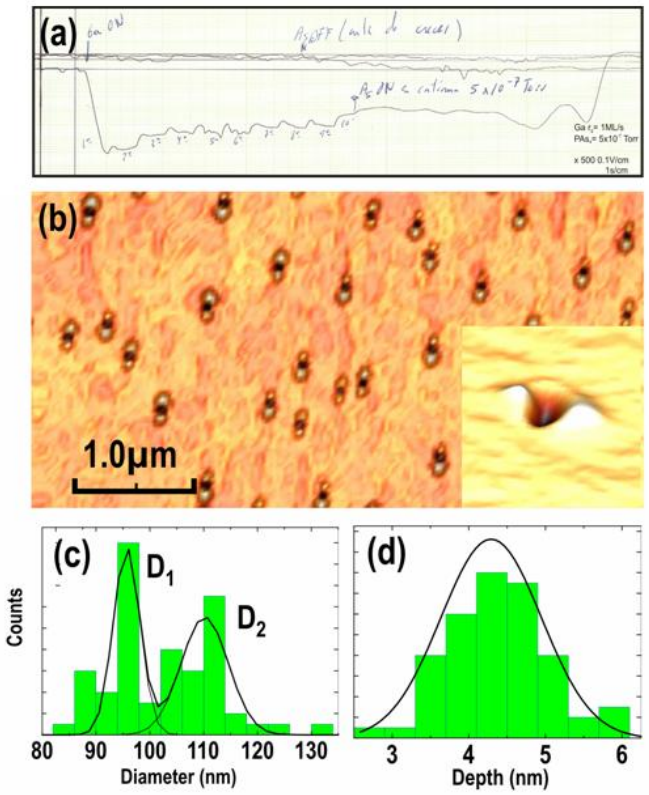

Figure 4.4. **(a)** RD spectra for the GaAs nanohole template formation process. **(b)** 5 µm x 5 µm AFM image showing a GaAs nanoholes template performed by droplet epitaxy technique. The inset shows a detailed 3D image of a nanohole. **(c)** Nanoholes template diameter distribution. **(d)** Nanoholes template depth distribution.

4.3.2. InP nanoholes template

The procedure followed for obtaining nanoholes templates on InP(001) substrates by droplet epitaxy, is analogous to the above described for GaAs(001) material. In this case, the In shutter is opened during 10 s with the In cell providing a flux equivalent to the growth of InP at 1 ML/s at a T_s= 350ºC. During this time, the P cell is also periodically opened during 0.2 s every 0.6 s. The rest of growth

parameters are also changed for accommodating to the InP system. In this sense, T_s is maintained this time at 350ºC with a phosphorus pressure, BEP P_2, of $5x10^{-7}$ Torr. Similar to the process on GaAs substrates, the initiated *nanodrilling* process is finally stopped by a 6 min-annealing step, at T_s= 350ºC and BEP P_2= $5x10^{-7}$ Torr.

Figure 4.5 (a) shows the InP(001) surface, that results after this patterning process. The RD spectrum for this process is also shown in **Figure 4.5 (b)**.

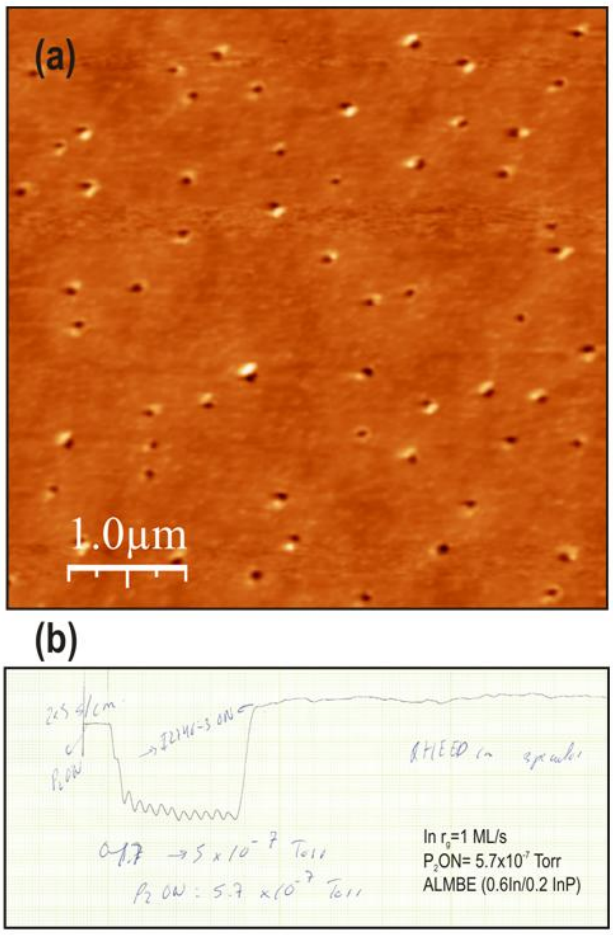

Figure 4.5. **(a)** 5 µm x 5 µm AFM image showing an InP nanoholes template performed by droplet epitaxy technique. **(b)** RD spectra for the nanoholes template process.

Nanoholes with a density of $2.5x10^{-8}$ cm^{-2} and mean dimensions of 58.7±10.4 nm in diameter and 5.7±1.0 nm in depth are obtained (**Figure 4.6**). As a difference to the case of using GaAs substrates, the fabricated nanoholes are now roughly circular and present only a side lobe randomly located at the border of the nanohole (**Figure 4.6 (b)** and **(c)**). This effect indicates that the lower T_s used in this novel *nanodrilling* process in comparison with the GaAs system, could inhibit any preferential diffusion of In on the surface.

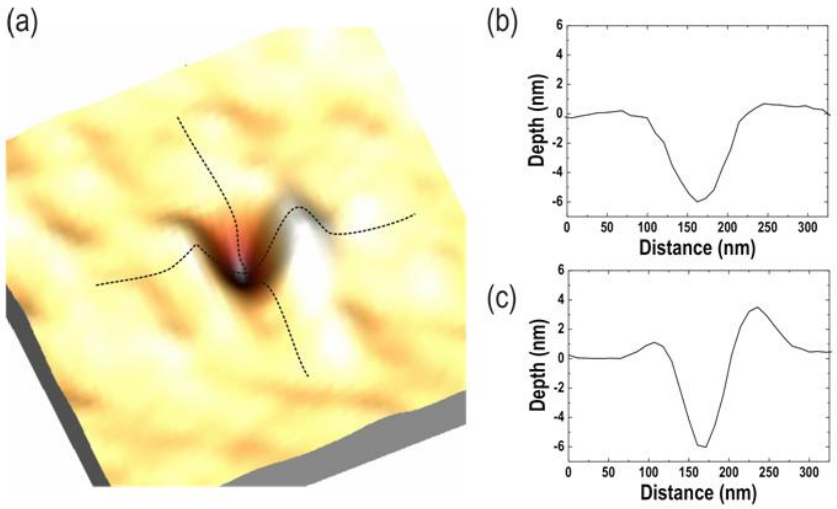

Figure 4.6. **(a)** 3D AFM image showing an InP nanohole fabricated by droplet epitaxy. **(b)** and **(c)**: Profiles along the nanohole.

These nanoholes are further used, as shown in section 4.5, to the deposition of InAs(P) material that results in the formation of nanostructures that hardly surpass the surface level. PL studies will show these nanostructures as QD emitting in the range (1.66,1.60) μm at 25 K.

4.4. InAs/GaAs nanostructures into GaAs nanoholes

In this section results on the formation of different InAs nanostructures into nanoholes formed on GaAs(001) substrates will be presented. As previously commented, a low density nanoholes template obtained by a "*nanodrilling process"* was used to nucleate inside them InAs QD with a certain control of size, aspect ratio and composition. Additionally, by changing some growth parameters in the deposition of InAs material and by the growth of QD stacked structures, InAs QD molecules in vertical and lateral arrangements have been obtained.

4.4.1. InAs quantum dots

This section starts with the description of the used growth procedures that give rise to the selective nucleation of single InAs QD inside the previously formed GaAs nanoholes. The relationship between dimensions and energy emission of these nanostructures will be presented together with the optical emission studies at the single nanostructure level.

On the nanoholes template shown in **Figure 4.4 (b)**, an amount of 1.4 ML of InAs was deposited at T_s= 510ºC following a growth sequence consisting of the deposition of 0.1 ML of InAs at a growth rate of 0.05 ML/s, followed by a pause of 2 s under As_2 flux, $BEPAs_2$= 7.5x10^{-7} Torr.

The results obtained by this InAs deposition conditions are shown in **Figure 4.7**. In particular, the section **(a)** of this figure shows a 5 μm x 5 μm AFM image of the resulting QD inside the GaAs nanoholes. A profile along the long axis of the nanostructures reveals two different kind of QDs labelled as **A** and **B** in the figure. The differences are better observed in **Figures 4.7 (b)** and **(c)**, where typical images obtained on smaller areas and the corresponding [*1-10*] profiles of type A and type B nanostructures are depicted. In order to obtain the real dimensions of the InAs QD, the profiles are compared with those obtained averaging a large number of nanoholes from a reference sample consisting in a GaAs (001) with nanoholes without any InAs deposition (grey profiles on **Figures 4.7 (b)** and **(c)**). On one hand, Type-A QD are h_1= 9.0±1.8 nm high before capping, as measured from the bottom of the seeding nanohole. They are less frequent in the ensemble and appear with a density of $1x10^7$ cm^{-2}. On the other hand, type-B QD (**Figure 4.7 (c)**) present a different topography as they do not protrude from their nanohole. Following the same procedure, it can be estimated their height to be h_2= 3.3±0.8 nm. In this case, the density obtained for type-B QD is $2x10^8$ cm^{-2}. At this point, it shall be noted that it was not found any QD in the regions between the nanoholes. This means that the used growth conditions were optimal for formation of nanostructures only into the nanoholes of patterned substrates.

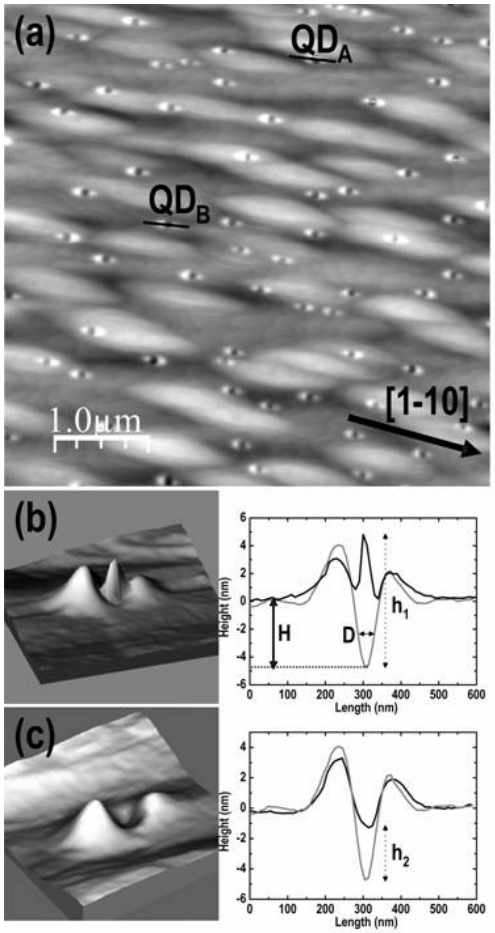

Figure 4.7. AFM images obtained in different areas of the sample are shown in **(a)** (5 μm x 5 μm), **(b)** and **(c)** (600 μm x 600 μm). At the right, together with the QD typical profiles, a grey line has been drawn corresponding to the average profile of the GaAs nanoholes before InAs deposition.

The optical properties of the ensemble of this kind of QD are resumed in the next section.

· Optical properties of the ensemble of quantum dots

Figure 4.8 shows the power dependent emission spectra at 20 K for the QD shown in **Figure 4.7**. At low excitation density, besides the 1.448 eV emission peak from the wetting layer (WL), two broad bands are detected centred at 1.196 eV and 1.357 eV and labelled as A_0 and B_0, respectively. These bands correspond with the type-A and type-B QD families observed by AFM. At low temperatures, conventional InAs self-assembled QD exhibit ground state energies around 1.1-1.18 eV for capped QD of height in the range of 5-8 nm [70,71]. On the other hand, introducing an annealing step during the growth or afterwards, their height decreases to 2-3 nm shifting up the ground state energy well above 1.3 eV [72]. Therefore, it can be concluded that the height values found for type-A and type-B QD are compatible with the fundamental transitions observed in their PL spectra.

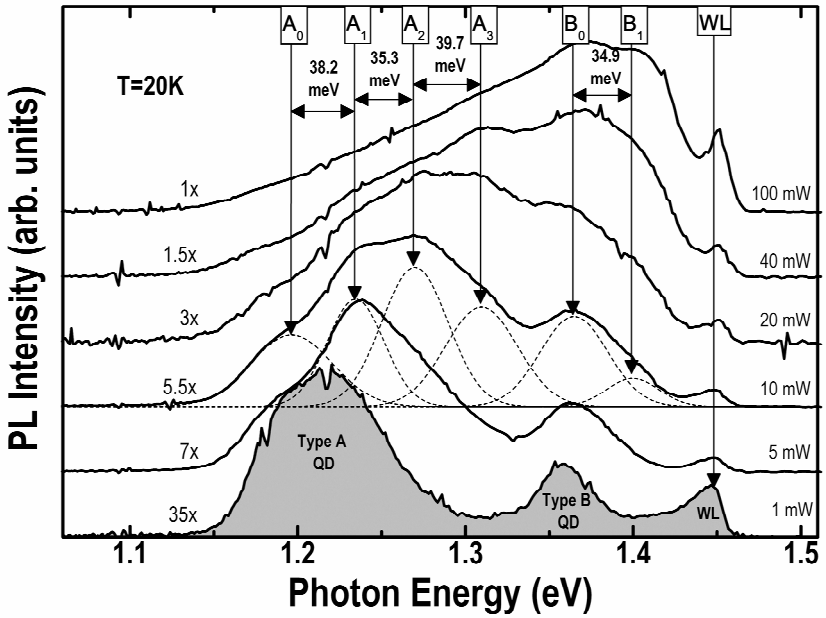

Figure 4.8. The evolution with the excitation power of the ensemble PL spectrum reveals the existence of two different QD families and the emission from excited bands at the indicated energies. A Gaussian fit has been included for the spectrum obtained at 10 mW.

In these QD, the emission peaks corresponding to transitions from excited states can also be studied since, due to their low density, they enter in the saturation regime at moderate excitation powers. In **Figure 4.8**, three excited emission bands peaked at 38.2, 73.5 and 113.2 meV above the ground state and labelled as A_1, A_2 and A_3 respectively, can be identified for type-A QD. The approximately constant excited state splitting found (ΔE~38 meV), indicates that the QD lateral confinement could be described by a smooth parabolic potential [73]. The average value of ΔE~38 meV is smaller by 30-50% than those reported in the literature for QD emitting below 1.2 eV [70,71], and suggests, within this model, that type-A QD exhibit a larger diameter than standing InAs/GaAs self-assembled QD with similar ground state energy. Finally, for the ensemble of type-B QD, it has been found only one excited state (B_1) splitted by

34.9 meV from its fundamental state in good correspondence with values reported in the literature for QD emitting above 1.3 eV.

· Size and homogeneity control of quantum dots

In this section results on the size control of the QD formed into the GaAs nanoholes template are presented. For these experiments the InAs growth conditions were changed to improve the size distribution of the formed nanostructures.

As it was commented in the introduction of this thesis, the selective nucleation of InAs inside GaAs nanoholes is strongly influenced by T_s, As molecule type (As_2, As_4) and pressure, and the In growth rate. In particular it has been observed that low In growth rates and low As pressures together with the use of As_4 species favours the In diffusion on GaAs(001) surfaces [74-76]. For this reason, an As_4 pressure as low as $5x10^{-7}$ Torr at T_s of 500ºC was used for the deposition of InAs in a new approximation (in the previous results, section 4.4.1, 1.4 ML of InAs was deposited at a growth rate of 0.5 ML/s, T_s= 510ºC and $BEPAs_2$= $2x10^{-6}$ Torr). Moreover, in this case, In was provided during the last annealing step of the nanoholes at a growth rate of 0.01 ML/s. Once the desired amount of In was deposited, the process was maintained providing only As_4 to complete the total annealing time of 6 min (section 4.3.1). After this step, the formed nanostructures were finally annealed under As_2 flux for 1 min at T_s= 510ºC and BEP= $5x10^{-7}$ Torr [26]

Results on the improved homogeneity of InAs QD grown by this last procedure are shown in **Figure 4.9**. A size dispersion as low as 6.0 % for the QD diameter and 5.6 % for the QD height is obtained.

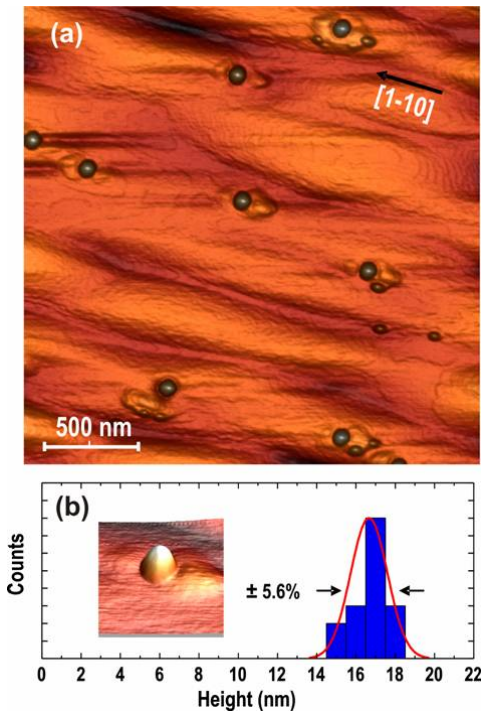

Figure 4.9. **(a)** AFM image of QD grown on a nanoholes template at PAs4 = 5x10-7 Torr and a Ts of 500ºC. **(b)** The QD height distribution shows a dispersion as low as 5.6%.

This size homogeneity is corroborated by the narrow PL peak (full width at half maximum (FWHM) of 16.5 meV) obtained for these nanostructures at 30 K, after being capped by a 100 nm-thick GaAs layer (**Figure 4.10**)

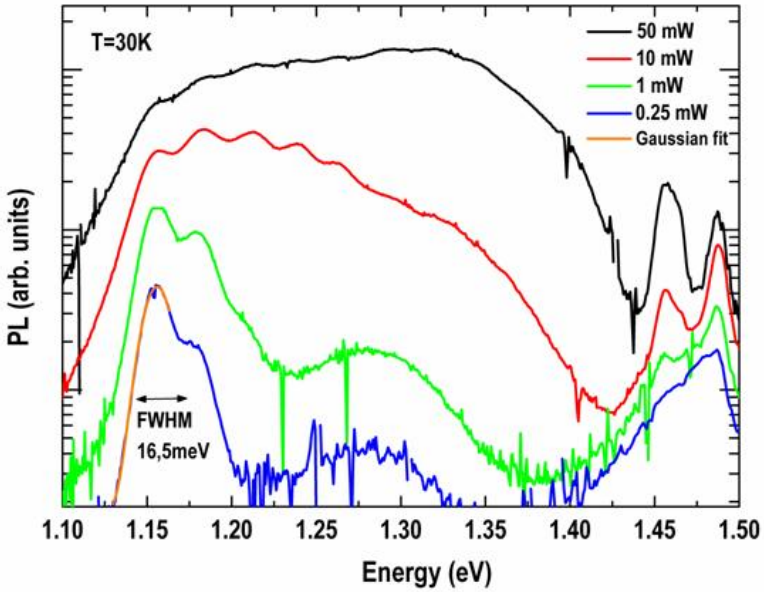

Figure 4.10. Photoluminiscence spectra at 30K from the QD shown in Figure 4.9 as a function of the excitation power. With increasing Pexc up to five excited states are observed. A FWHM as small as 16.5 meV is obtained by gaussian fit at a PEXC = 0.25 mW (orange line in the figure).

In this last figure is also observed the presence of a second PL peak at higher energies, this emission could come from a second QD family probably originated by the bimodal distribution previously commented in section 4.3.1 for the diameter of the nanoholes. It can be derived from these results that not only the InAs growth conditions but mainly the initial size distribution of Ga droplets, influence on the final development of different families of QD.

Using these improved InAs growth conditions, new samples were grown with the aim of obtaining a controlled filling of the nanoholes. To do this, the opening time of the In cell was varied to grow 1.1, 1.3, 1.5 and 1.7 ML of InAs on the nanoholes template. The results obtained by this new growth protocol are shown in **Figure 4.11**. In particular, the AFM images in **Figure 4.11 (a)** and **Figure 4.11 (b)** show the result of depositing 1.3 ML and 1.7 ML of InAs on the nanoholes template respectively. Similar to that obtained in **Figure 4.7** and **Figure 4.8**, it is observed on **Figure 4.11 (a)**, a bimodal size distribution in the QD nucleated at the nanoholes (labelled again in the figure as QD_A and QD_B). Accordingly, the nanoholes with smaller diameters would lead to QD protruding from the nanoholes, QD_A family, while larger nanoholes would lead to QD with a height that hardly surpass the surface level, QD_B family. The total average density of nanostructures, QD_A and QD_B, is the same as the initial nanoholes density, $\rho = 2x10^8$ cm^{-2}. **Figure 4.11 (b)** corresponds to the deposition of 1.7 ML of InAs, the critical value for QD formation on a flat substrate. A higher density of QD ($\rho = 2x10^9$ cm^{-2}) is observed, involving QD nucleation both inside

and outside the nanoholes. The QD formed at the nanoholes have typically diameters of D= 56±2 nm and height h= 20±1 nm referred to the flat surface plane, while those nucleated surrounding the nanoholes show a broader size distribution with mean values of D= 36±6 nm and h= 10±3 nm.

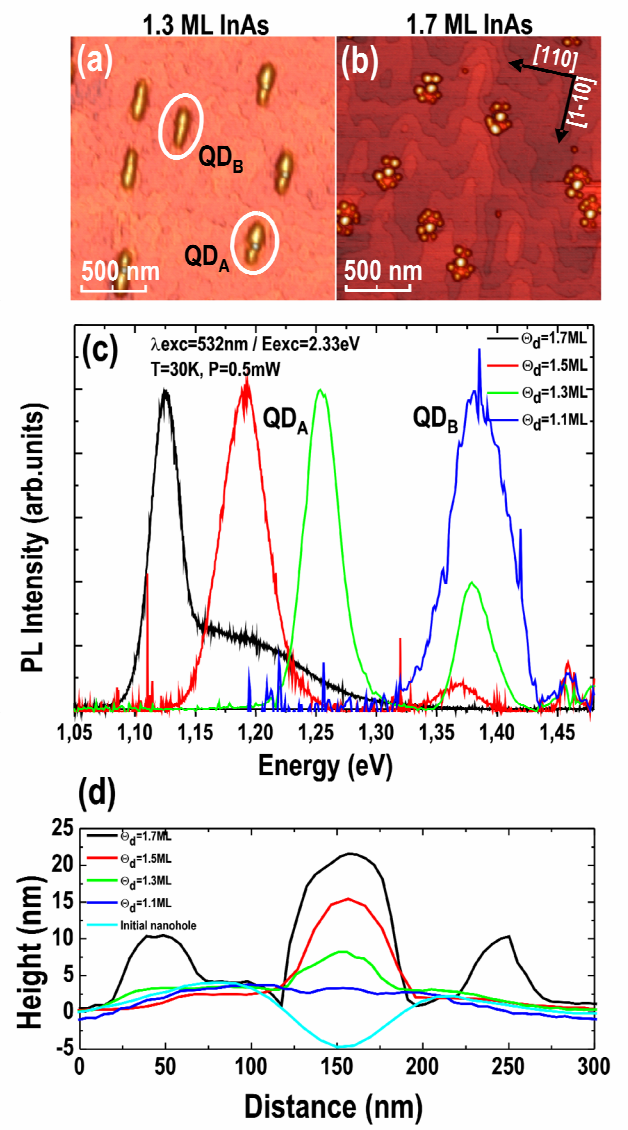

Figure 4.11. **(a)** 2 μm x 2 μm AFM image showing the GaAs nanoholes template topography after growing 1.3 ML of InAs. **(b)** 2 μm x 2 μm AFM image showing the GaAs nanoholes template topography after growing 1.7 ML of InAs. QD are also nucleated surrounding the filled nanohole. **(c)** Photoluminescence spectra after growing 1.1, 1.3, 1.5 and 1.7 ML of InAs on the GaAs nanoholes template. Two families of emission peaks corresponding to the double distribution of the nanohole diameter are observed (QDA, QDB). **(d)** AFM profiles showing the filling of the GaAs nanohole from the initial empty state to the nucleation of 1.1, 1.3, 1.5 and 1.7 ML of InAs.

Concerning the optical emission, **Figure 4.11 (c)** shows the normalized nanostructures PL emission at an excitation power of 0.05 mW for 1.1, 1.3, 1.5 and 1.7 ML of InAs (blue, green, red and black lines respectively), deposited over the nanoholes template produced at the cap layer surface (100 nm-thick GaAs layer in this case). In the case of 1.1 ML of InAs (blue line) a single and broad peak (FWHM= 47 meV) centred at 1.385 eV is observed. For 1.3 ML of InAs (green line in the figure) two emission peaks are obtained at 1.25 eV (FWHM= 33 meV) and 1.379 eV (FWHM= 31 meV). Two emission peaks are also obtained at 1.19 eV (FWHM= 44 meV) and 1.367 eV (FWHM= 31 meV) for 1.5 ML of InAs deposited (red line in the figure).

In the case of 1.1 ML of InAs, the broad PL emission peak observed would reflect the broad size distribution of initial nanoholes, inset of **Figure 4.4**. However, a direct correlation between the size of the nanoholes and QD is not possible as no protruding QD are clearly observed (**Figure 4.12**).

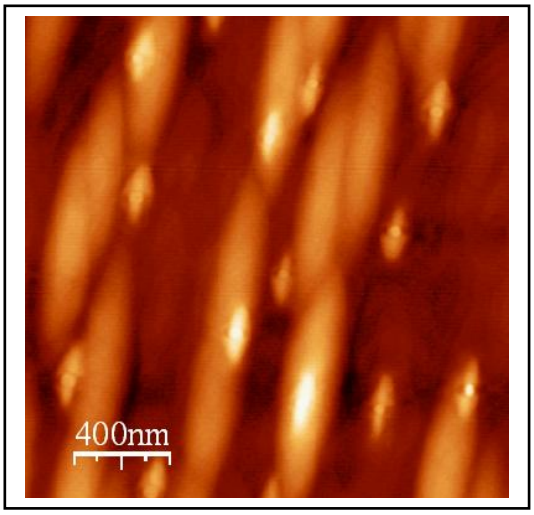

Figure 4.12. 2 μm x 2 μm AFM image showing QD formed into the nanoholes after depositing 1.1 ML of InAs.

On the other hand, according to the previous topographic images (**Figure 4.11 (a)**), the pair of PL peaks observed in the spectra for 1.3 and 1.5 ML of InAs would respectively correspond to the emission of QD_B (peak at higher energies) and QD_A (peak at lower energies).

For 1.7 ML of InAs deposited, two main PL peaks at 1.12 and 1.18 eV (FWHM= 27 meV and 117 meV respectively) can be observed. According to the AFM image shown in **Figure 4.11 (b)** and the QD size distributions obtained, they can be ascribed to QD formed inside and outside of the nanoholes respectively. In this case, all the QD in the nanoholes protrude, QD_A type, as the filling of the nanoholes is large enough.

Thus, focusing on the situation where QD are formed at the nanoholes, QD_A and QD_B, a clear dependence can be observed in the emission energy of the two QD families with the amount of InAs material deposited, permitting an actual control of the PL emission by the appropriate choice of the amount of InAs deposited.

The close correlation between PL results and size of the QD is further illustrated in **Figure 4.11 (d)**. In particular, the height profiles across the QD formed at the nanoholes with emission at lower energies (QD_A corresponding to 1.3, 1.5 and 1.7 ML of InAs) are shown in this figure. It is also represented for comparison the profile of the QD formed at the nanoholes in the cases of 1.1 ML (QD_B) and the starting nanohole. An enlargement of the QD at the nanoholes with increasing amount of InAs deposited is clearly observed. In the case of 1.7 ML of InAs deposited, the profile of QD surrounding the original nanohole is also shown. It can be observed that these surrounding QD are a bit smaller than QD_A, which correspond to 1.3 ML of InAs (measured from the bottom of the nanohole). In spite of that, their PL emission peak is centred at a lower energy. A plausible explanation of this effect is that the composition of the QD formed at

the nanoholes is different to that of those formed outside, reflecting a different QD formation process. In fact, previous works [77] have pointed out the diffusion of both Ga and In atoms to the nanoholes, giving rise to $In_XGa_{1-x}As$ QD. As a simple approximation, considering that the surrounding QD and QD_A of 1.3 ML have the same size and that the surrounding QD are almost 100% In content, it can be interpolated the In content between the surrounding QD (~100% InAs) and GaAs bandgap (0% InAs). According to this, from the QD_A PL emission energy peak, it is obtained an x= 80% In content for the QD formed at the nanoholes. Anyway, it has to be emphasized that this is a coarse approximation and a model taking into account also the size and composition of QD would be necessary.

Summarizing, it has been obtained a controlled selective nucleation of homogeneous InAs QD into GaAs nanoholes previously formed by DE. A useful consequence of this result is that with the use of a pattern of nanoholes with a fixed depth and density, the size of the QD is directly related to the amount of InAs filling the nanoholes with independence of their density, as opposed to the QD formation by a self-assembling process.

· Optical properties of a single quantum dot

As it has been advanced in the previous section, μPL measurements were performed on the QD formed into the nanoholes. The sample studied corresponds to the AFM image shown in **Figure 4.7** where 1.4 ML of InAs was deposited and further capped by a 100 nm-thick GaAs layer for PL measurements. The measurements were performed using a fiber based confocal microscope with a diffraction limited spot size running at 5 K [78]. As commented, the low density produced by the used patterning process allows the investigation of only one QD at a time, **Figure 4.13**. It has been studied several QD of the type-B family throughout the sample surface (detector cut-off at ~1000 nm) finding similar groups of spectral lines for all of them. Increasing the laser excitation at the WL band edge, the biexciton recombination peak (XX^0) can be easily identified from its superlinear dependence on excitation power, **Figure 4.14**. At the same time, at low energies, several lines arise and dominate the single QD spectrum as the excitation intensity is raised. The relative splittings found among the different μPL lines are characteristic of negatively charged exciton recombination in QD of this size [73]. Yet, this assignment can be further confirmed by measuring the polarization resolved spectrum for each line as shown in **Figure 4.13 (b)**. As expected, the X^0 and XX^0 peaks experience opposite shifts upon 90 degrees turn of the linear polarization analyzer aligned along the [*1-10*] crystal direction. The maximum splitting of Δ_1~38 μeV is due to the anisotropic exchange interaction between electrons and holes in asymmetric QD. Since this interaction is suppressed due to the singlet nature of the singly charged exciton (X^{1-}), this fact can be used to identify its emission peak as shown in the inset of the same figure.

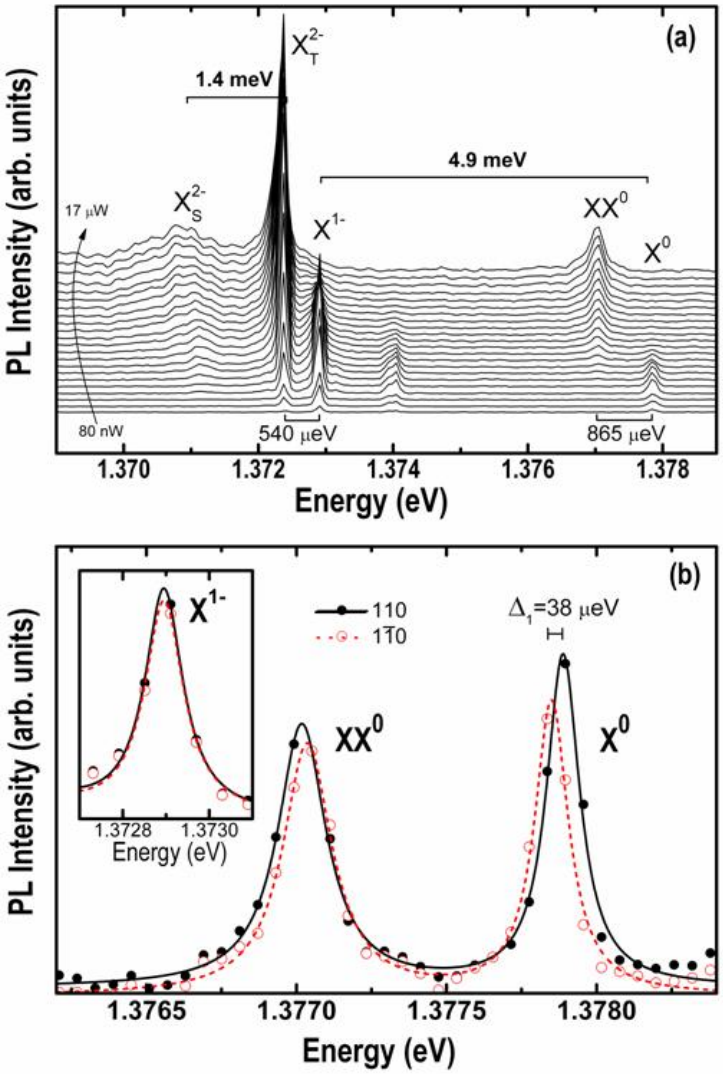

Figure 4.13. **(a)** Micro-PL spectra of a single type-B QD measured for increasing excitation intensities. The emission peaks corresponding to different excitonic species have been identified by their power and polarization behaviour as discussed in the text (S and T mean singlet and triplet, respectively). **(b)** Polarized spectra recorded for the same single QD along perpendicular crystal directions and showing the splitting of the neutral states.

It has to be noticed that the rather small value found for Δ_1 indicates an approximately round in-plane confinement potential which makes these nanostructures interesting for applications based on the generation of polarization entangled photon pairs [79].

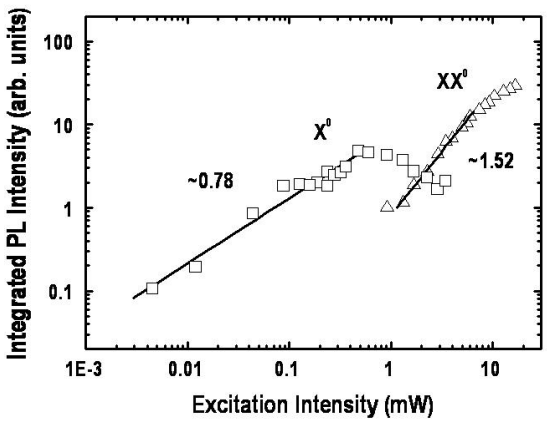

Figure 4.14. L-L plot of the power-dependent μPL integrated intensities for the exciton (X0) and biexciton (XX0) lines. The slopes of the linear fits are indicated.

Finally, to explain the dominant role of negatively charged species recombination in this sample it shall be noted that the templated growth method, as already commented in section 4.3.1, is based on the deposition of metallic Ga droplets. If the crystallization process is incomplete, a number of arsenic vacancies will remain in the surroundings of the QD. These defects are known to produce localized states near the conduction band which can easily transfer their electrons to the QD [80]. Several recent works explain how under selective optical pumping, [81,82] or increasing the excitation power, [83,84] this situation will lead to preferential emission from negatively charged exciton species as it is observed in this study.

4.4.2. Vertical quantum dot molecules (VQDM)

As previously commented in the introduction of this thesis (section 1.1.2), there is a significant interest in using "artificial molecules" formed by two quantum mechanically coupled QD for the realization of quantum gates involving two-quit operations [85]. In such systems, the coupling involves tunnelling of electrons and holes between two adjacent dots separated by a thin intermediate barrier layer of thickness *d*. In particular, it has been observed [86] that for a 4 nm-thick intermediate tunnelling layer, the coupling strength is optimized for the spectroscopic observation of large electron (actually the electron component of the exciton wave function) anticrossing energy splittings [86] (these anticrossing effects account for the exciton wave function hybridization into bonding and antibonding states which are intrinsic effects that arise when a molecule structure is formed (section 1.1.2) [86]). It is, however, technologically challenging to obtain resonant quantum-mechanical coupling due to size, composition, and strain inhomogenities inherent in the MBE growth of QD. In this sense, great efforts have been dedicated to the formation of vertical coupled QD by self assembling processes [87]. The fabrication process using in the literature leading to vertically aligned QD is based on the elastic-stress fields induced by QD from lower-lying layers on the top surface, promoting by further InAs deposition the growth of a second QD above it. By this growth procedure, the possibility of tuning the emission energy of one of the QD at the same time that is maintained unaltered the emission properties of the other, although possible, is difficult to achieve. This tuning effect would permit to build symmetric VQDM, in which the energy emission of both QD forming the molecule is matched, and asymmetric VQDM, in which the energy emission of one QD is blue-shifted or red-shifted respect to the other [86-88]. Apart from a this lack of control in size of the QD forming the VQDM, by a self-assembling process there is an intrinsic inter-dependent nature between the QD size and density that makes difficult the design of QD of a desired size and with a low enough density for its spectroscopic study at the single nanostructure level [89].

For these reasons, we have developed a process that optimizes the growth of coupled structures in vertical arrangement by the use of a low density nanoholes template fabricated by DE. In particular, we have used the already presented ability to obtain size controlled QD in the template to form low density

VQDM with a certain energy configuration control. To do this, after the controlled deposition of InAs in a first layer of nanostructures, a GaAs tunnelling layer was grown for further deposition of InAs material that, by a strain-driven process, define a second layer of nanostructures located on top of the first ones.

Thus, the growth procedure started with the filling of previously formed nanoholes with InAs material. In particular, three different samples with amounts of 1.2, 1.4 and 1.5 ML of InAs were grown at growth conditions as those described in section 4.4. Once formed the first layer of QD (QD_1), a GaAs intermediate layer with a thickness of 4 nm (*d*= 4 nm), was subsequently grown to guarantee a large tunnelling effect as previously commented. The growth of this layer was performed by the ALMBE growth technique [90] at T_s= 450ºC, r_gGaAs= 0.5 ML/s and $BEPAs_4$= $2x10^{-6}$ Torr. At this moment, for completing the molecule structure, a second layer of QD, QD_2, located above the QD_1, was grown by the deposition of 0.9 ML of InAs at the same conditions used for the underlying nanostructures.

Finally, with the aim of studying the optical emission of the resulting QD molecule structures, a 155 nm-thick GaAs layer was grown initially (first 20nm) at T_s= 510ºC and $BEPAs_4$= $2x10^{-6}$ Torr and finished at T_s= 580ºC and $BEPAs_4$= $2x10^{-6}$ Torr. **Figure 4.15** shows a schematics diagram of these samples.

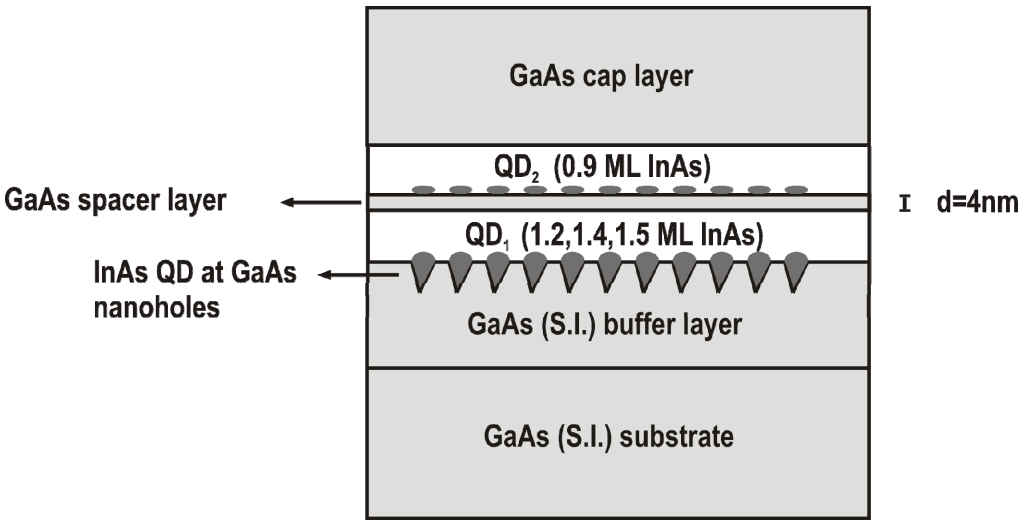

Figure 4.15. Schematic diagram of the samples with vertical QD molecule structures. The first nanostructure (QD1), is formed by depositing 1.2, 1.4 or 1.5 ML of InAs into the GaAs nanoholes previously formed by a nanodrilling process. After growing 4 nm of GaAs spacer layer, a second nanostructure (QD2), is formed on top of QD1 by depositing 0.9 ML of InAs.

TEM images were obtained to establish the real structural configuration of the resulting molecules. In this sense, **Figure 4.16 (a)** and **(b)** shows the corresponding 002 dark field (cross sectional) TEM micrographs to the cases of 1.4 and 1.2 ML of InAs deposited into the nanoholes as QD_1. The presence of InAs material is shown in these figures as bright areas. Accordingly, it can be clearly observed the formation of a double structure that consists of two InAs QD separated by the corresponding WLs that leave in between them a 4 nm-thick GaAs spacer layer. In the case of depositing 1.4 ML of InAs (**Figure 4.16 (a)**),

QD_1 clearly presents a bigger size than QD_2 nucleated on top of it. On the other hand, when 1.2 ML of InAs are deposited (**Figure 4.16 (b)**), QD_1 is similar to its respective QD_2 and comparing to the case of depositing 1.4 ML, it clearly presents, as expected, a lower size.

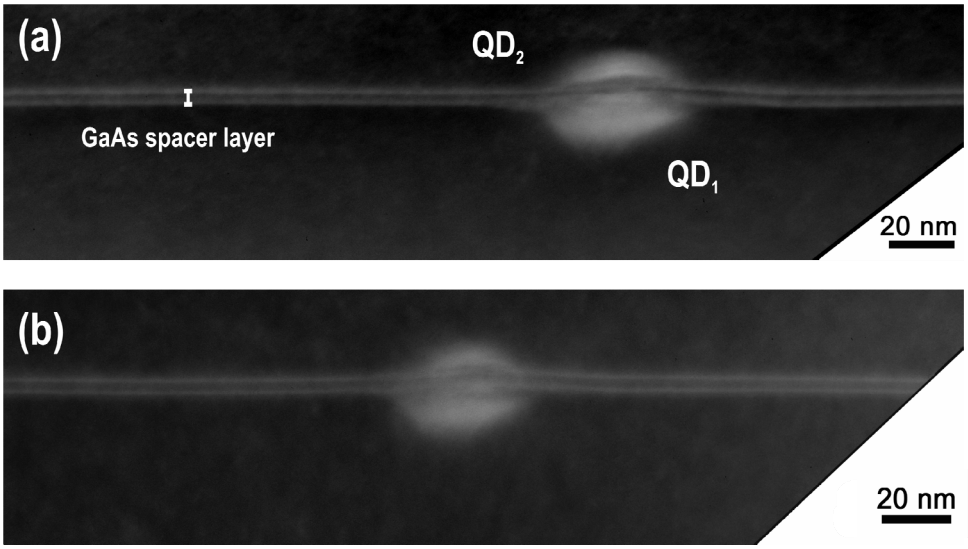

Figure 4.16. **(a)** 002 dark field (cross sectional) TEM micrographs of two vertically aligned QD formed after the deposition of 1.4 ML of InAs into a GaAs nanohole (QD1), the growth of a 4 nm-thick GaAs tunneling layer and a final deposition of 0.9 ML of InAs (QD2). We observe that in this case QD1 is bigger than QD2. **(b)** TEM image of the formed molecules when 1.2 ML of InAs is deposited to form the nanostructure QD1. As a difference with the previous case, it can be clearly observed that QD1 is now closer in size to QD2. (These TEM images were taken at University of Cádiz)

It is noticeable that as a difference of what happens in the strain-driven formation of QD_2, or in general, in a self-assembling process, QD_1 forms at a lower level to the WL, clearly indicating their formation mechanism in the preferential nucleation of InAs into previously fabricated GaAs nanoholes.

According to these results, the aimed tuning effect on the size of QD_1 by the use of nanoholes, has been successfully obtained. On the other hand, despite this change in size of QD_1 the strain profile seems to produce the nucleation of QD_2 with similar dimensions in all cases. This effect could be ascribed, see results in section 4.7.1, to a quick saturation of the QD_2 equilibrium size when the GaAs tunnelling layer is as narrow as 4 nm and the strain profile from the underlying InAs is, therefore, quite large. In this sense, it has to be noticed that a variation of the nanostructures interlayer thickness at the same time that the amount of InAs is maintained, could also provide a tuning effect on the size of QD_2.

Concerning the optical properties of these paired structures, **Figure 4.17** shows the PL signal for the three different samples grown. In particular, the black, red and blue lines in the figure correspond to the 1.2 ML(QD_1)/4 nm/0.9 ML(QD_2), 1.4 ML/4 nm/0.9 ML and 1.5 ML(QD_1)/4 nm/0.9 ML(QD_2) molecule structures respectively. The nomenclature used indicates the amount of InAs deposited inside the nanoholes in the first term (QD_1), the tunnelling GaAs layer thickness in the second and the amount of InAs deposited for the top surface QD strain-driven formation in the third (QD_2). The presence of two main convoluted peaks

can be observed in all these three PL emissions. By measuring their excitation power dependence, their origin can be ascribed to the formation of two different QD families.

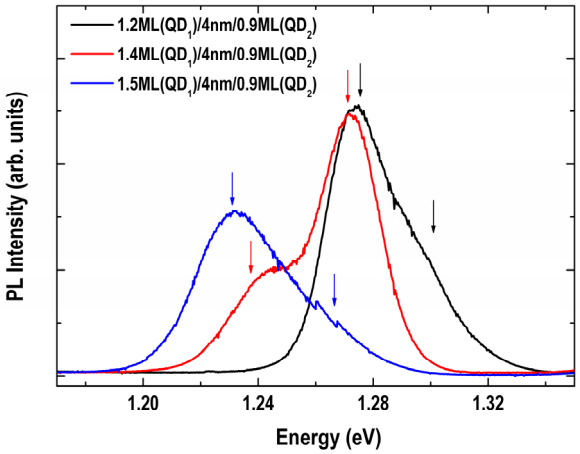

Figure 4.17. Photoluminiscence spectra for the three different vertical QD molecules grown. In black, red and blue lines it is represented the 1.2 ML/4 nm/0.9 ML, 1.4 ML/4 nm/0.9 ML and 1.5 ML/4 nm/0.9 ML molecule structures respectively. The nomenclature used indicates the amount of InAs deposited inside the nanoholes in the first term, the tunneling GaAs layer thickness in the second and the amount of InAs deposited forming the QD2 in the third. Arrows in the figure point out the two families of QD for each structure.

Combining these optical emission results with those obtained by TEM structural analysis, it can be established a direct correspondence of the different emission peaks to the recombination of carriers at the upper and lower QD of the molecule structure, QD_2 and QD_1 respectively. **Figure 4.18** shows as filled areas the three different PL emissions that would correspond to the QD_1 family in the three molecule structures grown. As expected, the effect of the different amount of InAs deposited makes the emission energy of the QD_1 to be tuned in a wide range.

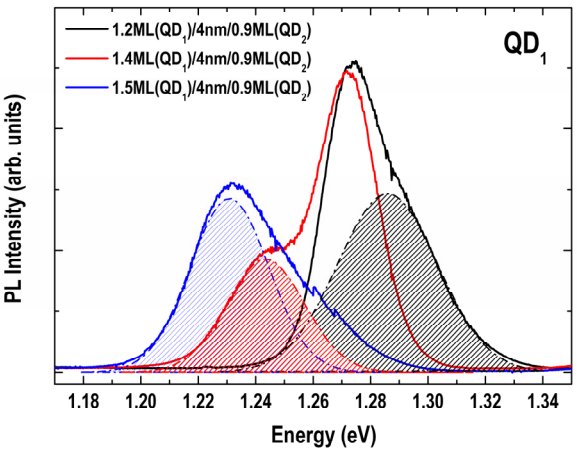

Figure 4.18. PL emission that can be ascribed to the QD_1 family in the three molecule structures grown, are represented as filled areas.

In a similar way, **Figure 4.19** shows the emission of the remaining three PL peaks that would come from the QD_2 family in these structures. It can be observed that in this last case the emission peaks are located almost at the same energy, indicating, as it has been previously advanced, that the size of these QD_2 remains unchanged despite of the different amount of InAs underneath deposited.

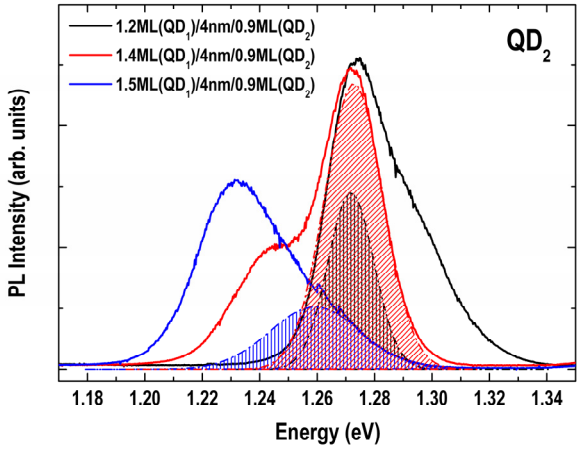

Figure 4.19. PL emission that can be ascribed to the QD2 family in the three molecule structures grown, are represented as filled areas.

Table 4.1 lists the different values of the emission peaks energies ascribed to QD_1 and QD_2. The tendency of the emission energy for QD_1 is indicated with an arrow in the table.

InAs (ML) QD_1	InAs (ML) QD_2	Peak energy (eV)	
		QD_1	QD_2
1.2	0.9	1.286	1.272
1.4	0.9	1.243	1.272
1.5	0.9	1.230	1.260

Table 4.1. Emission peaks energies ascribed to QD1 and QD2. The QD1 emission energy increases as a function of the amount of InAs deposited. An arrow in the table accounts for this tunning effect.

In summary, as a conclusion of these results, it can be stated that by varying the amount of InAs deposited at a nanohole template formed by DE, emission of the first layer of QD can be tuned for obtaining symmetric or asymmetric vertically coupled quantum molecules, As in previous experiments using DE patterning process, the density of QD molecules is low enough ($2x10^8$ cm^{-2}) to permit their integration as active elements in photonic microcavities and perform spectroscopic studies at the single nanostructure level.

· Schottky diode structures for electron injection in VQDM

For a deep study of the quantum coupling properties of a single VQDM it is necessary to have the possibility of establishing a controlled mechanism for carrier injection into the nanostructures. With this purpose, this section shows a sample growth design and the technological processes followed for obtaining a n-intrinsic Schottky photo-diode structure that permits to study the emission properties of the nanostructures, at the same time that is controlled the injection of electrons into them. This effect is achieved by applying an external electric field to the sample that varies the relative position of the electron energy levels of the nanostructures with respect to the Fermi energy of the whole structure. The operation of such a device is outlined in **Figure 4.20**.

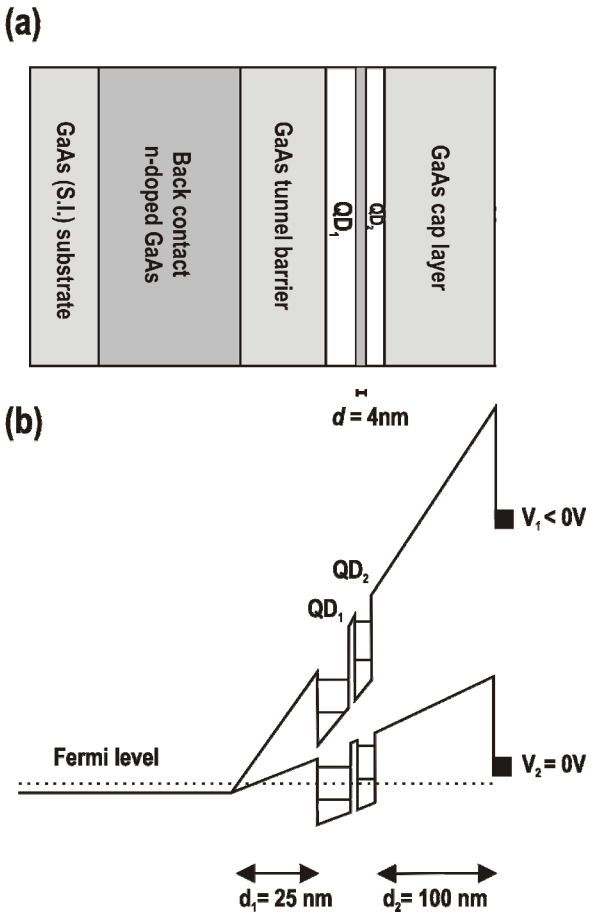

Figure 4.20. (a) Schematic diagram of the samples with embedded vertical QD molecules for n-intrinsic Schottky diode operation. **(b)** Diagram of the conduction band of the structure under two different polarization voltages.

In particular, designing the sample geometry, d_1 and d_2 in the figure, and known the Schottky barrier, U_{Sch}, it is possible to engineer the bending of the conduction energy band in the structure (**Figure 4.20 (b)**). This effect can be assumed to be linear and it is called "*Law of the lever*" in analogy to the Archimedes's Law.

$$E = \left(\frac{d_1}{d_1 + d_2} \right) x\, e\, x \left(U_{Sch} - V_g \right) \quad (eV) \qquad \textbf{Equation 4.1}$$

Equation 4.1 accounts for this lever effect where "e" is the absolute electron charge value and V_g the external applied polarization voltage.

Figure 4.20 (a) shows a schematic diagram of the samples grown for n-intrinsic Schottky photo-diode operation. First, a 200 nm-thick n-doped GaAs buffer layer was grown on a semi-insulating GaAs (001) substrate. Then, a 25 nm-thick non-intentionally doped GaAs layer (d_1 in **Figure 4.20**) was grown to provide an effective carrier tunnelling channel to the QD of the first layer (QD_1 in **Figure 4.20**). The active layer, the VQDM, is identical to that previously described reproducing the same growth protocol and the same growth conditions. Once formed these 1.2 ML(QD_1)/4 nm/0.9 ML(QD_2), 1.4 ML(QD_1)/4 nm/0.9 ML(QD_2) and 1.5 ML(QD_1)/4 nm/0.9 ML(QD_2) molecule structures, a cap layer consisting of a 155 nm-thick non-intentionally doped GaAs layer was finally grown (d_2 in **Figure 4.20**).

For the fabrication of the n-intrinsic Schottky photo-diode, different technological steps involving UV-lithographic, chemical etching and metallization processes were followed (**Table 4.2**) [91].

	Step	Description
1	Optical Lithography	Definition of ring-shaped windows in a photoresinlayer deposited on the sample for the fabrication of Ohmic contacts after chemical etching
2	Chemical etching	Chemical etching of GaAs through the windows opened in step 1. This process is performed up to the n-doped GaAs is reached, using $H_3PO_4 : H_2O_2 : H_3O$ (2:1:26) with a GaAs etching rate of 3 nm/s
3	Ohmic contact	Deposition of metal layer for ohmic contact at the n-type layer of the structure. n-type: Au (10 nm) / Ge (15 nm) / Au (100 nm) Oxygen plasma stripper at 50 W during 1 min. Annealing under N_2 and H_2 at 275ºC during 1 min and at 350ºC during 3 min.
4	Lift-Off	Resin layer dissolution: (Acetone + Ultrasonics) + Isopropyl + H_2O
5	Optical Lithography	Definition of circle-shaped windows in a photoresin deposited on the sample. These windows will define the Schottky contacts on the top surface in between the Ohmic contacts.
6	Schottky contact	Deposition of metal layer for semi-transparent contact: Cr (5 nm) / Au (5 nm)
7	Lift-Off	Resin layer dissolution: (Acetone + Ultrasonics) + Isopropyl + H_2O
8	Encapsulation	Au wiring to an alumina platform by ball-bonding

Table 4.2. Technological steps followed for the fabrication of a n-intrinsic Schottky photo-diode.

Figure 4.21 depicts a schematic illustration of the final device configuration. In a first process the ohmic contact at the underlying n-doped GaAs layer (back contact) is built by electron-beam deposition of a trilayer composed of Au (10 nm) /Ge (15 nm) /Au (100 nm) and posterior annealing process under N_2 and H_2 atmosphere at 350ºC during 3 min. In a second step, to make possible the photo-emission study of the nanostructures, a semi-transparent Schottky contact is fabricated by the electron-beam deposition of a double structure consisting of 5 nm of Cr on top of 5 nm of Au.

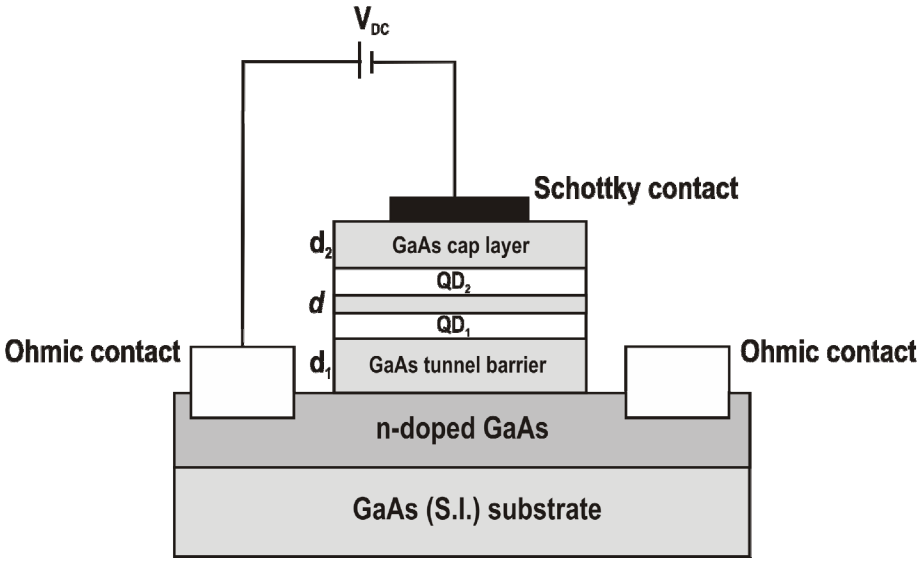

Figure 4.21. Schematic diagram of the n-intrinsic Schottky photo-diode device. d_1, d_2, and *d* represent the thickness of the GaAs tunnel barrier, GaAs cap layer and GaAs intermediate layer, respectively.

A photograph of the device obtained is shown in **Figure 4.22**. Up to nine devices are fabricated in a piece of sample of 7 mm x 7 mm. Once fabricated the devices, these are wired by ball-bonding to a piece of alumina with well-defined metallic contacts.

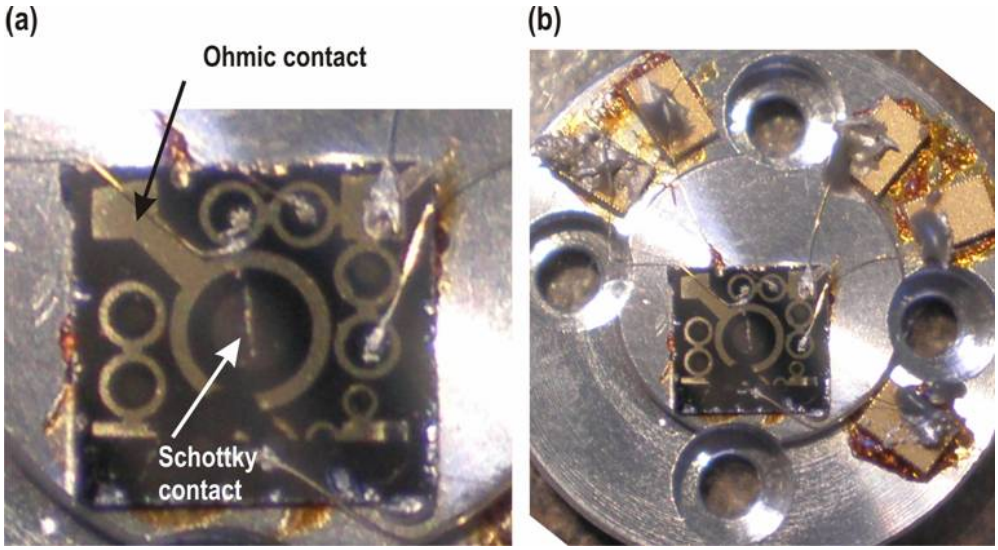

Figure 4.22. Photographs of the final Schottky photo-diode devices.

A typical current-voltage characteristic or I-V curve of the as-fabricated diodes at low temperature (T= 30 K) is shown in **Figure 4.23**. In this case, the Schottky contact was connected to ground while a range of voltages (from -2.1 to 0.27 V in this case) was applied to the back contact. It can be observed that the current at reverse bias is negligible at -2 V. Under forward bias a value of 0.2 V for U_{sch} is obtained.

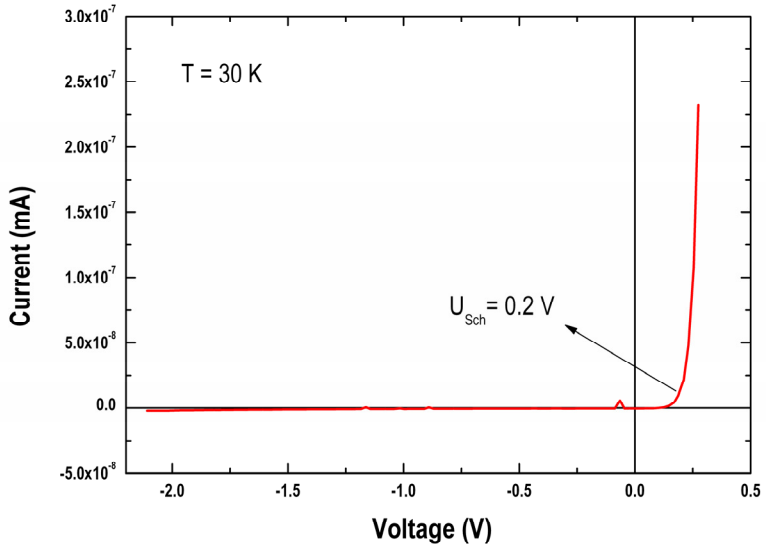

Figure 4.23. Typical current-voltage characteristic of the n-intrinsic Schottky photo-diode device.

These conduction properties show these devices suitable for an optimized electron injection in the VQDM in a quite wide range of applied voltages facilitating the study of their quantum coupling nature in the μPL characterization experiments.

4.4.3. Quantum posts (QPs)

Recently, a new III-V nanostructure resembling a vertical QWr (larger dimension along the growth direction) called nanorod or Quantum Post (QP), the name usually depends on the growth procedure, has been widely studied in the literature due to its unique technological potential. Nanorods are usually fabricated by VLS technique and have opened up new horizons in the fabrication of quantum schemes that integrate QD, QWr and p-n junctions [92,93]. However, one of the major problems with these nanorod and nanowire structures has been their positioning and contacting to electrodes [94]. As an alternative, a novel approach based on the self-assembling growth of height-controlled (In,Ga)As QPs embedded within an MBE grown heterostructure, has been recently studied [95]. Comparing to the nanorods, since these nanostructures are self-assembled and embedded into a heterostructure, they are potentially free of surface traps [96].

As previously described, a QP is a short vertical QWr connected to a seed QD. The height of this QP can be controlled with nanometer precision up to 60 nm [97], and the aspect ratio can be engineered. By using these properties, the potential of such a structure has been probed in recent publications by the demonstration of an exciton memory cell using QPs [97]. In particular, it has been obtained that in this system, both, electrons and holes, remain localized within the same nanostructure in which they are generated, maintaining the phase between the electron and the hole. By applying an electric field along the QP axis, electrons and holes can be spatially separated toward opposite ends of the nanostructure to

produce a large electrostatic dipole moment and a large increase in the radiative lifetime of the exciton. In this device, the stored excitons can be reconverted into photons simply by switching a gate voltage after a defined time. In this sense, storage times exceeding 30 ms at 7 K have been demonstrated [97].

For further detailed studies on individual QP, is important to develop a growth technology that will permit to combine these nanostructures with an optical microcavity. This way, an increase of the light extraction and a significant improvement of the signal/noise ratio in electron-hole mutual spin coherence experiments, could be obtained. Also, the large dipole moment associated with the hole and the electrons, makes the QP a very attractive structure for reaching the strong coupling regime in coupled QP-optical microcavity devices.

As already presented in this chapter, DE has arisen in the formation of new nanostructures framework as an innovative growth technique that as a difference to a self-assembling process, has permitted the formation of QD and VQDM with a certain control of size at the same time that a low density of $2x10^{-8}$ cm^{-2} is maintained. These properties make this technique suitable for an optimal QP fabrication and integration in more advanced devices. In particular, the formation of QPs is a natural step forward once QDM are formed. So, following the growth procedure explained in section 4.4.2, DE was used in this work to tune the size of a seeded QD that would permit the further definition of the QP lateral dimensions. The height of such structures, in a similar protocol followed in already published works [98], will be controlled by the growth of a designed number of stacked QD layers. As advanced the density of nanostructures obtained by this technique will be low enough, $2x10^{-8}$ cm^{-2}, for permitting further single QP characterization.

The structure grown is schematically illustrated in **Figure 4.24** and **Figure 4.25 (a)**.

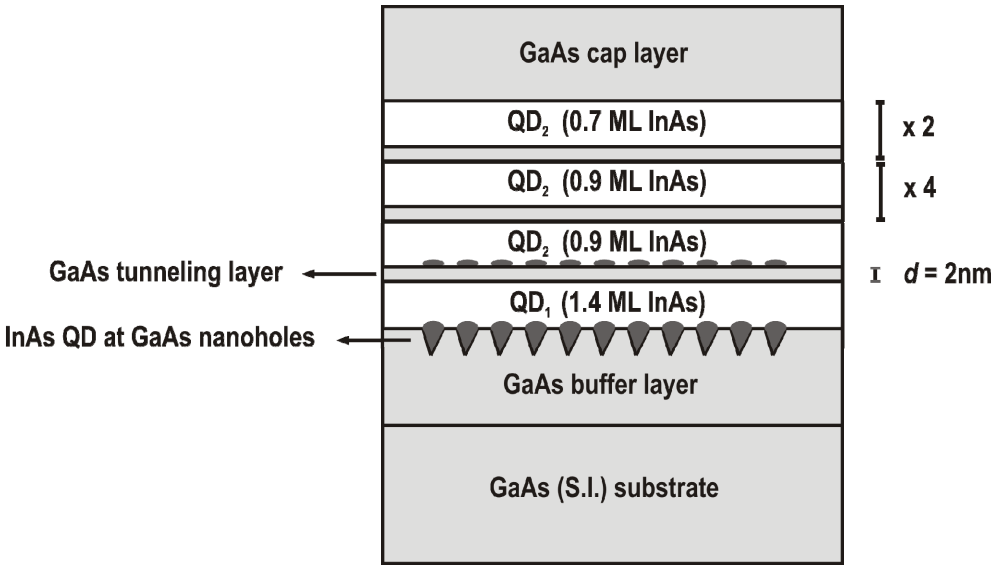

Figure 4.24. Schematic diagram of the Quantum Posts grown in this work

On a semi-insulating GaAs (001) substrate a 200 nm-thick n-doped GaAs buffer layer was firstly grown. At this moment, a nanohole template is formed by DE and 1.4 ML of InAs is deposited. The growth sequence and conditions are identical to that presented for the formation of a VQDM with the difference that the process for capping a new strain-driven InAs nucleation is here repeated 7 times. As a difference, in this case a 2 nm-thick non-intentionally doped GaAs buffer layer separates the seed QD to the following nanostructure formed on top; this narrower GaAs layer in between the InAs nanostructures is aimed to ensure a good uniformity of material within the QP. Thus, using the nomenclature previously defined for the VQDM, the QPs are formed by an initial 1.4 ML/ 2 nm/ 0.9 ML structure that is further followed by a number of 2 nm/ 0.9 ML repeated steps. Due to the accumulation of strain at the top surface with increasing steps, the last two InAs nucleation processes in this work, consisted of the deposition of a lower amount of InAs, 0.7 ML that ensures a more uniform diameter along the structure.

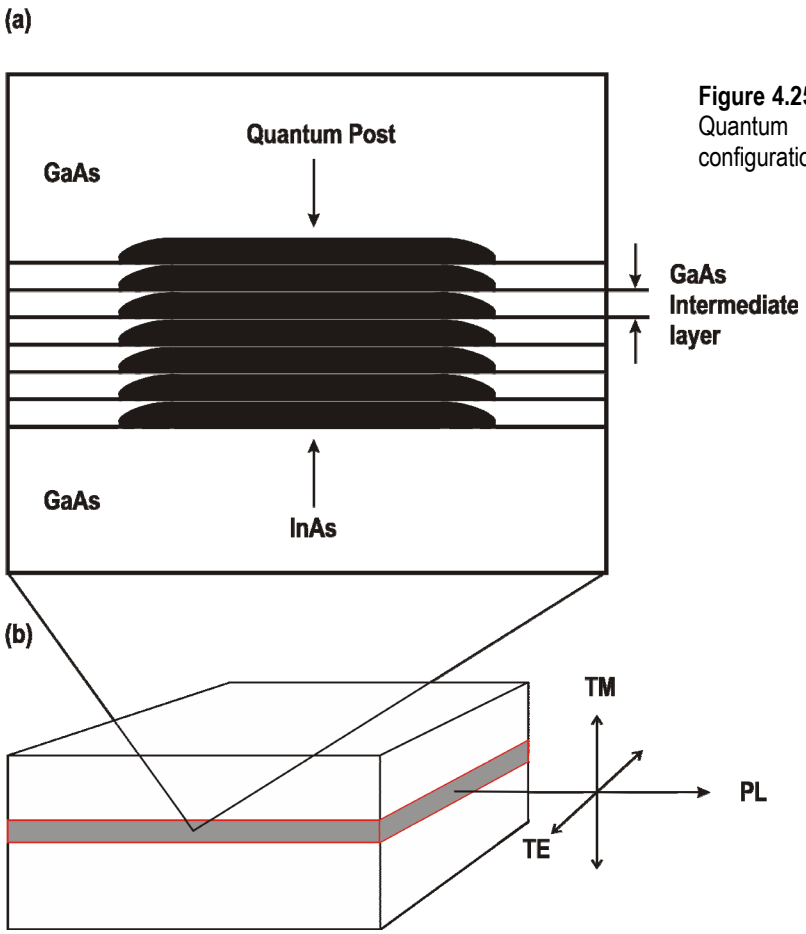

Figure 4.25. (a) Schematic diagram of a Quantum Post. **(b)** PL-measurement configuration.

As a good test to study the real aspect ratio (height/base width ratio) of these QP it has been performed preliminary measurements of their optical polarization properties.

· **PL polarization measurements**

Generally, polarization of optical transitions in a quantum structure depends on the confinement direction because of the selection rules for the optical transitions [99]. Since the ground state of a QD is the heavy-hole exciton state, light polarization of the ground-state PL is perpendicular to the confinement direction.

If a change in the aspect-ratio of a QD is induced [100,101] as it is the case of forming QPs (**Figure 4.25 (a)**), the optical polarization properties are varied according to their new confinement properties [95]. For this reason, linear-PL polarization spectra were measured from the cleaved and uncoated edge surface of the QPs sample. This way, the PL intensity corresponding to the transverse-electric (TE) and transverse-magnetic (TM) modes can be measured via setting an analyzer along the in-plane and growth directions respectively, experimental configuration in **Figure 4.25 (b)**.

Figure 4.26 shows the maximum of the QP PL peak as the analyzer is rotated 360º in the plane parallel to the edge of the sample (red line connecting red squares). As a comparison values for self-assembled QD are also represented (blue line connecting blue squares).

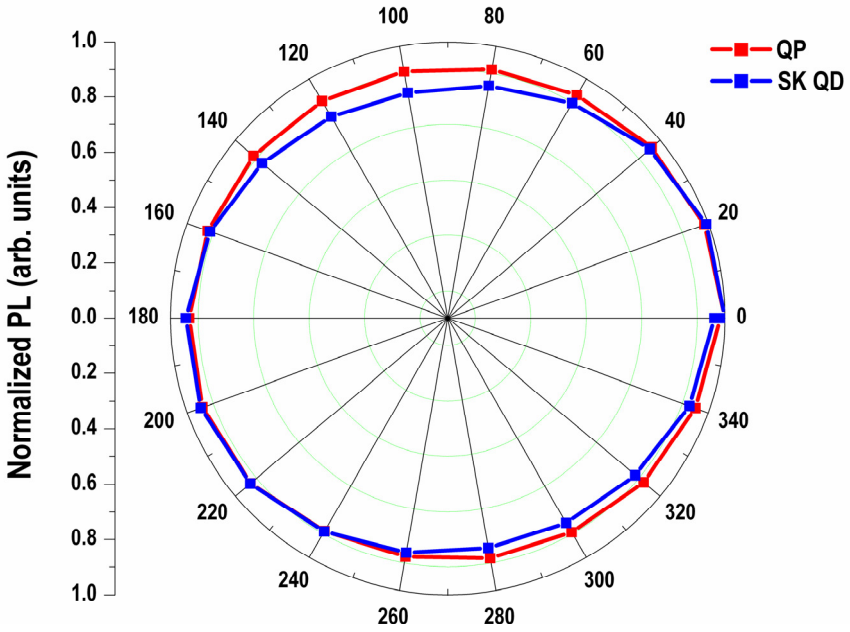

Figure 4.26. Maximun of the QP PL peak as the analyzer is rotated 360º in the plane parallel to the edge of the sample. The case of having SK QD as active nanostructures is also depicted for comparison.

These data show that the difference of intensities between the minima of the curves that correspond to the TM component and the maxima that in turn would correspond to the TE component is in average 14 % for the QD and a reduced 6 % for the QPs. This effect means that a change of the aspect-ratio in the QP structures has been produced. DE technique is reaffirmed therefore, as a useful fabrication method for

obtaining low density vertical structures with a certain control of height and most important, diameter, from the seeded QD. However, for a better understanding and a useful application of these structures, further structural (TEM) and optical (μPL) characterization is necessary.

4.4.4. Lateral quantum dot molecules (LQDM)

As commented in section 1.1.2, the formation of different distributions of QD in close proximity permits a precise study of coupling and coherence that is strictly necessary for the creation of future functional units in the field of quantum computing and communication [102]. In this way, the growth of vertically stacked self assembled QD, section 4.4.2, has been deeply studied during the last years allowing the direct observation of controlled coupling in QDM [86]. For applications, however, the development of a lateral configuration of coupled nanostructures is highly desirable as it would extend the coupling to two dimensions and it would facilitate the gating technology. Experimentally, the lateral coupling of two adjacent QD has been recently demonstrated [103]. In this work, the fabrication method is based on the growth selectivity of QD into previously in situ etched nanoholes [104]. In a simple similar way, DE technique has emerged, as already presented in this chapter, as a straightforward *in situ* fabrication method that permits to obtain, in a self-assembled way, templates of low density nanoholes on GaAs substrates. A new use of these templates, subject of this section, is the development of a growth procedure to form In(Ga)As quantum dot molecules positioned in a lateral arrangement along the GaAs [*110*] direction. In particular, by using the low density, $2x10^8$ cm^{-2}, GaAs nanohole template and by changing the arsenic pressure at which InAs is grown on it, the possibility to select the formation of single QD or QD pairs inside each of the nanoholes is demonstrated.
The emission properties of these QD pairs, both of the ensemble (macroPL) and at the single nanostructure level (μPL) will be shown in next sections. The results show signatures of lateral coupling between the QD forming the pair.

In this case, as in the growth of the rest of nanostructures performed by the DE technique, the growth procedure starts by an initial GaAs surface flattening consisting of the growth of a 0.5 μm-thick undoped buffer layer at T_s= 580ºC by MBE. Once obtained an optimal GaAs surface, the substrate temperature T_s is decreased to 500ºC and the nanoholes template formation is performed. On this kind of patterned surface, 1.5 ML of InAs is deposited using two different As_2 pressures while keeping constant the rest of growth parameters. $BEPAs_2$ used was $3.5x10^{-7}$ Torr and $1x10^{-6}$ Torr. InAs was deposited following a growth sequence consisting of 0.1 ML at a growth rate of 0.05 ML/s followed by a pause of 2 s under the used As_2 flux. The substrate temperature was maintained during the InAs deposition process at 510ºC. A (2x4) surface reconstruction was always observed during InAs deposition at the used As_2 pressures.

Once the InAs is deposited, a 100 nm-thick cap layer was grown. It consisted of an initial 20 nm-thick GaAs layer grown at T_s= 510ºC under As_2 at $BEPAs_2$= 1x10^{-6} Torr and a final 80 nm-thick GaAs layer at conventional GaAs growth conditions, T_s= 580ºC and $BEPAs_4$= 2x10^{-6} Torr. Finally, on the top surface, the process for obtaining uncapped nanostructures on the nanoholes template was repeated for AFM topographic measurements.

Figure 4.27 shows AFM images corresponding to the deposition of 1.5 ML of InAs into the formed GaAs template at the two different As_2 pressures used. In particular, **Figure 4.27 (a)** shows the nucleation result that is obtained when the lower As_2 pressure ($BEPAs_2$= 3.5x10^{-7} Torr) is used during InAs deposition. It can be observed that a single QD is nucleated inside each of the nanoholes. The single QD occupancy is around 95%. In the inset of this figure a 0.5 µm x 0.5 µm 3D AFM image shows in detail one of these single QD that naturally resembles those obtained in previous sections. A different InAs nucleation behaviour is observed in **Figure 4.27 (b)**; in this case, by using the higher As_2 pressure ($BEPAs_2$= 1x10^{-6} Torr) during InAs deposition, QD pairs aligned along the GaAs [*110*] direction are formed inside each of the GaAs nanoholes. The occupancy of QD pairs for this case is around 98% indicating a highly selective nucleation process at the nanoholes. Again, the inset of this figure shows one of the QD pairs in a 0.5 µm x 0.5 µm 3D AFM image.

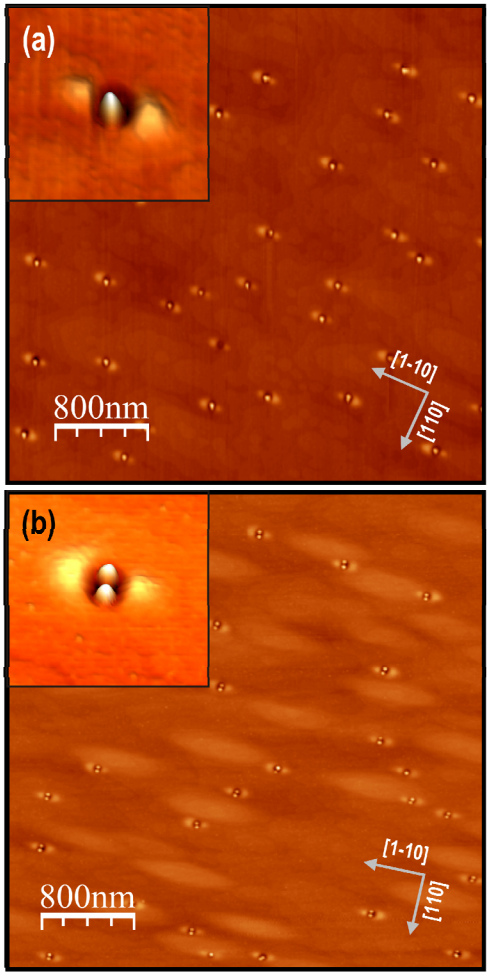

Figure 4.27. (a) 4 µm x 4 µm AFM image showing single QD into GaAs nanoholes after the deposition of 1.5 ML of InAs at BEPAs2 = 3.5x10-7 Torr. The inset shows a detailed 3D image of a single QD. **(b)** 4 µm x 4 µm AFM image showing QD pairs formed into GaAs nanoholes after the deposition of 1.5 ML of InAs at BEPAs2 = 1x10-6 Torr. The inset shows a detailed 3D image of a QD pair.

In **Figure 4.28** detailed 0.25 µm x 0.25 µm 3D AFM images for the initial nanohole, single QD and QD pair structures, are shown. At their right, corresponding profiles along the GaAs [*110*] direction are also shown. The nanoholes, as already commented in previous sections, are elongated structures along the GaAs [*110*] direction with dimensions along this direction typically of 95 nm (**Figure 4.28 (a)**). It has to be noticed that experiments reproducing the same growth conditions for the InAs nanostructures formation but without opening the In cell were performed and no significant differences in the dimensions of these nanoholes were observed.

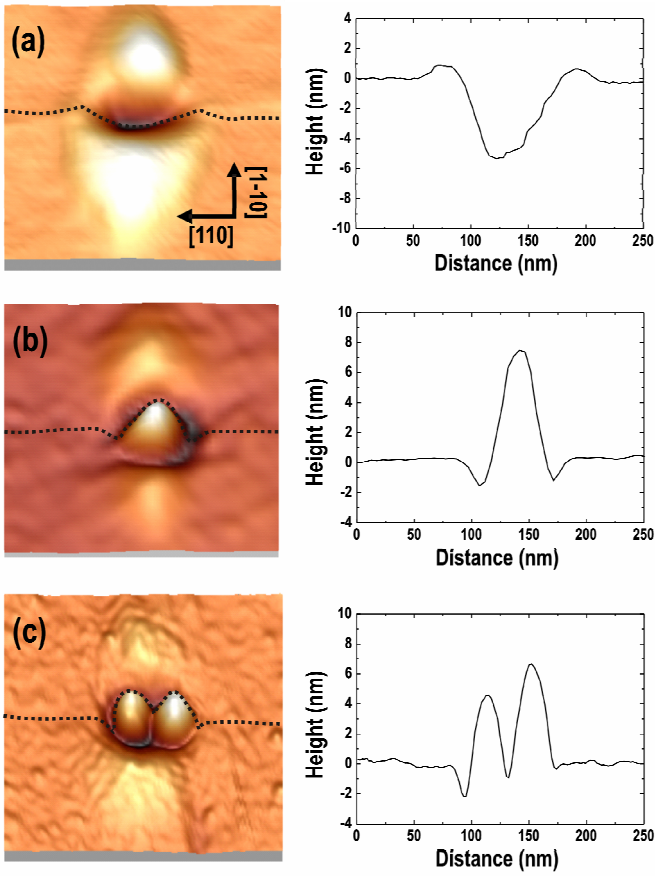

Figure 4.28. 0.25 µm x 0.25 µm 3D AFM images corresponding to: **(a)** the initial GaAs nanohole, **(b)** single quantum dot occupancy at the nanohole and **(c)** QD pair formation. Respective profiles of the nanoholes, single QD and QD pairs are shown on the right.

Although AFM tip convolution effects at these small holes impede any possible facet identification inside them, it is expected, according to their orientation, that the lateral walls would be mainly B-type (As-terminated) facets with steps along [*110*] direction. In the case of single QD at the nanoholes (**Figure 4.28 (b)**), these nanostructures show mean diameter of 58±3 nm and height of 7.4 nm (height fluctuation of ±11%), both quantities referred to the flat surface plane. In the case of QD pairs formation (**Figure 4.28 (c)**), systematic differences for QD heights are observed into the pairs; this effect permits to calculate two different height distributions, as represented in **Figure 4.29**, with average values of 5.3 nm ±17% and 6.6 nm ±24%. It can be also observed in the QD pairs that the separation edge to edge between adjacent QD

is practically zero within AFM resolution. A mean value of 37±4 nm is obtained for their diameter and peak to peak separation. According to previous reports on QD molecules [104] this QD peak inter-distance is short enough to potentially observe quantum coupling phenomena.

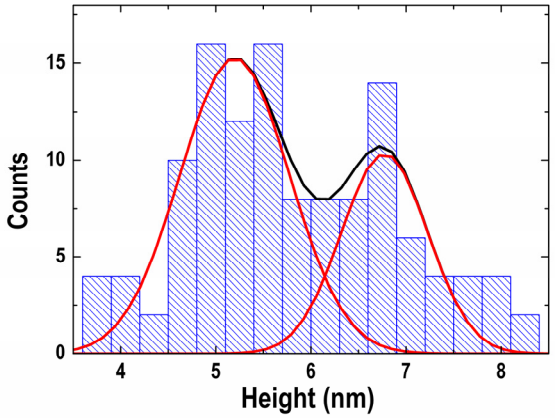

Figure 4.29. Distribution of QD heights in the QD pair sample.

It has to be noticed that, as clearly observed in **Figure 4.28 (b)**, single QD at the nanoholes are larger in size than those forming the pairs. However, it has been observed that this size effect does not lead to a different PL peak energy (**Figure 4.30**). A similar QD PL energy emission in spite of size differences reflects that single QD and QD pairs have a different In(Ga)As composition that would be explained by a different Ga and In filling ratio at the nanoholes for the two different As_2 pressures used in this work. In this sense, previous works have shown that the change of reactivity of the different facets with arsenic pressure causes changes in the incorporation rates of the element III atoms [77,105]. Thus, at the lower As_2 pressure, the incorporation of Ga would be more efficient at the nanoholes inducing the formation of high Ga content In(Ga)As single QD [45]. Altogether, it seems that the role of arsenic pressure on the nucleation of either one or two QD inside otherwise identical nanoholes would be a change of Ga/In intermixing leading to the formation of QD with different composition and equilibrium size. The final result is that for the same nanoholes profile, one QD (larger size, higher Ga content) or two QD (smaller size, lower Ga content) are nucleated at the nanoholes.

· Optical properties of the ensemble of QD pairs

The already commented PL emission of the lateral QD pairs is shown in **Figure 4.30**. In particular, for comparison, the normalized ground state PL from the QD and the QD pairs as a function of the excitation power are shown in **Figure 4.30 (a)** and **(b)**, respectively. The low excitation powers used in these experiments (P_0= 0.03 mW) avoid any emission from excited states as seen by their linear dependence with the integrated PL intensity [106]. In the case of single QD, **Figure 4.30 (a)**, it is observed a peak at 1.175 eV with a FWHM of 42 meV. On the other hand, for paired nanostructures, **Figure 4.30 (b)**, the emission, centred at 1.18 eV, presents a broader FWHM of 63 meV at P_0 and an asymmetric band broadening with increasing excitation power. This asymmetric effect occurs at the high-energy side of the

PL band and is attributed [106,107] to carrier redistribution between small and large QD in the pair. As excitation power increases, the initial emission from large QD saturates and carrier recombination increases in small QD (with emission at higher energies).

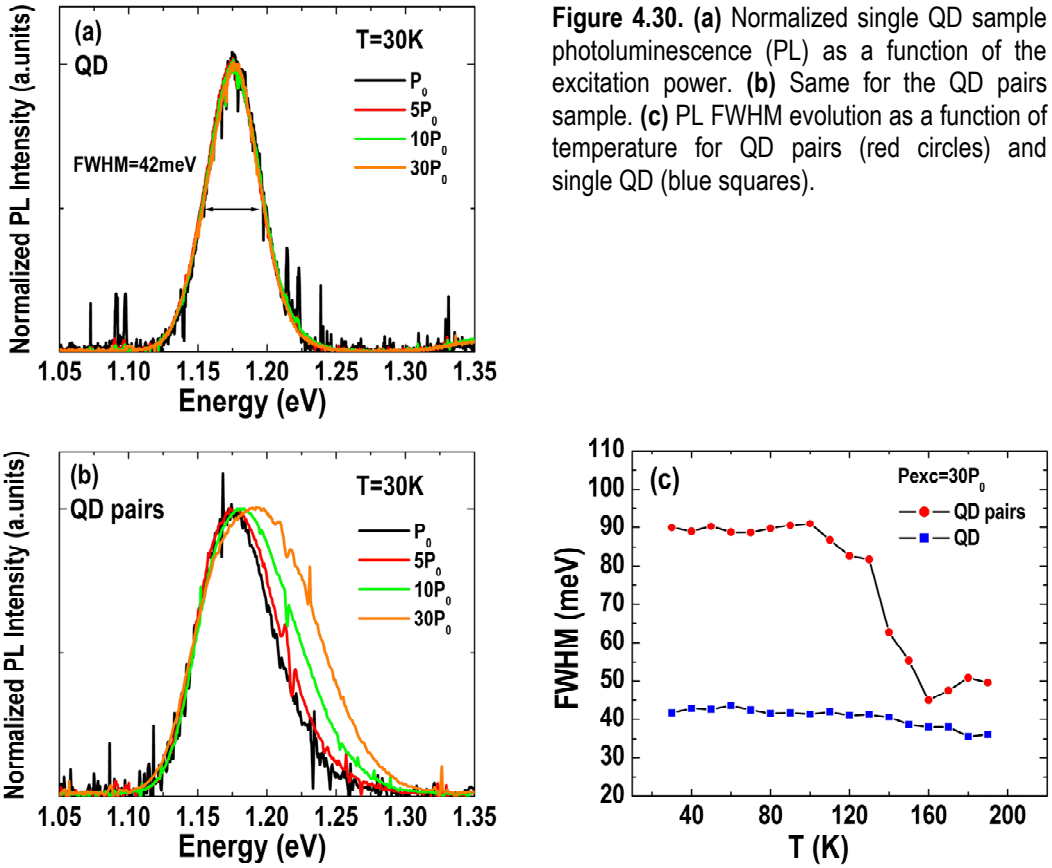

Figure 4.30. (a) Normalized single QD sample photoluminescence (PL) as a function of the excitation power. **(b)** Same for the QD pairs sample. **(c)** PL FWHM evolution as a function of temperature for QD pairs (red circles) and single QD (blue squares).

Additional information on the carrier transfer between QD can be derived from the temperature dependence of the FWHM for the ground state as shown in **Figure 4.30 (c)**. In this new figure, the PL FWHM at P_{exc}= $30P_0$ from QD pairs (red circles) can be compared to that from isolated QD (blue squares). In both samples, thermally activated carrier redistribution from the QD towards the wetting layer and barrier is expected [108]. This phenomena accounts for the decrease of the FWHM of PL signal at ~130 K. However, for the QD pairs a clear change of the slope initiates at 90 K which can not be explained within this framework. When the QD are close enough to each other (as it is the case in the QD pairs), a new mechanism for carrier distribution that is not present in the case of single QD is activated. According to previous works [106,107] this must be related to carrier tunnelling, that would be the cause of the charge redistribution between the QD in the pairs. These PL results related to emission lineshape dependence with excitation power and FWHM evolution with T can be considered as a signature of quantum coupling in the QD pairs. However, further optical studies on individual LQDM pairs are necessary to firmly establish the existence of QD molecules in this system.

· Optical properties of a single LQDM as a function of a lateral electric field

As it was previously introduced for VQDM, for a deep study of the quantum coupling properties of a single QD pair is necessary to carry out μPL characterization experiments in which it is possible to establish a controlled carrier injection into the nanostructures by applying an electric field. As the QD are now laterally aligned, the fabrication technology is simplified. In particular, it is possible to build metallic contacts at the surface plane with the nanostructures to be studied located in between them. **Figure 4.31** shows optical microscopy and AFM images of the contacts arrangement in the sample. By using this configuration, a controlled flow of carriers is established along a nanostructures channel via the supply of a certain voltage difference into the metallic contacts.

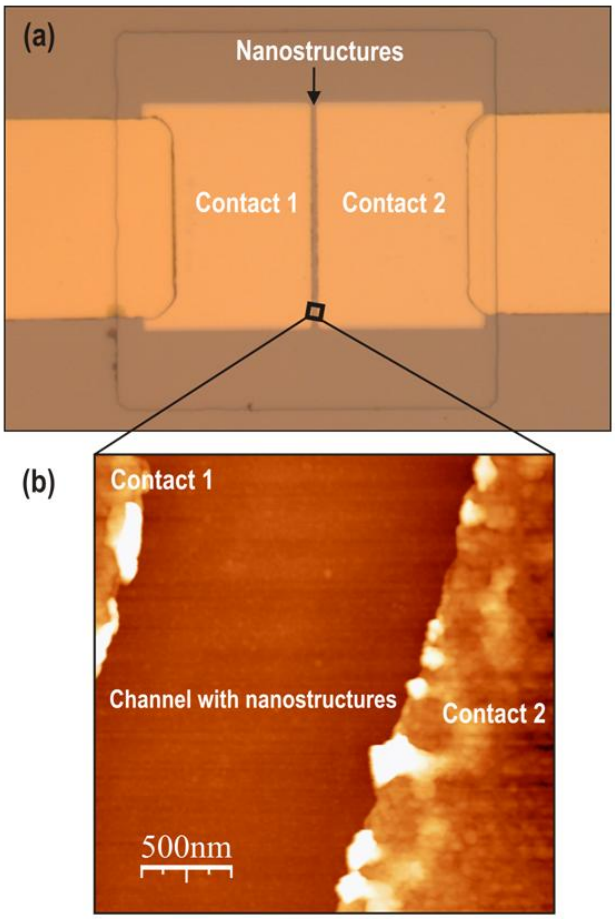

Figure 4.31. Optical microscopy **(a)** and AFM **(b)** images of the device built for a lateral injection of carriers to the nanostructures.

The most relevant features from the point of view of quantum tunnelling phenomena can be investigated analyzing the energy dispersion of individual micro-PL emission lines as a function of the applied voltage. The result of such experiment is shown in **Figure 4.32**. The upper panel represents a full sweep of the external gate from negative to positive bias. The evolution is approximately symmetric around zero due to the also symmetric contact configuration. At very large bias, no electrons are allowed in the conduction band due to tunnelling out to the barrier. Therefore, the emission lines are quenched in this range. Around

zero, the number of trapped charges is maximum and the emission consists of broader lines associated to multiply charged excitons. In the region in between, the charge configuration changes in a one by one basis as reflected by the clear jumps of the emission energy following a typical Coulomb blockade ladder. [109] In our case, since two QDs are present, the line multiplicity is doubled if compared with a single QD, but the charging dynamics remain unaffected indicating the lack of quantum tunnelling in this case.

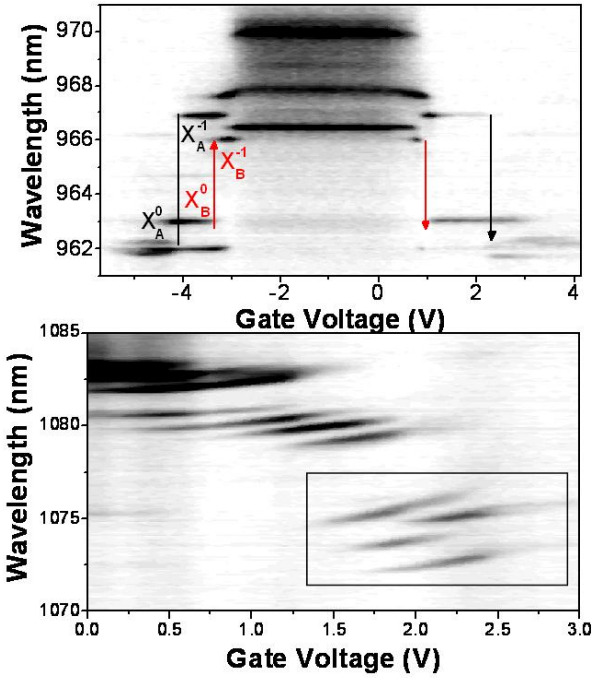

Figure 4.32. Upper panel: full sweep of the external gate from negative to positive bias in a QD pair. Lower panel: evolution in the positive bias range for a different QD pair. The highlighted region shows four lines which anticross each other on changing the electric field.

On the lower panel, the evolution in the positive bias range has been represented for a different QD pair. The highlighted region shows four lines which anticross each other on changing the electric field. Similar anticrossing behaviour has been associated to the presence of quantum tunnelling in other QDM systems. Its precise extent in our case is currently under investigation.

4.5. InAs(P)/InP nanostructures into InP nanoholes

Semiconductor QD based on the InAs/InP heteroepitaxial system are interesting for their use in laser devices emitting at 1.55 μm, compatible with optical fiber communications [110]. However, under usual MBE conditions the self-assembling process in this system leads to the formation of QWr elongated along the [*1-10*] direction on InP (001) surfaces, which are in principle more efficient for elastic energy relaxation [111]. In this sense, this section presents a technological approximation that by the use of a

nanohole template performed by DE at high T_s and further InAs deposition, permits to obtain novel low density ($2.5x10^{-8}$ cm^{-2}) InAs(P) QD on InP (001) substrates.

In particular, once obtained a template on an epitaxial InP (001) surface, **Figure 4.33 (a)**, two different samples corresponding to the deposition of 0.5 ML (**Figure 4.33 (b)**) and 1 ML of InAs (**Figure 4.33 (c)**) were grown for QD formation into the nanoholes. As the nanoholes density on InP substrates is low, $2.5x10^{-8}$ cm^{-2}, the growth conditions used for this InAs deposition resembled those for the formation of isolated QWr on InP substrates [112]. In particular, it was used a pulsed sequence in which during 1 s amounts of 0.1 ML of InAs are alternated with As beam exposure periods of 2 s. During this process $BEPAs_4$ and T_s are maintained at $3x10^{-6}$ Torr and 480ºC, respectively.

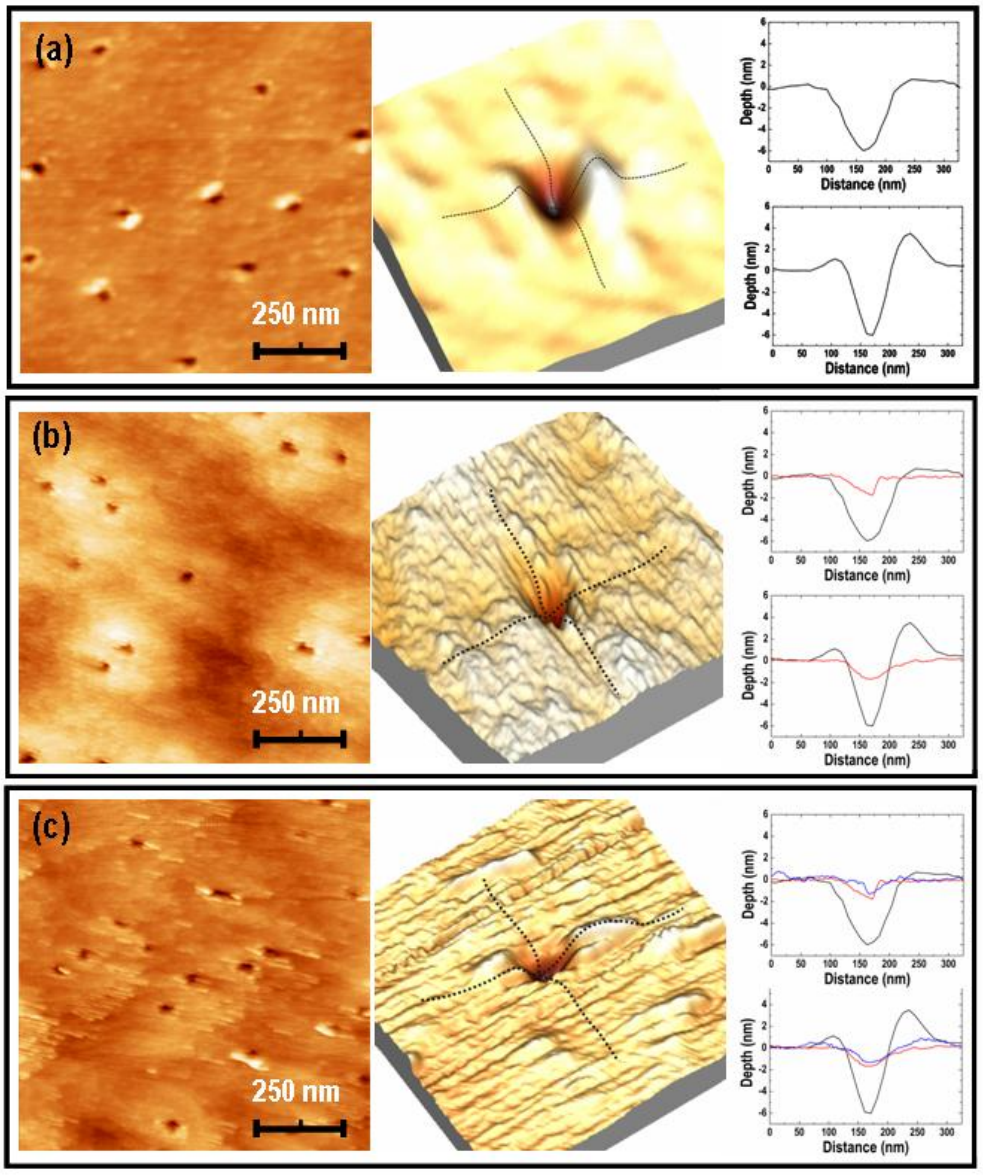

Figure 4.33. (a) 2 µm x 2 µm AFM image showing an InP nanoholes template performed by droplet epitaxy technique. **(b)** 2 µm x 2 µm AFM image showing the resulting surface once an amount of 0.5 ML of InAs is deposited on the nanoholes template. **(c)** 2 µm x 2 µm AFM image showing the resulting surface once an amount of 1 ML of InAs is deposited on the nanoholes template. At the right of these images, more detailed 0.5 µm x 0.5 µm AFM images and their corresponding profiles along [110] and [1-10] directions are also shown.

Figure 4.33 (b) shows a 2 μm x 2 μm AFM image of the resulting surface after an amount of 0.5 ML of InAs has been deposited on the nanoholes template. It can be observed that the initial nanoholes, with mean dimensions of 59±10 nm in diameter and 5.7±0.9 nm in depth (data from section 4.3.2), are now filled with InAs as their depth, measured from an average performed in a 5 μm x 5 μm AFM image, is clearly reduced to 1.3±0.4 nm (profiles in **Figure 4.33 (b)**). On the other hand, the diameter presents a similar mean value of 56±7 nm. Besides this filling effect at the nanoholes, it can be observed in the AFM image the assembling of short InAs dashes or elongated structures, at the boundaries of the nanoholes. In this sense, the initial stage on the formation of isolated QWr has been previously studied [113] showing the areas of high density of steps, as it is the surrounding of a nanohole, as the location of preferential nucleation for InAs material.

On the other hand, **Figure 4.33 (c)** shows a 2 μm x 2 μm AFM image of the resulting surface once an amount of 1 ML of InAs is deposited on the nanoholes template. At the right of this image a detailed 0.5 μm x 0.5 μm AFM image is also shown. In a similar way to that obtained for the case of depositing 0.5 ML of InAs, the nanoholes depth from these images clearly points out a filling effect since its mean value is reduced to 1.3 ± 0.3 nm (profiles in **Figure 4.33 (b)**). As in the previous case, the diameter of the nanoholes remains unaltered despite of the InAs material deposition. It is noticeable in this case, that apart from the nanoholes filling effect, well-defined QWr are formed at the boundaries of the nanoholes and at the mono-atomic terraces of the InP (001) epitaxy surface [114].

From these results it can be derived that once the InAs material at the nanoholes reaches an equilibrium size, new InAs material starts to nucleate at different locations of the substrate inducing the formation of well formed QWr.

Once capped by a 20 nm-thick InP layer, the nanostructures nucleated at the nanoholes can be optically studied by measuring their PL emission at low temperature. **Figure 4.34** shows the PL at 25 K for the case of depositing 0.5 ML of InAs on the substrate (black line) and the emission obtained at the same experimental conditions for the case of depositing 1 ML of InAs (gray line). Both curves have been obtained at an excitation power of 5 mW and λ_{exc}= 808 nm.

For the case of depositing 0.5 ML of InAs (black line) it can be observed three main emission peaks at energies A_1= 1.03 eV, A_2= 0.99 eV and A_3= 0.76 eV. According to previous PL studies on InAs QWr on InP(001) substrates [106], emission at A_1 and A_2 would correspond to InAs WL regions of different thicknesses and to the formation of QWr of a few ML in height. The third peak at A_3= 0.76 eV / 1.63 μm presents a much wider FWHM of 70 meV and, according to previous studies in the InAs/InP system [112], it is rather unlikely that it would come from the formation of QWr or QW with monolayer fluctuations. Thus, it can be ascribed the emission at A_3 to those nanostructures that partially fill the previously formed nanoholes.

For the case of 1ML of InAs deposited, six different peaks are observed at the following energies, B_1= 1.03 eV, B_2= 0.97 eV, B_3= 0.92 eV, B_4= 0.87 eV, B_5= 0.84 eV and B_6= 0.75 eV. In this case, it seems clear that the emission at B_1 and B_2 would correspond to the formation of a WL of InAs, while the emissions at B_3, B_4

and B_5, would come from the formation of QWr at the substrate terraces, as seen in **Figure 4.33** The peak labelled B_6 is close in energy (0.75 eV) and width (FWHM= 88meV) to peak A_3 from the sample with 0.5 ML of InAs deposited. This correspondence indicates that B_6 comes from the emission of QD formed into the nanoholes.

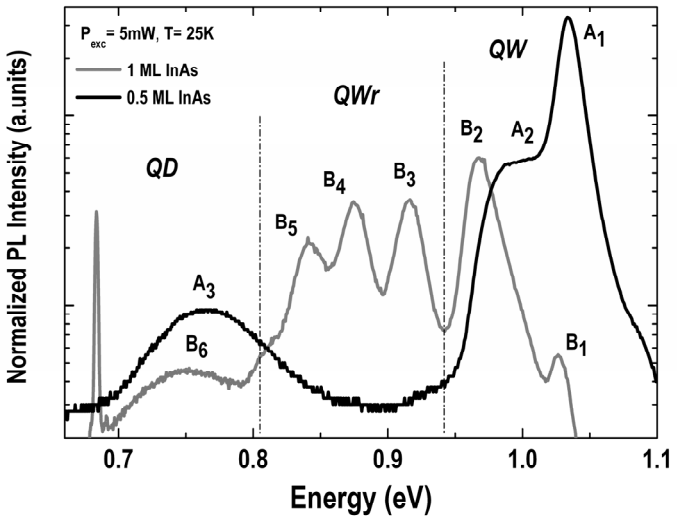

Figure 4.34. Photoluminiscence at 25 K for the cases of depositing 0.5 ML (black line) and 1 ML (gray line) of InAs on the InP nanoholes template. Both curves are obtained at an excitation power of 5 mW.

The low PL intensity observed for the emission band ascribed to QD in both samples, could be related to the low density of nanostructures achieved with the used DE technique, $2x10^8$ cm^{-2}.

On the other hand, it can be noticed that the QD emission for 0.5 ML and 1 ML of InAs slightly differs in energy, A_3= 0.76 eV and B_6= 0.75 eV. This effect corroborates the similar filling of the nanoholes for the different amount of InAs material at the nanoholes previously measured by AFM topography.

Additional information on the QD nature can be obtained by their dependence with the excitation power. In this direction, **Figure 4.35** shows the QD PL emission as a function of the excitation power when 0.5 ML of InAs are deposited into the nanoholes.

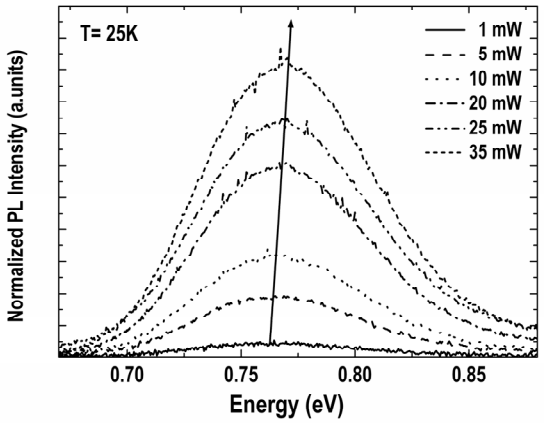

Figure 4.35. Photoluminiscence as a function of the excitation power for the case of depositing 0.5 ML of InAs on the InP nanoholes template. A black arrow is depicted highlighting the observed PL peak tendency.

This sample was chosen to show the QD emission properties because in the case of 1 ML of InAs deposited, the presence of other emission close to the QD emission makes more difficult any interpretation of the results.
The PL results show that as the excitation power is increased from 1 mW to 35 mW, the PL band widens towards its high energy side and the peak is slightly blue-shifted to 1.60 μm. A black arrow in the figure accounts for this behaviour. This effect can be ascribed to state filling effects in these nanostructures and it has been previously observed for InAs/InP QD grown by MBE [115].

In summary, according to these results, it can be concluded that low density, $2x10^8$ cm^{-2}, InAs(P) QD on InP(001) substrates have been obtained via the selective nucleation of InAs material into InP nanoholes previously formed by a DE *nanodrilling* process.

4.6. Ga(As)Sb/GaAs Qrings

In this section, a development of the droplet epitaxy technique that leads to the formation of Ga(As)Sb Qrings is presented. The photoluminescence properties of these nanostructures showing characteristic features of a type II band alignment are also presented in section 4.7.1.

As it was presented in section 4.2, the formation mechanism of different GaAs nanostructures by DE is based on the initial formation of metallic Ga droplets and their posterior crystallization under As flux. In particular, it is proposed [62-64] that at high substrate temperatures, the key mechanisms in this process are the As diffusion rate from the underneath GaAs substrate through the Ga droplet, the diffusion of Ga forming the droplet towards the substrate surface and the formation of GaAs at the Ga droplet boundaries. In the framework of this theory a natural novel approach to form new nanostructures is to change the V-group element under which the Ga droplets are crystallized. In this context, a new experimental procedure to form Ga(As)Sb-GaAs Qrings by using an antimony flux is hereinafter described.

As in the rest of the growth protocols carried out by DE technique in this thesis, the initial GaAs substrate is firstly flattened. To do this, a 0.5 μm-thick undoped GaAs buffer layer was grown at a growth rate of 0.5 ML/s, $BEPAs_4$ of $2x10^{-6}$ Torr and T_s= 580ºC by MBE. At this moment, Ts is decreased to 500ºC and the Ga shutter opened during 7 s, at an equivalent GaAs rate of 0.5 ML/s, for Ga droplet formation. For the Ga droplets crystallization the sample is exposed to Sb during 60 s at BEPSb of $3x10^{-7}$ Torr and T_s= 200ºC. For PL characterization, a similar sample with the nanostructures capped by a 47 nm-thick GaAs layer deposited at r_g= 0.5 ML/s was grown. The initial 60 ML of GaAs (17 nm) were grown at T_s= 450ºC with a $BEPAs_2$ of $2x10^{-6}$ Torr by ALMBE. The cap layer is completed by MBE growth at T_s= 580ºC and $BEPAs_4$ of $2x10^{-6}$ Torr. For morphological studies, an additional layer of Qrings was grown on this surface, using the above described conditions.

Figure 4.36 shows the AFM topography of a sample with a single uncapped layer of nanostructures. It is observed ring-like structures with a density ρ= $2x10^8$ cm^{-2}; the average dimensions, measured respect to the flat surface (rms=0.24 nm), are 2.9±0.4 nm in contour height and 128±5 nm and 176±5 nm in outside diameter along the [*110*] and [*1-10*] GaAs directions respectively. At their centre, a hole with an average depth of 1.0±0.3 nm is also observed (**Figure 4.36 (b)**).

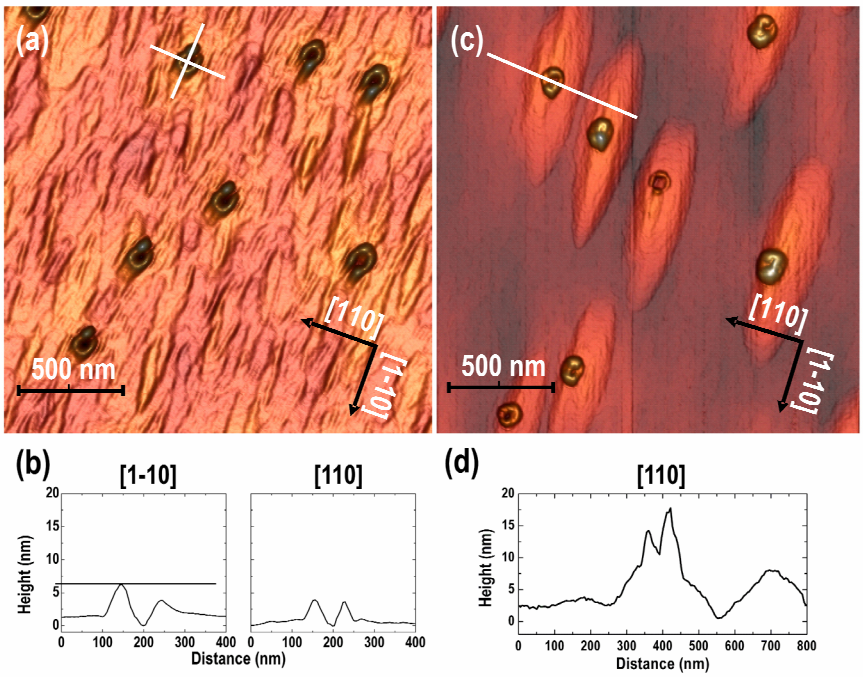

Figure 4.36. (a) 2 μm x 2 μm 3D AFM image showing Ga(As)Sb nanostructures grown by droplet epitaxy technique. **(b)** Profiles along the [1-10] and [110] directions of uncapped Q-rings. **(c)** 2 μm x 2 μm AFM image of Ga(As)Sb nanostructures grown on a 47 nm thick GaAs layer that caps the nanostructures shown on (a). **(d)** Profile along the [110] direction of a Qring nucleated on top of a mound.

A side lobe with an average height of 5.9±0.4 nm is always formed at the edge of each ring as can be noticed in the AFM profiles of **Figure 4.36 (b)**. These side lobes systematically appear along the [*1-10*] direction. A similar observation has been made for InAs Qrings, but in the later case, two symmetrical lobes along the [*1-10*] direction are observed for each ring [116]. These morphological features are expected to strongly influence the optical properties of the nanostructures, as vertical confinement together with composition are the key factors that determine the emission wavelength.

The AFM topography in **Figure 4.36 (c)** shows Qrings formed on the 47 nm-thick cap layer surface. We observe that Q-rings are nucleated on top of elongated structures formed on an otherwise flat GaAs surface (rms roughness of 0.4 nm). The elongated structures (mounds) appear with exactly the same density measured for the uncapped Qrings. Their typical dimensions are 900 nm along the [*1-10*] direction, 200 nm along the [*110*] direction and 9 nm in height (**Figure 4.36 (d)**). Similar mounds have been reported

for layers grown on top of both strained and unstrained nanostructures [117,119] (experiments related to the formation and use of these structures are presented in section 4.7). As it is well known, these mounds result from the incomplete planarization of the initial condition of the surface upon further growth [120,121]. The Qrings formed on the mounds are 124±11 nm in outside diameter along [*110*], with holes 9.3±3.5 nm in depth referred to the highest point of the ring.

As clearly observed, the nanostructures nucleated on the flat GaAs (001) surface (**Figure 4.36 (a)** and **(c)**) present a superior uniformity in size and shape in comparison with those nucleated on top of mounds (**Figure 4.36 (b)** and **(d)**). As already commented, the formation of GaAs Qrings using droplet epitaxy at high substrate temperature (T_s= 500ºC) has been explained on the basis of Ga droplets reacting chemically with the GaAs substrate because of an imbalance of As chemical potential [62]. In our particular growth process, under antimony atmosphere, the crystallization will be more complex, involving not only As incorporation in the Ga droplets from the GaAs matrix, but also incorporation of Sb from the incoming flux and the accompanying strain due to lattice mismatch. The nanostructures grown on top of the mounds will be influenced not only by the above mentioned effects, but also by the non uniform surface stress profile due to the buried nanostructures. This additional stress contribution may affect the kinetics of the process, leading to the observed dispersion in the Qrings shape (**Figure 4.36 (c)**).

The nucleation of a Qring on top of each mound, and the mounds themselves, suggest the existence of a buried nanostructure underneath. An univocal correspondence between the surface mounds and the buried Qrings would lead to a selective formation of new nanostructures on top of these, as the strain induced by the capped nanostructures would create a local energy minima for Sb atoms incorporation at that location [122]. Besides the results obtained by AFM (**Figure 4.36 (c)**), TEM results illustrate this effect. **Figure 4.37** depicts a 002 dark field cross section image obtained close to [*110*] zone axis of a buried Qring correlated with a ring on surface. This correlation is systematically found for other Qrings analyzed in the electron transparent area of the TEM sample.

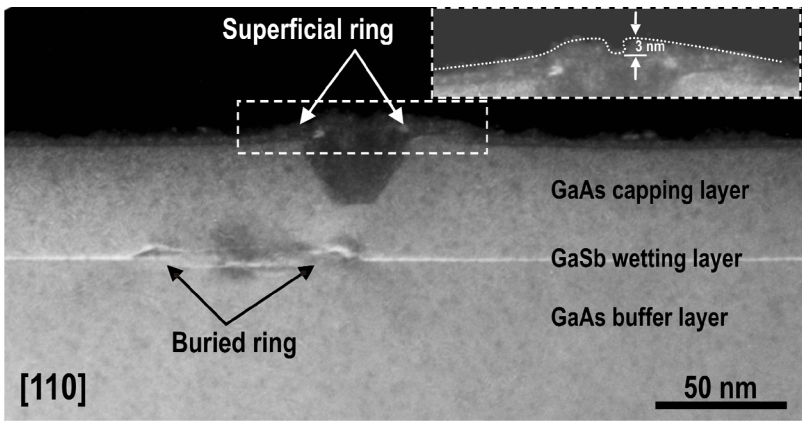

Figure 4.37. 002 dark field cross sectional TEM micrograph showing a buried Ga(As)Sb Qring correlated with a superficial ring, obtained close to [110] zone axis. The inset in the figure shows the 3 nm-deep hole of the Qring at the surface, in good agreement with the AFM measurements. (TEM image taken at University of Cádiz).

A shift of 43 nm along [*1-10*] is measured between both rings (buried and superficial). The superficial valley at the surface (see inset of **Figure 4.37**) corresponds with that measured by AFM. The dark contrast with trapezoidal shape observed in the nanostructure at the surface would be related to the central opening of the original nanohole formed during the strain-mediated crystallization under Sb. As a previous related work indicates [119], these TEM results reflect the complex droplet crystallization process, which in this case also incorporates the effect of strain. A deeper study is needed to fully understand the observed TEM images. However, it seems rather clear that the hole of the superficial Qring is located above one of the lobes of the buried one (probably the higher lobe), indicating that below each mound there is one Qring. This effect is exceptionally important in the fabrication of new devices framework as it was commented in chapter 1.

4.6.1. Optical properties

The PL signal of the buried nanostructures is shown in **Figure 4.38 (a)** (blue line) together with that of a reference sample (black line). The reference sample was grown reproducing the same experimental conditions (Sb pressure, substrate temperature and growth interruptions) except for the Ga deposition that was restricted to 1 ML to avoid any formation of droplets.

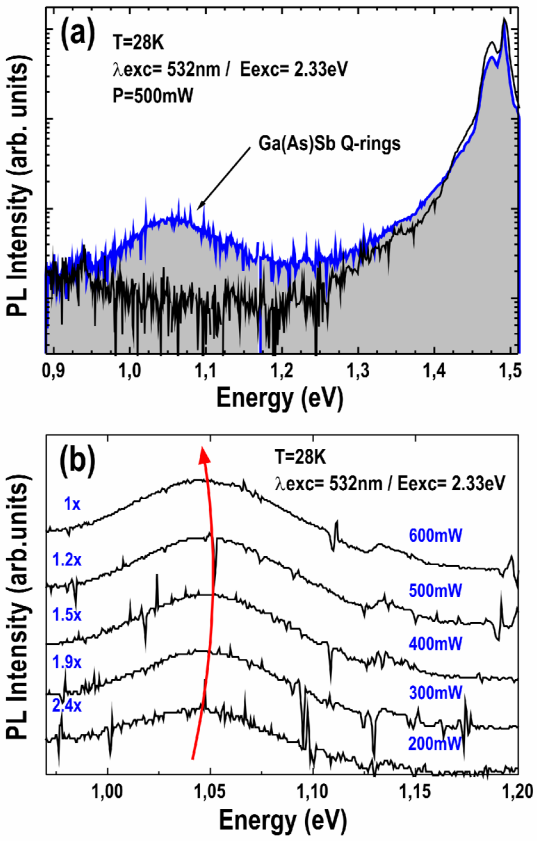

Figure 4.38. (a) Photoluminescence spectra from the Ga(As)Sb Qring-like nanostructures sample (blue line) as compared to a reference sample that does not contain nanostructures (black line). The nanostructures show a broad band emission at 1.05 eV. **(b)** Evolution of the Qrings PL as a function of the excitation power.

At high energies, the emission from the substrate and a peak at 1.45 eV possibly due to the emission from a Ga(As)Sb wetting layer is observed in both samples [123]. A broad PL band at 1.05 eV is observed only in the sample with nanostructures. Owing to the low density of nanostructures and the type II band alignment between GaAs and GaSb, a low PL intensity is expected. In terms of wavelength and PL width, this emission is similar to that previously reported from GaSb quantum dots in a GaAs matrix [124,125]. A FWHM of 104 meV for this band at an excitation power of 500 mW is obtained by fitting the PL signal with a Gaussian line-shape.

Figure 4.38 (b) shows the PL emission of the nanostructures as a function of the excitation power. The curved arrow drawn on this figure is a guide to the eye to show the behaviour of the peak energy, obtained by a Gaussian fit, with increasing excitation power. At the lower excitation powers used in this experiment (<400 mW), a 7 meV blue-shift is observed. This blue-shift clearly points out the type II band alignment of these nanostructures [124,125]. For excitation powers above 400 mW, a red-shift of the PL peak energy is observed, most likely due to sample heating.

In summary, as a conclusion of this section, DE technique has been extended to the formation of low density type II Ga(As)Sb Qrings on GaAs(001) surfaces with optical properties according to a type II band alignment. Moreover, the capping process of these nanostructures has resulted in the formation of surface mounds that are correlated with the buried nanostructures as demonstrated by TEM analysis, permitting a very useful surface identification of the optically active Qrings. This result might be highly relevant for the fabrication of quantum optics devices, since it will allow defining the exact active nanostructure location with a simple and non-destructive surface topography measurement.

4.7. Top surface identification of buried nanostructures

In the previous section, results on the top surface localization of Ga(As)Sb Qrings after the growth of a GaAs cap layer were presented. At the used growth conditions for capping, the underneath nanostructures seems to be revealed at the top surface as mounding features that match their density (**Figure 4.36 (c)**). In particular, the correspondence between these mounds and the buried nanostructures was confirmed by different approaches as TEM analysis and posterior selective strain-driven formation of new Qrings on top of them at distances, 47 nm in this case, at which the strain profile seems to be well propagated.

For the case of using QD into the nanoholes, section 4.4.1, when these nanostructures are capped at typical MBE conditions (using $T_s = T_{QD}$ and $BEPAs_4 = 2x10^{-6}$ Torr at the initial stages and $T_s = 580ºC$ and $BEPAs_4 = 2x10^{-6}$ Torr at the end of the process) coalesced mounds are always observed, **Figure 4.39**, preventing any possible surface localization of the active nanostructures [120,121].

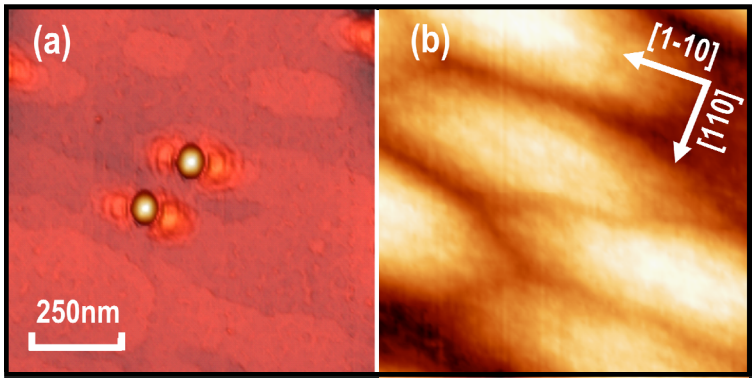

Figure 4.39. 1 µm x 1 µm AFM images corresponding to: **(a)** the initial InAs QD formed into GaAs nanoholes fabricated by droplet epitaxy and **(b)** the GaAs surface that results after capping by 50 nm of GaAs the nanostructures shown in (a) at typical MBE growth conditions. Coalesced mounds elongated along the [1-10] GaAs direction are observed.

However, previous works have tackled the possibility of a QD top surface localization by the growth of stacked structures [126] or, more recently, by evaluating the morphology of the surface once a single layer of nanostructures is capped [117]. In this direction, this section shows that a capping process similar to that previously described for Ga(As)Sb Qrings, can be extended to the case of growing InAs QD into GaAs nanoholes, as it is confirmed by the formation of mounds that unequivocally mark the buried nanostructures. In particular, by performing different experiments of preferential nucleation of InAs at the top mounding surface, the strain-driven process that originates new QD located on top of the mounds is explored as a function of the amount of InAs deposited and the distance to the buried nanostructures. By using ALMBE growth technique [90], the univocal correspondence between buried nanostructures and surface morphological features can be maintained up to 100 nm-thick cap layers.

Finally, in the framework of these results, the different contributions to the surface chemical potential that influence on the selective preferential growth, see section 2.1.4, are also discussed.

The experimental procedure started, as in previous works presented in this thesis, with the growth of a 0.5 µm-thick undoped GaAs buffer layer at r_g= 0.5 ML/s, BEP As_4 of 2x10^{-6} Torr and T_s= 580ºC on GaAs(001) substrates by MBE. The rms roughness of this surface is typically 0.24 nm. T_s is then decreased to 500ºC and a GaAs nanohole template is firstly performed, see section 4.3.1. During the last annealing step of this process the In cell was also opened, depositing in this case 1.4 ML of InAs at r_g= 0.01 ML/s, for QD formation inside the nanoholes. After this InAs deposition, the arsenic cell was maintained opened until completion of the nanoholes 6 min-annealing step. After this, the surface was finally exposed during 1 min to As_2 flux at T_s= 510ºC and BEP 5x10^{-7} Torr.

The as-formed QD with dimensions, 14±1 nm in height and 50±2 nm in diameter, and density 2x10^8 cm^{-2}, were then capped by a GaAs layer. As previously commented, in order to study the resulting cap layer surface morphology and its possible correlation with the buried nanostructures, the thickness of these GaAs cap layers is varied. In particular, 25 and 100 nm-thick GaAs layers are grown at r_g= 0.5 ML/s. In the

case of the 25 nm-thick cap layer growth, the initial 15 nm are grown at T_s= 510ºC and changing BEP As_2 from 5x10^{-7} to 9x10^{-7} Torr while the remaining 10 nm of GaAs are grown at typical MBE conditions; T_s= 580ºC and $BEPAs_4$= 2x10^{-6} Torr. In the case of the 100 nm-thick cap layer growth, the first 20 nm of GaAs are initially grown as before, T_s= 510ºC and changing $BEPAs_2$ from 5x10^{-7} to 9x10^{-7} Torr, while the remaining 80 nm are deposited, with the aim of preserving as much as possible the initial morphology, by ALMBE growth technique at T_s= 450ºC and $BEPAs_4$= 2x10^{-6} Torr. Finally, after the growth of these 25 or 100 nm-thick GaAs cap layers, different amounts of InAs are deposited for AFM topographic studies. In particular 1.4, 1.5 and 1.6 ML of InAs are deposited at 0.01 ML/s, T_s= 510ºC and $BEPAs_4$= 5x10^{-7} Torr.

Figure 4.40 shows 1 µm x 1 µm 3D AFM images for capped InAs QD and posterior top surface InAs deposition. The corresponding images are distributed in columns for the two different cap layer thicknesses grown (25 and 100 nm) and in files for the different amount of InAs deposited (0, 1.4, 1.5 and 1.6 ML). As advanced, it is firstly noticeable in this image that the surface morphology obtained just after capping the nanostructures is similar with independence of the GaAs cap layer thickness (**Figure 4.40 (a, e)**). In particular mounds elongated along the [*1-10*] direction with the same density of the initial buried nanostructures, ρ= 2x10^8 cm^2, are observed. Their dimensions are around 700 nm in length, 150 nm in width and 7 nm in height for the 25 nm-thick cap layer and similar dimensions excepting a smaller height of 4 nm for the 100 nm-thick cap layer.

As already commented for the growth of Qrings, if it is assumed that the mounds are formed just over the buried nanostructures, new InAs material deposited on the surface would preferentially nucleate at their top if the underlying strain is large enough. In the case of 25 nm-thick cap layers, **Figure 4.40 (b)** shows the AFM image after depositing 1.4 ML of InAs on the mounding surface shown in **Figure 4.40 (a)**. Notice that the amount of InAs deposited is far from the critical for QD formation on a flat surface (~1.7 ML) at the used experimental conditions. This means that QD formation is not expected unless InAs growth is enhanced at preferential sites of the surface. It can be observed in the derivate image at the inset of this figure an incipient InAs cluster appearing on top of each mound. This effect corroborates the supposition about the presence of an underneath QD in each of the formed mounds. If more InAs is deposited, **Figure 4.40 (c)**, bigger nanostructures are formed on the top of these surface features. **Figure 4.40 (d)** shows the situation when 1.6 ML of InAs are deposited on this surface. At this amount of InAs, besides the QD formed at the top of the mounds, QD decorating the lateral slopes of the mounds are observed. This result indicates that once the QD at the top surface reach an equilibrium size, the steps forming the mounds become new preferential nucleation sites for InAs material. This result means that besides strain-related nucleation mechanisms, another energetic term that takes into account also curvature-related considerations has to be considered [122].

Figure 4.40 (e) shows, the top surface that results after capping the nanostructures with a 100 nm-thick GaAs layer. As above commented, mounds with the same density as that of the buried nanostructures and similar dimensions than those previously observed for the case of 25 nm-thick cap layers are

obtained. However, in this case, when 1.4, 1.5 and 1.6 ML of InAs are deposited on this surface, no nucleation of InAs QD at the top of mounds is observed (**Figure 4.40 (f), (g)** and **(h)** respectively). This result indicates that the non-uniform strain profile induced by the buried nanostructures does not propagate up to a distance of 100 nm and, therefore, only curvature-related effects are then to be considered in the preferential nucleation of InAs.

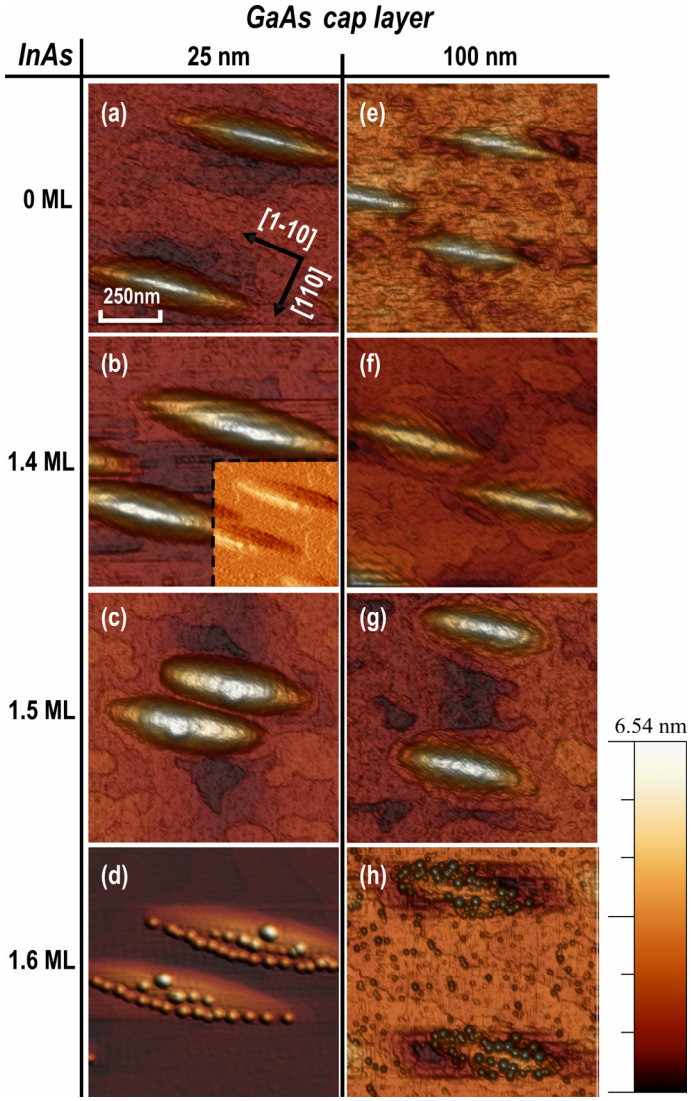

Figure 4.40. Left column shows 1 μm x 1 μm 3D AFM images of the mounding surface that results after growing a 25 nm-thick-GaAs cap layer **(a)** and after 1.4ML **(b)**, 1.5ML **(c)** and 1.6ML **(d)** of InAs is deposited on this surface. The inset in **(b)** corresponds to the derivative image and is shown to highlight the presence of 3D InAs nuclei forming at the top of the mounds.
Right column shows 1 μm x 1 μm 3D AFM images of the mounding surface that results after growing a 100nm-thick-GaAs cap layer **(e)** and after 1.4ML **(f)**, 1.5ML **(g)** and 1.6ML **(h)** of InAs is deposited on this surface. See text for the growth conditions of the different GaAs cap layers.

In a similar way to the previous result obtained for the thinner cap layer (25 nm, **Figure 4.40 (d)**), when the amount of InAs deposited is 1.6 ML (**Figure 4.40 (h)**), that is, when the critical thickness for the growth of QD on a flat surface is almost reached, well defined QD at the lateral slopes of the mounds are obtained together with the formation of incipient InAs islands all over the surface. It can be noticed that, as a difference to that observed in **Figure 4.40 (d)**, QD are now nucleated at both slopes of the mounds. The fact that only one of the slopes of the mounds is nucleating QD in the case of growing 25 nm-thick GaAs cap layers seems to be related to the presence of a large non-uniform strain profile at that short distances

from the buried nanostructures. However, more experiments are needed to a better understanding on this surface anisotropic effect [127].

Related to the formation of the mounds, it is well known that after covering nanostructures by a thin cap layer, the surface is not fully flattened and the resulting surface show characteristic mounding features [120,121]. For increasing cap layer thickness, these mounds start to enlarge and coalesce making difficult any possible correspondence with the buried nanostructures. However, as commented in section 1.1.3, for most applications thick cap layers and top surface localization are strictly necessary. In this sense, the results shown here demonstrate that under an appropriate growth process the morphology of the cap layer surface does not depend on its thickness. In particular, by using a low enough initial substrate temperature (510ºC in this case) and posterior ALMBE growth mode, it has been possible to inhibit any enlargement and further coalescence of the mounds at cap layer thickness as large as 100 nm.

In summary, as a conclusion of this section and the previous results on top surface localization presented for Ga(As)Sb Qrings, it can be stated that after an appropriate capping process of optically active nanostructures, the resulting GaAs top surface shows a characteristic mounding morphology that permits a direct localization of the buried nanostructures even at cap layer thickness as large as 100 nm. Moreover, different experiments based on the nucleation of new top surface nanostructures once 25, 50 and 100 nm-thick GaAs cap layers were grown, have permitted a direct observation of the different preferential sites for nanostructures formation when strain and/or curvature related mechanisms are involved.

As already highlighted, these results are of high technological interest for the fabrication of devices as single photon emitters, where the location of the nanostructures after being buried is a critical issue.

4.8. Summary and conclusions

In this chapter results on the formation of templates of nanoholes on GaAs (001) and InP (001) substrates by the use of a novel patterning technique based on the DE growth mode at high T_s have been presented. In particular, by using the templates themselves and by incorporating As and Sb as V-group element during the droplets crystallization process it has been possible to obtain a great variety of nanostructures of different nature and configuration. In particular, it has been presented the formation and the structural and optical emission studies of the following nanostructures:

In the InAs/GaAs system by filling the previously formed nanoholes:

- InAs/GaAs QD.

  A controlled selective nucleation of InAs material into the GaAs nanoholes has been obtained, permitting the formation of highly homogeneous QD distributions. In particular, by

using a pattern of nanoholes with a fixed depth and density, it has been possible to select the size of the QD, as a function of the amount of InAs deposited, at the same time that the density of nanostructures is maintained. This is a key advantage of this process over the self-assembling process of nanostructures formation, where these two parameters are inter-dependent.

Moreover, the μ-PL study points out to a highly symmetric shape of these nanostructures and the probable presence of arsenic vacancies in the QD surroundings that could be ascribed to an incomplete droplet crystallization.

- InAs/GaAs Vertical Quantum Dot Molecules (VQDM).

  The size control of the InAs QD formed at the nanoholes, has been used to obtain symmetric and asymmetric vertically coupled quantum molecules with a low enough density suitable for their single spectroscopic study. TEM results show in detail the structural configuration of these nanostructures. Additionally, n-intrinsic Schottky diode structures to control the injection of electrons in these nanostructures by an external applied electric field have been fabricated.

- InAs/GaAs Lateral Quantum Dot Molecules (LQDM).

  We have obtained that the As pressure used during InAs deposition into the nanoholes is a key parameter in order to control the formation of either single QD or QD pairs, permitting up to a 98% of pairs of QD occupancy, at the nanoholes.

  The ensemble photoluminescence (PL) emission of the QD pairs, in particular, the evolution of the emission peak and FWHM as a function of excitation intensity and temperature, shows these QD pairs as laterally coupled quantum systems.

  Moreover, preliminary μ-PL study of these nanostructures as a function of a laterally applied electric field has shown anticrossing spectra indicating the presence of quantum tunnelling phenomena between these QDM.

In the InAs/InP system by filling the previously formed nanoholes:

- InAs(P)/InP QD.

  In a similar way to that obtained by the nucleation of InAs QD into GaAs nanoholes, novel low density, $2x10^8$ cm^{-2}, InAs QD on InP (001) substrates have been obtained via the selective nucleation of InAs material into InP nanoholes. The PL emission of these nanostructures shows a broad band centred at 1.65 μm.

In the Ga(As)Sb/GaAs system by varying the atmosphere at which the droplets are crystallized.

- Ga(As)Sb Qrings.

  In this case, the droplet epitaxy technique has been extended to the formation of low density Ga(As)Sb Qrings on a GaAs surface showing good optical properties according to a type II band alignment. Moreover, the capping process of these nanostructures resulted in the formation of surface mounds that are correlated with the buried nanostructures, as demonstrated by TEM analysis.

Related to this last result on the identification of Ga(As)Sb buried nanostructures once capped, it has been also developed in this work a growth method that permits to extend this effect to the InAs/GaAs system. In particular, it has been demonstrated that this mounding morphology can be maintained even at cap layer thickness as large as 100 nm. Moreover, different experiments based on the nucleation of new top surface nanostructures once 25, and 100 nm-thick GaAs cap layers were grown, have permitted a direct observation of the different preferential sites for nanostructures formation when strain and/or curvature related mechanisms are involved.

References

[1] N. Koguchi, S. Takahashi, and T. Chikyow, J. Cryst. Growth **111**, 688 (1991).
[2] N. Koguchi, K. Ishige, and S. Takahashi, J. Vac. Sci. Technol. B **11(3)**, 787 (1993).
[3] N. Koguchi, and K. Ishige, Jpn. J. Appl. Phys. **32**, 2052 (1993).
[4] M. Volmer, and A. Z. Weber, Phys. Chem. **199**, 277 (1926).
[5] C. H. Lee, C. Park, H. J. Lee, K. S. Lee, S. J. Park, C. G. Park, S. K. Noh, and N. Koguchi, Jpn. J. Appl. Phys. **37**, 7158 (1998).
[6] K. Watanabe, N. Koguchi, and Y. Gotoh, Jpn. J. Appl. Phys. **2(39)**, L79 (2000).
[7] S. Sanguinetti, K. Watanabe, T. Tateno, M. Wakaki, N. Koguchi, T. Kuroda, F. Minami, and M. Gurioli, Appl. Phys. Lett. **81**, 613 (2002).
[8] S. Sanguinetti, K. Watanabe, T. Kuroda, F. Minami, Y. Gotoh, and N. Koguchi, J. Cryst. Growth, **242**, 321 (2002).
[9] S. Sanguinetti, K. Watanabe, T. Tateno, M. Gurioli, P. Werner, M. Wakaki, and N. Koguchi, J. Cryst. Growth, **253**, 71 (2003).
[10] V. Mantovani, S. Sanguinetti, M. Guzzi, E. Grilli, M. Gurioli, K. Watanabe, and N. Koguchi, J. Appl. Phys. **96**, 4416 (2004).
[11] T. Mano, K. Watanabe, S. Tsukamoto, H. Fujioka, M. Oshima, and N. Koguchi, J. Cryst. Growth **209**, 504 (2000).
[12] J. M. Lee, D. H. Kim, H. Hong, J. C. Woo, and S. J. Park, J. Cryst. Growth **212**, 67 (2000).
[13] S. Sanguinetti, T. Mano, M. Oshima, T. Tateno, M. Wakaki, and N. Koguchi, Appl. Phys. Lett. **81**, 3067 (2002).
[14] J. S. Kim, and N. Koguchi, Appl. Phys. Lett. **85**, 5893 (2004).
[15] T. Satoh, and K. Yamaguchi, Jap. J. Appl. Phys. **44(4B)**, 2672 (2005).
[16] J. S. Kim, M. Kawabe, and N. Koguchi, Appl. Phs. Lett. **88**, 072107 (2006).
[17] B. L. Liang, Zh. M. Wang, J. H. Lee, K. Sablon, Y. I. Mazur, and G. J. Salamo, Appl. Phys. Lett. **89**, 043113 (2006).

[18] J. H. Lee, Zh. M. Wang, B. L. Liang, K. A. Sablon, N. W. Strom, and G. J. Salamo, Semicond. Sci. Technol. **21**, 1547 (2006).
[19] J. H. Lee, Zh. M. Wang, N. W: Strom, Y. I. Mazur, and G. J. Salamo, Appl. Phys. Lett. **89**, 202101 (2006).
[20] B. L. Liang, Zh. M. Wang, J. H. Lee, K. A. Sablon, Y. I. Mazur, and G. J. Salamo, Appl. Phys. Lett. **89**, 213103 (2006).
[21] Zh. M. Wang, B. L. Liang, K. A. Sablon, J. H. Lee, Y. I. Mazur, N. W. Strom, and G. J. Salamo, Small **2**, 235 (2007).
[22] N. W. Strom, Zh. M. Wang, J. H. Lee, Z. Y. AbuWaar, Y. I. Mazur, and G. J. Salamo, Nanoscale Res. Lett. **2**, 112 (2007).
[23] C. Zhao, Y. H. Chen, B. Xu, P. Jin, and Z. G. Wang, Appl. Phys. Lett. **91**, 033112 (2007).
[24] P. Alonso-González, B. Alén, D. Fuster, Y. González, L. González, and J. Martínez-Pastor, Appl. Phys. Lett. **91**, 163104 (2007).
[25] Y. I. Mazur, Z. Y. AbuWaar, T. D. Mishima, J. H: Lee, G. G. Tarasov, B. L. Liang, V. G. Dorogan, M. E. Ware, Zh. M. Wang, M. B. Johnson, and G. J. Salamo, J. Appl. Phys. **104**, 044310 (2008).
[26] P. Alonso-González, D. Fuster, L. González, J. Martín-Sánchez, and Y. González, Appl. Phys. Lett. **93**, 183106 (2008).
[27] J. S. Kim, M. S. Jeong, C. C. Byeon, D. K. Ko, J. L. Lee, J. S. Kim, I. S. Kim, and N. Koguchi, Appl. Phys. Lett. **88**, 241911 (2006).
[28] T. Mano, T. Kuroda, M. Yamagiwa, G. Kido, K. Sakoda, and N. Koguchi, Appl. Phys. Lett. **89**, 183102 (2006).
[29] K. Kuroda, T. Kuroda, K. Watanabe, T. Mano, K. Sakoda, G. Kido, and N. Koguchi, Appl. Phys. Lett. **90**, 051909 (2007).
[30] Ch. Heyn, A. Stemmann, A. Schramm, H. Welsch, W. Hansen, and Á. Nemcsics, Appl. Phys. Lett. **90**, 203105 (2007).
[31] K. Kuroda, T. Kuroda, K. Sakoda, G. Kido, and N. Koguchi, Physica E **40**, 310 (2007).
[32] T. Kihira, S. Tanaka, M. Yamagiwa, Y. Ogawa, F. Minami, and N. Koguchi, J. of Luminiscence **128**, 800 (2008).
[33] T. Mano, K. Mitsuishi, Y. Nakayama, T. Noda, and K. Sakoda, Appl. Sur. Sci. **254**, 7770 (2008).
[34] M. Abbarchi, M. Gurioli, A. Vinattieri, S. Sanguinetti, M. Bonfanti, T. Mano, K. Watanabe, T. Kuroda, and N. Koguchi, J. Appl. Phys. **104**, 023504 (2008)..
[35] T. Kuroda, N. Ikeda, T. Mano, Y. Sugimoto, T. Ochiai, K. Kuroda, S. Ohkouchi, N. Koguchi, K. Sakoda, and K. Asakawa, Appl. Phys. Lett. **93**, 111103 (2008).
[36] M. Abbarchi, C. A. Mastrandea, T. Kuroda, T. Mano, K. Sakoda, N. Koguchi, S. Sanguinetti, A. Vinattieri, and M. Gurioli, Phys. Rev. B **78**, 125321 (2008).
[37] M. Abbarchi, F. Troiani, C. Mastrandea, G. Goldoni, T. Kuroda, T. Mano, K. Sakoda, N. Koguchi, S. Sanguinetti, A. Vinattieri, and M. Gurioli, Appl. Phys. Lett. **93**, 162101 (2008).
[38] Zh. M. Wang, K. Holmes, Y. I. Mazur, K. A. Ramsey, and G. J. Salamo, Nanoscale Res. Lett. **1**, 57 (2006).
[39] T. Mano, T. Noda, M. Yamagiwa, and N. Koguchi, Thin Solid Films **515**, 531 (2006).
[40] M. Yamagiwa, T. Mano, T. Kuroda, T. Tateno, K. Sakoda, G. Kido, and N. Koguchi, Appl. Phys. Lett. **89**, 113115 (2006).
[41] R. Pomraenke, C. Lienau, Y. I. Mazur, Zh. M. Wang, B. L. Liang, G. G. Tarasov, and G. J. Salamo, Phys. Rev. B **77**, 075314 (2008).
[42] J. H. Lee, K. Sablon, Zh. M. Wang, and G. J. Salamo, J. Appl. Phys. **103**, 054301 (2008).
[43] K. A. Sablom, J. H: Lee, Zh. M. Wang, J. H: Shultz, and G. J. Salamo, Appl. Phys. Lett. **92**, 203106 (2008).
[44] B. L. Liang, Zh. M. Wang, X. Y. Wang, J. H. Lee, Y. I. Mazur, C. K. Shih, and G. J. Salamo, ACS Nano **2(11)**, 2219 (2008).
[45] P. Alonso-González , J. Martín-Sánchez, Y. González, B. Alén, D. Fuster and L. González, ACS Cryst. Growth Des.9(5), 2525 (2009).
[46] T. Mano, and N. Koguchi, J. Cryst. Growth **278**, 108 (2005).

[47] Z. Gong, Z. C. Niu, S. S. Huang, Z. D. Fang, B. Q. Sun, and J. B. Xia, Appl. Phys. Lett. **87**, 093116 (2005).
[48] T. Noda, and K. Koguchi, Physica E **32**, 550 (2006).
[49] Z. Y. AbuWaar, Y. I. Mazur, J. H. Lee, Zh. M. Wang, and G. J. Salamo, J. Appl. Phys. **101**, 024311 (2007).
[50] T. Mano, T. Kuroda, K. Mitsuishi, M. Yamagiwa, X. J. Guo, K. Furuya, K. Sakoda, and N. Koguchi, J. Cryst. Growth **301**, 740 (2007).
[51] J. H. Lee, Zh. M. Wang, K. Sablon, and G. J. Salamo, ACS Cryst. Growth Des. **8(2)**, 690 (2007).
[52] J. H. Lee, Zh. M. Wang, M. E. Ware, K. C. Wijesundara, M. Garrido, E. A. Stinaff, and G. J. Salamo, ACS Cryst. Growth Des. **8(6)**, 1945 (2008).
[53] C. Zhao, Y. H. Chen, B. Xu, C. G. Tang, Z. G. Wang, and F. Ding, Appl. Phys. Lett. **92**, 063122 (2008).
[54] A. Stemman, Ch. Heyn, T. Köppen, T. Kipp, and W. Hansen, Appl. Phys. Lett. **93**, 123108 (2008).
[55] P. Alonso-González, L. González, D. Fuster, Y. González, A. G. Taboada, J.M. Ripalda, A. M. Beltrán, D. L. Sales, T. Ben and S. I. Molina, ACS Cryst.Growth Des. **9(2)**, 1216 (2009).
[56] T. Mano, T. Kuroda, S. Sanguinetti, T. Ochiai, T. Tateno, J. Kim, T. Noda, M. Kawabe, K. Sakoda, G. Kido, and N. Koguchi, Nano Letters **5(3)**, 425 (2005).
[57] T. Kuroda, T. Mano, T. Ochiai, S. Sanguinetti, K. Sakoda, G. Kido, and N. Koguchi, Phys. Rev. B **72**, 205301 (2005).
[58] T. Kuroda, T. Mano, T. Ochiai, S. Sanguinetti, T. Noda, K. Kuroda, K. Sakoda, G. Kido, and N. Koguchi, Physica E **32**, 46 (2006).
[59] J. H. Lee, Zh. M. Wang, Z. Y. AbuWaar, N. W. Strom, and G. J. Salamo, Nanotechnology **17**, 3973 (2006).
[60] S. Huang, Z. Niu, Z. Fang, H. Ni, Z. Gong, and J. Xia, Appl. Phys. Lett. **89**, 031921 (2006).
[61] Ch. Heyn, A. Stemman, A. Schramm, H. Welsch, and W. Hansen, Phys. Rev. B **76**, 075317 (2007).
[62] Zh. M. Wang, B. L. Liang, K. A. Sablon, and G. J. Salamo, Appl. Phys. Lett. **90**, 113120 (2007).
[63] C. Z. Tong and S. F. Yoon, Nanotechnology **19**, 365604 (2008).
[64] X. L. Li, and G. W. Yang, J. Phys. Chem. C **112**, 7693 (2008).
[65] R. I. Schawarz, Thin solid Films **L3**, 66 (1980).
[66] S. Koshiba, Y. Nakamura, M. Tsuchiya, H. Noge, H. Kano, Y. Nagamune, T. Noda, and H. Sakaki, J. Appl. Phys. **76**, 4138 (1994).
[67] X. Q. Shen, D. Kishimoto and T. Nishinaga, Jap. J. Appl. Phys. **33**, 11 (1994).
[68] A. Y. Cho and J. R. Arthur, Prog. Solid State Chem. **10**, 157 (1975).
[69] R. D. Piner, J. Zhu, F. Xu, S. Hong, C. A. Mirkin, Science **283**, 661 (1999).
[70] S. Raymond, S. Fafard, P. J. Poole, A. Wojs, P. Hawrylak, and S. Charbonneau, Phys. Rev. B **54**, 11548 (1996).
[71] M. Grundmann, N. N. Ledentsov, O. Stier, J. Böhrer, D. Bimberg, V. M. Ustinov, P. S. Kopev, and Zh. I. Alferov, Phys. Rev. B **53**, 10509 (1996).
[72] A. Greilich, M. Schwab, T. Berstermann, T. Auer, R. Oulten, D. Yakovlev, M. Bayer, V. Stavarache, D. Reuter, and A. Wieck, Phys. Rev. B 73, 045323 (2006).
[73] B. Alén, J. Martínez-Pastor, D. Granados, and J. M. García, Phys. Rev. B **72**, 155331 (2005).
[74] H. Yasuda, F. Matsukura, Y. Ohno, H. Ohno, Appl. Sur. Sci. **166**, 413 (2000.
[75] K. Yamaguchi, K. Yujobo, and T. Kaizu, Jap. J. Appl. Phys. **39**, L1245 (2000).
[76] B. J. Riela, K. Hinzera, S. Moisaa, J. Frasera, P. Finniea, P. Piercyb, S. Fafarda, Z.R. Wasilewskia, J. Crys. Growth **236**, 145 (2002).
[77] R. Songmuang, S. Kiravittaya, O. G. Schmidt, Appl. Phys. Lett. **82**, 2892 (2003).
[78] "Phd thesis: Espectroscopía óptica confocal aplicada al estudio de cajas cuánticas aisladas de InAs", B. Alén, Universidad de Valencia (2004).
[79] R. M. Stevenson, R. J. Young, P. Atkinson, K. Cooper, D. A. Ritchie, and A. J. Shields, Nature **439**, 179 (2006).
[80] H. Q. Xu, and U. Lindefelt, Phys. Rev. B **41**, 5979 (1990).
[81] E. S. Moskalenko, K. F. Karlsson, P. O. Holtz, B. Monemar, W. V. Schoenfeld, J. M. Garcia, and P. M. Petroff, Phys. Rev. B **64**, 085302 (2001).

[82] G. Muñoz-Matutano, B. Alén, J. Martínez-Pastor, L. Seravalli, P. Frigeri, and S. Franchi, Nanotechnology **19**, 145711 (2008).
[83] A. Hartmann, Y. Ducommun, E. Kapon, U. Hohenester, and E. Molinari, Phys. Rev. Lett. **84**, 5648 (2000).
[84] D. V. Regelman, E. Dekel, D. Gershoni, E. Ehrenfreund, A. J. Williamson, J. Shumway, A. Zunger, W. V. Schoenfeld, and P. M. Petroff, Phys. Rev. B **64**,
165301 (2001).
[85] P. Borri, W. Langbein, U. Woggon, M. Schwab, M. Bayer, S. Fafard, Z. Wasilewski, and P. Hawrylak, Phys. Rev. Lett. **91**, 267401 (2003).
[86] H. J. Krenner, M. Sabathil, E. C. Clark, A. Kress, D. Schuh, M. Bichler, G. Abstreiter, and J. J. Finley Phys. Rev. Lett. **94**, 057402 (2005).
[87] E. A. Stinaff, M. Scheibner, A. S. Bracker, I. V. Ponomarev, V. L. Korenev, M. E. Ware, M. F. Doty, T. L. Reinecke, D. Gammon, Science **311**, 636 (2006).
[88] G. G. Tarasov, Z. Y. Zhuchenko, M. P. Lisitsa, Y. I. Mazur, Zh. M. Wang, G. J. Salamo, T. Warming, D. Bimberg, and H. Kissel, Semiconductors **40**, 79 (2006).
[89] Z. R. Wasilewski, S. Fafard, J. P. McCaffrey, J.Cryst.Growth **201**, 1131 (1999)
[90] F. Briones, L. González, and A. Ruiz, Appl. Phys. A: Solids Surf. **A49**, 729 (1989).
[91] D. Granados, Thesis "Nanoestructuras autoensambladas mediante epitaxia por haces moleculares de InAs sobre substratos de GaAs(001): De los puntos cuánticos a los anillos cuánticos" IMM-UAM (2006).
[92] H. A. Nilsson, C. Thelander, L. Froberg, J. B. Wagner, and L. Samuelson, Appl. Phys. Lett. **89**, 163101 (2006).
[93] M. T. Bjork, B. J. Ohlson, T. Sass, A. I. Persson, C. Thelander, M. H. Magnusson, K. Deppert, L. Wallenberg, and L. Samuelson, Appl. Phys. Lett. **80**, 1058 (2002).
[94] N. Skold, L. S. Karlsson, M. W. Larsson, M. E. Pistol, W. Selfert, J. Tragardh, and L. Samuelson, Nano Lett **5**, 1943 (2005).
[95] Q. Zhu, K. F. Karlsson, E. Pelucchi, and E. Kapon, Nano Lett **7**, 2227 (2007).
[96] J. Ristic, E. Calleja, A. Trampert, S. Fernández-Garrido, C. Rivera, U. Jahn, and K. H. Ploog, Phys. Rev. Lett **94**, 146102 (2005).
[97] H. J. Krenner, C. E. Pryor, J. He, and P. M. Petroff, Nano Lett **8**, 1750 (2008).
[98] J. He, H. J. Krenner, C. Pryor, J. P. Zhang, Y. Wu, D. G. Allen, C. M. Morris, M. S. Sherwin, and P. M. Petroff, Nano Lett **7**, 802 (2007).
[99] P. Y. Yo and M. Cardona "Fundamentals of Semiconductors" Springer.
[100] T. Kita, O. Wada, H. Ebe, Y. Nakata, and M. Sugawara, Jap. J. Appl. Phys. **41**, L1143 (2002).
[101] P. Jayavel, T. Kita, O. Wada, H. Ebe, M. Sugawara, Y. Arakawa, Y. Nakata, and T. Akiyama, Jap. J. Appl. Phys. **44**, 2528 (2005).
[102] L. Robledo, J. Elzerman, G. Jundt, M. Atatüre, A. Högele, S. Fält, A. Imamoglu, Science **320**, 772 (2008)..
[103] G. J. Beirne, C. Hermannstädter, L. Wang, A. Rastelli, O. G. Schmidt, and P. Michler, Phys. Rev. Lett. **96**, 137401 (2006).
[104] L. Wang, A. Rastelli, S. Kiravittaya, P. Atkinson, F. Ding, C. C. B. Bufon, C. Hermannstädter, M. Witzany, G. J. Beirne, P. Michler, and O. G. Schmidt, N. J. Phys. **10**, 045010 (2008).
[105] X.Q. Shen, D. Kishimoto, and T. Nishinaga, Jpn. J. Appl. Phys. **33**, 11 (1994).
[106] B. L. Liang, P. S. Wong, N. Nuntawong, A. R. Albrecht, J. Tatebayashi, T. J. Rotter, G. Balakrishnan, and D. L. Huffaker, Appl. Phys. Lett. **91**, 243106 (2007).
[107] T. v. Lippen, A. Yu. Silov, and R. Nötzel, Phys.Rev.B **75**, 115414 (2007).
[108] S. Sanguinetti, M. Henini, M. Grassi, M. Capizzi, P. Frigeri, and S. Franchi, Phys.Rev.B **60**, 8276 (1999).
[109] B. Alén, J. Martínez-Pastor, D. Granados, and J. M. García Phys. Rev. B **72**, 155331 (2005)
[110] F. Suárez, D. Fuster, L. González, Y. González, J. M. García, and M. L. Dotor, Appl. Phys. Lett. 89, 091123 (2006).
[111] J. M. García, L. González, M. U. González, J. P. Silveira, Y. González, and F. Briones, J. Cryst. Growth **227**, 975 (2001).

[112] B. Alén, J. Martínez-Pastor, A. García-Cristóbal, L. González, and J.M. García, Appl. Phys. Lett. **78**, 4025 (2001).
[113] S. I. Molina, M. Varela, D. L. Sales, T. Ben, J. Pizarro, P. L. Galindo, D. Fuster, Y. González, L. González, and S. J. Pennycook, Appl. Phys. Lett. **91**, 143112 (2007).
[114] B. Alén, D. Fuster, Y. González, L. González, and J. Martínez-Pastor, Appl. Phys. Lett. **89**, 233126 (2006).
[115] D. Fuster, A. Rivera, B. Alén, P. Alonso-González, Y. González, and L. González. Appl. Phys. Lett. **94**, 163104 (2009).
[116] N. A. J. M. Kleemans, I. M. A. Bominaar-Silkens, V. M. Fomin, V. N. Gladilin, D. Granados, A. G. Taboada, J. M. García, P. Offermans, U. Zeitler, P. C. M. Christianen, J. C. Maan, J. T. Devreese, P. M. Koenraad, Phys. Rev. Lett. **99**, 146808 (2007).
[117] K. Hennessy, A. Badolato, M. Wigner, D. Gerace, M. Atatüre, S. Gulde, D. Fält, E. L. Hu, A. Imamoglu, Nature **445**, 896 (2007).
[118] P. Atkinson, S. Kiravittaya, M. Benyoucef, A. Rastelli, O. G. Schmidt, Appl. Phys. Lett. **93**, 101908 (2008).
[119] Zh. M. Wang, Yu. I. Mazur, K. A. Sablon, T. D. Mishima, M. B. Johnson, and G. J. Salamo, Phys. Stat. sol. **6**, 281 (2008).
[120] A. Ballestad, B. J. Ruck, M. Adamcyk, T. Pinnington, and T. Tiedje, Phys. Rev. Lett. **86**, 2377 (2001).
[121] G. Constantini, A. Rastelli, C. Manzano, P. Acosta-Diaz, R. Songmuang, G. Katsaros, O. G. Schmidt, K. Kern, Phys. Rev. Lett. **96**, 226106 (2006).
[122] B. Yang, F. Liu, M. G. Lagally, Phys. Rev. Lett. **92**, 025502 (2004).
[123] M. C. Lo, S. J. Huang, C. P. Lee, S. D. Lin, S. T. Yen, Appl. Phys. Lett. **90**, 243102 (2007).
[124] D. Alonso-Álvarez, B. Alén, J. M. García, J. M. Ripalda, Appl. Phys. Lett. **91**, 263103 (2007).
[125] R. Suzuki, A. Hogg, Y. Arakawa, J. Appl. Phys. **85**, 8349 (1999).
[126] A. Badolato, K. Hennessy, M. Atatüre, J. Dreiser, E. Hu, P. M. Petroff, A. Imamouglu, Science **308**, 1158 (2005).
[127] H. Hu, H. J. Gao, and F. Liu, Phys. Rev. Lett. **101**, 216102 (2008).

V

CONCLUSIONS

5.1. CONCLUSIONS

In this thesis three different technological approaches have been developed for the fabrication of III-V semiconductor nanostructures on patterned substrates with a certain control of density, size, shape, composition and spatial distribution.

The main conclusions obtained for each approximation are described below.

· In a first approach, a mask based on a nanoporous alumina layer was fabricated by the electrochemical anodization of an epitaxial 1 μm-thick Al layer on GaAs (001) substrate, previously grown by MBE at RT. In particular, by extending the electrochemical process a few nanometers in the GaAs substrate, a large area distribution of nanoholes on the substrate was finally obtained.
The main conclusions derived from this process are the following:

- The epitaxial growth of a 1 μm-thick Al layer on GaAs (001) substrates by MBE, results in a very flat (rms= 1.51 nm) (110) oriented monocrystalline layer.

- The anodic oxidation of these thin Al layers is enough to yield an alumina surface with ordered nanoholes suitable to be transferred to the underlying GaAs substrate.

- The Al layer acts as a good mask preserving the flatness and cleanliness of the substrate as demonstrated once the formed alumina is removed.

- The pregrowth sample treatment with atomic H and the posterior GaAs buffer layer growth at low substrate temperature, yield an optimal surface suitable for further InAs QD formation.

- All InAs QD formed; nucleate into the nanoholes, demonstrating that the whole process is valid for site-selective formation of QD.

· In a second approach, a novel combination of ozone oxidation/oxide etching process was developed to transfer to a GaAs substrate the order of a patterned resin layer, previously designed by laser interference lithography (LIL). This process can be extended to any other lithographic technique.
The main conclusions derived from this work can be summarized as follows:

- A novel ozone oxidation / citric acid oxide etching process allows transferring a pattern designed by an external lithographic technique with nanometric resolution.

- The different *ex situ* (oxygen plasma, developer, remover and HF dips) and *in situ* (atomic H irradiation) pregrowth preparation processes of the patterned substrate and the posterior GaAs buffer layer growth at low substrate temperature, yield an optimal semiconductor surface suitable for further selective formation of InAs QD.

- The nucleation, and therefore, the QD distribution on a GaAs surface is imposed by the pattern transferred from the resin layer.

- The most important, the PL emission from the QD ordered by this technological process is similar in intensity to those formed by a self-assembled process on a reference sample.

· In a third approach results on the formation of templates of nanoholes on GaAs (001) and InP (001) substrates by the use of a novel patterning technique based on the droplet epitaxy growth process at high T_s have been presented. In particular, by using the templates themselves and by incorporating As and Sb as V-group element during the droplets crystallization process it has been possible to obtain a great variety of nanostructures of different nature and configuration. In particular, we have studied the formation, structural and optical emission characteristics of the following nanostructures:

In the InAs/GaAs system by filling the previously formed nanoholes:

- InAs/GaAs QD.

  A controlled selective nucleation of InAs material into the GaAs nanoholes has been obtained, permitting the formation of highly homogeneous QD distributions. In particular, by using a pattern of nanoholes with a fixed depth and density, it has been possible to select the size of the QD, as a function of the amount of InAs deposited, at the same time that the density of nanostructures is maintained. This is a key advantage of this process over the self-assembling process of nanostructures formation, where these two parameters are inter-dependent.
  Moreover, the μ-PL study points out to a highly symmetric shape of these nanostructures and the probable presence of arsenic vacancies in the QD surroundings that could be ascribed to an incomplete droplet crystallization.

- InAs/GaAs Vertical Quantum Dot Molecules (VQDM).

  The size control of the InAs QD formed at the nanoholes, has been used to obtain symmetric and asymmetric vertically coupled quantum molecules with a low enough density suitable for their single spectroscopic study. TEM results show in detail the structural configuration of these nanostructures. Additionally, n-intrinsic Schottky diode structures to control the injection of electrons in these nanostructures by an external applied electric field have been fabricated.

- InAs/GaAs Lateral Quantum Dot Molecules (LQDM).

  We have obtained that the As pressure used during InAs deposition into the nanoholes is a key parameter in order to control the formation of either single QD or QD pairs, permitting up to a 98% of pairs of QD occupancy, at the nanoholes.
  The ensemble photoluminescence (PL) emission of the QD pairs, in particular, the evolution of the emission peak and FWHM as a function of excitation intensity and temperature, shows these QD pairs as laterally coupled quantum systems.
  Moreover, preliminary μ-PL study of these nanostructures as a function of a laterally applied electric field has shown anticrossing spectra indicating the presence of quantum tunnelling phenomena between these QDM.

In the InAs/InP system by filling the previously formed nanoholes:

- InAs(P)/InP QD.

  In a similar way to that obtained by the nucleation of InAs QD into GaAs nanoholes, novel low density, $2x10^8$ cm^{-2}, InAs QD on InP (001) substrates have been obtained via the selective nucleation of InAs material into InP nanoholes. The PL emission of these nanostructures shows a broad band centred at 1.65 μm.

In the Ga(As)Sb/GaAs system by varying the atmosphere at which the droplets are crystallized.

- Ga(As)Sb Qrings.

  In this case, the droplet epitaxy technique has been extended to the formation of low density Ga(As)Sb Qrings on a GaAs surface showing good optical properties according to a type II band alignment. Moreover, the capping process of these nanostructures resulted in the formation of surface mounds that are correlated with the buried nanostructures, as demonstrated by TEM analysis.

Related to this last result on the identification of Ga(As)Sb buried nanostructures once capped, it has been also developed in this work a growth method that permits to extend this effect to the InAs/GaAs system. In particular, it has been demonstrated that this mounding morphology can be maintained even at cap layer thickness as large as 100 nm. Moreover, different experiments based on the nucleation of new top surface nanostructures once 25, and 100 nm-thick GaAs cap layers were grown, have permitted a direct observation of the different preferential sites for nanostructures formation when strain and/or curvature related mechanisms are involved.

Conclusiones

En este trabajo de tesis se han abordado tres distintas aproximaciones tecnológicas con el objetivo de fabricar nanoestructuras semiconductoras III-V con control en tamaño, densidad, forma, composición y distribución espacial sobre substratos grabados.

Las conclusiones más importantes para cada una de la aproximaciones llevadas a cabo se resumen a continuación.

· En una primera aproximación se ha fabricado una máscara de alumina porosa mediante la oxidación anódica de una capa de aluminio de 1 micra de espesor crecida epitaxialmente por MBE sobre un substrato de GaAs (001). Continuando el proceso electroquímico unos pocos nanómetros en el GaAs se ha conseguido fabricar un patrón de nanoagujeros en área extensa.

Las principales conclusiones derivadas de este trabajo son las siguientes:

- El crecimiento epitaxial de aluminio por MBE sobre substratos de GaAs (001) da lugar a capas planas (rms= 1.51 nm) de aluminio monocristalino con orientación predominante (110).

- El proceso de oxidación anódica llevado a cabo en capas de aluminio muy delgadas (1 micra) ha permitido obtener superficies de alúmina porosa con una buena distribucion ordenada de nanoagujeros.

- La capa de aluminio/alúmina preserva la planitud y limpieza del substrato.

- El tratamiento de la superficie grabada con hidrógeno atómico y el posterior crecimiento de una capa tampón de GaAs a baja temperatura dejan una superficie óptima para la posterior nucleación selectiva de InAs.

- Los puntos cuánticos formados nuclean 100% en los nanoagujeros fabricados.

· En una segunda aproximación tecnológica se ha desarrollado un proceso combinado de oxidación con ozono y ataque químico para transferir el orden previamente establecido por litografía de interferencia láser en una máscara a un substrato de GaAs. Este proceso de transferencia puede ser extendido a cualquier otra técnica litográfica.

Las principales conclusiones derivadas de este trabajo son las siguientes:

- El proceso combinado de oxidación selectiva con ozono y posterior ataque químico con ácido cítrico permite transferir con resolución nanométrica un grabado previamente diseñado con una técnica de litografía externa.

- Los diferentes tratamientos de la superficie grabada, tanto *ex situ* (plasma de oxígeno, revelador y ácido fluorhídrico) como *in situ* (hidrógeno atómico, dentro de la campana de crecimiento), previos al crecimiento epitaxial dejan una superficie óptima para el crecimiento selectivo de puntos cuánticos de InAs.

- La nucleación y por tanto distribución de puntos cuánticos obtenida es impuesta por el patrón transferido a través de la máscara utilizada..

- La intensidad de fotoluminiscencia de los puntos cuánticos obtenidos sobre una muestra grabada es similar a la de unos puntos autoensamblados.

· En una tercera aproximación tecnológica se ha utilizado una novedosa técnica de grabado *in situ* basada en la técnica de crecimiento por epitaxia de gotas (del inglés *droplet epitaxy*) que permite la formación de distribuciones de nanoagujeros de baja densidad ($2x10^8$ cm^{-2}) sobre substratos de GaAs (001) e InP (001). Mediante el uso de los nanoagujeros y la incorporación de antimonio durante su proceso de formación ha sido posible obtener una gran variedad de nanoestructuras semiconductoras. En particular se ha estudiado la formación y propiedades de las siguientes estructuras:

En el sistema InAs/GaAs:

- Puntos cuánticos de InAs/GaAs.

  Se ha conseguido un gran control en el crecimiento selectivo de InAs en agujeros de GaAs permitiendo la formación de distribuciones de puntos cuánticos muy homogéneas. En particular, controlando la cantidad de InAs depositada sobre los nanoagujeros ha sido posible obtener un cierto control en el tamaño del punto cuántico resultante, y por tanto en su emisión óptica, al mismo tiempo que la densidad total de nanoestructuras formadas se mantiene igual a la de nanoagujeros iniciales. Este resultado es una clara ventaja frente a los procesos de formación autoensamblados en los que estos dos parámetros son interdependientes.

- Moléculas verticales de puntos cuánticos de InAs/GaAs

  El control obtenido en el tamaño de los puntos cuánticos formados en los nanoagujeros se ha utilizado para la formación controlada de moléculas de puntos cuánticos acoplados verticalmente. La estructura de estas moléculas se ha estudiado en detalle mediante microscopía de transmisión de electrones. También se han fabricado dispositivos diodo de tipo Schottky que mediante la aplicación de un campo eléctrico externo permiten obtener un control en la inyección de electrones en estas nanoestructuras y así poder estudiar su naturaleza cuántica en óptimas condiciones.

- Moléculas laterales de puntos cuánticos de InAs/GaAs.

  Mediante el control del tipo de arsénico (As_2 o As_4) utilizado durante la deposición de InAs se ha obtenido un gran control en la formación de puntos cuánticos simples o moléculas laterales de puntos cuánticos dentro de los nanoagujeros.

En el sistema InAs/InP:

- Puntos cuánticos de InAs(P)/InP.

Mediante un proceso similar al llevado a cabo en el sistema InAs/GaAs, se ha conseguido obtener distribuciones de baja densidad de puntos cuánticos de InAs en nanoagujeros formados sobre substratos de InP (001)..

En el sistema Ga(As)Sb/GaAs:

- Anillos cuánticos de Ga(As)Sb.

  Mediante la incorporación de antimonio en el proceso de cristalización de gotas de galio, se ha conseguido extender la técnica de epitaxia por gotas para la obtención de anillos cuánticos de Ga(As)Sb de baja densidad sobre substratos de GaAs (001). Además, el proceso de tapado de estas nanoestructuras con GaAs da como resultado la formación de montículos superficiales que están correlacionados con las nanoestructuras enterradas permitiendo así, su localización en superficie.

List of publications

- ***"Ordered InAs QDs using prepatterned substrates by monolithically integrated porous alumina"*** P. Alonso-González, J.Martín-Sánchez, M.S. Martín-González, Y. González, and L. González. J. Crystal Growth **294**, 168 (2006).

- **"New process for high optical quality InAs quantum dots grown on patterned GaAs(001) substrates"** P. Alonso-González, L. González, Y. González, D. Fuster, I. Fernández-Martínez, J. Martín-Sánchez and L. Abelmann. Nanotechnology **18**, 355302 (2007).

- **"Formation and optical characterization of single InAs quantum dots grown on GaAs nanoholes"** P. Alonso-González, B. Alén, D. Fuster, Y. González, L. González and J. Martínez-Pastor. Appl. Phys. Lett. **91**, 163104 (2007).

- **"Low density InAs quantum dots with control in energy emission and top surface location"** P. Alonso-González, D. Fuster, L. González, J. Martín-Sánchez and Y. González. Appl. Phys. Lett. **93**, 183106 (2008).

- **"Improvement of InAs quantum dots optical properties in close proximity to GaAs(001) substrate surface"** J. Martín-Sánchez, Y. González, P. Alonso-González and L. González. J. Crystal Growth **310**, 46768 (2008).

- **"Formation of spatially Adressed Ga(As)Sb Quantum Rings on GaAs(001) substrates by Droplet Epitaxy"** P. Alonso-González, L. González, D. Fuster, Y. González, A. G. Taboada, J.M. Ripalda, A. M. Beltrán, D. L. Sales, T. Ben and S. I. Molina. ACS Cryst. Growth Des. **9(2)**, 1216 (2009).

- **"Formation of lateral low density In(Ga)As quantum dot pairs in GaAs nanoholes"** P. Alonso-González , J. Martín-Sánchez, Y. González, B. Alén, D. Fuster and L. González. ACS Cryst. Growth Des**. 9(5)**, 2525 (2009).

- **"Site-controlled lateral arrangements of InAs quantum dots grown on GaAs(001) patterned substrates by AFM local oxidation nanolithography"** J. Martín-Sánchez, P. Alonso-González, J. Herranz, Y. González and L. González. Nanotechnology **20**, 125302 (2009).

- **"Direct formation of InAs quantum dots grown on InP (001) by solid-source molecular beam epitaxy"** D. Fuster, A. Rivera, B. Alén, P. Alonso-González, Y. González, and L. González. Appl. Phys. Lett. **94**, 133106 (2009).

- **"Surface localization of buried III-V semiconductor nanostructures"** P. Alonso-González, L. González, D. Fuster, J. Martín-Sánchez, and Y. González. Nanoscale Res. Lett. (Accepted) (2009).

- **"Single photon emission from site-controlled InAs quantum dots grown on GaAs patterned substrates"** J. Martín-Sánchez, G. Muñoz-Matutano, B. Alén, Y. González, P. Alonso-González, J. Canet-Ferrer, D. Fuster, J. Herranz, L. González, J. Martínez-Pastor, and F. Briones. ACS Nano (Accepted) (2009).